

EVALUATING STABLE ISOTOPE AND
GEOCHRONOLOGIC TECHNIQUES FOR
PALEOCLIMATE RECONSTRUCTION: CASE STUDY
OF THE SANTA CRUZ FORMATION, ARGENTINA

by

Robin B. Trayler

A dissertation
submitted in partial fulfillment
of the requirements for the degree of
Doctor of Philosophy in Geosciences
Boise State University

December 2018

Robin B. Trayler

SOME RIGHTS RESERVED



This work is licensed under a Creative
Commons Attribution 4.0 International
License.

BOISE STATE UNIVERSITY GRADUATE COLLEGE

DEFENSE COMMITTEE AND FINAL READING APPROVALS

of the dissertation submitted by

Robin B. Trayler

Dissertation Title: Evaluating Stable Isotope and Geochronological Techniques
for Paleoclimate Reconstruction: Case Study of the Santa
Cruz Formation, Argentina

Date of Final Oral Examination: 30 November 2018

The following individuals read and discussed the dissertation submitted by student Robin B. Trayler, and they evaluated his presentation and response to questions during the final oral examination. They found that the student passed the final oral examination.

Matthew J. Kohn, Ph.D.	Chair, Supervisory Committee
Mark Schmitz, Ph.D.	Member, Supervisory Committee
Richard F. Kay, Ph.D.	Member, Supervisory Committee
Christopher L. Hill, Ph.D.	Member, Supervisory Committee

The final reading approval of the dissertation was granted by Matthew J. Kohn, Ph.D., Chair of the Supervisory Committee. The dissertation was approved by the Graduate College.

ACKNOWLEDGEMENTS

I would like to thank everyone who assisted me during my time at Boise State. In particular, my advisor Matt Kohn and committee members, Mark Schmitz, Christopher Hill, and Richard Kay were of tremendous help. I also thank my fellow students Jake Anderson, Claire Harrigan, and Darin Schwartz for many helpful discussions, proof reading, and walks. Finally, I could not have done this without the support and love of Elizabeth Black.

ABSTRACT

Stable isotope analysis has become the method of choice for many studies investigating the paleoecology and paleoclimate of fossil mammal faunas. While organic tissues (collagen, keratins, proteins) persist for $< 10^5$ years highly mineralized tooth enamel is resistant to alteration and degradation and faithfully preserves its isotopic composition for millions ($> 10^6$) years. Reconstructing past climates from these records relies on both understanding both micro-scale mechanisms of isotope incorporation into individual teeth, and macro-scale changes in isotope compositions over hundreds of thousands or millions of years. In this dissertation I address three questions.

First, how does the geometry and timing of tooth enamel mineralization affect isotope compositions? Tooth enamel mineralization occurs in two stages with different geometries and proportions of chemical components. In chapter one I present oxygen isotope data and high-resolution major element compositional maps of forming tooth enamel to clarify the process of enamel mineralization. Oxygen isotope results show that enamel records the isotopic composition of only second stage mineralization. Given this, ideal enamel sampling strategies should follow the geometry of second stage mineralization. High resolution maps of calcium density for several teeth reveal that enamel mineralizes at a high angle relative to the underlying dentine, suggesting that existing techniques are appropriate.

Second, how can geochronology and stratigraphic information be convolved to strengthen interpretations of paleoclimate proxy records? Many reconstructions of past

climates rely on proxy records (e.g. pollen, isotope samples) distributed through a stratigraphic section. Interpreting these data in a global context relies on both the ability to determine the absolute age of some stratigraphic positions, and a model that describes the relationship between stratigraphic position and age, allowing the age of unknown positions to be determined. In chapter two I report new U-Pb ages for several volcanic tuffs from the Santa Cruz Formation of southern Argentina. U-Pb data commonly exhibit complexities which make existing age-depth models unsuitable. I modified an existing age-depth model to better account for variations in absolute age, relative age, and the complex age uncertainties that often arise from magmatic crystal populations.

Finally, I present a case study from the Santa Cruz Formation, Argentina. Fossil rich sediments span the initiation of the mid-Miocene climatic optimum, the most recent period of greenhouse conditions in the Cenozoic. carbon isotope-based estimates of mean annual precipitation reveal a progressive aridification of Patagonia with precipitation decreasing prior to the mid-Miocene climatic optimum. This trend is interrupted by the onset of greenhouse conditions which drove a rebound in precipitation and increase in global temperatures.

TABLE OF CONTENTS

ACKNOWLEDGEMENTS	iv
ABSTRACT	v
LIST OF TABLES	xi
LIST OF FIGURES	xiii
CHAPTER ONE: TOOTH ENAMEL MATURATION REEQUILIBRATES OXYGEN ISOTOPE COMPOSITIONS AND SUPPORTS SIMPLE SAMPLING METHODS	1
Abstract	2
1.1. Introduction.....	3
1.2. Enamel Mineralogy and Formation.....	4
1.3. Modeling Enamel Isotope Compositions	6
1.4. Materials and Methods	9
1.4.1 Stable Isotopes.....	9
1.4.2 Major Element Distributions	12
1.5. Results	13
1.5.1 Stable Isotopes.....	13
1.5.2 Phase Shifts	14
1.5.3 Compositional Mapping.....	14
1.6. Discussion.....	15
1.6.1 Lack of Phase Shifts Between $\delta^{18}\text{O}_C$ and $\delta^{18}\text{O}_P$	15
1.6.2 Geometry of Enamel Maturation	18

1.6.3 Implications for Subsampling	20
1.7. Conclusions.....	22
CHAPTER TWO: AN IMPROVED APPROACH TO AGE-DEPTH MODELING IN DEEP TIME: IMPLICATIONS FOR THE SANTA CRUZ FORMATION, ARGENTINA	32
Abstract	32
2.1. Introduction.....	33
2.2. Bayesian Modeling.....	34
2.2.1 Bayesian Age-Depth Modeling with Bchron	35
2.3. Geologic Setting of Santa Cruz Formation Samples.....	37
2.4. Materials and Methods	38
2.4.1 U-Pb Geochronology	38
2.4.2 Model Modifications.....	39
2.5. Results	42
2.5.1 U-Pb CA-ID-TIMS	42
2.5.2 Model Validation.....	42
2.5.3 Modeling the Santa Cruz Formation.....	43
2.6. Discussion.....	45
2.6.1 Bayesian Conditioning of Radioisotopic Ages.....	45
2.6.2 Using Age-Depth Models to Fine-Tune Ages.....	46
2.6.3 Implications for Santa Cruz Formation Correlation	47
2.6.4 Using Age-Depth Models to Interpret Proxy Records.....	48
2.7. Conclusions.....	50
CHAPTER THREE: PATAGONIAN ARIDIFICATION AT THE ONSET OF THE MID-MIOCENE CLIMATIC OPTIMUM.....	62

Abstract	62
3.1. Introduction.....	63
3.2. Background.....	66
3.2.1 Miocene Climate of Patagonia	66
3.2.2 Stable Isotopes in Enamel and Bone.....	68
3.3. Materials and Methods	70
3.3.1 Fossil Collection and Sampling.....	70
3.3.2 Precipitation Estimations	72
3.3.3 Temperature Estimations	73
3.3.4 Age-Depth Modeling and Isotope Compositions	73
3.4. Results	74
3.4.1 Bulk Isotope Compositions	74
3.4.2 Intra-Tooth Isotope Zoning	75
3.4.3 Age-Depth Modeling and Smoothing.....	76
3.5. Discussion.....	77
3.5.1 Ecology of Santa Cruz Formation Ungulates.....	77
3.5.2 Carbon Isotopes and Climate	78
3.5.3 Oxygen Isotopes and Climate.....	80
3.5.4 Isotopic Zoning and Seasonality.....	82
3.5.5 Comparisons to Other Proxies.....	82
3.5.6 Comparisons to General Circulation Models	84
3.6. Conclusions.....	85
REFERENCES.....	94

APPENDIX A	116
APPENDIX B	125
APPENDIX C	155

LIST OF TABLES

Table 1.1.	Model parameters for the Passey and Cerling (2002) model.....30
Table 1.2.	Descriptive statistics for tooth stable isotope data. ¹ Late Pleistocene. ² Data from Pellegrini et al. (2011)31
Table 2.1.	GPS coordinates and elevation, composite stratigraphic position and weighted mean ages for for all samples. CV = Cañadón de las Vacas, CO = Cerro Observatorio, KAN = Killik Aike Norte, CBT = Cabo Buen Tiempo, PLC = Puesto Estancia la Coasta.59
Table 2.2.	Summary statistics of the likelihood and posterior age for each tuff from the Cañadón de las Vacas section. Weighted mean ages uncertainties are reported as a mean $\pm 2\sigma$, all other ages are reported as a median and 95% highest density interval. ¹ Weighted mean ages and summed probability distributions recalculated from data for individual ⁴⁰ Ar/ ³⁹ Ar laser fusion analyses from Perkins et al. (2012) provided by Matthew Heizler at the New Mexico Geochronological Research Laboratory (personal communication).....60
Table 2.3.	Summary statistics of the likelihood and posterior age for each tuff from the Lago Posadas section. Weighted mean ages uncertainties are reported as a mean $\pm 2\sigma$, all other ages are reported as a median and 95% highest density interval. weighted mean ages are originally reported in (Blisniuk et al., 2005) and recalibrated by Perkins et al. (2012).....61
Table 3.1.	Summary statistics for all taxonomic groups. Note that the Toxodontidae group represents a combination of Nesodon and Adinotherium.....92
Table 3.2.	Statistical comparisons of $\delta^{18}O$ values for Santa Cruz Formation herbivores. NS = no significant difference ($p > 0.05$), S = significant differences ($p < 0.05$).....93
Table A1.	Stable isotope data from all sampled teeth. IMHM = Idaho Museum of Natural History. BSU = Boise State University. Superscript and subscript indicate upper or lower tooth, respectively 117
Table B1.	Zircon LA-ICPMS concentrations. Ablation using a 213 nm wavelength laser, spot size of 25 microns, repetition rate of 10 Hz, and fluence of ~5

	J/cm ² . Trace element concentrations in ppm, calculated using the mean count rate method, internal standardization to ²⁹ Si, and calibration to NIST 610 and 612 glass standards.....	134
		141
Table B2.	Zircon LA-ICPMS U-Pb geochronology. Isotope ratios and ages are reported without initial common Pb correction; gas blank-corrected mass 204 signals were generally irresolvable from zero. Isotope ratio and apparent age errors do NOT include systematic calibration errors of 0.19% for the 207Pb/206Pb ratio, and 0.63% for the 206Pb/238U ratio (1s). Trace element concentrations in ppm, calculated using the mean count rate method, internal standardization to ²⁹ Si, and calibration to NIST 610 and 612 glass standards. Ablation using a 213 nm wavelength laser, spot size of 25 microns, repetition rate of 10 Hz, and fluence of ~5 J/cm ² . % disc. = relative discordance calculated as 100*(1-(206Pb/238U date/207Pb/206Pb date)	142
		148
Table B3.	Input file for the summed probability distribution model. Tracer and decay constant uncertainties were propagated onto individual zircon grain ages to allow direct comparison to ⁴⁰ Ar/ ³⁹ Ar ages included in the model. See Supplementary Methods for more details. ¹ Data for individual ⁴⁰ Ar/ ³⁹ Ar laser fusion analyses from Perkins et al. (2012) provided by Matthew Heizler at the New Mexico Geochronological Research Laboratory (personal communication).	150
Table B4.	Input file for the weighted mean model. ¹ Weighed mean ages recalculated from individual laser fusion analyses of Perkins et al. (2012) provided by Matthew Heizler at the New Mexico Geochronological Research Laboratory (personal communication).	152
Table C1.	Bulk stable isotope data for Chapter 3.....	156
Table C2.	Serial sampled stable isotope data for Chapter 3.	161

LIST OF FIGURES

- Figure 1.1. Simplified schematic diagram showing two possible models of enamel formation. A) apposition initiates at the occlusal (wear) surface and progresses towards the root at a low angle relative to the enamel-dentine junction. B-C) Maturation progresses through the matrix following the same geometry as apposition. The orientation of isotopic contours (dashed lines) parallels apposition. D-E) maturation progresses through the matrix following a different geometry from apposition. The orientation of isotopic contours does not parallel apposition. Solid lines are the predicted isotopic contours if maturation re-equilibrates appositional mineral. F) Relationship between Passey and Cerling (2002) model parameters and enamel mineralization.....24
- Figure 1.2 A) Modeled oxygen isotope compositions for enamel with different initial mineral fractions (f_{app}). Model outputs are phase shifted relative both to the input signal but also to model outputs with differing f_{app} . Therefore, $\delta^{18}O_C$ ($f_{app} = 0.50$; Sydney-Zax et al., 1991) should be a 1:1 mixture of appositional and maturational compositions while $\delta^{18}O_P$ ($f_{app} = 0.25$; Passey and Cerling, 2002) is more heavily weighted towards maturation. B) Cross correlation between $f_{app} = 0.25$ and $f_{app} = 0.50$. Vertical red line indicates the lag associated with the highest correlation coefficient. .25
- Figure 1.3. Plots of paired CO_3 and PO_4 $\delta^{18}O$ values and their corresponding cross correlations. See Table 2 for descriptive statistics for each tooth. A) *Equus ferus caballus*, B) *Bison* sp., C) *Capra hircus*, D) *Cervus elaphus* (M-00-49), E) *Cervus elaphus* (M-00-59).26
- Figure 1.4. X-ray maps of calcium zoning for teeth with both mature (occlusal) and immature (apical) enamel. A) *Lama guanacoe*, B) *Odocoileus hemionus*, C) *Equus ferus caballus*, D) *Ovis aries*, E) *Bos taurus*. Warm colors indicate higher relative concentrations; blue/purple = pore space. Dashed boxes indicate areas over which calcium concentration profiles were plotted (Fig. 5). Box: schematic representations of enamel formation with inferred angles of maturation (dashed line).27
- Figure 1.5. Relative calcium compositional profiles along the dashed boxes in Fig. 4. A) *Lama guanacoe*, B) *Odocoileus hemionus*, C) *Equus ferus caballus*, D) *Ovis aries*, E) *Bos taurus*. Concentrations were normalized using a linear transformation such that fully mature enamel and appositional enamel reflect mineralization fractions of 1.0 and 0.25 respectively. Box:

Smoothed curves plotted with the same distance scale and shifted so the points of maximum curvature align. In all cases the transition from high to low calcium concentrations occurs over a length scale of 2-4mm.....28

- Figure 1.6. Carbon isotope compositions (note reversed axis) versus depth from outer enamel surface for slices of *Bos taurus* enamel (After Zazzo et al., 2005). The animal was switched from a pure C3 to pure C4 plant diet to induce a large change in its carbon isotope composition. Grey bar indicates the outermost 0.3 mm of enamel, approximately the thickness of the outer enamel shelf observed on our compositional map of *Bos taurus* enamel (Fig. 4). The outer enamel layer is compositionally biased by the dietary shift to C4 plants, suggesting later mineralization. Box: Interpolated carbon isotope compositions based on the six depth profiles of Zazzo et al. (2005). Carbon isotope contours suggest late mineralization for the outer enamel surface, while mineralization of the inner enamel layer progresses more rapidly. Vertical dashed lines indicate sample locations. Contour interval is 1‰.....29
- Figure 2.1. Map of tuff localities. Localities are abbreviated in the text as: Cañadón de las Vacas = CV, Cerro Observatorio = CO, Rincón del Buque = RB, Puesto Estancia La Costa = PLC, Cabo Buen Tiempo = CBT, Killik Aike Norte = KAN.....52
- Figure 2.2. Ten example chronologies. Note that a wide variety of chronologies are possible in the lower section, while the upper section where ash beds are more closely spaced requires tightly bunched model paths.....53
- Figure 2.3. U-Pb Concordia and ranked age plots for all analyzed samples. Shaded symbols indicate analyses included in weighted mean calculations. The light grey band on ranked age plots indicates the weighted mean. All uncertainties are shown as 2σ54
- Figure 2.4. Correlation diagram for Santa Cruz Formation localities considered in this study. The geographic location of each locality is shown in Figure 1. Colored stratigraphic columns are used to form the composite section shown in Figure 5. Greyscale stratigraphic columns for Cabo Buen Tiempo, Killik Aike Norte and Puesto Estancia La Costa modified from Perkins et al. (2012).....55
- Figure 2.5. Age models and simplified stratigraphic column for the composite for the Cañadón de las Vacas – Cerro Observatorio – Rincon de Buque section. Colored polygons are the specified likelihood distribution for each tuff. The 95% highest density interval (shaded grey area) indicates the model uncertainty for all interpolated points between tuffs, while the black line indicates the median. A) Model results using weighted mean ages as likelihood inputs. B) Model results using the summed probability

distribution function for each tuff as likelihood input. C) Difference between the two models. As expected, model uncertainties are higher in B because of the increased variance of the specified likelihoods. The difference in the model median is close to zero in the lower section, while in the upper section model B is shifted towards younger ages.56

- Figure 2.6. Comparison between the likelihood (shaded polygon) and posterior (dashed line) probability distribution functions for the Toba Blanca. A) Weighted mean likelihood function. B) summed probability distribution likelihood function. While both the posterior distribution for both models is shifted towards younger ages, the effect is more pronounced in B. Zircon populations often show prolonged periods of crystallization, with only the youngest populations accurately representing the eruptive age. .57
- Figure 2.7. A) Age-depth model for Lago Posadas. Pink points and error bars indicate the median and 95% HDI model ages for paleosol carbonate nodules. B) Plot of the carbon isotope composition of paleosol carbonates versus stratigraphic position. a weighted moving average with a 5m window size. C) Plot of carbonate carbon isotope compositions versus age. Error bars indicate the 95% HDI of age for each point as in A. Black line is the median of 100,000 Gaussian weighted moving averages (0.2 Ma window size), where the age of each point was allowed to vary probabilistically based on age model results. 95% of the moving average models fall within the shaded pink area.58
- Figure 3.1. Map showing regional geography and Santa Cruz Formation fossil localities. Bold localities are included in this study (modified from Vizcaíno et al. 2012).....87
- Figure 3.2. $\delta^{13}\text{C}$ vs $\delta^{18}\text{O}$ values for Santa Cruz Formation herbivores and bone. Large symbols with error bars are the mean $\pm 2\sigma$ for each taxonomic group. Vertical dashed lines at -15‰ and -7.5‰ indicate the cutoffs for closed canopy forests and mixed C3-C4 environments (see section 3.2.2 for details).88
- Figure 3.3. Carbon (squares) and oxygen (circles) isotope zoning profiles from Santa Cruz Formation ungulate tooth enamel, arranged in increasing stratigraphic level. Error bars indicate analytical reproducibility for replicates of NIST120c (2σ). Error bars for $\delta^{13}\text{C}$ values are smaller than the symbols. A) Nesodon, B) Homalodotherium, C) Nesodon, D) Astrapotherium, E) Nesodon.....89
- Figure 3.4. A) Age-depth model for a composite section of the Cañadon de las Vacas and Rincón del Buque localities. Colored polygon are the probability distribution functions for each dated tuff (Trayler et al., in review). Colored points and error bars indicate the median age and uncertainty

(95% CI) of fossil bone and enamel samples. B) Plot of enamel $\delta^{13}\text{C}$ values versus age. Solid black line is the median smoothed isotope composition accounting for uncertainties in isotope composition and age. 95% of all smoothing models fall within the pink-shaded area. Dashed purple line is the $\delta^{13}\text{C}$ of atmospheric CO_2 (+ 6‰ for ease of plotting) calculated following the methods of Tipple et al. (2010) using benthic foraminifera data (purple dots) from Holbourn et al. (2015). Dashed black lines are predicted changes to isotope compositions given starting isotope compositions similar to those observed at ~ 17.5 Ma, $\delta^{13}\text{C}_{\text{atm}}$, and allowing ΔMAP to vary by ± 500 mm. Shaded grey area corresponds to peak warming at the onset of the MMCO (Holbourn et al., 2015). C) plot of enamel and bone $\delta^{18}\text{O}$ values versus age. Solid black line is the median smoothed isotope composition accounting for uncertainties in isotope composition and age. Inward facing arrows indicate inferred decreases in temperature, outward facing arrows are temperature increases. Purple dots are oxygen isotope compositions of benthic foraminifera (Holbourn et al., 2015) for comparison.....90

Figure 3.5.	Estimates of mean annual precipitation (blue) and mean annual temperature (pink) from tooth enamel and bone stable isotope compositions. Shaded areas represent the 95% confidence while solid line represent the median. Estimates of MAT based on wood physiognomy of plant macrofossils from the lower Santa Cruz Formation (vertical bars; Brea et al., 2012), niche metrics and cenograms (dashed line, $\text{MAP} > 1000$; Kay et al., 2012b), fauna and sedimentological evidence (dashed line, $\text{MAP} < 1000$; Vizcaíno et al., 2010), and tegu lizard fossils (dashed line, $\text{MAP} > 200$ mm, $\text{MAT} > 14^\circ\text{C}$; Fernicola and Albino, 2012) are also shown. Green line and shaded area are boron isotope based atmospheric CO_2 concentrations (Greenop et al., 2014). Shaded grey corresponds to peak warming at the onset of the MMCO as in Fig. 3.4.....91
Figure B1.	Superimposed trace plots of each model parameter from 500 independent simulations 153
Figure B2.	Superimposed density plots of each model parameter from 500 independent simulations. 154

CHAPTER ONE: TOOTH ENAMEL MATURATION REEQUILIBRATES OXYGEN
ISOTOPE COMPOSITIONS AND SUPPORTS SIMPLE SAMPLING METHODS

This chapter was published by Elsevier in the journal *Geochimica et Cosmochimica Acta* and should be referenced appropriately as below.

Traylor, R. B., Kohn, M. J., 2017. Tooth enamel maturation reequilibrates oxygen isotope compositions and supports simple sampling methods. *Geochimica et Cosmochimica Acta* 198, 32-47.

Reproduced by permission of Elsevier.

Abstract

Oxygen isotope and major element zoning patterns of several disparate ungulate teeth were collected to evaluate the timing and geometry of enamel formation, records of isotope zoning, and tooth enamel sampling strategies. Isotopic zoning in mammalian tooth enamel encodes a sub-annual time series of isotopic variation of an animal's body water composition, with a damping factor that depends on the specifics of how enamel mineralizes. Enamel formation comprises two stages: precipitation of appositional enamel with a high $\text{CO}_3:\text{PO}_4$ ratio, followed by precipitation of maturational enamel with a lower $\text{CO}_3:\text{PO}_4$. If appositional and maturational enamel both contribute to isotope compositions (but with different $\text{CO}_3:\text{PO}_4$), and if isotope compositions vary seasonally, paired $\delta^{18}\text{O}$ values from CO_3 and PO_4 profiles should show a spatial separation. CO_3 isotope patterns should be shifted earlier seasonally than PO_4 isotope patterns. Such paired profiles for new and published data show no resolvable shifts, i.e. CO_3 and PO_4 $\delta^{18}\text{O}$ profiles show coincident maxima and minima. This coincidence suggests that enamel maturation reequilibrates appositional isotope compositions. If enamel maturation establishes enamel isotope compositions, the geometry of maturation, not apposition, should be considered when devising sampling protocols. X-ray maps of Ca zoning show that the majority of enamel (inner and middle layers) mineralizes heavily at a high angle to the external tooth surface and the enamel-dentine junction over length scales of 2-4mm, while the outer enamel surface mineralizes more slowly. These data suggest that isotopic sampling strategies should parallel maturational geometry and focus on interior enamel to improve data fidelity. The magnitude of isotopic damping is also smaller than

implied in previous studies, so tooth enamel zoning more closely reflects original body water isotopic variations than previously assumed.

1.1. Introduction

Stable isotopes in mammalian tooth enamel are commonly used to address a variety of ecological and climatological questions (see reviews of: Clementz, 2012; Koch, 1998, 2007; Kohn and Cerling, 2002). Unlike bone and dentine, enamel is not strongly susceptible to diagenetic alteration, so it faithfully preserves biogenic isotope compositions over millions of years. Teeth also mineralize progressively from tooth tip to root and are not remodeled after formation, so they encode and preserve a sub-annual times series of isotopic variations in the animal. Subsampling to extract these variations has become a well-established technique to investigate sub-annual fluctuations in climate and feeding ecology (e.g., Balasse, 2002; Fricke et al., 1998; Fricke and O'Neil, 1996; Kohn et al., 1998). However, because enamel formation consists of multiple discontinuous stages of mineralization, isotopic zoning within a tooth does not perfectly record the instantaneous isotope composition of an animal or environment, rather the record is damped relative to this variation (Passey and Cerling, 2002). Several authors have proposed approaches to minimize this problem, either by subsampling strategies (Blumenthal et al., 2014; Holroyd et al., 2014; Hoppe et al., 2004; Zazzo et al., 2012) or by numerical modeling and inversion (Passey et al., 2002, 2005). Both these approaches rely on accurate understanding of the timing and geometry of enamel formation.

In this paper, we examine chemical and isotopic systematics in tooth enamel to critically evaluate how it forms and encodes its isotope composition. In the first part of the paper we show that while enamel forms via a two-stage process, only second stage

mineralization appears to contribute to the isotope compositions recorded in teeth – compositions essentially reequilibrate during maturation so that the physical and isotopic character of first-stage mineralization appears irrelevant to isotope studies. In the second part we use X-ray composition mapping of several developing teeth to investigate the complexities of second-stage mineralization and its relationship to existing subsampling strategies. The geometry of second-stage mineralization bears little to no resemblance to first-stage mineralization. Consequently, even if apposition-stage isotopic compositions were partially preserved, proposed sampling strategies based on first-stage microstructure alone should be avoided.

1.2. Enamel Mineralogy and Formation

Enamel is the most highly mineralized tissue in mammals and contains nearly 100% bioapatite mineral. Chemically, bioapatite is $\text{Ca}_5(\text{PO}_4)_3\text{OH}$ with carbonate (CO_3) substitutions in the phosphate (PO_4) and hydroxyl (OH) sites (Elliott, 2002). Both the carbonate and phosphate components are commonly analyzed for their stable isotope compositions. Of the two, carbonate analysis is more common, both because it archives two isotope systems, carbon and oxygen, and because analysis is simpler. Enamel phosphate is thought to be more resistant to diagenesis, leading to its use primarily on geologically older fossils (Kohn and Cerling, 2002).

Enamel microtexture in mammals is broken into two broad categories, radial and decussate enamel, distributed in three regions of enamel – outer, central, and inner regions – from the outer enamel surface (OES) to the enamel-dentine junction (EDJ). Radial enamel commonly forms the outer and inner enamel layers, although the inner layer varies in thickness (Koeingswald et al., 1993; Pfretzschner, 1992). In radial enamel,

enamel prisms are oriented perpendicular to either the OES or EDJ. Decussate enamel prisms intersect and cross at shallow to high angles (crisscross) and bundle together to form optically distinct, macroscopically visible bands called Hunter-Schreger bands. Decussate enamel makes up the central and sometimes inner layers of enamel, and therefore, the majority of enamel volume in large mammals (Koenigswald and Sander, 1997; Moss-Salentijn et al., 1997).

Enamel mineralization takes place in two distinct stages, apposition (first-stage) and maturation (second-stage; Fig. 1.1; Robinson et al., 1978, 1979; Suga, 1979; 1982). Here we refer to the two correspondingly distinct mineral components as appositional and maturational bioapatite. During apposition, mineralization initiates at the occlusal or wear surface of the tooth and progresses towards the root. A protein matrix forms and is seeded with diffuse enamel crystallites (Fig. 1.1A). The surface of new apposition forms a low angle relative to the EDJ, such that sequential appositional layers imbricate. In fully mineralized enamel, incremental growth bands called striae of Retzius record the orientation of the appositional front (Hillson, 1986). The angle of apposition for several groups of ungulates is commonly $\sim 5\text{-}15^\circ$ relative to dentine (Hoppe et al., 2004; Kierdorf and Kierdorf, 1997; Kierdorf et al., 2006, 2012, 2013). The appositional matrix is mineral poor, with only ~ 25 wt% bioapatite (Moss-Salentijn et al., 1997; Passey and Cerling, 2002). While the total mineral content of the appositional matrix is low, however, appositional bioapatite within is carbonate rich, containing twice as much CO_3 as fully mature enamel (Robinson et al., 1979; Sydney-Zax et al., 1991). This difference in mineral content vs. CO_3 content is crucial to our study – if appositional bioapatite is retained in the final enamel, it contributes $\sim 25\%$ of the total mineral (PO_4) but $\sim 50\%$ of

total CO₃. The innermost enamel layer, a 10-20 μm band along the EDJ, differs from this pattern of mineralization because it is heavily mineralized – at least 50% – early in enamel formation (Blumenthal et al., 2014; Suga, 1979, 1982; Tafforeau et al., 2007). Because this layer is so thin and rarely isolated for analysis, we do not consider its isotope systematics.

After apposition, enamel undergoes a prolonged maturation stage. Similar to apposition, maturation progresses from occlusal surface to root, although not necessarily at the same rate or with the same geometry (Fig. 1.1B & 1.1D). Maturation occurs earlier and faster in the inner and central enamel layers, with the outer enamel layer mineralizing last. During this stage, crystallites coarsen and infill, reducing organic contents to final concentrations of ≤1 wt% (Hillson, 1986; Robinson et al., 1979, 1978; Suga, 1979, 1982) and depositing the remaining ~75 wt% mineral and ~50 wt% of carbonate (Robinson et al., 1979; Sydney-Zax et al., 1991). While bulk enamel has a carbonate content of 3-4 wt% it is heterogeneously distributed ranging from ~5 wt% near the EDJ to ~3 wt% at the OES (Zazzo et al., 2005).

1.3. Modeling Enamel Isotope Compositions

If bulk enamel represents contributions from both appositional and maturational bioapatite, a bulk isotope composition should represent an average of their respective compositions, weighted by the amount contributed during each stage:

$$\delta_{final} = \delta_{app} \times f_{app} + \delta_{mat} \times (1 - f_{app}) \quad (1.1)$$

where δ_{final} = the final isotope composition of mature enamel, δ_{app} and δ_{mat} are the isotope compositions of appositional and maturational bioapatite respectively, and f_{app} is the fraction of the isotope deposited during apposition (Fig 1.1C & 1.1E).

Passey and Cerling (2002) modeled this concept using two equations (see Table 1.1 for model parameters):

$$\delta_{ei} = (f_{app} \times \delta_{mi}) + (1 - f_{app}) \times \frac{\sum_{n=i+1}^{i+l_m} \delta_{mn}}{l_m} \quad (1.2)$$

$$\delta_{ci} = \frac{1}{l_a} \sum_{n=i-l_a}^i \delta_{en} \quad (1.3)$$

where δ_{ei} = the isotope composition at any point i , f_{app} is the decimal fraction of enamel formed during apposition, and δ_{ci} = the isotope composition of enamel at i , averaged over a column through the thickness of enamel. Equation 1.2 implies that isotope compositions reflect a contribution from appositional bioapatite (first term on the right-hand side), and a time integrated contribution from maturational bioapatite over the length of maturation (second term on the right-hand side). The Passey and Cerling (2002) model makes four assumptions: 1) Maturation length (l_m) is constant (no variations in tooth enamel mineralization rate along the length of a tooth); 2) Maturation initiates immediately after apposition (no time lags between apposition and maturation); 3) The geometry of maturation parallels apposition (no variations in mineralization rate with depth, such as early mineralization of the central Hunter-Schreger bands); 4) both appositional and maturational bioapatite contribute to the final isotope composition of enamel (no resorption or recrystallization of appositional bioapatite).

Although the concentration of phosphate is virtually identical between appositional and maturational bioapatite, the concentration of carbonate differs systematically – there is about twice as much carbonate in appositional bioapatite as in fully formed enamel (Sydney-Zax et al., 1991). These differences imply that the oxygen isotope composition of carbonate vs. phosphate components should be weighted differently in equation 1.1. In both cases:

$$f_{app} = \frac{f_{mineral,app}}{f_{mineral,final}} \times \frac{wt\%_{i,app}}{wt\%_{i,final}} \quad (1.4)$$

where $f_{mineral,app}$ and $f_{mineral,mat}$ are the fractions of mineral in appositional and final (completely mature) enamel, respectively (normally 25% and 100%), and $wt\%_{i,app}$ and $wt\%_{i,final}$ are the weight percents of the component i in appositional and final bioapatite respectively. For phosphate $wt\%_{PO_4,app}$ and $wt\%_{PO_4,final}$ are virtually identical (e.g. Ca/P weight ratios are identical; Hiller et al., 1975; Sydney-Zax et al., 1991). So f_{app} follows mineral content: 25% appositional bioapatite would contribute 25% of the PO_4 in fully formed enamel. For carbonate however, $wt\%_{CO_3,app}$ is $\sim 2 \times wt\%_{CO_3,final}$, so 25% appositional bioapatite would contribute $\sim 50\%$ of the CO_3 in fully formed enamel. This in turn implies that the carbonate component of enamel is weighted towards an earlier period of enamel formation than the phosphate component and that seasonal variations in $\delta^{18}O$ should be recorded differently in CO_3 vs. PO_4 components.

We explored the quantitative implications of differing values of f_{app} for CO_3 and PO_4 using the Passey and Cerling (2002) model, assuming $f_{CO_3,app} = 0.50$ and $f_{PO_4,app} = 0.25$ (Fig. 1.2). We assumed published values for the length scales of maturation ($l_m \sim 25\text{mm}$; Balasse, 2002) and apposition ($l_a \sim 15\text{mm}$; Passey and Cerling, 2002). Because $f_{CO_3} \neq f_{PO_4}$ oxygen isotope zoning patterns in these components should be phase shifted relative to one another. Similarly, the oxygen isotope offset, $\Delta(CO_3-PO_4)$, measured between paired samples should vary systematically, which may help explain why reported $\Delta(CO_3-PO_4)$ values for enamel are not constant (Bryant et al., 1996; Fox and Fisher, 2001; Martin et al., 2008; Pellegrini et al., 2011; Zazzo et al., 2004).

Within the context of model predictions, and our overall goal of understanding how mineralization patterns affect isotope records, we addressed two specific questions:

First, are oxygen isotopes in the carbonate and phosphate components shifted relative to one another, as predicted. A phase shift, if present, implies that the two components record isotopes differently, which must be considered in interpreting PO₄ vs CO₃ isotope data. Conversely, the lack of a phase shift would imply that maturation overprints or re-equilibrates appositional mineral, removing its contribution to the bulk isotope composition of mature enamel.

Second, what is the geometry of enamel maturation? Since appositional enamel forms at a low angle relative to the EDJ, sampling perpendicular to the EDJ cross cuts weeks or months of appositional features (Holroyd et al., 2014). However, since maturation deposits 50% of carbonate and 75% phosphate, the orientation of mineralization is crucial to understanding how isotopes are recorded within a tooth. Additionally, the length scale of maturation strongly influences the degree to which isotope variations are damped (Eq. 1.2).

1.4. Materials and Methods

1.4.1 Stable Isotopes

We selected five teeth for stable isotope analysis. Three teeth – horse (*Equus ferus caballus*), goat (*Capra hircus*), and bison (*Bison* sp.) – were fully mineralized and should reflect their post maturation isotopic compositions. For isotopic analyses we identified fully mature enamel based on hardness and texture. Immature enamel is soft (Passey and Cerling, 2002) with a fibrous texture and could be easily scraped from a tooth using a scalpel, while highly mineralized tissue required the use of a drill. We also selected two immature elk (*Cervus elaphus*) teeth. Since these teeth are partially mineralized, the isotopic input from maturation should be minimized over the region of apposition.

Sampled teeth were cleaned with a carbide burr and rinsed with ethanol to remove surficial material before sampling. Serial samples were hand milled perpendicular to the growth axis using a Dremel® rotary tool and a 0.5mm carbide dental drill bit. This resulted in 86 subsamples across the five teeth (See Appendix A). Approximately 8 mg of enamel powder were pretreated using the approach of Koch et al. (1997). We first oxidized residual organics overnight using excess 30% hydrogen peroxide. The hydrogen peroxide was decanted, and the powder was rinsed twice with deionized water. After rinsing, the powders were treated with a 1.0 M Ca-acetate – acetic acid buffer overnight to remove labile carbonates. After pretreatment the powders were rinsed three times with deionized water and dried in a vacuum oven at 40 °C. After pretreatment each sample was split and analyzed for both PO₄ and CO₃ oxygen isotopes.

The CO₃ component of enamel was analyzed by digestion in phosphoric acid using a 2010 ThermoFisher Gasbench II coupled with a Delta V Plus continuous flow isotope ratio mass spectrometer, located in the Stable Isotope Laboratory, Department of Geosciences, Boise State University. The PO₄ component was re-precipitated as Ag₃PO₄ using the following method. An ~1.0 mg aliquot of enamel powder was dissolved in 200 μL 0.5 M nitric acid over several hours. After the powder was fully dissolved the solution was neutralized by added 150 μL of 0.5 potassium hydroxide. 400 μL of 0.36 M potassium fluoride was added to precipitate calcium as calcium fluoride. The remaining liquid was transferred to a clean centrifuge tube and reacted with 500 μL of silver amine solution (0.2 M silver nitrate, 0.5 M ammonium nitrate, 0.74 ammonium hydroxide) at 50 °C overnight to form Ag₃PO₄ (Basset et al., 2007; O’Neil et al., 1994). The resulting precipitate was rinsed five times in deionized water and analyzed using the

same mass spectrometer coupled with a ThermoFisher TC/EA. All CO₃ oxygen isotope compositions were standardized to Vienna Standard Mean Ocean Water (VSMOW) using the NBS-18 and NB-19 calcite standards. Analytical reproducibility was $\pm 0.24\text{‰}$ (NBS-18; $\pm 2\sigma$) and $\pm 0.34\text{‰}$ (NBS-19; $\pm 2\sigma$). Phosphate oxygen isotope compositions were standardized to VSMOW using the IAEA-601, IAEA-CH3 and IAEA-CH6 standards. Analytical reproducibility was $\pm 0.44\text{‰}$ (IAEA-601; $\pm 2\sigma$), $\pm 0.46\text{‰}$ (IAEA-CH6; $\pm 2\sigma$), and $\pm 0.56\text{‰}$ (IAEA-CH3; $\pm 2\sigma$). Bioapatites and calcite acid fractionation factors exhibit systematic differences (Passey et al., 2007). To ensure consistent $\Delta(\text{CO}_3\text{-PO}_4)$ measurements between teeth we made small adjustments to our data based on repeated analysis of NIST-120c, a phosphorite with similar chemistry to bioapatite. Analytical reproducibility was $\pm 0.47\text{‰}$ (2σ) for the CO₃ component and $\pm 0.73\text{‰}$ (2σ) for the PO₄ component. We assume a phosphate $\delta^{18}\text{O}$ value of 21.7‰ (Chenery et al., 2010) and a carbonate $\delta^{18}\text{O}$ value of 28.5‰ (Kohn et al., 2015), and corrected our data to reflect a $\Delta(\text{CO}_3\text{-PO}_4)$ of 6.8‰ for concurrently analyzed NIST-120c. These corrections do not affect any of our interpretations. All isotope compositions are reported in the standard delta (δ) notation.

To investigate the predicted phase shifts between carbonate bound ($\delta^{18}\text{O}_\text{C}$) and phosphate bound ($\delta^{18}\text{O}_\text{P}$) oxygen isotope compositions, we treated our data as independent time series and calculated cross correlations between both data sets using R v3.1.2. Cross correlation determines the optimal alignment between two time series by repeatedly calculating a correlation coefficient while varying the lag between the two series (Fig. 2). This approach assumes a near constant mineralization rate and a regular sampling interval. The mean sampling interval (Δx) over all teeth is 2.08 ± 1.50 mm

($\text{mean} \pm 2\sigma$). The cross-correlation approach expresses any lag as an integer number (n) of sampling intervals. Therefore, if $n = 2$ and $\Delta x = 2.08$ mm the lag will be identified as 4.16 mm. It is important to note that any lag predicted using the Passey and Cerling (2002) model represents the minimum possible lag because the model assumes that maturation initiates immediately after apposition (i.e. $\Delta t_{\text{app-mat}} = 0$). However, if maturation initiates some time after the cessation of apposition, as our X-ray maps imply (see below) $\Delta t_{\text{app-mat}} > 0$. This relationship implies that lags between carbonate and phosphate data should be larger than the model predicts, because appositional and maturational bioapatite are separated by a larger period of time.

Pellegrini et al. (2011) suggested that CO_3 oxygen isotope zoning shows greater attenuation than PO_4 isotope zoning. The authors used a t-test on the pooled standard deviations of $\delta^{18}\text{O}_\text{C}$ and $\delta^{18}\text{O}_\text{P}$ values calculated independently for each tooth. For example, an individual tooth (tooth “A”) might exhibit standard deviations in $\delta^{18}\text{O}_\text{P}$ and $\delta^{18}\text{O}_\text{C}$ of σ_C and σ_P . These two values constitute a single pair for tooth A. A second tooth (tooth “B”) would provide a second pair of σ_C and σ_P values. These pairs were calculated across all teeth and a t-test performed on pooled σ_C and σ_P . In addition to replicating this technique we also compared the variances of $\delta^{18}\text{O}_\text{C}$ and $\delta^{18}\text{O}_\text{P}$ values using F-tests. We set significance at $p < 0.05$ for both tests.

1.4.2 Major Element Distributions

Major element compositional distributions were measured across five teeth with forming enamel. Slices of enamel were removed from each tooth parallel to the growth axis, mounted on glass slides, and polished using 0.3 μm alumina. After polishing, enamel slices were gold coated and imaged. Mule deer (*Odocoileus hemionus*) and cow

(*Bos taurus*) X-ray maps were collected using a Cameca SX-50 electron probe housed in the Electron Microscopy Center, University of South Carolina. Guanaco (*Lama guanacoe*), sheep (*Ovis aries*), and horse (*Equus ferus caballus*) X-ray maps were collected using a Cameca SX-50 electron probe housed in the Department of Geological Sciences, Brigham Young University, Utah. For both instruments, operating conditions included an expanded beam (5-10 μm) and 15 kV accelerating voltage. We used stage mapping, a 200 nA beam current, pixel sizes of 15 μm , and count times of 50 ms/pixel, and collected all data using wavelength dispersive spectrometers.

We use calcium X-ray maps as a proxy for mineral content. The geometry of maturation appears in X-ray maps as a transition between the poorly mineralized appositional matrix (low X-ray intensity) and the fully mature enamel (high X-ray intensity). We calculated changes in relative calcium concentrations over a window that included both fully mature and immature enamel using ImageJ (Abràmoff et al., 2004). When a clear maturational boundary is present we define the angle of maturation as the angle measured from the EDJ, proximal to the occlusal surface.

1.5. Results

1.5.1 Stable Isotopes

Teeth display moderate to strong zoning in both $\delta^{18}\text{O}_\text{P}$ and $\delta^{18}\text{O}_\text{C}$ values (Fig. 1.3; Table 1.2). The single bison M³ is the most strongly zoned with total variations of 11.1‰ and 9.8‰ for CO_3 and PO_4 oxygen isotope compositions (Fig. 1.3B). The two elk teeth have the smallest total variation of ~2.5‰ (Fig. 1.3D-E). In contrast to the results of Pellegrini et al. (2011) our results do not show a consistent attenuation of $\delta^{18}\text{O}_\text{C}$ values relative to $\delta^{18}\text{O}_\text{P}$ values. A t-test of the pooled intra-tooth standard deviations across all

sampled teeth shows no significant difference between $\delta^{18}\text{O}_\text{C}$ and $\delta^{18}\text{O}_\text{P}$ values ($p = 0.08$). Likewise, an F-test of pooled data reveals no significant difference in variances ($p = 0.63$).

1.5.2 Phase Shifts

Cross correlations between $\delta^{18}\text{O}_\text{C}$ and $\delta^{18}\text{O}_\text{P}$ values show no detectable lag between the two components (Table 1.2; Fig. 1.3F). We also performed statistical tests on data for 8 teeth originally reported in Pellegrini et al. (2011). In general, isotopic zoning in their data is lower than in teeth sampled for this study, and subsample spacing is also higher (2.7 ± 2.0 mm; $\text{mean} \pm 2\sigma$). These considerations reduce the reliability of calculated lags. Four teeth indicate zero lag, whereas two teeth suggest a small positive lag and two teeth a small negative lag.

1.5.3 Compositional Mapping

X-ray maps of relative calcium concentrations in immature and mature enamel reveal key mineralization details (Fig. 1.4). Appositional enamel is highly porous, and maturation reduces porosity. The heavily mineralized innermost enamel layer occurs as a thin band separating dentine from the majority of enamel and is barely visible at the resolution of these images. With the exception of *Bos taurus* visible calcium zones at the boundary between mature and immature enamel are oriented at high ($>45^\circ$) oblique angles relative to the EDJ (Fig. 1.4A-D). This zoning defines the orientation of the maturation front. *Odocoileus* and *Lama* have similar maturation angles of $\sim 60^\circ$ (Fig. 1.4A-B), while the *Ovis* maturation angle is steeper ($\sim 80^\circ$; Fig. 4D). Unlike the results of Hoppe et al. (2004) who suggest that maturation in horses takes place at a low angle, calcium zoning in the sampled horse is oriented approximately perpendicular to dentine

($\sim 90^\circ$; Fig. 1.4C). Each of these teeth also has a distinctive outer enamel “shelf” such that the innermost $\sim 3/4$ of enamel is heavily mineralized while the outermost enamel layer is more weakly mineralized. Contrasting with the relatively simple geometry of the other teeth, chemical maps in *Bos* enamel (Fig. 1.4E) reveal a maturation “wedge” or “plume” with the apex of the wedge falling apically about midway between the OES and EDJ, i.e. centered within the region of decussate enamel and Hunter-Schreger bands.

Compositional profiles (Fig. 1.5) show marked decreases in calcium concentrations across the maturation front. Transitions from high (mature) to low (immature) concentrations occur over a length scale of 2-4 mm in *Equus*, *Ovis*, *Lama* and *Odocoileus* (Fig. 1.5A-D) as determined by measuring the distance between the points of maximum curvature on plots of composition vs. distance. This transition is more protracted in *Bos* (Fig. 1.5E), with the profile rapidly reaching $\sim 80\%$ mineralization over a ~ 4 mm interval and then gradually increasing over ~ 6 mm to its maximum mineralization.

1.6. Discussion

1.6.1 Lack of Phase Shifts Between $\delta^{18}\text{O}_C$ and $\delta^{18}\text{O}_P$

Of the 13 teeth considered, 9 have no detectable lag between $\delta^{18}\text{O}_C$ and $\delta^{18}\text{O}_P$, including all new data collected in this study. And while re-analysis of teeth from Pellegrini et al. (2011) reveals small lags, the detected lags are not consistent, with small negative lags detected in two teeth and positive lags in two others. With the exception of sample STCE, teeth with calculated lags have the lowest correlation coefficients and smallest oxygen isotope variation, so are most susceptible to analytical errors or other sources of noise. Because the detected lags are inconsistent we cannot explain these

results as arising from a physiological process. Preferential diagenetic alteration of the CO_3 component might explain these anomalies. In general, isotopic exchange between enamel and fluid should shift the mean isotopic value and attenuate the overall range, but not phase shift. However, phase shifts in $\delta^{18}\text{O}_\text{C}$ compositions are possible if CO_3 is preferentially removed from different crystallographic sites (Roche et al., 2010) and if the sites are differentially filled during apposition or maturation. Because we do not know whether different sites are filled during different stages of growth, such a view is at present speculative.

Why do highly zoned teeth fail to show phase shifts? Possible explanations include:

- 1) The growth rate of the teeth is sufficiently rapid that no lag is resolvable.

The magnitude of a lag is related to the growth rate of the tooth. For example, ever growing rodent teeth have rapid enamel growth rates of $\sim 150\text{-}440$ mm/yr implying a very small time period of c. 2 weeks between the start of apposition and the end of maturation (see Kohn, 2004). In this case our methods probably would not resolve any lag between $\delta^{18}\text{O}_\text{C}$ and $\delta^{18}\text{O}_\text{P}$. Conversely, enamel growth rates for ungulates are $\sim 30\text{-}60$ mm/yr (Kohn, 2004). Model predictions for these teeth imply minimum lags of $\sim 1\text{-}2$ months between $\delta^{18}\text{O}_\text{C}$ and $\delta^{18}\text{O}_\text{P}$ values, or physical offsets of $\sim 2.5\text{-}5$ mm. Such offsets should be resolvable from our data suggesting some other explanations.

- 2) Enamel mineral may re-equilibrate during maturation either by recrystallization and exchange of appositional mineral or by oxygen isotope diffusion between enamel and body fluids. Zazzo et al. (2010) investigated the contribution of appositional CO_3 to the final enamel carbon isotope composition using carbon isotope from the teeth of sheep

that were switched between a diet of C₃ and C₄ plants. The authors fit the Passey and Cerling (2002) model to serially sampled $\delta^{13}\text{C}$ values, while varying the value of f_{app} . Values of f_{app} of either 0.0 or 0.50 produced the best model fits suggesting that at least a partial re-equilibration of carbon isotopes is possible. For this process to occur, however, some mechanism for preserving appositional features is required. For example, incremental structures and fluorescent labels with appositional geometries are observed in mature enamel (Kierdorf et al., 2013). How are these preserved?

For physical structures, inasmuch as mineral replacement reactions are often pseudomorphous (Putnis, 2002), appositional structures might be preserved even as appositional crystals are replaced and isotopically reequilibrate. Consideration of the chemical process of maturation implies that that mineral-bound fluorescent labels should be preserved. Calcium concentrations in body fluids are low (~40 ppm; Driessens and Verbeeck, 1990), implying Ca enrichment factors of $\sim 10^4$ between bioapatite and serum. Thus, enamel serves as a highly effective Ca sink, limiting any exchange of Ca between enamel and serum. Any Ca in serum at the site of enamel maturation is simply scavenged into new-formed crystals. This process severely limits the potential for any Ca or Ca-chelating labels to leave the maturation site. Even so, some post appositional mobility is observed as fluorescent labels and radio-phosphorous distributions broaden during maturation (Robinson et al., 1974; cf. fig. 1, Kierdorf et al., 2013).

Diffusional exchange would also preserve physical structures. Although intracrystalline diffusion rates in apatite are slow (Cherniak, 2000), faster diffusion rates are possible in the near surface region of minerals (Stipp et al., 1992). For crystallites with a sufficiently high surface area to volume ratio, such as bioapatite, this effect could

allow rapid diffusional exchange on a whole crystal scale (Kohn, 2008). Since serum is composed primarily of water, the reservoir of exchangeable oxygen is more than sufficient to reset oxygen isotope compositions during maturation. Low Ca concentrations in serum, however, imply that Ca exchange and alteration of fluorescent labels would be limited.

1.6.2 Geometry of Enamel Maturation

Enamel apposition occurs at a consistently low angle relative to the EDJ in horses (Hoppe et al., 2004). Various labeling techniques record similarly shallow appositional angles in sheep, cows, and deer (Kierdorf and Kierdorf, 1997; Kierdorf et al., 2006, 2012, 2013), as do trace element distributions in primate enamel (Austin et al., 2013). However, our compositional maps clearly show that the geometry of enamel maturation may be complex and is independent of appositional geometry. An important implication is that incremental features that record appositional geometries, such as striae of Retzius, do not indicate either the geometry of maturation (Fig. 1.4) or the distribution of isotopes within the enamel. Inasmuch as most enamel mineralizes during maturation, not apposition, sampling strategies based on incremental features alone will be invariably flawed and should be avoided.

Our data agree with complementary observations for diverse taxa that show that the outer enamel layer mineralized later than the inner and center enamel layers (Blumenthal et al., 2014; Suga, 1982). The outer enamel “shelf” appears to make up about a quarter of the total enamel volume. Its late mineralization implies that it should record a later period of time relative to the inner and central layers. Data for a cow whose diet was switched from pure C₃ plants (enamel $\delta^{13}\text{C} \sim 12\text{‰}$) to pure C₄ plants (enamel

$\delta^{13}\text{C} \sim 0\%$; Zazzo et al., 2005) support this inference (Fig. 1.6). The dietary switch caused the cow's $\delta^{13}\text{C}$ to increase through time. Microsamples through the thickness of enamel show higher $\delta^{13}\text{C}$ values for the outer ~ 0.3 mm of enamel, relative to interior enamel. A reversal in isotope composition is evident in the center of one profile, and suggests that the central (decussate) enamel mineralized earlier than radial enamel on either side. This mineralization behavior is consistent with the “wedge” of mineralization that we imaged in our cow enamel (Fig. 1.4E).

Possible textural differences (radial vs. decussate) and location (nearer the EDJ vs. nearer the OES) combine to influence the timing of enamel maturation. For example, if enamel had a consistent texture throughout its thickness it might mineralize with a simple planar geometry: earliest at the EDJ, at some intermediate time in the middle of enamel and last at the OES. The model of Passey and Cerling (2002) mimics this pattern. If decussate enamel experiences earlier and more rapid mineralization, however, a more complex geometry results in which radial enamel near the EDJ could mineralize at the same time or even later than decussate enamel in the middle followed last by radial enamel near the OES. This view qualitatively explains some features of the compositional maps (Fig. 1.4, especially *Lama*, *Odocoileus* and *Bos*) but whether it applies across enamel types and animal groups requires further investigation.

Generalized models require estimates of l_m which is rare. Passey and Cerling (2002) estimated l_m for *Hippopotamus amphibius* (~ 65 mm), *Bos taurus* (~ 15 mm), and *Bison bison* (~ 25 mm), based on bulk phosphorus content for samples milled perpendicular to the growth axis. This technique integrates a column of enamel into a single sample, however, so it is unable to resolve geometric complexities in enamel

maturation. Using backscattered electron imagery of an *Equus* (horse) tooth, Blumenthal et al. (2014) estimated l_m of the inner and central enamel layers as ~28 mm. Their maturation trends are non-linear however, and ~60% of new enamel mass is added to appositional enamel over a much shorter distance, reaching 80-90% of final bioapatite mineral in < 10 mm. If this rapid initial stage of maturation (representing ~60% of final bioapatite mass) isotopically resets appositional bioapatite (representing 25% of final bioapatite mass), 80-90% of the isotope composition is established over a short distance and correspondingly short period of time.

Bendrey et al. (2015) proposed an exponentially decreasing growth rate in horse molars. Similarly, Kierdorf et al. (2013) report a decreasing mineralization rate near the enamel-root contact for sheep molars. Both these models imply rapid, near-linear growth rates for the majority (~80% of total length) of enamel, with a rapid decrease in mineralization rate near the enamel-root contact. Our samples nearly all fall outside the near root region of the tooth where mineralization rates slow. Therefore, our estimates of maturation duration should represent a near maximum maturation rate. Rapid maturation implies a relatively small value of l_m and substantially decreases the magnitude of isotopic damping (Eq. 1.2; Passey and Cerling, 2002). That is, depending on the specifics of maturation geometry and rate, tooth enamel may preserve an isotopic record of an animal's body composition with higher fidelity than other studies (e.g. Kohn, 2004) have inferred.

1.6.3 Implications for Subsampling

Our observations show that the inner and central enamel layers mineralize heavily over a length scale of 2-4 mm. The outermost layer mineralizes later but makes up only

~25% of the total enamel thickness. Therefore, a majority of enamel mineralizes over a relatively short length. Since enamel growth rates are known or inferable from isotope zoning for many taxa (Kohn, 2004), the maturation length can be converted to time simply by dividing by the growth rate. Yearly mineralization rates vary among taxa but are commonly 30-60 mm/year for ungulates (Kohn, 2004). Therefore, a length scale of maturation of 2-4 mm equates to a maturation rate for the inner and central enamel of 1/2 to 1 1/2 months. The length scale of mineralization for the outermost enamel is much more poorly known, but backscattered electron images of horse enamel suggest it is at least 2 times the length scale for the inner enamel (Blumenthal et al., 2014). These sparse data suggest a maturation rate of at least 1-3 months.

Several studies have proposed strategies to reduce the damping associated with progressive mineralization. Hoppe et al. (2004) suggest milling along low-angle striae of Retzius, parallel to appositional microtextures. Maturation clearly does not follow appositional geometry in any of the diverse taxa we studied. The high angle commonly observed between the maturation front and the EDJ suggests that milling at a low angle averages more than simple perpendicular sampling and degrades seasonal signals. Cerling and Sharp (1996) used *in situ*, laser ablation to analyze fossil enamel $\delta^{13}\text{C}$ and $\delta^{18}\text{O}$ values. Similarly, Blumenthal et al. (2014) used secondary ion mass spectrometry to collect $\delta^{18}\text{O}$ values from the highly mineralized innermost enamel layer. While these *in situ* methods offer micron scale spatial resolution, they incorporate oxygen isotopes from three possible sources: hydroxyl, phosphate, and carbonate. The hydroxyl site is especially subject to diagenesis, so while bulk *in situ* analysis may be acceptable for modern specimens, its use on fossils may skew results, perhaps by as much as 1‰ (Kohn

et al., 1999). Furthermore, models that link tooth enamel and drinking water isotope compositions make predictions for either the PO_4 component or CO_3 component, not bulk analysis of all oxygen bearing species.

By far the most common method of sampling enamel for stable isotope analysis is the use of a handheld dental drill or similar tool to mill samples perpendicular to the EDJ. This technique preferentially samples the outer and middle enamel layers, combining enamel from partially separated periods of mineralization. Carbon isotope depth profiles (Fig. 6; Zazzo et al., 2005) clearly show that the outer enamel layer records time shifted isotope values, while the inner and central layers preserve isotope “contours” nearly perpendicular to the EDJ. Selectively targeting central and inner enamel, either through micro-milling (i.e. Zazzo et al., 2005) or bulk removal of the outer enamel layer may reduce damping of isotope values associated with enamel maturation.

1.7. Conclusions

New and previously published oxygen isotope data show that carbonate and phosphate components of enamel record the same period of time, without a spatial or temporal lag, contrasting with current models. We suggest that enamel maturation isotopically reequilibrates the oxygen isotope composition of appositional bioapatite. In principle reequilibration should affect carbon isotopes as well, since carbon concentrations in serum are high. The effect on other commonly analyzed enamel components (i.e. trace elements) is unclear, although the persistence of Ca-binding labels in mature enamel suggest that little re-equilibration takes place in this case. X-ray chemical maps demonstrate that the inner and central enamel layers mineralize before the outermost enamel, dominantly over a narrow interval of 2-4 mm. These inner layers also

mineralize at a high angle relative to the EDJ. Since maturation precipitates the majority of enamel bioapatite, and may isotopically reset some components, isotope sampling strategies should preferentially mimic maturational, not appositional geometries; we also recommend physically removing the outer enamel layer prior to sampling, or otherwise focusing on inner enamel whenever possible.

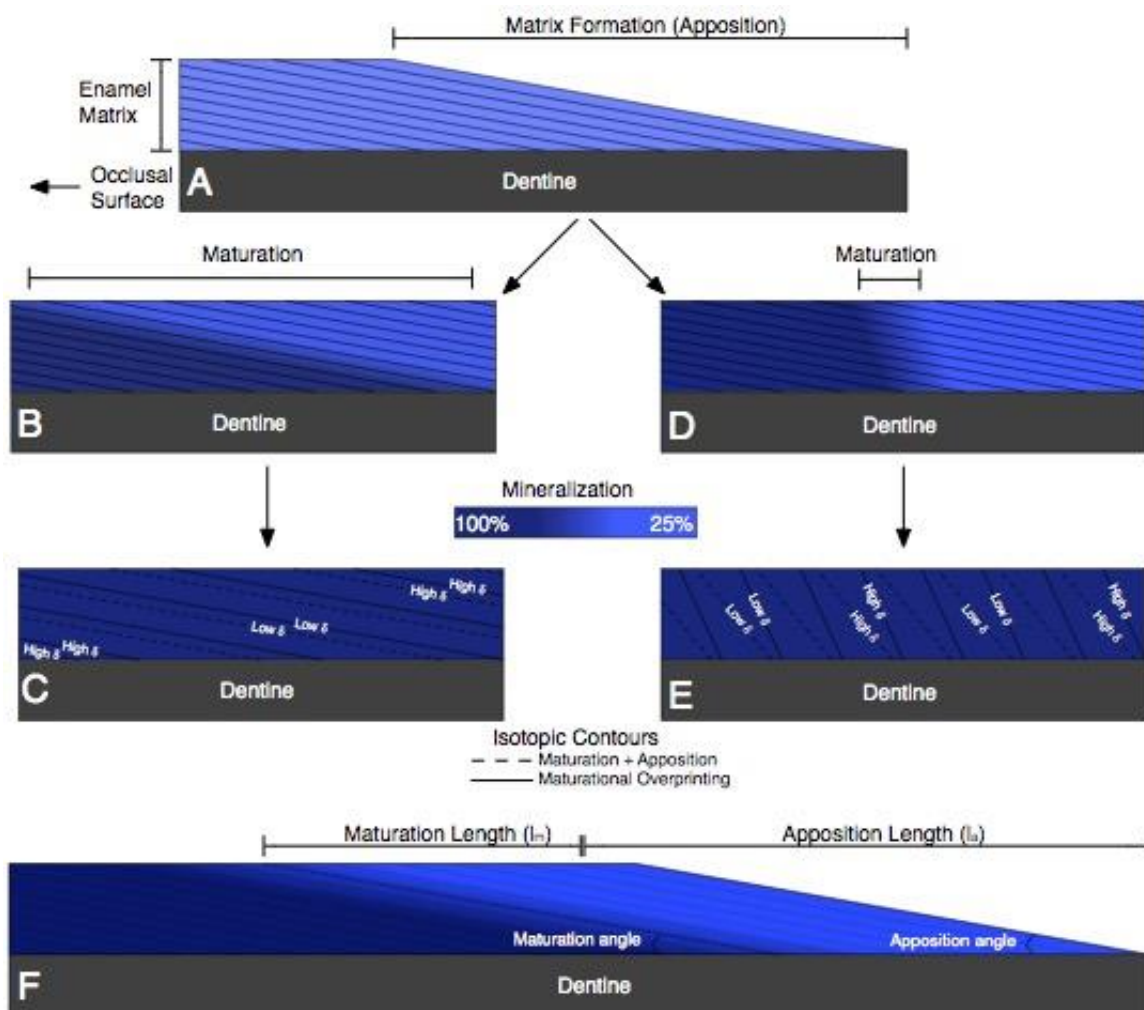


Figure 1.1. Simplified schematic diagram showing two possible models of enamel formation. A) apposition initiates at the occlusal (wear) surface and progresses towards the root at a low angle relative to the enamel-dentine junction. B-C) Maturation progresses through the matrix following the same geometry as apposition. The orientation of isotopic contours (dashed lines) parallels apposition. D-E) maturation progresses through the matrix following a different geometry from apposition. The orientation of isotopic contours does not parallel apposition. Solid lines are the predicted isotopic contours if maturation re-equilibrates appositional mineral. F) Relationship between Passey and Cerling (2002) model parameters and enamel mineralization.

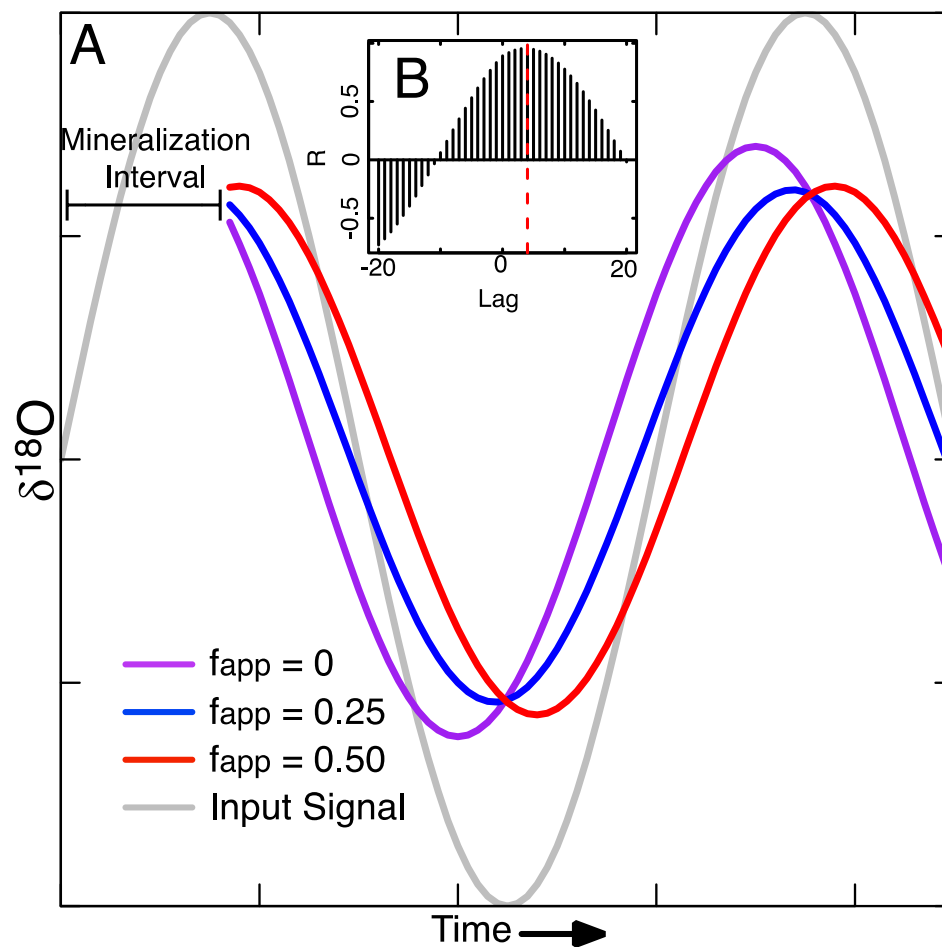


Figure 1.2 A) Modeled oxygen isotope compositions for enamel with different initial mineral fractions (f_{app}). Model outputs are phase shifted relative both to the input signal but also to model outputs with differing f_{app} . Therefore, $\delta^{18}O_C$ ($f_{app} = 0.50$; Sydney-Zax et al., 1991) should be a 1:1 mixture of appositional and maturational compositions while $\delta^{18}O_P$ ($f_{app} = 0.25$; Passey and Cerling, 2002) is more heavily weighted towards maturation. B) Cross correlation between $f_{app} = 0.25$ and $f_{app} = 0.50$. Vertical red line indicates the lag associated with the highest correlation coefficient.

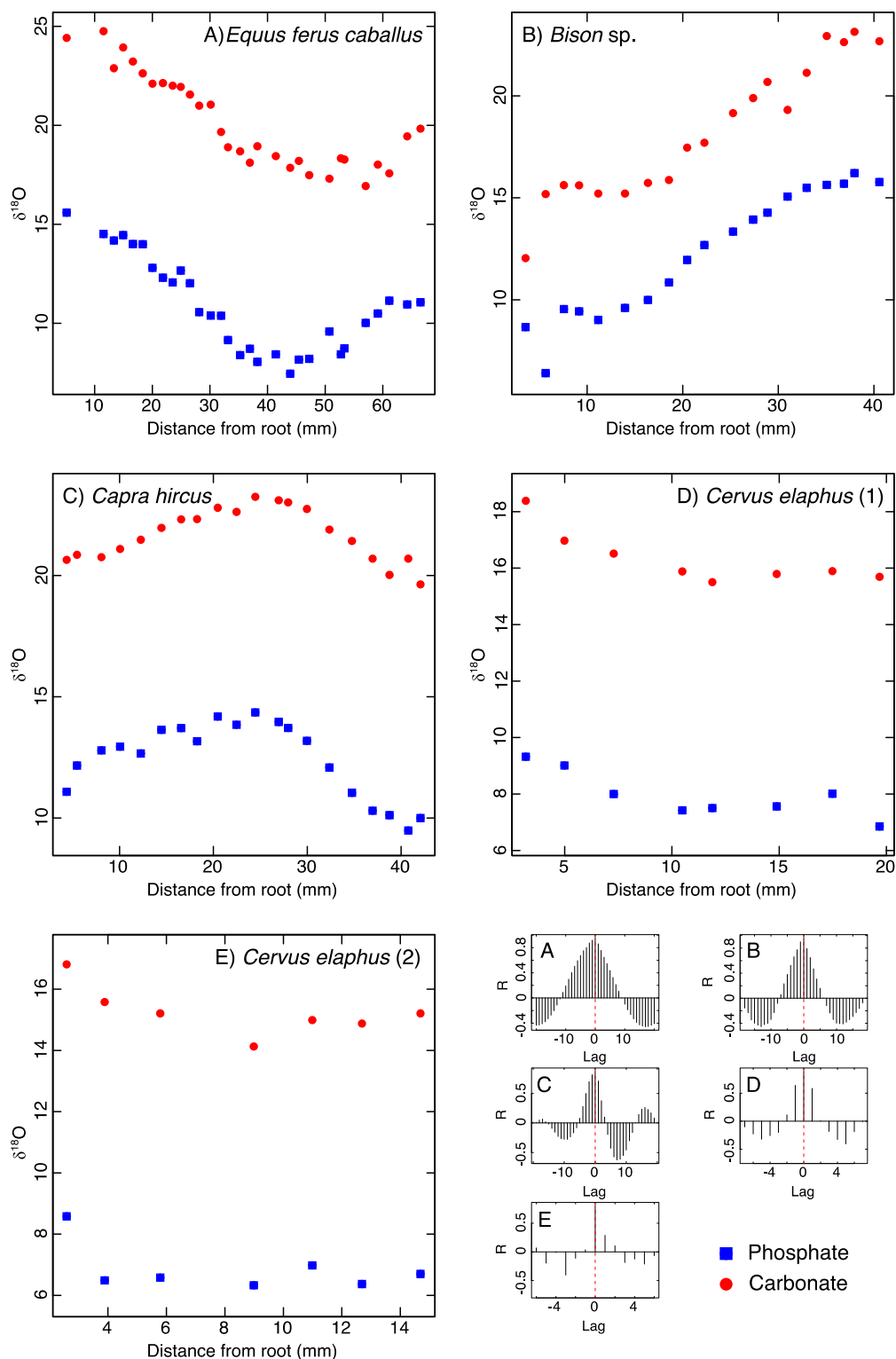


Figure 1.3. Plots of paired CO_3 and PO_4 $\delta^{18}\text{O}$ values and their corresponding cross correlations. See Table 2 for descriptive statistics for each tooth. A) *Equus ferus caballus*, B) *Bison sp.*, C) *Capra hircus*, D) *Cervus elaphus* (M-00-49), E) *Cervus elaphus* (M-00-59).

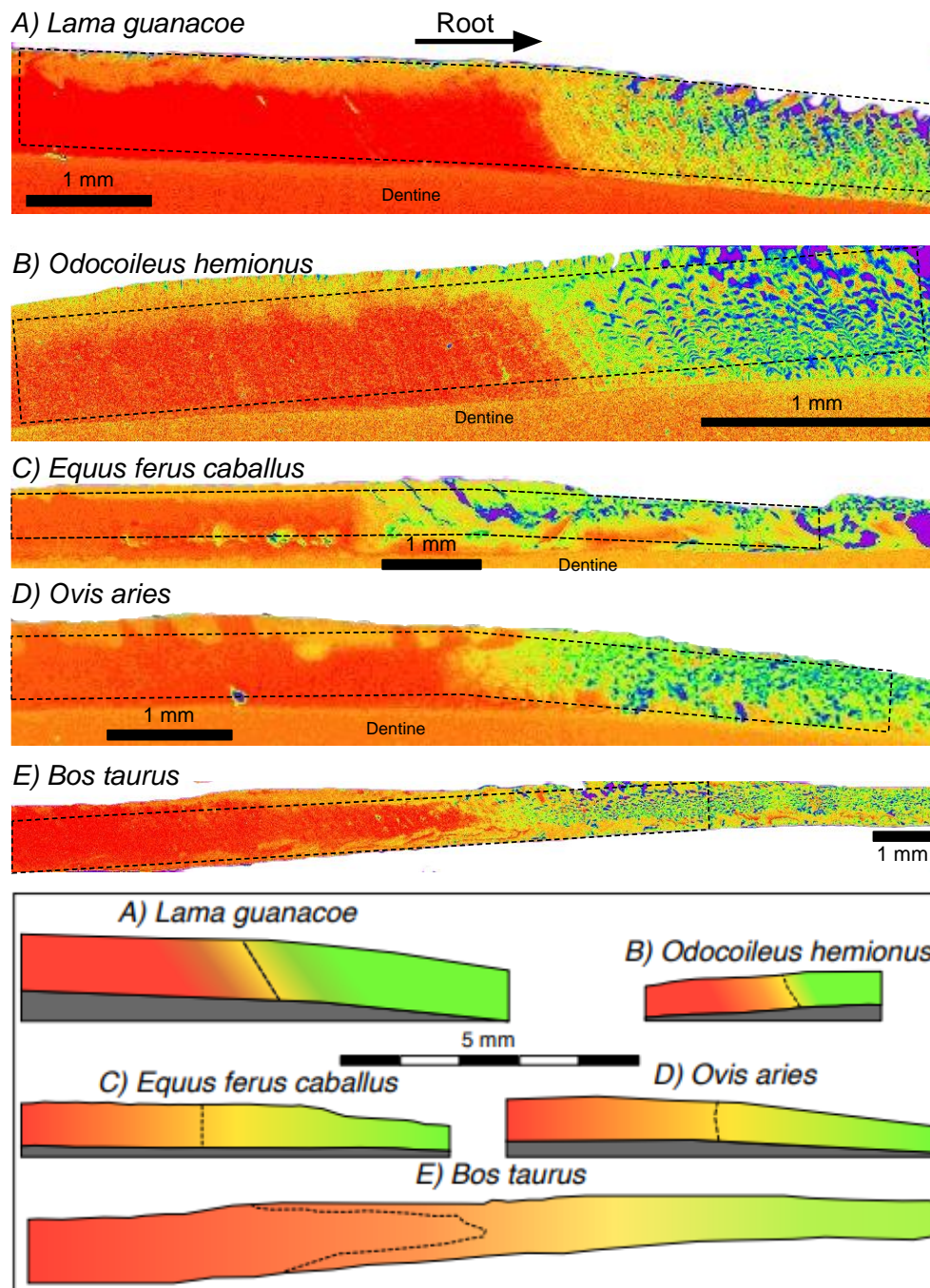


Figure 1.4. X-ray maps of calcium zoning for teeth with both mature (occlusal) and immature (apical) enamel. A) *Lama guanacoe*, B) *Odocoileus hemionus*, C) *Equus ferus caballus*, D) *Ovis aries*, E) *Bos taurus*. Warm colors indicate higher relative concentrations; blue/purple = pore space. Dashed boxes indicate areas over which calcium concentration profiles were plotted (Fig. 5). Box: schematic representations of enamel formation with inferred angles of maturation (dashed line).

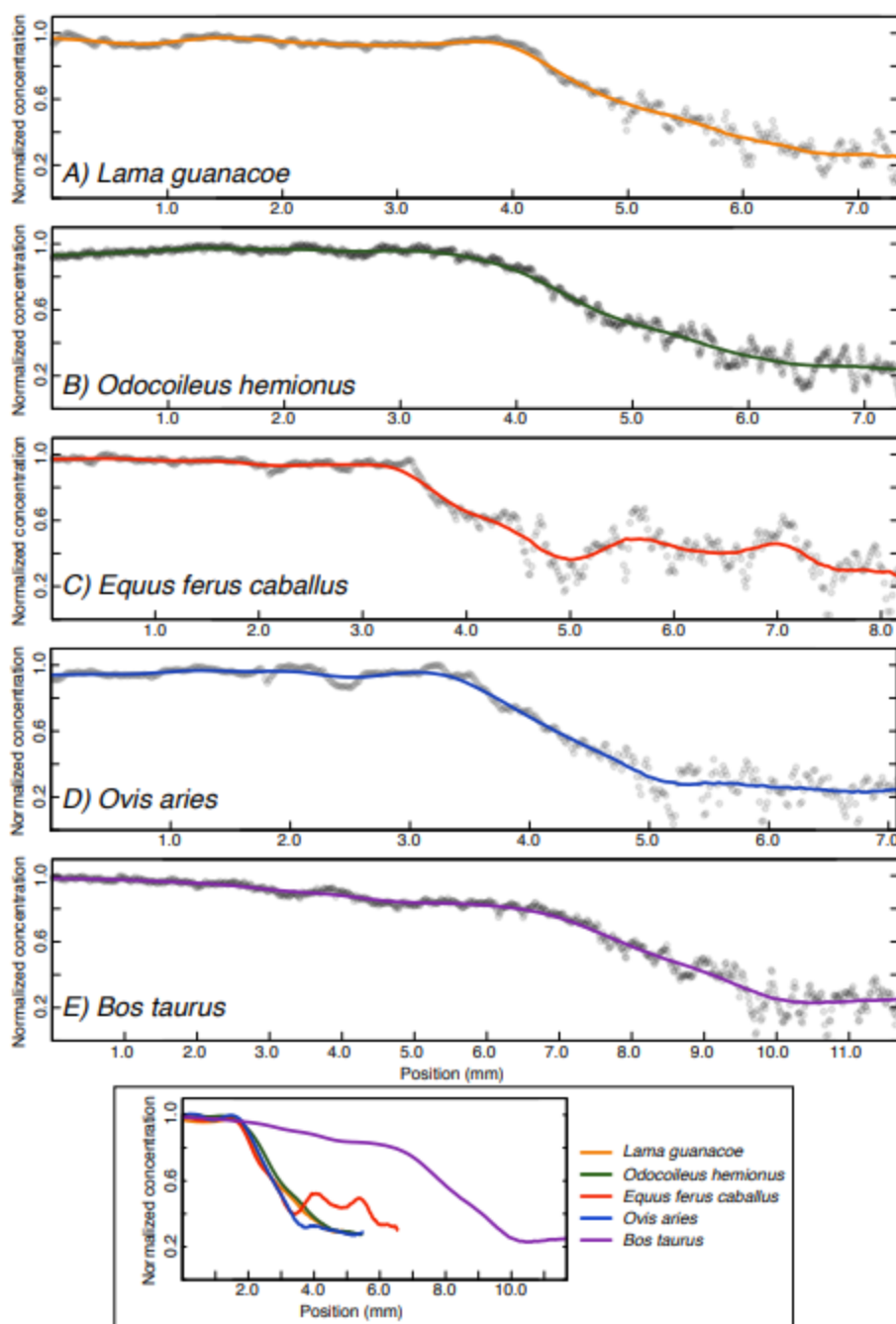


Figure 1.5. Relative calcium compositional profiles along the dashed boxes in Fig. 4. A) *Lama guanacoe*, B) *Odocoileus hemionus*, C) *Equus ferus caballus*, D) *Ovis aries*, E) *Bos taurus*. Concentrations were normalized using a linear transformation such that fully mature enamel and appositional enamel reflect mineralization fractions of 1.0 and 0.25 respectively. Box: Smoothed curves plotted with the same distance scale and shifted so the points of maximum curvature align. In all cases the transition from high to low calcium concentrations occurs over a length scale of 2-4mm.

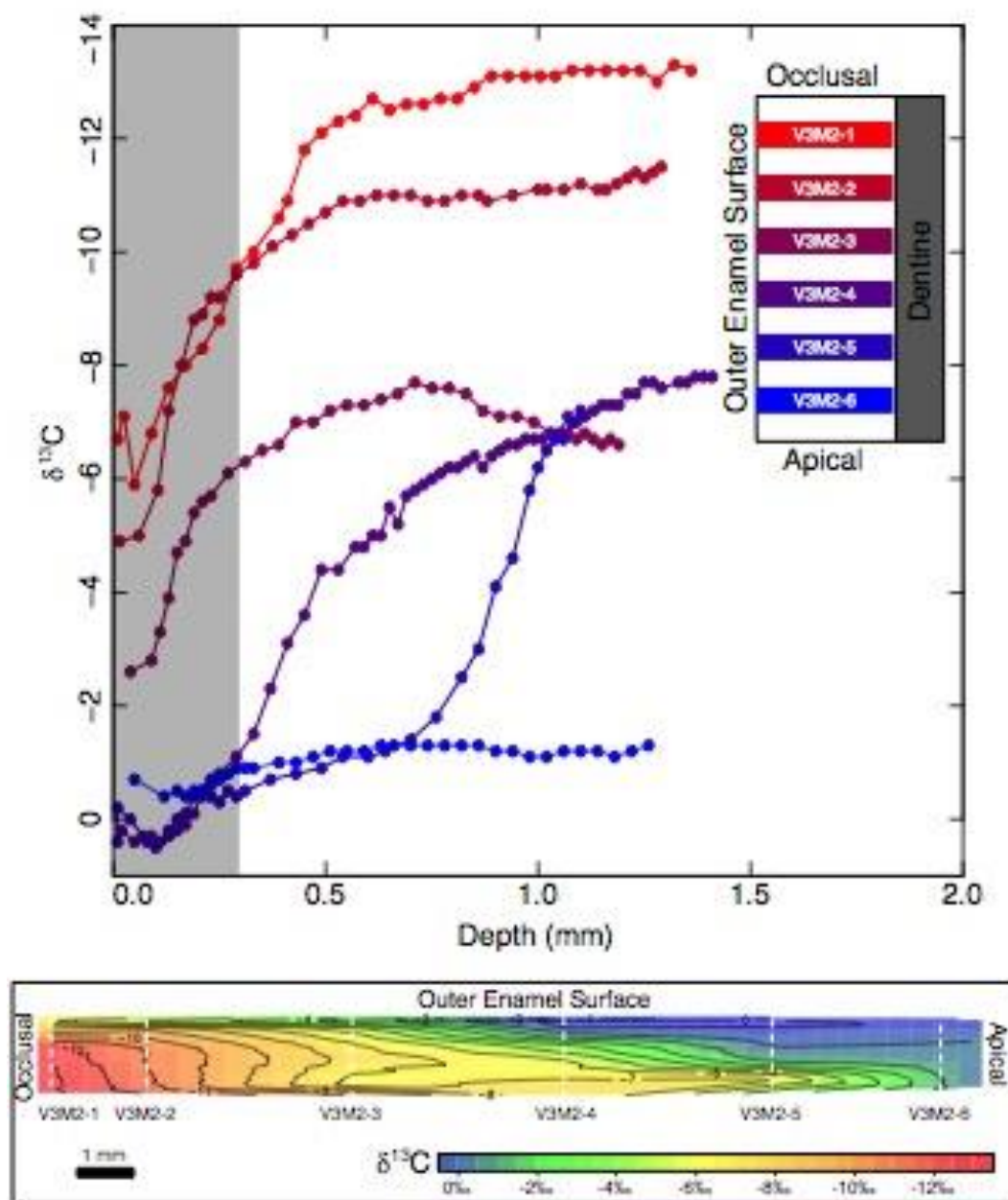


Figure 1.6. Carbon isotope compositions (note reversed axis) versus depth from outer enamel surface for slices of *Bos taurus* enamel (After Zazzo et al., 2005). The animal was switched from a pure C3 to pure C4 plant diet to induce a large change in its carbon isotope composition. Grey bar indicates the outermost 0.3 mm of enamel, approximately the thickness of the outer enamel shelf observed on our compositional map of *Bos taurus* enamel (Fig. 4). The outer enamel layer is compositionally biased by the dietary shift to C4 plants, suggesting later mineralization. Box: Interpolated carbon isotope compositions based on the six depth profiles of Zazzo et al. (2005). Carbon isotope contours suggest late mineralization for the outer enamel surface, while mineralization of the inner enamel layer progresses more rapidly. Vertical dashed lines indicate sample locations. Contour interval is 1‰.

Table 1.1. Model parameters for the Passey and Cerling (2002) model.

Parameter	Definition
δ_{ei}	Final isotope composition of mature enamel
f_i	Fraction of mineral formed during apposition
δ_{mi}	Isotope composition of enamel formed during apposition
δ_m	Isotope composition of enamel formed during maturation
l_m	Length scale of maturation
l_a	Length scale of apposition
δ_{ci}	Isotopic composition of a sampled column of enamel

Table 1.2. Descriptive statistics for tooth stable isotope data. ¹Late Pleistocene. ²Data from Pellegrini et al. (2011)

Taxa/Sample	n	Subsample Spacing	Mean	Range	Mean	Range	$\Delta(\text{CO}_3\text{-PO}_4)\pm 1\sigma$ (‰)	Best Lag	R
		Mean $\pm 1\sigma$ (mm)	$\delta^{18}\text{O}_p$ (‰)	$\delta^{18}\text{O}_p$ (‰)	$\delta^{18}\text{O}_c$ (‰)	$\delta^{18}\text{O}_c$ (‰)			
<i>Equus ferus caballus</i>	32	2.1 \pm 1.0	11.0	8.1	20.1	7.8	9.3 \pm 1.1	0	0.95
<i>Bison</i> sp. (28150) ¹	19	2.0 \pm 0.5	12.3	9.8	18.2	11.1	5.9 \pm 1.2	0	0.96
<i>Capra hircus</i>	20	2.0 \pm 0.4	12.5	3.6	21.6	4.9	9.1 \pm 0.8	0	0.87
<i>Cervus elaphus</i> (M-00-49)	8	2.4 \pm 0.6	6.0	2.5	14.3	2.9	8.3 \pm 0.4	0	0.89
<i>Cervus elaphus</i> (M-00-59)	7	2.0 \pm 0.6	6.9	2.3	15.2	2.7	8.3 \pm 0.4	0	0.8
<i>Cervus elaphus</i> (CACE) ^{1,2}	8	1.9 \pm 0.1	17.9	2.8	27.2	2.3	9.3 \pm 0.2	0	0.99
<i>Cervus elaphus</i> (PLCE) ^{1,2}	9	2.2 \pm 0.2	17.7	2.9	26.6	3.0	9.0 \pm 0.4	0	0.99
<i>Cervus elaphus</i> (STCE) ^{1,2}	6	2.4 \pm 0.4	18.5	1.5	27.6	1.5	9.1 \pm 0.5	-1	0.95
<i>Cervus elaphus</i> (PZCE) ^{1,2}	10	2.0 \pm 0.3	17.2	3.5	26	3.2	8.9 \pm 0.4	0	0.98
<i>Equus hydruntinus</i> (PZEH) ^{1,2}	15	3.0 \pm 0.5	15.9	2.4	24.5	1.0	8.6 \pm 0.6	1	0.6
<i>Equus hydruntinus</i> (STEH) ^{1,2}	12	4.8 \pm 1.2	18.7	1.0	27.5	0.9	8.8 \pm 0.4	-1	0.68
<i>Equus hydruntinus</i> (VAEH) ^{1,2}	36	2.3 \pm 0.4	18.4	2.7	27.1	2.0	8.8 \pm 0.4	0	0.84
<i>Equus hydruntinus</i> (PLEH) ^{1,2}	22	3.0 \pm 0.9	17.7	2.9	26.7	1.2	9.0 \pm 0.5	1	0.83

CHAPTER TWO: AN IMPROVED APPROACH TO AGE-DEPTH MODELING IN
DEEP TIME: IMPLICATIONS FOR THE SANTA CRUZ FORMATION,
ARGENTINA

Abstract

Accurate age-depth models for proxy records are crucial for inferring changes to the environment through space and time, yet traditional methods of constructing these models assume unrealistically small age uncertainties and do not account for many geologic complexities. Here we modify an existing Bayesian age-depth model to better account for absolute ages, relative ages among strata, and variations in sedimentation rates, and magmatic crystal populations, whose dispersion can reflect inheritance, crystal residence times and daughter isotope loss. We illustrate this approach by calculating an age-depth model with a contiguous and realistic uncertainty envelope for the Miocene Santa Cruz Formation (early Miocene; Burdigalian), Argentina. The model is calibrated using new, high-precision isotope dilution U-Pb zircon ages for stratigraphically located interbedded tuffs, where weighted mean ages range from ~16.7 to 17.6 Ma average uncertainties of ± 0.04 Ma. Our new data compare favorably with previously published $^{40}\text{Ar}/^{39}\text{Ar}$ ages. We also present a simple method to propagate age-depth model uncertainties to previously published stable isotope data collected from the Santa Cruz Formation paleosols using a Monte Carlo technique. This approach allows us to estimate

robust uncertainties on isotope composition through time, and for comparisons of terrestrial records to other proxy records.

2.1. Introduction

Placing measurements of proxy records (e.g., fossils, geochemical data, pollen abundances) in a broader geochronologic context is crucial for inferring environmental and faunal variations in space and time. For proxy records where stratigraphic position is known, chronology construction relies on both accurate and precise age determinations and an age-depth model that describes the relationship between stratigraphic position and time. This process is complicated by the underlying uncertainties in both the age determinations and the nature of sediment accumulation. Furthermore, datable materials are often intermittently distributed and are not necessarily co-located with the proxy record, entailing uncertainty in correlation and interpolation.

Considerable effort has been expended on how best to interpolate time from dated to undated stratigraphic positions, and variety of proposed statistical methods have been proposed (see reviews of: Blaauw and Heegaard, 2012; Parnell et al., 2011) for this purpose. Broadly, these methods can be split into two categories: classical and Bayesian models. Classical age-depth modeling encompasses a variety of linear, spline, and polynomial interpolation methods that aim to fit a smooth curve that relates stratigraphic position to age. The resulting models do not necessarily pass through each measured age, instead they are fit as close as possible to each point, usually by a least squares approach (Bennett, 1994). With the addition of Monte Carlo methods to simulate the underlying uncertainties in age, classical models may produce satisfactory chronologies. However, they have several limitations. First, classical models do not consider stratigraphic

relationships among samples and may produce chronologies that violate superposition and imply negative accumulation rates (See Fig. 6 in Blaauw and Heegaard, 2012). Second, these methods often underestimate the uncertainties associated with undated positions (De Vleeschouwer and Parnell, 2014).

Bayesian Models offer an alternative to the classical approach by combining data (age determinations) and prior information (stratigraphic positions) to generate a satisfactory posterior chronology. Originally developed for radiocarbon calibration and chronology construction (Blaauw and Christen, 2005; Bronk Ramsey, 2008; Haslett and Parnell, 2008), Bayesian age-depth modeling has become increasingly applied to other types of geochronologic data (Baresel et al., 2017; De Vleeschouwer and Parnell, 2014; Sahy et al., 2015; Wotzlaw et al., 2018).

In this paper we present a modified version of an existing Bayesian age-depth model, *Bchron* (Haslett and Parnell, 2008), for use with U-Pb and $^{40}\text{Ar}/^{39}\text{Ar}$ geochronologic data. We then illustrate our approach for the Miocene (Burdigalian) Santa Cruz Formation of southern Argentina (Fig. 2.1). We use our new dates, cast within a Bayesian framework, as a test case to address two broad questions. First, how does the inclusion of prior information affect the interpretation of the non-symmetric uncertainties that arise from the analysis of several individual mineral grains (i.e. zircon, sanidine)? Second, how can the significant uncertainties associated with age-depth models be considered in the interpretations of proxy records?

2.2. Bayesian Modeling

Bayesian models attempt to estimate unknown *parameters* (θ ; age and uncertainty at each specified stratigraphic level) based on observed *data* likelihoods (x ; probability

distributions of age measured at specific levels) and *prior* information about these *parameters* (here, stratigraphic superposition and limits on sedimentation rates). The relationship between these terms is formalized in Bayes theorem:

$$P(\theta|x) \propto \frac{P(x|\theta)}{P(x)} \times P(\theta) \quad (2.1)$$

The first term on the right-hand side of equation 2.1 is the conditional probability of the data given the proposed parameters, i.e. how likely the proposed age distribution for a particular stratigraphic level assuming a set of proposed parameters (θ). The second term is the probability associated with any prior knowledge about those parameters, i.e. how prior constraints such as stratigraphic superposition affect the probability of the proposed parameters. The left-hand term is the posterior conditional probability of the proposed parameters, i.e. what are the most probable ages given our dates (x) and what we know about their stratigraphic superposition.

In many cases Bayes equation is cannot be solved analytically, so we instead generate a representative sample of the posterior distribution using Markov Chain Monte Carlo methods. Markov Chain Monte Carlo uses a variety of probabilistic proposal algorithms to produce a random sample of the posterior distribution. Given a large enough sample size and adequate exploration of parameter space, this sample should be representative of the “true” posterior distribution and should have the same underlying summary statistics (Kruschke, 2015).

2.2.1 Bayesian Age-Depth Modeling with Bchron

Originally designed for radiocarbon calibration and age-depth modeling, `Bchron` is available as an open source R package (Haslett and Parnell, 2008). `Bchron` generates an age model, given: age determinations, associated uncertainties, and stratigraphic

positions. The model treats sedimentation as a series of accumulation events of varying duration and amount, where the number of accumulation events is drawn from a Poisson distribution and the amount of accumulation is drawn from a gamma distribution. These two processes are related using a compound Poisson-gamma distribution to describe the *prior* probability of the sedimentation events (Haslett and Parnell, 2008). In addition to the parameters associated with age determinations, `Bchron` uses two hyperparameters (μ , ψ) to control the mean and dispersion of the compound Poisson-gamma distribution. Because these hyperparameters (μ , ψ) are calculated over the entire section, accumulation paths that have roughly the same mean accumulation rate are effectively favored. This method results in a model that is piecewise linear and allows for a wide variety of possible accumulation paths (Fig. 2.2).

A piecewise linear process is desirable for several reasons. First, the process is monotonically increasing such that stratigraphically higher positions are always younger than those below, thus capturing the fundamental stratigraphic principle of superposition. Second, the process allows for a wide range of sedimentation paths and there is no *a priori* assumption of smoothly varying sedimentation rates. While classical methods often assume that accumulation rates vary only at dated positions or vary smoothly in between, a piecewise linear process with a varying number of change points allows for segments that imply near-zero (disconformity-like) to very rapid accumulation rates (Haslett and Parnell, 2008). Confidence intervals of chronologies based on classical methods often exhibit a waist or hourglass effect where model uncertainties counterintuitively decrease as distance from dated positions increases, underestimating uncertainty at these positions (De Vleeschouwer and Parnell, 2014; Telford et al., 2004).

Conversely, by allowing the number of sedimentation events to vary by both duration and amount, Bchron model probabilities are presented as a highest density interval (HDI), which is similar to a confidence interval but makes no prior assumptions about the distribution shape. These HDI's take on a sausage-like shape where uncertainty increases with distance from dated positions. This phenomenon captures the expectation that error should increase in areas poorly constrained by data.

2.3. Geologic Setting of Santa Cruz Formation Samples

We focus on the Santa Cruz Formation because it is one of the most fossiliferous sedimentary sequences in South America and provides an unparalleled opportunity to link paleoclimate and faunal evolution immediately prior to the mid-Miocene climatic optimum (Vizcaíno et al., 2012b). The formation is part of the Miocene infill of the South American Austral Basin. It trends NW – SE, is bounded by the Patagonian Andes in the west and the Deseado Massif in the northeast and is open to the Atlantic Ocean towards the east and southeast. During the Miocene, Andean uplift and crustal loading drove an increase in accommodation space, allowing the accumulation of the terrestrial deposits of the Santa Cruz Formation (Blisniuk et al., 2005; Bown and Fleagle, 1993; Cuitiño et al., in press; Fosdick et al., 2013; Marshall, 1976). Outcrops of these Santa Cruz Formation deposits are extensive, with exposures from the Andean foothills to the Atlantic coast (Blisniuk et al., 2005; Cuitiño and Scasso, 2010; Fleagle et al., 2012; Malumián et al., 1999; Marshall, 1976; Tauber, 1994, 1997a, b). While geographically widespread, the exposures are discontinuous, and depositional idiosyncrasies make some sections less amenable to dating. However, such a large region of the Santa Cruz Formation is

exposed, allowing age controls from multiple localities to be integrated using lithological and tephrochronological correlations (see Fig. 2.2 in Perkins et al., 2012).

There has been considerable effort to constrain the age of the Santa Cruz Formation and its fossil localities. K-Ar dates placed the Santa Cruz Formation in the late-Early to Middle Miocene (Evernden et al., 1964; Marshall et al., 1977) and to 16 – 17 Ma (Marshall et al., 1986). $^{40}\text{Ar}/^{39}\text{Ar}$ analyses for coastal exposures include a range from ~19.3 to ~16.2 Ma (Fleagle et al., 1995) and an age of 16.68 ± 0.11 Ma for a tuff from the Killik Aike Norte locality (Tejedor et al., 2006). Dates from western exposures ranged from 22.4 to 14.2 Ma (Blisniuk et al., 2005). To synthesize these ages, Perkins et al. (2012) and Fleagle et al. (2012) reported new $^{40}\text{Ar}/^{39}\text{Ar}$ ages for several tuffs, recalibrated previous dates, correlated tuffs (and their ages) across many Santa Cruz Formation localities using tephrochronology and constructed a chronostratigraphic framework for much of the Santa Cruz Formation. More recently Cuitiño et al. (2016) reported four U-Pb ages from strata exposed along the Río Bote and Río Santa Cruz, allowing correlation from western to eastern exposures.

2.4. Materials and Methods

2.4.1 U-Pb Geochronology

We analyzed tuffs from Six Santa Cruz Formation localities: Cañadón de las Vacas, Rincón del Buque 3, Cerro Observatorio, Killik Aike Norte, Cabo Buen Tiempo, and Puesto Estancia La Costa (Fig. 2.1, Locality information in Table 2.1). See Appendix B for detailed descriptions of sample locations. Combined with the stratigraphic framework of Perkins et al. (2012), our new mapping and stratigraphic sections allows correlations among these sites (Fig. 2.4). Historically the coastal Cerro Observatorio

(CO) locality has been grouped with the Cañadón de las Vacas locality (CV) which occurs ~6 km NW and slightly inland of the coastal exposures of CO. In this study we refer to the coastal exposures (alone) as CO and to the inland exposures as CV. We follow the abbreviations of Perkins et al. (2012) for locality and tuff names whenever possible to facilitate comparisons of our ages with theirs.

All mineral separations and isotope analysis took place in the Boise State Isotope Geology Laboratory using methods described in the Appendix B.

2.4.2 Model Modifications

In this study we modified the Bchron compound Poisson-gamma age-depth model for use with U-Pb and $^{40}\text{Ar}/^{39}\text{Ar}$ data. Our model is implemented as an R package, available for download at <https://github.com/robintrayler/modifiedBChron>. Here we outline our modifications.

Assignment of age uncertainties: We allow individual dates to be grouped to form a summed probability distribution function. Modern high precision dates on single mineral crystals from volcanic rocks often demonstrate dispersion beyond analytical uncertainty (Jicha et al., 2016; Rivera et al., 2013). Consequently, the resulting age uncertainty for each dated horizon is a complicated probability distribution function that we model as a summed probability distribution function. We have included the ability to combine individual dates based on a grouping variable (e.g., from the same stratigraphic horizon). Within each group, individual dates and uncertainties are modeled as either a normal or uniform distribution, as specified by the user, and then summed to form the final probability distribution function for each dated horizon.

Markov Chain Monte Carlo implementation: We implement an adaptive Markov Chain Monte Carlo algorithm to remove the need for data rescaling. `Bchron` and our model use a Markov Chain Monte Carlo and a Metropolis-Hastings algorithm to evaluate Bayes equation and produce a posterior sample for each model parameter. Briefly, for each iteration of the Markov Chain a new parameter is proposed from a Gaussian proposal distribution centered on the current parameter value. The proposed parameter and current parameter are compared and accepted or rejected probabilistically (Brooks et al., 2011; Chib and Greenberg, 1995; Kruschke, 2015). In effect the algorithm randomly walks through the parameter space. The efficiency of this algorithm depends heavily on an appropriately scaled proposal distribution. However, without *a priori* information about the target distribution, selecting an appropriately scaled proposal distribution is difficult. `Bchron` approaches this problem by rescaling the data (age determinations, age uncertainties, stratigraphic positions) to limit the possible size of the proposal distribution. While this approach is appropriate for radiocarbon chronologies, it is inflexible for data that may be presented in thousands (ka), millions (Ma) or billions (Ga) of years as they require vastly different scaling factors. We use an adaptive proposal algorithm to ensure that the parameter space (i.e. the set of all possible values for a parameter) is efficiently explored. In this method the proposal distribution for each dated horizon is defined as:

$$\theta_i = N(\theta_{i-1}, c_d^2 \sigma_h^2) \quad (2.2)$$

Where θ_{i-1} is the current model age at a specific horizon, θ_i is the proposed model age, and, σ_h^2 is the variance of the previous h iterations in the chain and c_d is a scaling factor (Gelman et al., 1996). In effect the variance of each model parameter is monitored

during each simulation and a unique proposal distribution for each parameter is adjusted accordingly.

Outlier rejection: We have removed automated outlier rejection. Instead we prescreen our data for outliers using a variety of established criteria based on the physical mechanisms of crystal growth and open system behavior in volcanic rocks. Outlier dates for mineral crystals primarily arise from three processes. First, open system behavior resulting from the loss of radiogenic daughter isotopes bias analyses to apparently younger ages. Second, mineral inclusions within a crystal may have anomalous daughter to parent isotope ratios and/or initial daughter contents, that contaminate and bias the resulting dates to apparently older ages. Finally, inheritance or recycling of geologically older crystals produces dates that are older than the eruptive age of the target magmatic event. A variety of analytical methods have been developed to minimize these systematic outliers for U-Pb and $^{40}\text{Ar}/^{39}\text{Ar}$ data. For zircon crystals, chemical abrasion prior to analysis, reduces the influence of open system behavior and contamination by selectively removing inclusions and damaged portions of the zircon lattice most susceptible to loss of radiogenic lead (Mattinson, 2005). When lead loss is intransigent, even after chemical abrasion, its effect may be identified, allowing these samples can be manually excluded, through comparisons of covariance between $^{206}\text{Pb}/^{238}\text{U}$ and $^{207}\text{Pb}/^{235}\text{U}$ (Wetherill, 1956, 1963). Likewise, the development of the step heating method for $^{40}\text{Ar}/^{39}\text{Ar}$, coupled with carefully examination of the resulting age spectrum for argon bearing minerals, using a plot of cumulative ^{39}Ar versus age and a reverse isochron diagram allow open system behavior in these systems to be monitored (McDougall and Harrison, 1999). For both dating systems, crystal recycling or inheritance, either from much older country rock

(xenocrysts) or slightly older volcanic materials from the same volcanic system (antecrysts) may produce dates older than the actual time of eruption. Xenocrysts that are significantly older than the dominant age mode are trivial to reject. Slightly older antecrysts may be removed by the application of several statistical rejection criteria (Michel et al., 2016), however we focus here on the ability of Bayesian age modeling to objectively mitigate these antecryst effects by quantitatively rejecting older age modes using superpositional constraints.

2.5. Results

2.5.1 U-Pb CA-ID-TIMS

Detailed description of each sample, LA-ICPMS data, and individual CA-ID-TIMS analyses are reported in **Appendix B**.

Weighted mean U-Pb ages ranged from 17.6 to 16.8 Ma (Table 2.1). Concordia and ranked age plots (Fig. 2.3) reveal complex behavior. While individual zircon dates from some tuffs (KARG-15-01) are tightly grouped, other samples (CV-10, Toba Blanca, CV-13) are either less precise or exhibit dispersion likely resulting from processes discussed above.

2.5.2 Model Validation

The goal of Markov Chain Monte Carlo algorithms is to produce a posterior sample that is stable, representative, and reproducible (Kruschke, 2015). The underlying compound Poisson – gamma process of `Bchron` has been repeatedly validated. Using synthetic data, Haslett and Parnell (2008) showed that ~ 80 – 95% of model HDI's encompass the “true” accumulation path. Similarly, leave-one-out cross validation on a variety of sediment cores show that ~ 50% of excluded age determinations fall

completely within model HDI's (Parnell et al., 2011). Given this previous validation, we focused on examining the performance of our model across repeated model runs.

To assess model performance, we generated 500 individual simulations for the Santa Cruz Formation data set. Each simulation is comprised of 10,000 iterations with the initial 5,000 steps discarded to allow the model to stabilize (i.e. burn-in). First, we examined the trajectory of each model parameter using trace plots (**Fig. B1**). Individual trace plots for each parameter stabilize quickly and mix well. Comparing all 500 model simulations, shows no visual difference between model runs for each parameter. Similarly, probability density estimates (kernel density estimates) of each model parameter are visually indistinguishable between simulations (**Fig. B2**). We also monitored variability in the lower bounds, upper bounds, and median of the 95% HDI across all model runs. The median was stable and varied only slightly (± 0.004 Ma; 2σ). The lower and upper bounds of the HDI also show little change among iterations (± 0.006 Ma; 2σ).

2.5.3 Modeling the Santa Cruz Formation

We developed two age-depth models for the Santa Cruz Formation, based on a composite stratigraphic of the CV locality, one using weighted mean ages, and another using the summed probability distributions of all analytically acceptable grain dates as inputs. For each model we included dates from CV (KARG-15-01, CV-10, Toba Blanca), and those from the nearby RB3 (KARG-15-09) and CO (CV-13) localities. The stratigraphic positions of these tuffs were projected into the CV composite by proportionally scaling the distance between marker beds of known stratigraphic position

at each locality (Fig. 2.4). We also include $^{40}\text{Ar}/^{39}\text{Ar}$ ages for two tuffs at Cañadón de las Vacas (CO, CO3) previously reported by Perkins et al. (2012).

When weighted ages are used as the data likelihood for each tuff (Fig. 2.5A), the median for each age posterior distribution differs from the weighted mean ages by only a few thousand years (Table 2.2). In the upper section, where there is considerable overlap between weighted mean ages, median model ages are consistently younger (Fig. 2.6). Uncertainties for each tuff are also reduced compared to weighted means by 10 – 20% (0.01 – 0.04 Ma), reflecting the effect of each dated horizon on those nearby.

When using the summed probability distribution as the likelihood input (Fig. 2.5B), the model results show several differences compared to the weighted mean model. Median model ages are consistently shifted younger when compared to the median of the likelihood probability distribution. Once again, this effect is most common in the upper section where likelihood probability distributions overlap significantly. The magnitude of the shift is also greater with a maximum shift of 0.08 Ma for the CO3 tuff. Model uncertainties for each tuff are also reduced compared to the likelihood probability distribution. The magnitude of reduction in uncertainty is significant, with decreases of up to 40 – 50% (0.2 – 0.4 Ma) for some tuffs (CO, CV-10).

In both models, the model bounds (HDI's) are broadest in the area between the CV-13 and KARG-15-09 tuffs and are much larger than the HDI's of the tuffs. In the upper section where tuffs are more closely spaced, model HDI's are significantly smaller and are similar to those of the tuffs themselves. Both the weighted mean model and summed probability distribution model show the value of collecting high precision dates from closely spaced horizons.

2.6. Discussion

2.6.1 Bayesian Conditioning of Radioisotopic Ages

Interpreting the eruptive age of volcanic rocks has traditionally focused on careful examination of individual samples, without quantitative consideration of stratigraphic relationships. Similarly, the focus of age-depth modeling is usually to predict the age of points in between dated horizons (e.g. Baresel et al., 2017; De Vleeschouwer and Parnell, 2014; Wotzlaw et al., 2018), while the effect of the model on the input dates themselves is not usually explored. Our results show the value of a hybrid approach, using traditional methods to screen grain dates for outliers arising from diverse physical behaviors (inheritance, daughter isotope loss), while we use a Bayesian framework to condition the remaining grain's dates into eruptive ages that are consistent with superpositional constraints and incorporate the variance seen in many magmatic mineral populations. The value of exploring the model's effect on the input ages themselves is particularly evident in the upper portion of the composite section, where there is considerable overlap between the summed probability distributions of the closely spaced KARG-15-01, Toba Blanca, CV-10, and CO3 tuffs. In particular, the Toba Blanca (Fig. 2.6), CV-10, and CO3 tuffs have distinct younger modes that the `Bchron` algorithm favors over higher probability, older modes. In the lower section (KARG-15-09 and below), the less precise $^{40}\text{Ar}/^{39}\text{Ar}$ dates for the CO tuff exhibits considerable overlap of its probability distribution with both the CV-13 (below) and KARG-15-09 (above) tuffs. Here again the influence of a superposition constraint is evident as the overlapping portions of the CO probability distribution are ignored by the model, reducing the HDI on the CO tuff by ~50%.

Alternatively, using weighted mean ages as a likelihood input produces an age model with lower overall uncertainties for interpolated points and slightly more rapid accumulation rates in the upper section, while accumulation rates in the lower section remain similar. Since the likelihood probability distributions are modeled as symmetrical Gaussian distributions, the three upper-most tuffs lack the younger high probability “tails” present in the summed probability distribution model. Consequently, the shift of posterior distributions for each of these tuffs towards younger ages is less pronounced than in the summed probability distribution model.

Inheritance and prolonged periods of crystal growth in magma chambers often result in crystal populations with asymmetric probability distributions that may have distinctly younger or older tails (e.g. Toba Blanca, CV-10, CO3 tuffs). Accurately modeling an eruptive age in these cases is complicated by the dominant mode being apparently older than the youngest grains. By allowing the consideration of stratigraphic relationships between samples, our model identifies the younger, lower probability grains as the most probable eruptive age (Fig 2.5C, 2.6). Conversely, some samples (KARG-15-01) are tightly grouped around an expectation value (mean) with no obvious structure to their probability distributions that suggest younger or older modes. In these cases, using weighted mean likelihoods results in overall improved model uncertainties. Ultimately the choice of using weighed mean or summed probability distribution as likelihoods should be heavily influenced by the structure of the data.

2.6.2 Using Age-Depth Models to Fine-Tune Ages

While model results suggest that the age of several tuffs require slight adjustments, overall our U-Pb ages and modeled posterior ages are consistent with

previous radiometric ages for the Santa Cruz Formation. However, our data also include ages for 5 previously unanalyzed tuffs, which allows the refinement of correlations between localities.

The Toba Blanca is exposed in several coastal exposures of the Santa Cruz Formation (Tauber, 1994), and is distributed laterally over at least 500 km (Perkins et al., 2012), making it an important marker bed for the Santa Cruz Formation. Our weighted mean age for the Toba Blanca (16.868 ± 0.032 Ma) is within uncertainty of an $^{40}\text{Ar}/^{39}\text{Ar}$ age of 16.89 ± 0.05 Ma, previously published by Perkins et al. (2012). However, our age model results suggest that of the Toba Blanca is slightly younger than ($\sim 16.80 - 16.84$ Ma; Fig. 2.6), but within uncertainty of both the weighed mean and the HDI of the summed probability distribution for the individual crystal ages. Likewise, model results suggest that both the CV-10 and CO3 tuffs are somewhat younger than their weighted mean ages. In all three cases their probability distributions have distinct younger tails, suggesting that the older modes do not represent the eruptive age and instead record a prolonged period of crystal growth or inheritance. these complications present the question, what are the “correct” ages for these tuffs? In our view, given the observed dispersion in individual zircon ages, and the stratigraphic superposition relationship with a less complex tuff (i.e. KARG-15-01), the modeled posterior age for the summed probability distributions (Table 2.2) is the most robust and realistic eruptive age.

2.6.3 Implications for Santa Cruz Formation Correlation

Our data allows new correlations between the Cañadón de las Vacas composite section and other analyzed Santa Cruz Formation localities (Fig. 2.4). The weighted mean ages of the KAN-1 (Killik Aike Norte) and KARG-15-09 (Rincon del Buque 3) tuffs are

statistically indistinguishable and we therefore propose these coeval tuffs represent a single eruptive event. Given that the Rincon del Buque and Killik Aike Norte are separated by ~100 km, a new correlative tuff over this distance provides a valuable marker bed between the two localities. Sample KARG-15-08 (16.949 ± 0.030 Ma; CBT) was collected from the lowest exposed tuff at CBT and was previously identified as the KAN-2 tuff. The age of the tuff was inferred by Perkins et al. (2012) as ~16.9 Ma, which our is supported by our results. Given that the KAN-2 tuff is also exposed ~ 5 m above the KAN-1 tuff at Killik Aike Norte (Perkins et al., 2012; Tejedor et al., 2006), our results add a new age constraint for this locality.

2.6.4 Using Age-Depth Models to Interpret Proxy Records

Exposures of the Santa Cruz Formation at Lago Posadas (~ 47° 60' S 71° 51' W) preserve at least 500 m of stratigraphic section. Blisniuk et al. (2005) propose an age range of ~ 22 to 14 Ma, but reevaluation of the section by Perkins et al. (2012), Cuitiño et al. (2015) and (Cuitiño et al., in press) imply the base of the Santa Cruz Formation to be at ~ 19 Ma. Blisniuk et al. (2005) reported $^{40}\text{Ar}/^{39}\text{Ar}$ ages for 6 tuffs and stable carbon ($\delta^{13}\text{C}$) isotope composition of ~250 paleosol carbonate nodules from Lago Posadas. Paleosol nodules are uniformly distributed throughout the section (0 to 39 m between samples) and are not co-located with dated tuffs. We used our modified modeling approach discussed above to generate a new age-model for the Lago Posadas section, and show a simple method to propagate the significant uncertainties associated with age model outputs onto the paleoclimate proxy. We used weighted mean ages for the upper 5 tuffs as model inputs. We excluded the stratigraphically lowest age reported by Blisniuk et al. (2005) as Perkins et al. (2012) noted that this tuff (LP-10) was “unsuitable for an

age”, and regional correlations indicate a younger age at this level (Cuitiño et al., 2015; Perkins et al., 2012).

Using our model (Fig. 7a; Table 3), we estimated an age and its uncertainty for each carbonate nodule based on its stratigraphic position. These uncertainties are large, typically $> \pm 1$ Ma. Given that change in isotope composition are commonly used as a proxy for ecological, climatological, and tectonic change (Blisniuk and Stern, 2005; Koch, 1998; Poage and Chamberlain, 2001), incorporating these significant uncertainties in age into the analysis of the isotope proxy records is extremely important to accurately predicting changes.

Discrete proxy record samples (stable isotopes, pollen abundances etc.) are commonly transformed into a continuous record by applying a smoothing function. Most common smoothing functions (moving averages, polynomials, splines) assume that errors are either non-existent or normally distributed, which is inconsistent with our models’ prediction of age for each proxy record (carbonate nodules). Each age-depth model consists of many possible sample chronologies (e.g. Fig. 2.2). By using these individual chronologies to predict the age of the carbonate nodules, the age of each nodule is allowed to vary while still preserving the superpositional relationships among nodules. This is accomplished using the following steps.

- 1) Use age-depths model results to choose a set of ages for each proxy record based on its stratigraphic position.

- 2) Apply an appropriate smoothing function (in this case a moving average) to the proxy data (in this case carbon isotopes) given the chosen set of ages and store the results.

3) Repeat many times and calculate summary statistics (e.g. median, HDI) over all smoothed proxy records

A moving average through the Lago Posadas carbon isotope data versus stratigraphic position (Fig. 2.7B) illustrates the limitations of fitting a single smoothing function to a data set. In areas where there is seemingly low data density (e.g. approximately ~200 and 290 m) the single moving average model shows significant spikes in isotope composition. However, when age model uncertainties are considered it becomes clear that while there is low data density in a stratigraphic context, there are many other samples of similar ages in these areas whose uncertainties overlap (Fig. 2.7C). While the single moving average model shows several spikes and wiggles in isotope composition through time with a rapid increase ~ 200 m, propagated age model uncertainties instead suggests $\delta^{13}\text{C}$ values were stable from before ~ 17 Ma, increased gradually from 17 – 16 Ma, then remain essentially unchanged until the end of the record. Converting stratigraphic position to age also simplifies comparisons of proxy records between localities that lack correlative stratigraphic features by recasting data onto a common time scale.

2.7. Conclusions

While Bayesian age-depth modeling is commonly used with Quaternary radiocarbon ages, existing models have seen only limited use in other time periods. We have demonstrated many the applications of a modified Bayesian age-depth model using new U-Pb ages of zircon and existing $^{40}\text{Ar}/^{39}\text{Ar}$ ages from the Santa Cruz Formation. Proposed tuff correlations link exposures at to those at Killik Aike Norte to the upper

section at Cañadón de las Vacas and Rincón de Buque, providing a new correlation among the localities.

Model results are largely consistent with both our U-Pb and existing $^{40}\text{Ar}/^{39}\text{Ar}$ data for the Santa Cruz Formation requiring only small adjustments to ages. While these shifts are small, we view model results as the most robust estimate of age. In many cases the model improves uncertainties on imprecise data (i.e. CO, CO₃ tuffs). The greatest improvements occur for closely spaced tuffs are dated, further showing the value of dating several samples throughout a stratigraphic section. Allowing the model to explore the full variance present in magmatic zircon populations offers an outlier rejection method that quantitatively incorporates superposition. Using model uncertainties to inform the interpretation of proxy record data also shows promise. Reanalysis of carbon isotope data from Lago Posadas paleosol record reveals a gradual increase in $\delta^{13}\text{C}$ values from ~17 to 16 Ma, with a lack of higher frequency structure evident in previous analyses.

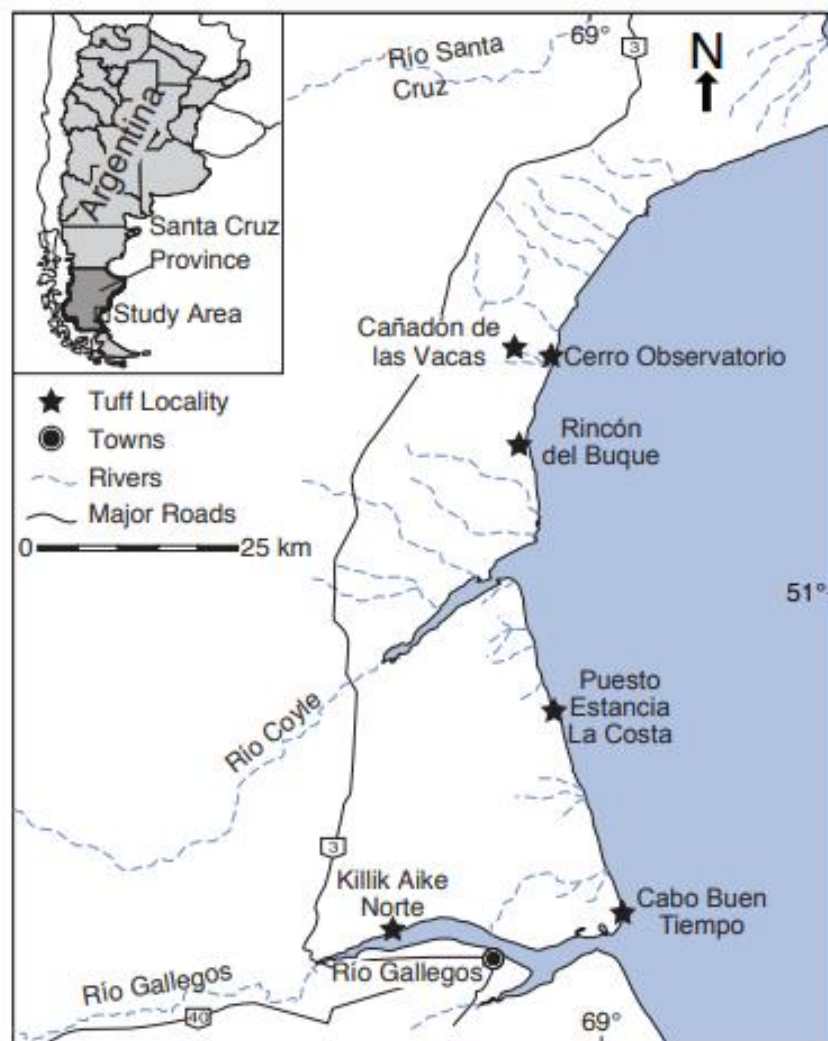


Figure 2.1. Map of tuff localities. Localities are abbreviated in the text as: Cañadón de las Vacas = CV, Cerro Observatorio = CO, Rincón del Buque = RB, Puesto Estancia La Costa = PLC, Cabo Buen Tiempo = CBT, Killik Aike Norte = KAN.

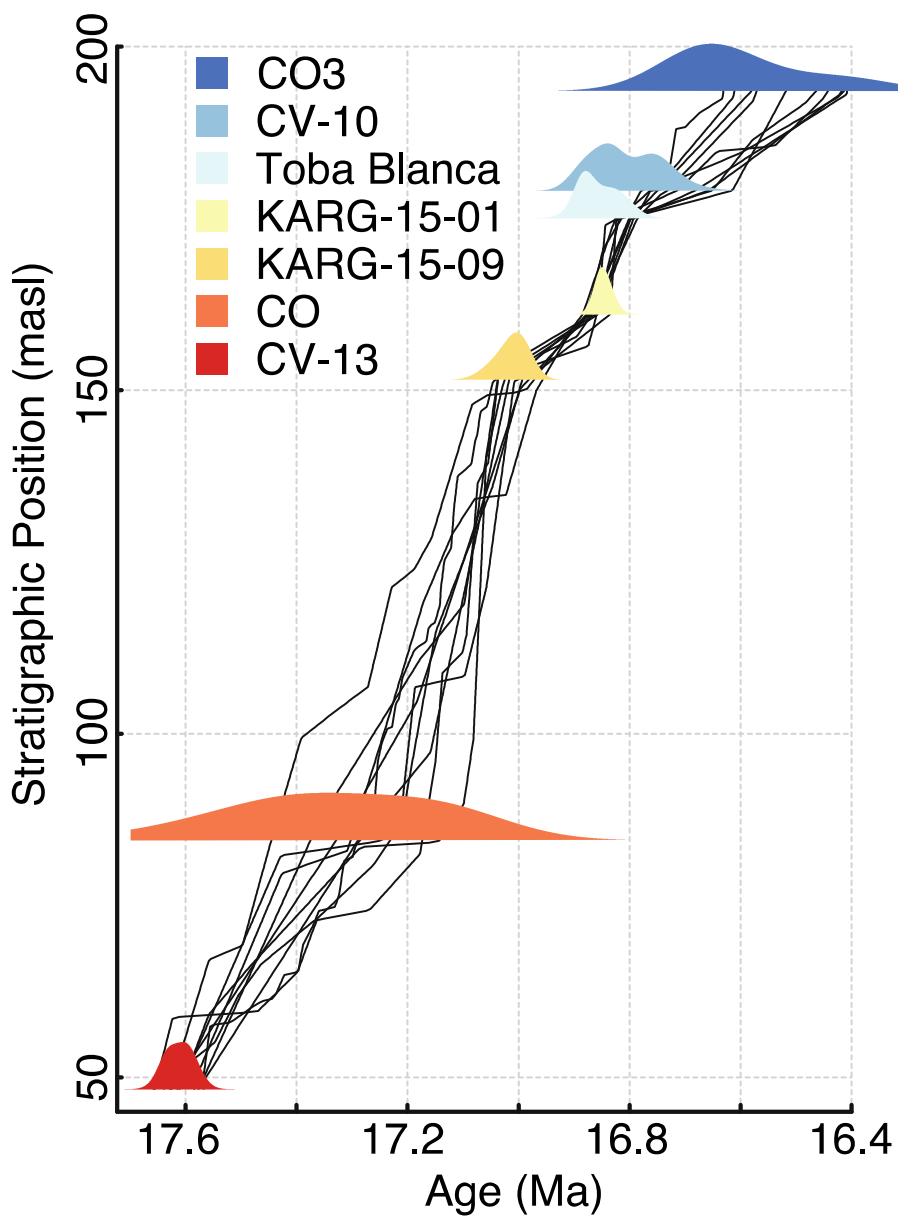


Figure 2.2. Ten example chronologies. Note that a wide variety of chronologies are possible in the lower section, while the upper section where ash beds are more closely spaced requires tightly bunched model paths.

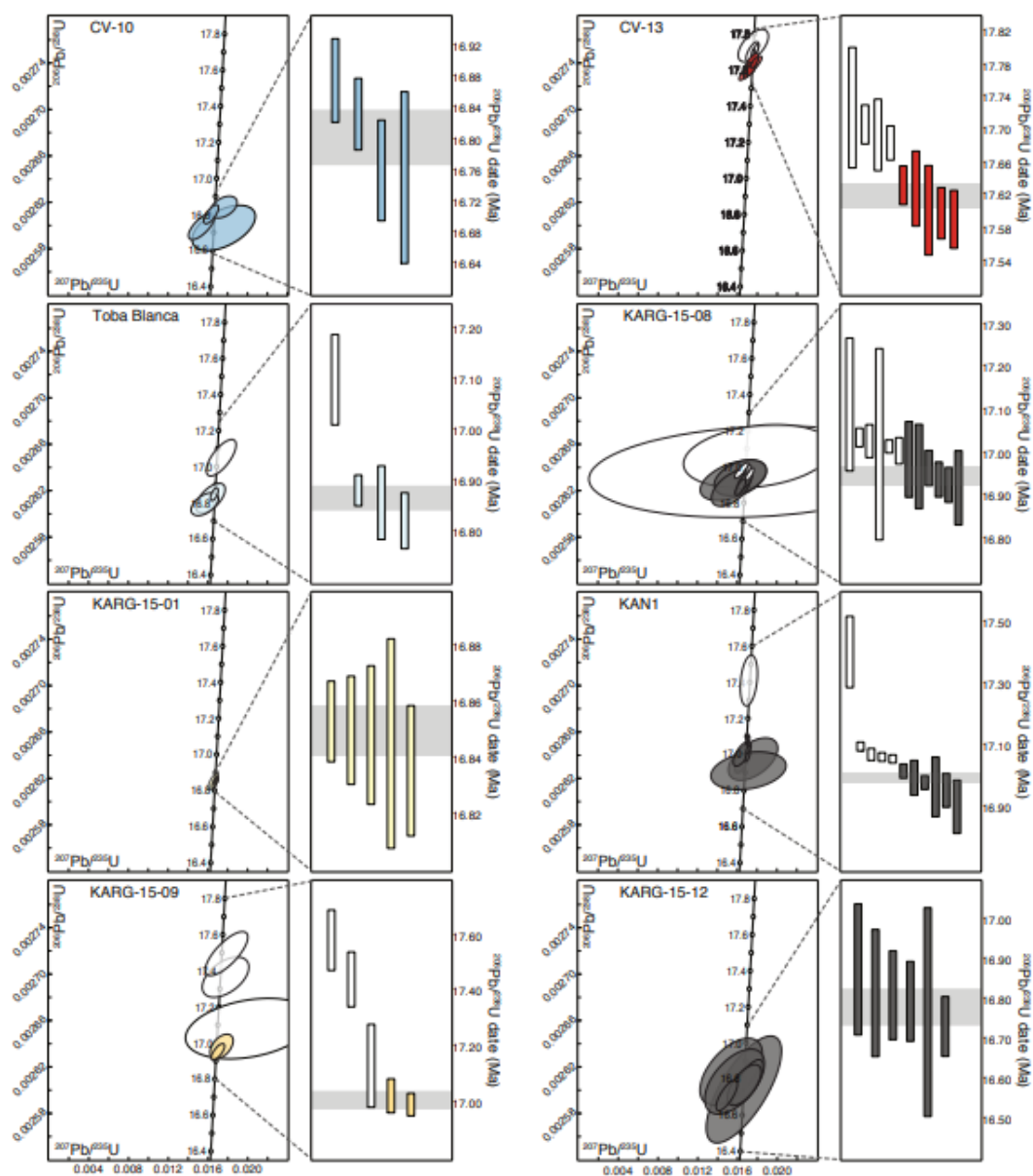


Figure 2.3. U-Pb Concordia and ranked age plots for all analyzed samples. Shaded symbols indicate analyses included in weighted mean calculations. The light grey band on ranked age plots indicates the weighted mean. All uncertainties are shown as 2σ .

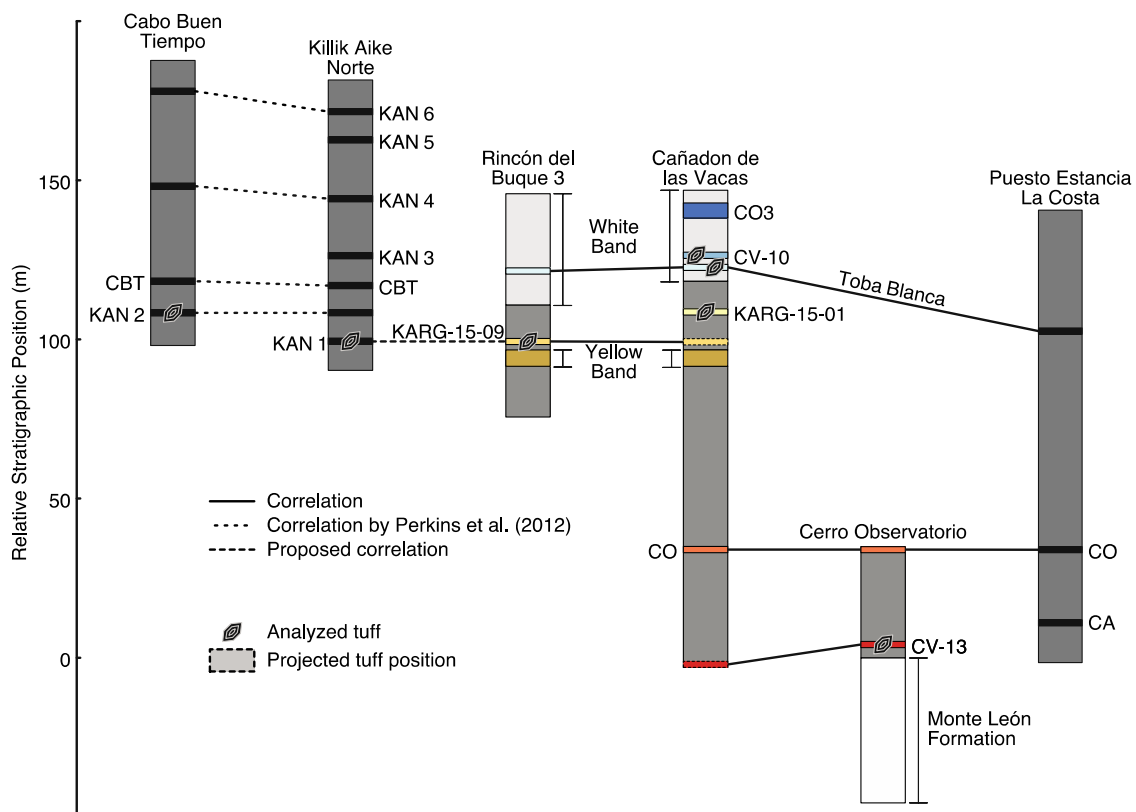


Figure 2.4. Correlation diagram for Santa Cruz Formation localities considered in this study. The geographic location of each locality is shown in Figure 1. Colored stratigraphic columns are used to form the composite section shown in Figure 5. Greyscale stratigraphic columns for Cabo Buen Tiempo, Killik Aike Norte and Puesto Estancia La Costa modified from Perkins et al. (2012).

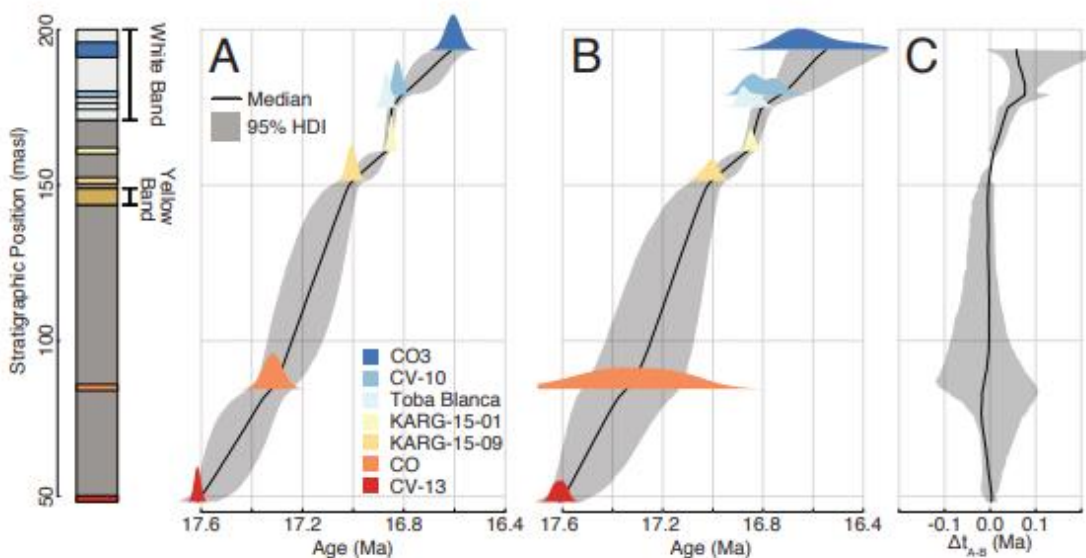


Figure 2.5. Age models and simplified stratigraphic column for the Cañadón de las Vacas – Cerro Observatorio – Rincon de Buque section. Colored polygons are the specified likelihood distribution for each tuff. The 95% highest density interval (shaded grey area) indicates the model uncertainty for all interpolated points between tuffs, while the black line indicates the median. A) Model results using weighted mean ages as likelihood inputs. B) Model results using the summed probability distribution function for each tuff as likelihood input. C) Difference between the two models. As expected, model uncertainties are higher in B because of the increased variance of the specified likelihoods. The difference in the model median is close to zero in the lower section, while in the upper section model B is shifted towards younger ages.

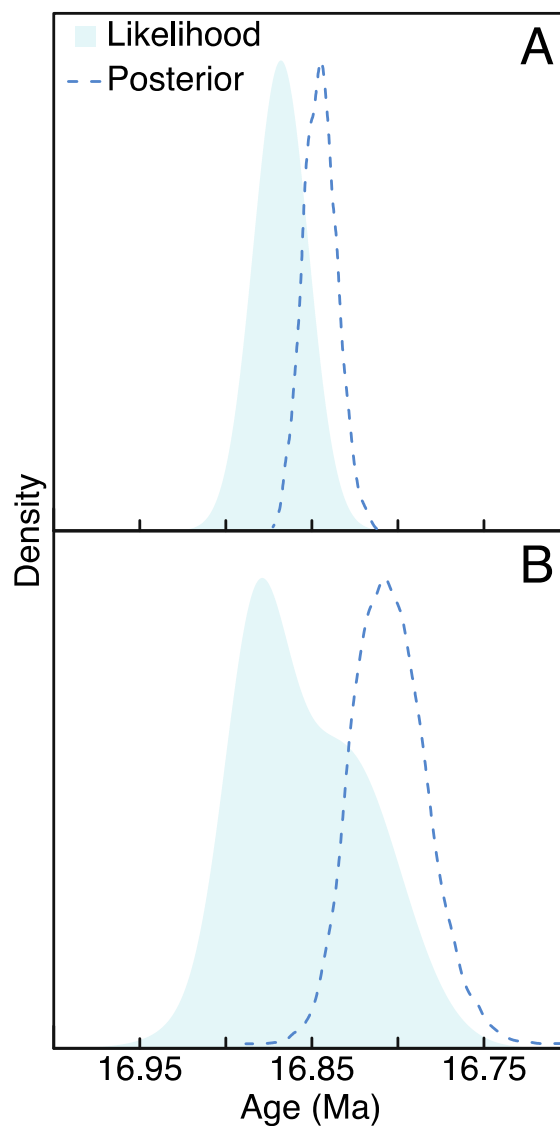


Figure 2.6. Comparison between the likelihood (shaded polygon) and posterior (dashed line) probability distribution functions for the Toba Blanca. A) Weighted mean likelihood function. B) summed probability distribution likelihood function. While both the posterior distribution for both models is shifted towards younger ages, the effect is more pronounced in B. Zircon populations often show prolonged periods of crystallization, with only the youngest populations accurately representing the eruptive age.

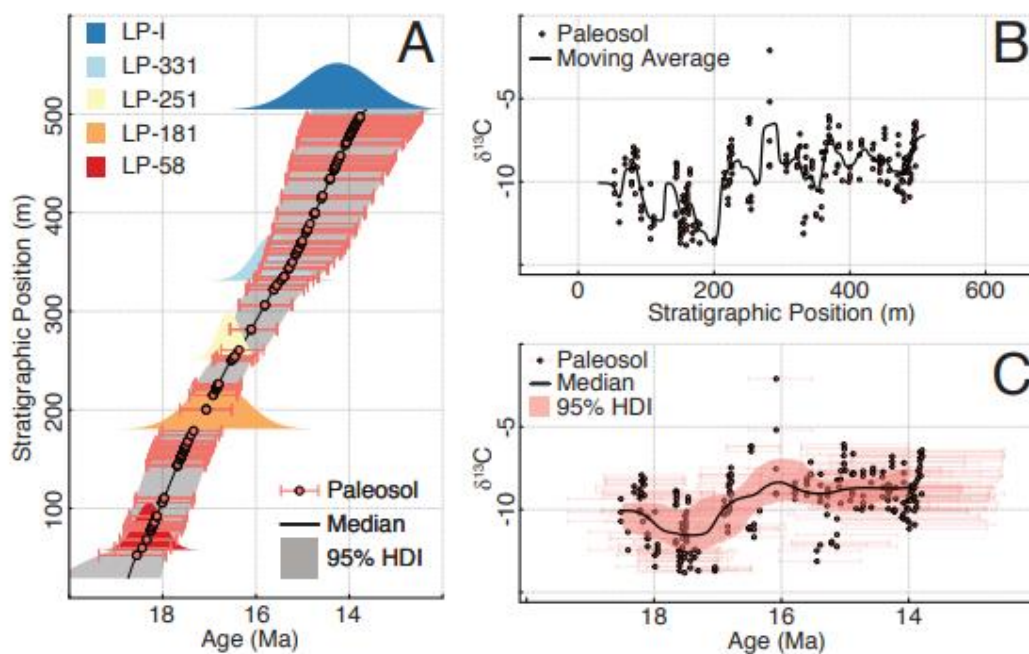


Figure 2.7. A) Age-depth model for Lago Posadas. Pink points and error bars indicate the median and 95% HDI model ages for paleosol carbonate nodules. B) Plot of the carbon isotope composition of paleosol carbonates versus stratigraphic position. a weighted moving average with a 5m window size. C) Plot of carbonate carbon isotope compositions versus age. Error bars indicate the 95% HDI of age for each point as in A. Black line is the median of 100,000 Gaussian weighted moving averages (0.2 Ma window size), where the age of each point was allowed to vary probabilistically based on age model results. 95% of the moving average models fall within the shaded pink area.

Table 2.1. GPS coordinates and elevation, composite stratigraphic position and weighted mean ages for for all samples. CV = Cañadón de las Vacas, CO = Cerro Observatorio, KAN = Killik Aike Norte, CBT = Cabo Buen Tiempo, PLC = Puesto Estancia la Coasta.

Sample	Locality	Latitude	Longitude	GPS elevation (m)	Stratigraphic Position (masl)	Weighted Mean Age (Ma)
CV-10	CV	-50.55754	-69.15467	195	179	16.825 ± 0.036
Toba Blanca	CV	-50.5572	-69.15482	185	175	16.868 ± 0.032
KARG-15-01	CV	-50.5646	-69.15071	181	161	16.850 ± 0.022
KARG-15-09	CV	-50.6550	-69.21211	96	84.5±2.5	17.006 ± 0.039
CV – 13	CO	-50.6016	-69.08627	-	48.25±3.13	17.615 ± 0.026
KAN1	KAN	-51.5747	-69.44655	4.9	-	16.996 ± 0.025
KARG-15-08	CBT	-51.52684	-68.95529	41	-	16.949 ± 0.030
KARG-15-12	PLC	-51.19278	-68.89952	105	-	16.783 ± 0.032

Table 2.2. Summary statistics of the likelihood and posterior age for each tuff from the Cañadón de las Vacas section. Weighted mean ages uncertainties are reported as a mean $\pm 2\sigma$, all other ages are reported as a median and 95% highest density interval. 1Weighted mean ages and summed probability distributions recalculated from data for individual $^{40}\text{Ar}/^{39}\text{Ar}$ laser fusion analyses from Perkins et al. (2012) provided by Matthew Heizler at the New Mexico Geochronological Research Laboratory (personal communication).

Sample	Locality	Weighted Mean Likelihood		Summed Probability Distribution Likelihood	
		Weighted Mean (Ma)	95% HDI Model age (Ma)	95% HDI (Ma)	95% HDI Model age (Ma)
$^1\text{CO3}$	CO	16.61 ± 0.060	$16.61 + 0.06 / - 0.06$	$16.62 + 0.21 / - 0.32$	$16.55 + 0.15 / - 0.26$
CV-10	CV	16.825 ± 0.036	$16.809 + 0.023 / - 0.030$	$16.812 + 0.102 / - 0.136$	$16.732 + 0.057 / - 0.080$
Toba Blanca	CV	16.868 ± 0.032	$16.845 + 0.017 / - 0.020$	$16.860 + 0.060 / - 0.082$	$16.806 + 0.039 / - 0.045$
KARG-15-01	CV	16.850 ± 0.022	$16.867 + 0.017 / - 0.019$	$16.848 + 0.031 / - 0.035$	$16.859 + 0.031 / - 0.029$
KARG-15-09	RB3	17.006 ± 0.039	$17.004 + 0.037 / - 0.034$	$17.010 + 0.071 / - 0.053$	$17.007 + 0.061 / - 0.049$
^1CO	CO	17.31 ± 0.08	$17.32 + 0.07 / - 0.07$	$17.32 + 0.41 / - 0.36$	$17.34 + 0.18 / - 0.20$
CV-13	CO	17.615 ± 0.026	$17.616 + 0.026 / - 0.026$	$17.612 + 0.053 / - 0.053$	$17.613 + 0.055 / - 0.053$

Table 2.3. Summary statistics of the likelihood and posterior age for each tuff from the Lago Posadas section. Weighted mean ages uncertainties are reported as a mean $\pm 2\sigma$, all other ages are reported as a median and 95% highest density interval. weighted mean ages are originally reported in (Blisniuk et al., 2005) and recalibrated by Perkins et al. (2012).

Sample	Stratigraphic Position (m)	Weighted Mean Likelihood	
		Weighted Mean (Ma)	95% HDI Model age (Ma)
LP-I	504.5	14.24 \pm 1.56	13.64 + 1.14 / - 1.35
LP-331	331.5	15.61 \pm 0.82	15.46 + 0.59 / - 0.68
LP-251	251.7	16.56 \pm 0.50	16.49 + 0.39 / - 0.45
LP-181	181.2	16.82 \pm 1.62	17.29 + 0.67 / - 0.61
LP-58	58.8	18.27 \pm 0.62	18.45 + 0.59 / - 0.60

CHAPTER THREE: PATAGONIAN ARIDIFICATION AT THE ONSET OF THE MID-MIOCENE CLIMATIC OPTIMUM

Abstract

Fossil rich sediments of the Santa Cruz Formation, Argentina, span the initiation of the mid-Miocene climatic optimum (MMCO), the most recent period of greenhouse conditions (warm, wet) in the Cenozoic. These conditions drove the expansion of tropical and subtropical ecosystems to much higher latitudes, with the Santa Cruz Formation the southern-most example. We collected new carbon and oxygen isotope compositions of herbivore tooth enamel from fossils ~ 17.4 to 16.4 Ma in age, to investigate ecological and climatic changes across the initiation of the MMCO. Enamel $\delta^{13}\text{C}$ values are consistent with a C_3 dominated ecosystem with moderate precipitation and mixed woodland and open areas. Serial sampled teeth reveal little zoning in $\delta^{13}\text{C}$ and $\delta^{18}\text{O}$ values, suggesting little seasonal variation in water and plant isotope compositions, or seasonal changes in diet.

Carbon isotope-based estimates of mean annual precipitation are consistent with aridification, with mean annual precipitation decreasing from $\sim 700 \pm 130$ mm/yr at 17.4 Ma to $\sim 340 \pm 90$ mm/yr at the start of the climatic optimum (~ 16.9 Ma), which corresponds to increasing global temperatures as indicated by marine proxy records, followed by a rebound to ~ 500 mm/yr by ~ 16.5 Ma. Oxygen isotopes reveal mean annual temperatures that are much warmer ($20 - 25^\circ\text{C}$) than modern temperatures in the

same region ($\sim 8^{\circ}\text{C}$) before the MMCO (20°C) with a significant increase in mean annual temperature to $\sim 25^{\circ}\text{C}$ by 16.4 Ma.

Our results agree with most previous floral and faunal estimates of temperature and precipitation for the Santa Cruz Formation and allow the robust estimation of secular changes to physical climate conditions. Our results show that most general circulation models underestimate temperature and overestimate precipitation for Miocene Patagonia.

3.1. Introduction

The mid-Miocene Climatic Optimum (MMCO; between 14 – 17 Ma) was the warmest period of the Neogene and one of the warmest of the Cenozoic, temporarily reversing a long-term global cooling trend that began in the late Paleocene (Zachos et al., 2001). Atmospheric CO_2 concentrations were high (Beerling and Royer, 2011). Terrestrial estimates from paleosols and stomatal density range from 400 – 800 ppmv (Kürschner et al., 2008; Retallack, 2009), while some marine carbon isotope records originally suggested somewhat lower concentrations of 200 – 300 ppm (Pagani et al., 1999; Pagani et al., 2005). More recent high resolution boron isotope ($\delta^{11}\text{B}$) records from foraminifera indicate low (~ 200 ppm) CO_2 concentrations at the onset of the MMCO (~ 17 Ma) followed by 100 ka oscillations between 300 and 600 ppm until 15.5 Ma (Greenop et al., 2014). General circulation models likewise require CO_2 concentrations of 300 – 600 ppm to accurately reproduce MMCO temperature and precipitation conditions suggested by other proxy records (Tong et al., 2009; You et al., 2009; Henrot et al., 2010). Importantly, most estimated MMCO CO_2 concentrations are similar to those projected over the coming century (IPCC, 2014) making the MMCO an important analog for future climates.

High atmospheric CO₂ concentrations during the MMCO drove a variety of ecological and climatic changes. Marine oxygen isotope records ($\delta^{18}\text{O}$) indicate a reduction in the east Antarctic ice sheet by 17 Ma to ~ 50% of modern size and a corresponding increase in sea surface temperatures (Flower and Kennett, 1993, 1994; Shevenell et al., 2004; Pekar and DeConto, 2006; Pekar and Christie-Blick, 2008; Cramer et al., 2011). A long-term increase in marine carbon isotope compositions ($\delta^{13}\text{C}$) beginning at ~ 16.9 Ma reflects increased burial of organic carbon, likely tied to increased marine and terrestrial primary productivity (Föllmi et al., 2005). Decreasing ice volume and increased sea surface temperatures reduced the meridional temperature gradient (Herold et al., 2010). Coupled with rising temperatures and increased precipitation (Mosbrugger et al., 2005; Böhme et al., 2011; Bruch et al., 2011), these conditions drove an expansion of terrestrial ecosystems dependent on warm, wet conditions to higher latitudes (Wolfe, 1985, 1994; Böhme, 2003; Hinojosa and Villagrán, 2005). Reptile and mammalian faunas indicative of warm humid forests migrated into Europe by the Early Miocene (Böhme, 2003; Costeur and Legendre, 2008; Domingo et al., 2009), while browsing ungulates reliant on highly productive woodlands diversified in North America (Janis et al., 2000). Palaeofloras show a similar expansion of vegetation in North and South America. Expansion of broadleaf forests in these areas decreased albedo, further increasing temperatures (Dutton and Barron, 1997), which drove a positive feedback towards enhanced warming.

The late-Early Miocene Santa Cruz Formation of Argentina (47 – 52° S Latitude; Fig. 3.1) records the southern-most extension of the MMCO expansion. Over the past century the Santa Cruz Formation has produced a wealth of mostly vertebrate fossils (see

reviews of: Vizcaíno et al., 2010; 2012). The fauna is remarkable for both its diversity and its preservation. Articulated skeletons are common and species diversity is similar to modern lowland tropical forests with marsupials, rodents, xenarthrans, primates, and a variety of ungulates well represented (Vizcaíno et al., 2012; Croft, 2013). Furthermore, the fauna includes a variety of taxa adapted to warm humid conditions (Brea et al., 2012; Fernicola and Albino, 2012; Kay et al., 2012a; 2012b) indicating physical conditions unlike the cool arid conditions that prevail in modern Patagonia. Many Santa Cruz Formation localities have been extensively dated to between 16 – 18 Ma (Fleagle et al., 1995; Fleagle et al., 2012; Perkins et al., 2012; Trayler et al., in review), making the fauna ideal for investigating changes to physical climate conditions (precipitation, temperature) at the onset of the MMCO.

While previous examinations of Santa Cruz Formation ecology and climate integrate several lines of floral, faunal, and sedimentological evidence (Croft, 2001; Vizcaíno et al., 2010; Kay et al., 2012b), these estimates either consider the formation as a whole or focus on a narrow stratigraphic, and therefore temporal, range. In this study we present new stable carbon ($\delta^{13}\text{C}$) and oxygen ($\delta^{18}\text{O}$) isotope compositions from fossil bone and tooth enamel recovered from Santa Cruz Formation strata spanning the initiation of the MMCO (c. 16.5 - 7.5 Ma; Trayler et al., in review). We use these data to address three questions:

- 1) How did high atmospheric CO_2 concentrations at the onset of the MMCO affect physical climate conditions of the Santa Cruz Formation? We use our stable isotope data coupled with existing geochronology to create a model of mean annual precipitation (MAP) and mean annual temperature (MAT) through this temporal interval.

We also use intra-tooth isotopic zoning to investigate the whether and how much seasonality changed through this interval.

2) Did changing physical conditions affect the ecology of large-bodied Santa Cruz Formation ungulates? This might be an expectation if changes in precipitation and temperature were sufficient to alter habitat type (e.g. more or less forested conditions).

How well do existing general circulation models predict physical conditions for mid-Miocene Patagonia? Models of MMCO conditions predict a high MAP (> 1000 mm/yr) and a cool MAT ($5 - 10^{\circ}\text{C}$) (Tong et al., 2009; Henrot et al., 2010; Herold et al., 2010; Herold et al., 2011). These models rely on proxy records to both inform model construction and validate model results, but as the majority of suitable terrestrial MMCO proxy sites are in the northern hemisphere (Herold et al., 2011), our data provide a new control on Patagonian climate during the MMCO.

3.2. Background

3.2.1 Miocene Climate of Patagonia

Modern conditions in our study area (Fig. 3.1) are cool (MAT $\sim 8^{\circ}\text{C}$) and semi-arid (MAP ~ 250 mm/yr). Most previous work suggest that Miocene conditions in Patagonia were significantly warmer and wetter. Tropical mammals diversified and expanded south during the early Miocene (Pascual and Ortiz Jaureguizar, 1990) and Patagonia was dominated by a mixture of drier lowlands interspersed with forested riparian areas. Megathermal forests reliant on high temperatures (MAT $> 24^{\circ}\text{C}$) expanded south and stabilized until at least the Middle Miocene followed by cooling and aridification in the Late Miocene (Barreda and Palazzesi, 2007). Floral evidence from the lower Santa Cruz Formation indicates a mixture of semi-arid temperate forests and humid

dense forests. Wood physiognomy suggest a MAT of $9.3 \pm 1.7^{\circ}\text{C}$ or $19.3 \pm 1.7^{\circ}\text{C}$, MAP of 869 ± 940 mm/yr, and a long (~7 months) dry season (Brea et al., 2012). Clay mineralogy, paleosol type, and fossil plant abundances suggest ecosystem changes over periods of a few ka, with older strata consistent with a mixed grassland – woodland environment which transitions into a more heavily vegetated environment, followed by a return to cooler and drier conditions (Matheos and Raigemborn, 2012).

Mammalian faunas also suggest a complex mosaic of coexisting of habitat types. Several species of arid-adapted armadillos are common (Vizcaíno et al., 2006), while the presence of glyptodonts, arboreal and terrestrial sloths, and anteaters indicates the presence of woodland and forested environments (Bargo et al., 2012). Large ungulates are also common. The hypsodont notoungulates (*Nesodon*, *Adinotherium*) have typically been reconstructed as mixed browser-grazers or grazers, although more recent morphological (Cassini et al., 2012; Cassini and Vizcaíno, 2012; Cassini, 2013) and microwear (Townsend and Croft, 2008) analysis suggests a browsing diet, requiring some woody vegetation. Croft (2001) used cenogram analysis (ranked plots of mammalian body mass) to compare the Santa Cruz Formation to 16 modern south American faunas, concluding the fauna was characteristic of a heavily forested, wet environment (but see critique of cenogram analyses by Kay et al. (2012b)). Alternatively, based on calculations of population densities, crop biomass, and terrestrial productivity, Vizcaíno et al. (2010) interpreted the paleoenvironment as a temperate forest and bushland-with a somewhat lower MAP of < 1000 mm/yr. Kay et al. (2012b) reviewed existing floral and faunal constraints and using niche metrics concluded that faunas from the lower Santa Cruz

Formation (~ 17.4 – 17.5 Ma) inhabited mixed forest – grasslands with MAP > 1000 mm/yr and MAT > 14°C.

3.2.2 Stable Isotopes in Enamel and Bone

Chemically, bone and tooth enamel is composed of hydroxylapatite [$\text{Ca}_5(\text{PO}_4)_3\text{OH}$], with carbonate (CO_3) substitution in the PO_4 and OH sites (Elliott, 2002). While bone carbonate is easily altered diagenetically at ambient temperatures (Kohn and Law, 2006), enamel is resistant to alteration retaining its primary isotope composition (Kohn and Cerling, 2002).

Tooth enamel mineralizes progressively from the occlusal (wear) surface towards the root and is not remodeled after formation (Pasey and Cerling, 2002). Mineralization occurs as a two-stage process – apposition and maturation – (Robinson et al., 1978; 1979; Suga, 1982) although only second stage maturation controls isotope compositions (Trayler and Kohn, 2017). Mineralization rates for ungulates vary but are commonly on the order of 40 – 60 mm/yr (Fricke et al., 1998; Kohn, 2004). Changing values of $\delta^{18}\text{O}$ and $\delta^{13}\text{C}$ track environmental conditions and diet: the $\delta^{18}\text{O}$ of an animal's body water tracks variations in the composition meteoric water throughout the year, with lower in winter and higher in summer. These changes are archived in tooth enamel with a damping effect related to the rate of mineralization and oxygen turnover in the animal (Kohn, 1996; Kohn et al., 1996; Pasey and Cerling, 2002; Podlesak et al., 2008). Changes to $\delta^{13}\text{C}$ values reflect changes in diet. Both records are attenuated by the rate of enamel mineralization and carbon turnover in the animal. Therefore, while teeth do not record the full range of isotope compositions over a period of tooth growth, isotopic zoning within enamel do reflect changes in seasonality and diet.

The oxygen isotope composition of tooth enamel is controlled by the composition of ingested water (Luz and Kolodny, 1985; Kohn, 1996; Kohn et al., 1996). In large herbivores, most ingested water is drinking water and enamel $\delta^{18}\text{O}$ values from modern mammals correlate well with meteoric water compositions (Kohn, 1996; Hoppe, 2006; Kohn and Dettman, 2007) although some drought tolerant taxa exhibit second order effects related to relative humidity (Levin et al., 2006).

The carbon isotope composition of enamel is controlled by diet. In herbivores, enamel $\delta^{13}\text{C}$ values reflect the plants they eat plus an enrichment factor. Studies of wild and captive herbivores suggest enrichments of + 13.3 – 14.6‰ (Passey et al., 2005), with an average of 14.1‰ for non-ruminants (Cerling and Harris, 1999). Protein phylogeny places many South American ungulates in a monophyletic clade with non-ruminant perissodactyls (Buckley, 2015). Likewise morphological similarities between perissodactyls and notoungulates suggest a hindgut fermentation for the latter group (Cassini et al., 2012). We therefore use 14.1‰ for all enamel – diet corrections.

All plants use one of three photosynthetic pathways (C_3 , C_4 , CAM) to fix atmospheric CO_2 , each resulting in characteristic carbon isotope compositions. C_4 plants (modern $\delta^{13}\text{C} = -12.1 \pm 1.1\text{‰}$) are mostly warm growing season grasses, sedges, and a small number of dicots. C_4 plants became a significant portion of global vegetation biomass only in the Late Miocene and Early Pliocene (Cerling et al., 1997), and are therefore unlikely to have contributed significantly to the diet of Santa Cruz Formation herbivores. Likewise, CAM plants rarely make up a significant portion of large herbivore diets today.

C₃ plants (trees, shrubs, herbs, cool season grasses) make up the majority of both modern and Early and Middle Miocene vegetation biomass. Modern C₃ δ¹³C values have a mean of -28.5‰ and range from -23 – -32‰ (Kohn, 2010). As mid-Miocene atmospheric CO₂ δ¹³C values were ~ 2.5‰ higher than modern values (Tippie et al., 2010), tooth enamel δ¹³C values lower than -7.5‰ (~ -24‰ + 14‰ + 2.5‰) should reflect a diet of pure C₃ plants. δ¹³C values in closed canopy forests are extremely low (< ~ -31‰) due to recycling of low δ¹³C CO₂ and low light levels in the understory (Van Der Merwe and Medina, 1991). δ¹³C values lower than -15‰ (~ -31‰ + 14‰ + 2.5‰) would be indicative of closed canopy forests.

3.3. Materials and Methods

3.3.1 Fossil Collection and Sampling

Fossil teeth and bone fragments of bone from large mammals were collected *in situ* from two Santa Cruz Formation localities, Cañadón de las Vacas and Rincón de Buque (Fig. 3.1). The stratigraphic position of each specimen was measured relative to marker beds of known position using a Jacobs staff. In most cases, teeth were identified to the genus level. We made no attempt to identify bone fragments. When collecting fossil teeth, we primarily targeted large ungulates for two reasons. First, these taxa are abundant throughout the section, allowing us to track the same genera through time; this allows us to compare data directly throughout the section. Second, large herbivores consume large amounts of vegetation, effectively integrating large swaths of vegetation into single enamel samples (Kohn, 2016).

All teeth were lightly abraded with a carbide burr to remove surficial material before sampling. About 10 mg of enamel powder was collected from each tooth using a

0.5 mm inverted cone carbide dental drill bit and a Dremel® rotary tool. We collected bulk enamel samples by drilling a single continuous groove parallel to the growth axis for the entire length of the available enamel. In most cases this process averages several cm of enamel into a single sample. We also collected serial samples from a subset of teeth to examine intra-tooth isotopic zoning. For these samples, we collected several samples along a tooth perpendicular to the growth axis.

We collected several ($n > 5$) bone fragments from the same stratigraphic horizon to make up a single composite bone sample. These fragments were sonicated in deionized water to remove surficial material and ground independently in a mortar. Equal volumes resulting powders were mixed.

After sampling we pretreated all enamel and bone powders following the procedures of Koch et al. (1997) to remove organic contaminants and labile carbonates. The isotope composition of the carbonate component of each sample was measured by phosphoric acid digestion using a 2010 ThermoFisher GasBench II coupled with a Delta V+ continuous flow isotope ratio mass spectrometer located in the Stable Isotope Laboratory, Department of Geosciences, Boise State University. All stable isotope analyses in this study are from the carbonate component and are reported in the standard delta notation relative to VPDB and VSMOW for $\delta^{13}\text{C}$ and $\delta^{18}\text{O}$ respectively. All analyses were standardized to VPDB ($\delta^{13}\text{C}$) and VSMOW ($\delta^{18}\text{O}$) using the NBS-18 and NBS-19 calcite standard reference materials. Analytical reproducibility for both standards was $\pm 0.1 - 0.2$ ($n = 46; 2\sigma$) for both $\delta^{13}\text{C}$ and $\delta^{18}\text{O}$. We also analyzed several replicates of NIST 120c, a phosphorite with chemistry similar to enamel and bone, as a preparation

standard. Analytical reproducibility for NIST120c was $-6.52 \pm 0.14\text{‰}$ ($n = 20$; 2σ) and $28.89 \pm 0.65\text{‰}$ ($n = 20$; 2σ) for $\delta^{13}\text{C}$ and $\delta^{18}\text{O}$ respectively.

3.3.2 Precipitation Estimations

C_3 plant $\delta^{13}\text{C}$ values are sensitive to aridity, with $\delta^{13}\text{C}$ values decreasing with increased water availability (Ehleringer and Cooper, 1988; Ehleringer, 1989; Farquhar et al., 1989; Diefendorf et al., 2010; Kohn, 2010). This relationship allows inference of habitat type, with higher $\delta^{13}\text{C}$ values associated with open habitats (savannah, scrublands) and lower values associated with closed habitats (forests). The dependency of the carbon isotope compositions of C_3 plants on water availability also allows mean annual precipitation to be calculated from enamel $\delta^{13}\text{C}$ values:

$$MAP = 10^{\left[\frac{\Delta^{13}\text{C} - 2.01 + 0.000198 \times \text{elevation} - 0.0129 \times \text{abs}(\text{latitude})}{5.88} \right] - 300} \quad (3.1)$$

where elevation and latitude are in meters and degrees (Kohn, 2010). While South America has moved westward since the Miocene, there have been only changes of less than 5° in the latitude and negligible changes elevation in the study area and we therefore use a modern elevation of ~ 20 m and latitude of -50.5° for all specimens. Even so, regression coefficients in equation 1 show that these two parameters have little overall effect on MAP calculations. $\Delta^{13}\text{C}$ is given by:

$$\Delta^{13}\text{C} = \frac{\delta^{13}\text{C}_{\text{atm}} - (\delta^{13}\text{C}_{\text{enamel}} - 14.1)}{1 + (\delta^{13}\text{C}_{\text{enamel}} - 14.1)/1000} \quad (3.2)$$

which corrects enamel $\delta^{13}\text{C}$ values for dietary enrichments and changes to atmospheric CO_2 $\delta^{13}\text{C}$ values (Kohn, 2010). We used the approach of Tipple et al. (2010) to calculate $\delta^{13}\text{C}_{\text{atm}}$ from the high resolution benthic foraminifera records of Holbourn et al. (2015).

We made no corrections to our data for changes in atmospheric CO_2 concentrations.

While controlled experiments imply a dependency between C_3 plant $\delta^{13}\text{C}$ values and

atmospheric CO₂ concentrations (Schubert and Jahren, 2012), modern and fossil proxy records do not resolve a dependence of plant δ¹³C values on atmospheric CO₂ concentrations (Kohn, 2016).

3.3.3 Temperature Estimations

While bone is mineralogically similar to enamel, it has a proportionally higher carbonate content (Driessens and Verbeeck, 1990) and is more finely crystalline, increasing its susceptibility to alteration during fossilization (Ayliffe et al., 1994; Trueman and Tuross, 2002). Dissolution and recrystallization of bone carbonate during fossilization occurs at ambient temperatures, and in equilibrium with soil carbonate (Kohn and Law, 2006). Given an independent record of water δ¹⁸O values (enamel) and the temperature dependence of CaCO₃-water oxygen isotope fractionation (Kim and O'Neil, 1997), bone oxygen isotope compositions are related to temperature:

$$MAT (^{\circ}C) = \frac{18030}{1000 \ln \left(\frac{1 + \frac{(\delta^{18}O_{bone} - 2.2)}{1000}}{1 + \frac{(1.15 \times \delta^{18}O_{enamel} - 36.3)}{1000}} \right) + 32.42} - 273.15 \quad (3.3)$$

where δ¹⁸O_{bone} and δ¹⁸O_{enamel} are expressed in VSMOW (Zanazzi et al., 2007).

3.3.4 Age-Depth Modeling and Isotope Compositions

Several dated tuffs occur at Cañadón de las Vacas and Rincón del Buque. U-Pb and ⁴⁰Ar/³⁹Ar geochronology constrains the age of these localities to between ~16.5 and ~17.5 Ma (Perkins et al., 2012; Trayler et al., in review). Because the precise stratigraphic position of each dated tuff is known, we used a modified version of the Bayesian age-depth model Bchron (Haslett and Parnell, 2008; Trayler et al., in review) to construct a continuous model of age and uncertainty estimates for a composite of the two localities. This approach allows us to calculate an age and age-uncertainty for each

enamel and bone sample based on its stratigraphic position. Briefly, Bchron model's sedimentation as a series of accumulation events of varying duration and amount while respecting stratigraphic superposition relationships. The model probabilistically allows sediment accumulation rates to vary using a Markov Chain Monte Carlo algorithm. The resulting age-depth model is piecewise linear and has uncertainties that intuitively expand in areas with widely spaced age constraints, reflecting a lower confidence in age in these areas.

Trayler et al. (in review) offer a Monte Carlo method to propagate age-depth model uncertainties onto paleoclimate proxy records while respecting the stratigraphic superposition relationships among the samples. This method involves four basic steps. 1) Use age-depth model results to estimate a set of ages for each bone and enamel sample, 2) Apply a smoothing function to the proxy data (stable isotope records) to attenuate high frequency noise. In this case we use a moving average, which weights all data points using a Gaussian kernel and a smoothing window size of 0.05 Ma. 3) Repeat steps 1 and 2 many times ($> 10,000$) and store the results. 4) Calculate summary statistics over all smooth isotope compositions. All age-depth modeling and data smoothing were performed using R v.3.3.3 (R Core Team, 2017).

3.4. Results

3.4.1 Bulk Isotope Compositions

Our enamel data come from three orders of mammals: Notoungulata, suborder Toxodontia, (*Adinotherium*, *Homalodotherium*, *Nesodon*), Astrapotheria (*Astrapotherium*), and undifferentiated Litopterna. Enamel $\delta^{13}\text{C}$ values have a mean value of $-11.4 \pm 2.3\text{‰}$ (2σ ; Table 3.1, Fig. 3.2), with a maximum value of -8.8‰ , consistent with a diet of

purely C₃ plants. Enamel $\delta^{18}\text{O}$ values have a mean value of $23.1 \pm 3.4\text{‰}$. Bone $\delta^{13}\text{C}$ and $\delta^{18}\text{O}$ values are similar to those of enamel with means of $-10.6 \pm 3.8\text{‰}$ and $21.8 \pm 1.8\text{‰}$, respectively. Stable isotope compositions and stratigraphic positions for all samples may be found in the appendix C.

Although we include undifferentiated *Toxodonta* data in later temperature and precipitation modeling calculations, we excluded these data from statistical tests because they represent a combination of *Adinotherium*, *Nesodon* and perhaps *Homalodotherium*. Because fossil ages span ~ 1 Ma (discussed below) we tested the equivalence of means among taxa using $\Delta^{13}\text{C}$ values (eq. 3.2) to correct for changes to $\delta^{13}\text{C}_{\text{atm}}$. *Nesodon*, *Adinotherium*, *Astrapotherium*, *Homalodotherium*, and Litopterna show no significant differences in $\Delta^{13}\text{C}$ values (ANOVA; $p > 0.05$). $\delta^{18}\text{O}$ values among taxa show statistically significant differences (ANOVA; $p < 0.05$). *Post hoc* pairwise t-tests (with Bonferroni correction; Table 3.2) reveal that *Astrapotherium* $\delta^{18}\text{O}$ values are significantly lower than all other taxa, and that Litopterna $\delta^{18}\text{O}$ values are significantly higher than all groups except *Homalodotherium*.

3.4.2 Intra-Tooth Isotope Zoning

We selected five molars for detailed subsampling, one *Astrapotherium*, one *Homalodotherium*, and three *Nesodon* (appendix C). Zoning profiles reveal low to moderate variation in carbon and oxygen isotope compositions over the length of each tooth (Fig. 3.3). Although enamel mineralization rates for notoungulates and astrapotheres are unknown, rates for horses and bovids vary between 40 and 60 mm/yr (Kohn, 2004; Trayler and Kohn, 2017) suggesting that our zoning profiles should represent about 1 to 1.5 years of enamel growth. Overall, $\delta^{13}\text{C}$ values within single teeth

are very consistent, with an average intra-tooth variation of $\pm 0.6\text{‰}$ (2σ). Carbon isotope compositions from one individual (CV-RT-15-016) displays an $\sim 2\text{‰}$ change in $\delta^{13}\text{C}$ values over ~ 20 mm which is the highest observed variability. $\delta^{18}\text{O}$ values show somewhat more variation, with an average intra-tooth variability of $\pm 1.6\text{‰}$ (2σ). Oxygen isotope zoning profiles do not reveal a clear structure, i.e. there is no quasi-sinusoidal variation in $\delta^{18}\text{O}$ values that usually results from strong seasonal variations in meteoric water isotope compositions. Instead three teeth show several mm of unchanged isotope compositions followed by brief excursions towards low $\delta^{18}\text{O}$ values.

3.4.3 Age-Depth Modeling and Smoothing

Model ages for enamel and bone samples span from ~ 17.4 Ma to ~ 16.4 Ma (Fig. 3.4A). Samples located near dated tuffs are best constrained and have uncertainties similar to the tuffs themselves. ($\sim \pm 0.03$ Ma), while samples that are stratigraphically farthest from dated tuffs have the highest uncertainties ($\sim \pm 0.28$ Ma). There are no significant differences in the stratigraphic distribution of different taxonomic groups (Kolmogorov-Smirnov test, $p > 0.05$), which allows us to combine all bulk enamel isotope data before smoothing.

We smoothed bulk enamel $\delta^{13}\text{C}$, bulk enamel $\delta^{18}\text{O}$ and bone $\delta^{18}\text{O}$ values using the Monte Carlo method outlined above (Traylor et al., in review). We allowed the isotope composition of each sample to vary by $\pm 1.6\text{‰}$ for oxygen and $\pm 0.6\text{‰}$ for carbon to reflect intra-tooth variations in isotope composition. Modeled enamel $\delta^{13}\text{C}$ values increased from -12‰ to $\sim -10.5\text{‰}$ between 17.4 and ~ 16.9 Ma, followed by a slight decrease before remaining unchanged until the end of the record (Fig. 3.4B). Enamel

$\delta^{18}\text{O}$ values followed a similar trajectory (Fig. 3.4C), with an increase from 23‰ to 24‰ between ~17.4 to ~16.9 Ma followed by a gradual increase until the end of the record.

3.5. Discussion

3.5.1 Ecology of Santa Cruz Formation Ungulates

All enamel $\delta^{13}\text{C}$ values fall between our outside the expected range for closed canopy forests ($< -15\text{‰}$). The lack of significant differences among herbivore carbon isotope compositions suggest dietary homogeneity or resource partitioning in ways not readily recorded as variations in carbon isotope compositions (e.g. feeding at different times, feeding on different parts of a plant, feeding on different plants with similar $\delta^{13}\text{C}$ values). Intermediate $\delta^{13}\text{C}$ values (-8 to -15‰) are usually interpreted as open woodlands or mixed woodland-scrubland environments (Kohn et al., 2005; Feranec and MacFadden, 2006; Traylor et al., 2015). Given the range of observed $\delta^{13}\text{C}$ values, all sampled herbivores were likely mixed feeders or browsers, moving between wooded and open areas but not closed-canopy systems.

Homalodotherium limb morphology indicates the ability to adopt a bipedal posture, freeing the forelimbs and mouth to browse in the lower canopy (Cassini et al., 2012). As this is a fairly specialized feeding niche, *Homalodotherium* $\delta^{13}\text{C}$ values place a constraint on the carbon isotope composition of the Santa Cruz Formation flora, i.e. $\delta^{13}\text{C}$ values similar to those observed in *Homalodotherium* should represent woodland habitats. Morphometric analysis has variously proposed a grazing or mixed feeding niche for the notoungulates *Nesodon* and *Adinotherium* (Cassini et al., 2012; Cassini and Vizcaíno, 2012; Cassini, 2013), while enamel microwear suggest a primarily leaf browsing diet for both taxa (Townsend and Croft, 2008). *Adinotherium* has the lowest

observed $\delta^{13}\text{C}$ values, with one individual plotting close to the closed canopy forest cutoff. Mean *Nesodon* $\delta^{13}\text{C}$ values are only slightly higher than *Adinotherium* values. Given the similarity among $\delta^{13}\text{C}$ values of *Homalodotherium*, *Nesodon*, and *Adinotherium*, our isotopic data are most compatible with a browsing diet for all these taxa. Similarly, our data are consistent with the interpretation of brachydont litopterns as browsers (Cassini et al., 2012; Cassini and Vizcaíno, 2012; Cassini, 2013).

While *Astrapotherium* $\delta^{13}\text{C}$ values do not differ significantly from other taxa, its $\delta^{18}\text{O}$ values are $\sim 2.5\%$ lower than the mean for all other taxa. Analysis of limb morphology led Avilla and Vizcaíno (2005) to conclude *Astrapotherium* was semi-aquatic, while Cassini et al. (2012) concluded its limbs resembled those of the Indian Rhinoceros (*Rhinoceros unicornis*) which commonly wallows and browses in lakes and rivers (Laurie et al., 1983). Increased water availability minimizes evaporative enrichment and allows the rapid turnover of body water. Both factors result in lower $\delta^{18}\text{O}$ values when compared to coexisting terrestrial herbivores (Clementz et al., 2008). We interpret low $\delta^{18}\text{O}$ values for *Astrapotherium* as evidence of a semi-aquatic lifestyle.

3.5.2 Carbon Isotopes and Climate

Linking changes in our data to changes to global climate is complicated by two factors. First, marine proxy records for this time period (Holbourn et al., 2015) have a much higher temporal resolution than our data, and second, our data have considerably higher variance than marine records. We therefore focus on changes to our smoothed isotope compositions, rather than raw enamel and bone data.

We predicted $\delta^{13}\text{C}$ trends that would result from three scenarios, a 500 mm/yr decrease ($\Delta_{\text{map}} = -500 \text{ mm/yr}$), 500 mm/yr increase ($\Delta_{\text{map}} = +500 \text{ mm/yr}$), and no change

to MAP ($\Delta_{\text{map}} = 0$ mm/yr). Changes in MAP were calculated relative to median carbon isotope compositions at beginning of our record (~ 17.5 Ma) and assume a linear change in MAP until the end of our record in each scenario.

Enamel $\delta^{13}\text{C}$ values increased by $\sim 1\text{‰}$ beginning at 17.4 Ma and reached a maximum at ~ 16.9 Ma. The enamel trend during this period closely tracks the predicted trend ($\Delta_{\text{MAP}} = -500$ mm/yr) for an increasingly dry environment (Fig 3.4B).

Quantitatively calculated MAP over the same interval reveals a significant drop with high MAP ($\sim 700 \pm 130$ mm/yr) at 17.4 Ma, decreasing to the lowest MAP ($\sim 340 \pm 90$ mm/yr) at 16.9 Ma (Fig. 5). Atmospheric CO_2 $\delta^{13}\text{C}$ values varied by only 0.25‰ during this period. Changes in atmospheric CO_2 carbon isotope compositions are reflected as changes to plant compositions in a 1:1 relationship, and therefore cannot fully explain the observed variations in enamel compositions. Likewise, while changes to atmospheric CO_2 concentrations have been proposed to affect plant carbon isotope compositions (Schubert and Jahren, 2012), increasing $p\text{CO}_2$ from ~ 200 to ~ 400 ppm during this period (Greenop et al., 2014) would imply a $\sim 2\text{‰}$ decrease in plant, and therefore herbivore, $\delta^{13}\text{C}$ values which is inconsistent with our observations.

The onset of the MMCO at ~ 16.9 Ma also marks the beginning of the “Monterey” carbon isotope excursion (Vincent and Berger, 1985). This excursion towards higher marine $\delta^{13}\text{C}$ was driven by increased marine and terrestrial productivity and carbon sequestration (Vincent and Berger, 1985; Föllmi et al., 2005), modulated by a series of 400 ka oscillations, which correspond to long period eccentricity (Holbourn et al., 2007; Ma et al., 2011). The first of these oscillations corresponds to an abrupt warming period between 16.9 and 16.7 Ma, possibly driven by enhanced insolation during high

eccentricity (Holbourn et al., 2015). This warming period corresponds to the observed $\delta^{13}\text{C}$ maximum in our data. Decreased benthic foraminifera $\delta^{13}\text{C}$ values during this period correspond with decreased $\Delta^{13}\text{C}$ between plants and atmospheric CO_2 , and consequently a decreased MAP. In our data, after 16.7 Ma, mean enamel $\delta^{13}\text{C}$ values decreased by $\sim 0.75\text{‰}$, although their uncertainties overlap values observed during peak warming. A further $\sim 0.5\text{‰}$ increase in atmospheric $\delta^{13}\text{C}$ values, driven by increased organic carbon sequestration (the "Monterey excursion"; Vincent and Berger, 1985; Holbourn et al., 2007), means that while MAP increases post 16.7 Ma, it remains lower ($\sim 530 \pm 220$) than MAP at 16.7 Ma, although within uncertainty of MAP calculated for the earlier wetter (700 ± 130 mm/yr, 17.4 Ma) and drier (340 ± 90 mm/yr, 16.9 Ma) times.

3.5.3 Oxygen Isotopes and Climate

Enamel and bone $\delta^{18}\text{O}$ values varied only slightly from 17.4 to 17.1 Ma. Modeled MAT values during this period are warm ($20 \pm 4^\circ\text{C}$; **Fig. 5**) with the exception of a negative excursion at 17.3 Ma. Benthic foraminifera $\delta^{18}\text{O}$ values are also stable during this period (17.1 – 17.4 Ma), suggesting little change to temperature (Holbourn et al., 2015). Increasing enamel $\delta^{18}\text{O}$ values by $\sim 1\text{‰}$ and a corresponding decrease in bone $\delta^{18}\text{O}$ values at ~ 17.0 Ma indicate a brief MAT excursion up to $25 \pm 7^\circ\text{C}$ at the onset of the MMCO. Abrupt global warming at 16.9 Ma (Holbourn et al., 2015), drove a reduction in East Antarctic ice sheet volume (Pekar and DeConto, 2006; Pekar and Christie-Blick, 2008), resulting in a $\sim 0.5\text{‰}$ decrease in marine $\delta^{18}\text{O}$ values as melting ice added ^{18}O depleted water to the oceans. The retreat of the east Antarctic ice sheet inland, coupled with an influx of fresh meltwater into the southern Atlantic reduced the production of Antarctic bottom water (Pekar and DeConto, 2006). In turn, reduced

bottom water production weakened thermohaline circulation, inhibiting the transport of warm equatorial waters south during this period (Schmitz, 1995; Pekar and DeConto, 2006). Despite a global temperature increase, calculated MAT in our section decreased between 17 and 16.7 Ma, with a minimum estimate of $19 \pm 4^\circ\text{C}$, at ~ 16.85 Ma. This temperature decrease suggests regional cooling, perhaps the result of reduced equatorial heat transport or influx of cold Antarctic water, or both. Low observed MAP during this period also suggest weakened circulation led to lower evaporation.

After ~ 16.7 Ma, enamel $\delta^{18}\text{O}$ values increased slightly, although high uncertainties for the youngest samples mean their uncertainties overlap those of all post 17 Ma values. Likewise, bone $\delta^{18}\text{O}$ values remain constant. Calculated MAT rebounds to high values until the end of the record with a maximum modeled temperature of $26 \pm 8^\circ\text{C}$ at 16.5 Ma. This rebound could reflect stabilization of the reduced Antarctic ice sheet, perhaps permitting warmer low latitude waters to influence Patagonian climate more strongly. Thus, despite an initial excursion towards lower temperatures and precipitation, southern Patagonia ultimately followed global trends in increased temperature and precipitation observed in numerous northern hemisphere records.

While uncertainties on estimated MAT are large, a stable MAT of $\sim 20^\circ\text{C}$ is unlikely because it would require the “true” MAT to fall near the upper confidence interval at 17.2 Ma, the lower confidence interval at 19.6 Ma, the upper interval at 16.8 Ma, and the lower interval at 16.5 Ma. As these regions represent overall lower probability, the likelihood of an invariant MAT is low.

Andean uplift during the Miocene enhanced orographic rain shadow of much of Patagonia, driving a long term aridification of the area (Blisniuk et al., 2005). While the

magnitude of uplift between 16.5 and 17.5 Ma is unclear, oxygen isotope lapse rates for the southern Andes predict a $-0.3\text{‰}/0.1\text{km}$ decrease in $\delta^{18}\text{O}$ values with increasing uplift (Poage and Chamberlain, 2001; Blisniuk and Stern, 2005). Given that enamel and bone $\delta^{18}\text{O}$ values show a gradual increase, we assume that Andean uplift did not significantly influence meteoric water isotope compositions during this period, and that observed changes are a result of larger scale climatic trends.

3.5.4 Isotopic Zoning and Seasonality

Overall, carbon and oxygen isotope zoning within individual teeth is less than 2‰ , suggesting small to moderate, seasonal change in precipitation and vegetation compositions. Modern precipitation and lake water $\delta^{18}\text{O}$ values for the study area each vary by nearly 20‰ (Mayr et al., 2007). Assuming enamel mineralization and body water residence times attenuates meteoric water variations by $\sim 50\%$ (Passey and Cerling, 2002; Kohn, 2004; Podlesak et al., 2008), modern teeth from the area would be expected to preserve $\delta^{18}\text{O}$ variations of $\sim 10\text{‰}$, much higher than the observed variation in fossil teeth. Given this we conclude there was no strong seasonality to precipitation $\delta^{18}\text{O}$. Likewise, low $\delta^{13}\text{C}$ variability within teeth suggest a stable flora that either did not face significant water stress throughout the year or was dormant during these periods.

3.5.5 Comparisons to Other Proxies

Most previous MAP and MAT estimates for the Santa Cruz Formation have focused on floras and faunas from several productive faunal levels (Tauber, 1994, 1997) of similar age ($\sim 17.4 - \sim 17.5$ Ma; Perkins et al., 2012). Consequently, these estimates represent a narrow period of time that best corresponds to our oldest data.

Wood physiognomy based estimates of MAT ($19.3 \pm 1.7^\circ\text{C}$; Brea et al., 2012) from the lower Santa Cruz Formation fall entirely within uncertainty of our MAT calculations for older fossils (> 17.2 Ma). An alternative MAT estimate from the same source of $9.4 \pm 1.7^\circ\text{C}$ (Brea et al., 2012) does not overlap our data but is also inconsistent with faunal data suggesting MAT $> 14^\circ\text{C}$ (Fericola and Albino, 2012; Kay et al., 2012b).

Estimates of MAP for the Santa Cruz Formation vary significantly with some estimates mutually exclusive. Based on calculations of population density, plant biomass, and above ground primary and secondary productivity, Vizcaíno et al. (2010) concluded the Santa Cruz Formation environment was a mixture of temperate forests and bushland with MAP < 1000 mm/yr. Comparisons of niche metrics for a variety of modern and fossil localities lead Kay et al. (2012b) to conclude MAP was between 1000 to 1500 mm/yr. MAP constraints based on reptile fossils (Fericola and Albino, 2012) effectively place a lower bound by requiring MAP > 200 mm/yr. Wood physiognomy based MAP calculations are imprecise (869 ± 940 mm/yr) and essentially agree with both the Kay et al. (2012b) and Vizcaíno et al. (2010).

Our MAP estimates at ~ 17.4 Ma ($\sim 700 \pm 130$ mm/yr) broadly agree with the Vizcaíno et al. (2010) and Brea et al. (2012), although the high uncertainty of wood physiognomy estimates allows MAP values that fall outside the range of our predictions. Our results do not agree with the estimates of Kay et al. (2012b). However, these estimates are based on the proportion of species that occupied different niches (e.g. herbivores, frugivores, grazers, arboreal) and include a large range of body sizes. Many of these taxa are small mammals that sample a small proportion of the landscape, so their

isotope compositions likely do not represent broad ecosystems. Moreover, many of these animals are xenarthrans (sloths, armadillos, anteaters), which lack enamel. The large taxa that we analyzed would have sampled a larger area of the landscape, making their isotope compositions more representative of the overall vegetation composition (Kohn, 2016).

3.5.6 Comparisons to General Circulation Models

Most general circulation models of the MMCO do not model changes to precipitation and temperature conditions and instead focus on specific time slices that may or may not overlap a stratigraphic section of interest. This is partially necessitated by the nature of suitable MAT and MAP proxy records for model validation. Suitable mid-Miocene proxy sites are heterogeneously distributed in both space and time (Herold et al., 2010), which requires models to be compared to records that are not necessarily coeval. Furthermore, most terrestrial proxy records are located in Europe and North America, with the southern hemisphere underrepresented. Given these limitations, how accurately do existing models of the MMCO predict the physical conditions of the Santa Cruz Formation? For these comparisons, we focus on our youngest results post 16.6 Ma, i.e. after the onset of the MMCO.

Our results predict significantly higher MAT ($\sim 25 \pm 8^\circ\text{C}$) and lower MAP ($\sim 550 \pm 195$ mm/yr) than most general circulation models. Herold et al. (2011) and Tong et al. (2009) predict MAP of 1000 – 1200 mm/yr, which is consistent with one estimate based on floras and faunas (Kay et al., 2012b). While Henrot et al. (2010) predict MAP similar to our results (~ 500 mm/yr), their model also predicts strongly seasonal precipitation, with $\sim 75\%$ occurring in southern hemisphere summer (DJF). Conversely, seasonality

estimates based on plant macrofossils (Brea et al., 2012) suggest long (7 month) dry summers. Both these estimates are inconsistent with our enamel zoning profiles.

Model derived MAT estimates are also consistently too low. While all models predicting temperatures of $\sim 10 - 15^{\circ}\text{C}$ for the study area (Tong et al., 2009; Henrot et al., 2010; Herold et al., 2011). Henrot et al. (2010) noted that their model underestimated MMCO warming for high latitudes, primarily by overestimating the meridional temperature gradient, concluding that more proxy records are needed at these latitudes to constrain physical conditions in these areas. Overall, general circulations models provide good estimates of climate parameters at low and mid-latitudes but require more refinement and proxy records at high latitudes for model validation. Our data provides one such record, however more high latitude localities are likely required to accurately model high latitude MMCO conditions.

3.6. Conclusions

High atmospheric CO_2 concentrations during the mid-Miocene climatic optimum drove a variety of changes to global climate. Carbon and oxygen isotopes from herbivore tooth enamel reveal that global warming at the onset of the MMCO (Holbourn et al., 2015) interrupted a trend towards increasing aridity in Patagonia. Mean annual precipitation decreased significantly before stabilizing during the MMCO. Regional MAT and MAP reductions at the onset of the MMCO suggest that increasing global temperatures and reduced Antarctic ice volume induced an ~ 0.3 ka negative feedback in Patagonia. This transitional period in Patagonia was followed by a rebound to higher MAP and MAT as regional climates began to parallel global increases in temperature and precipitation.

Carbon isotope-based MAP and MAT calculations are consistent with most previous floral and faunal estimates, although our ~1 Ma record reveals significant changes to both MAP and MAT through time. Enamel and bone oxygen isotope-based MAT calculations also agree with floral and faunal data, revealing temperatures significantly warmer ($\text{MAT} = 20 - 25 \text{ }^\circ\text{C}$) than modern conditions ($\text{MAT} \sim 8 \text{ }^\circ\text{C}$).

Finally, general circulation models consistently overestimate MAP and underestimate MAT for Miocene Patagonia but also rely on proxy records for validation that are almost completely restricted to the northern hemisphere. Our new temperature and precipitation proxy record from the southernmost terrestrial mid-Miocene site in extreme southern South America may help improve the accuracy of mid-Miocene models. As most models of future atmospheric CO_2 concentrations are similar to or exceed estimates for the MMCO (IPCC, 2014), understanding physical conditions and ecology during this time may help provide insight into future climate scenarios for southern South America.

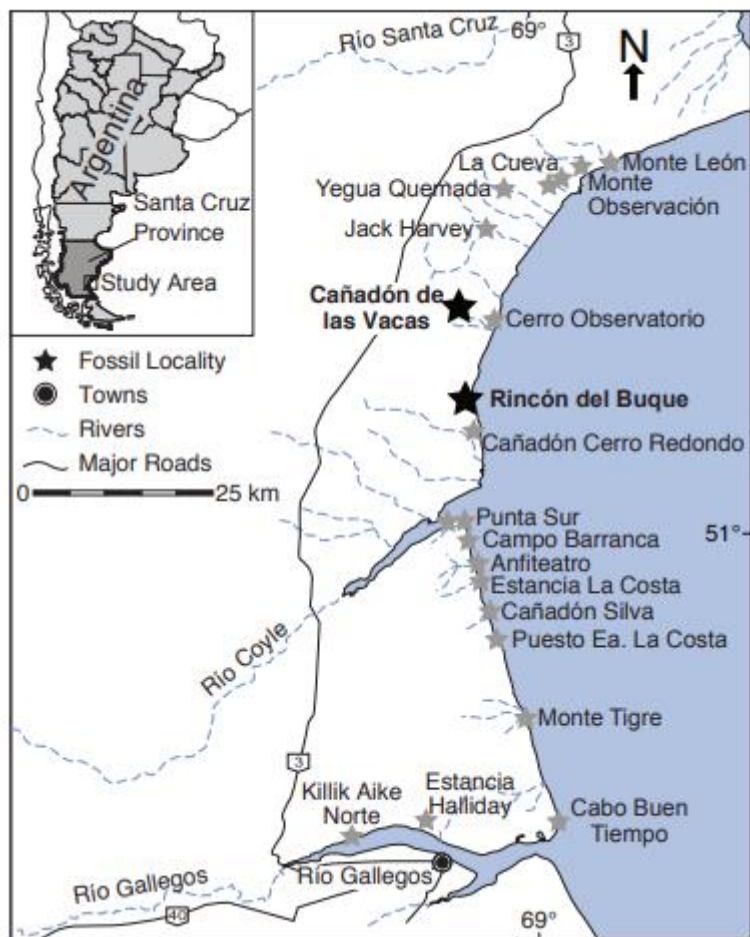


Figure 3.1. Map showing regional geography and Santa Cruz Formation fossil localities. Bold localities are included in this study (modified from Vizcaíno et al. 2012).

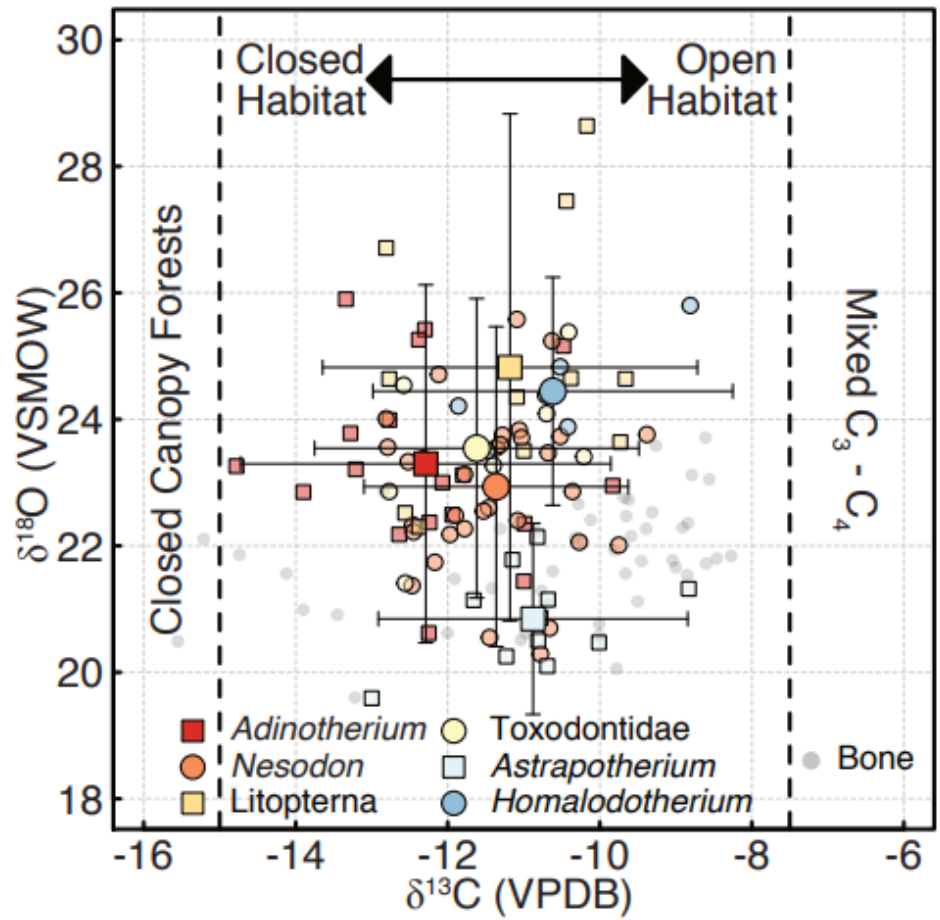


Figure 3.2. $\delta^{13}\text{C}$ vs $\delta^{18}\text{O}$ values for Santa Cruz Formation herbivores and bone. Large symbols with error bars are the mean $\pm 2\sigma$ for each taxonomic group. Vertical dashed lines at -15‰ and -7.5‰ indicate the cutoffs for closed canopy forests and mixed C₃-C₄ environments (see section 3.2.2 for details).

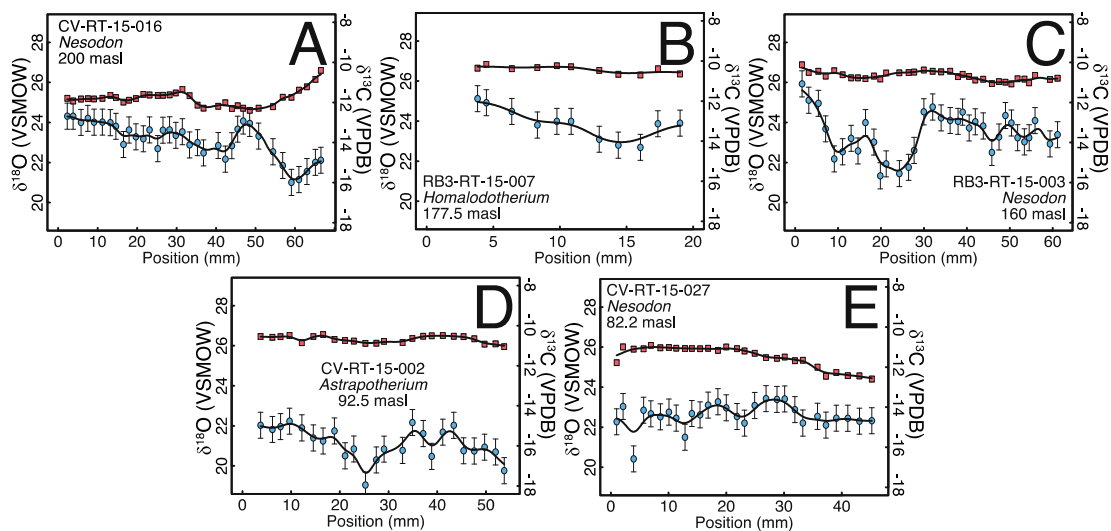


Figure 3.3. Carbon (squares) and oxygen (circles) isotope zoning profiles from Santa Cruz Formation ungulate tooth enamel, arranged in increasing stratigraphic level. Error bars indicate analytical reproducibility for replicates of NIST120c (2σ). Error bars for $\delta^{13}\text{C}$ values are smaller than the symbols. A) *Nesodon*, B) *Homalodotherium*, C) *Nesodon*, D) *Astrapotherium*, E) *Nesodon*.

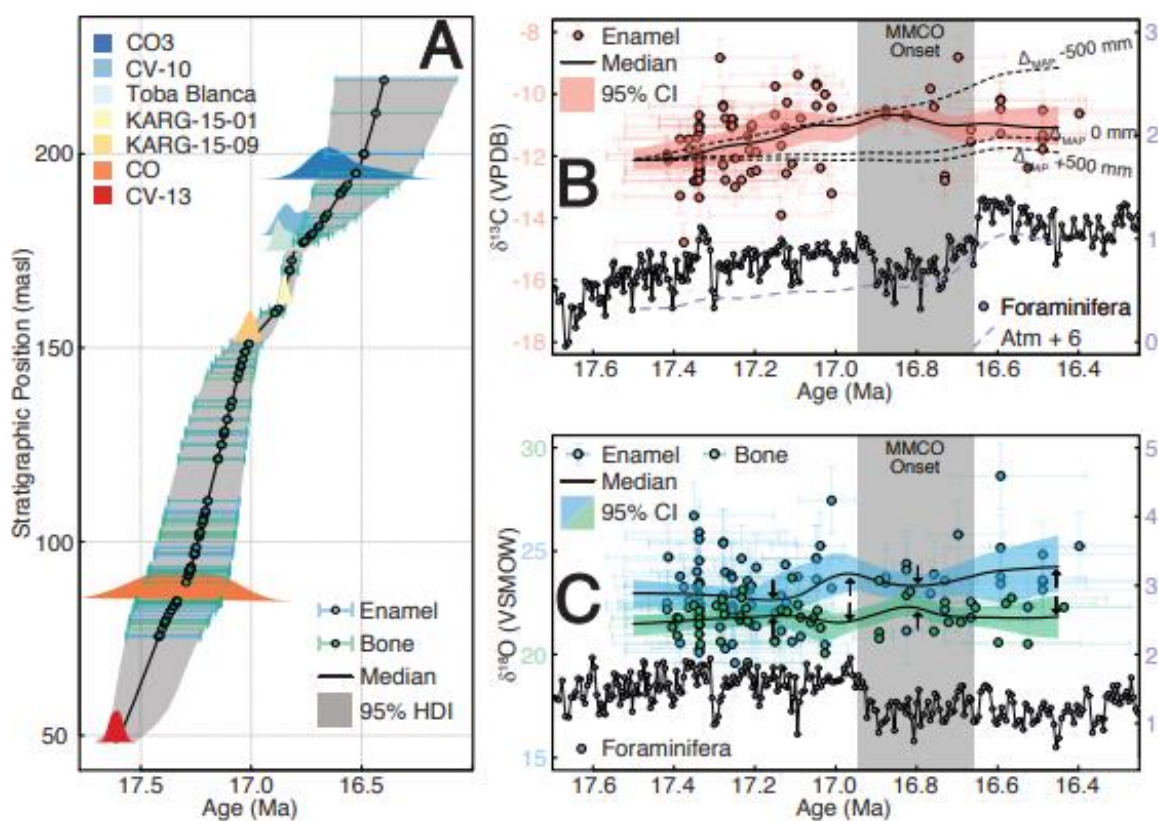


Figure 3.4. A) Age-depth model for a composite section of the Cañadon de las Vacas and Rincón del Buque localities. Colored polygons are the probability distribution functions for each dated tuff (Trayler et al., in review). Colored points and error bars indicate the median age and uncertainty (95% CI) of fossil bone and enamel samples. B) Plot of enamel $\delta^{13}\text{C}$ values versus age. Solid black line is the median smoothed isotope composition accounting for uncertainties in isotope composition and age. 95% of all smoothing models fall within the pink-shaded area. Dashed purple line is the $\delta^{13}\text{C}$ of atmospheric CO_2 (+6‰ for ease of plotting) calculated following the methods of Tipler et al. (2010) using benthic foraminifera data (purple dots) from Holbourn et al. (2015). Dashed black lines are predicted changes to isotope compositions given starting isotope compositions similar to those observed at ~17.5 Ma, $\delta^{13}\text{C}_{\text{atm}}$, and allowing ΔMAP to vary by ± 500 mm. Shaded grey area corresponds to peak warming at the onset of the MMCO (Holbourn et al., 2015). C) plot of enamel and bone $\delta^{18}\text{O}$ values versus age. Solid black line is the median smoothed isotope composition accounting for uncertainties in isotope composition and age. Inward facing arrows indicate inferred decreases in temperature, outward facing arrows are temperature increases. Purple dots are oxygen isotope compositions of benthic foraminifera (Holbourn et al., 2015) for comparison.

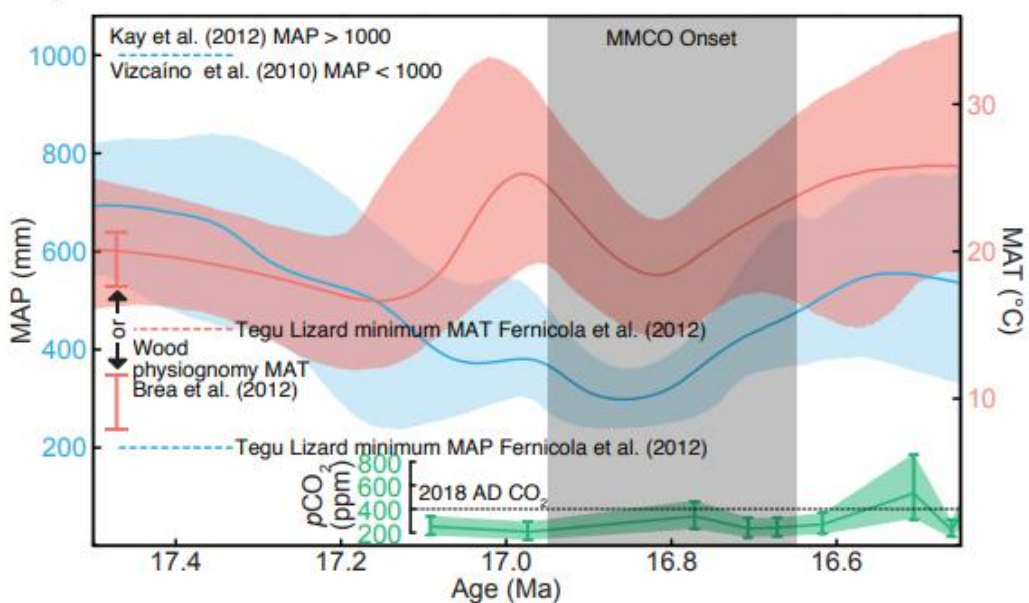


Figure 3.5. Estimates of mean annual precipitation (blue) and mean annual temperature (pink) from tooth enamel and bone stable isotope compositions. Shaded areas represent the 95% confidence while solid line represent the median. Estimates of MAT based on wood physiognomy of plant macrofossils from the lower Santa Cruz Formation (vertical bars; Brea et al., 2012), niche metrics and cenograms (dashed line, MAP > 1000; Kay et al., 2012b), fauna and sedimentological evidence (dashed line, MAP < 1000; Vizcaino et al., 2010), and tegu lizard fossils (dashed line, MAP > 200 mm, MAT > 14°C; Fernicola and Albino, 2012) are also shown. Green line and shaded area are boron isotope based atmospheric CO₂ concentrations (Greenop et al., 2014). Shaded grey corresponds to peak warming at the onset of the MMCO as in Fig. 3.4.

Table 3.1. Summary statistics for all taxonomic groups. Note that the Toxodontidae group represents a combination of Nesodon and Adinotherium.

Taxa	$\delta^{13}\text{C}$		$\delta^{18}\text{O}$		n
	Mean	2σ	Mean	2σ	
<i>Nesodon</i>	-11.36	1.74	22.94	2.53	32
<i>Adinotherium</i>	-12.23	2.43	23.30	2.83	18
Litopterna	-11.18	2.46	24.82	4.01	11
<i>Astrapotherium</i>	-10.88	2.03	20.84	1.51	11
<i>Homalodotherium</i>	-10.62	2.37	24.44	1.80	5
Undifferentiated Toxodontidae	-11.62	2.13	23.54	2.37	8

Table 3.2. Statistical comparisons of $\delta^{18}\text{O}$ values for Santa Cruz Formation herbivores. NS = no significant difference ($p > 0.05$), S = significant differences ($p < 0.05$).

Taxa	<i>Astrapotherium</i>	<i>Homalodotherium</i>	Litopterna	<i>Nesodon</i>
<i>Adinotherium</i>	S	NS	S	NS
<i>Astrapotherium</i>	-	S	S	S
<i>Homalodotherium</i>	-	-	NS	NS
Litopterna	-	-	-	S

REFERENCES

- Abràmoff, M.D., Magalhães, P.J., Ram, S.J., 2004. Image Processing With ImageJ. *Biophotonics international* 11, 36-43.
- Avilla, L., Vizcaíno, S., 2005. Locomotory pattern of *Astrapotherium magnum* (Owen)(Mammalia: Astrapotheria) from the Neomiocene (Colhuehuapian–Santacrucian) of Argentina, II Congresso Latino-Americano de Paleontologia de Vertebrados, Rio de Janeiro, Brazil.
- Ayliffe, L.K., Chivas, A.R., Leakey, M.G., 1994. The retention of primary oxygen isotope compositions of fossil elephant skeletal phosphate. *Geochimica et Cosmochimica Acta* 58, 5291-5298.
- Balasse, M., 2002. Reconstructing dietary and environmental history from enamel isotopic analysis: time resolution of intra-tooth sequential sampling. *International Journal of Osteoarchaeology* 12, 155-165.
- Baresel, B., Bucher, H., Brosse, M., Cordey, F., Guodun, K., Schaltegger, U., 2017. Precise age for the Permian–Triassic boundary in South China from high-precision U-Pb geochronology and Bayesian age–depth modeling. *Solid Earth* 8, 361-378.
- Bargo, M.S., Toledo, N., Vizcaino, S.F., 2012. Paleobiology of Santacrucian Sloths and Anteaters, in: Vizcaíno, S.F., Kay, R.F., Bargo, M.S. (Eds.), *Early Miocene Paleobiology in Patagonia: High-Latitude Paleocommunities of the Santa Cruz Formation*, pp. 216 - 242.
- Barreda, V., Palazzesi, L., 2007. Patagonian vegetation turnovers during the Paleogene-early Neogene: origin of arid-adapted floras. *The botanical review* 73, 31-50.

- Bassett, D., Macleod, K.G., Miller, J.F., Ethington, R.L., 2007. Oxygen isotopic composition of biogenic phosphate and the temperature of Early Ordovician seawater. *Palaios* 22, 98-103.
- Beerling, D.J., Royer, D.L., 2011. Convergent cenozoic CO₂ history. *Nature Geoscience* 4, 418.
- Bendrey, R., Vella, D., Zazzo, A., Balasse, M., Lepetz, S., 2015. Exponentially decreasing tooth growth rate in horse teeth: implications for isotopic analyses. *Archaeometry* 57, 1104-1124.
- Bennett, K., 1994. Confidence intervals for age estimates and deposition times in late-Quaternary sediment sequences. *The Holocene* 4, 337-348.
- Blaauw, M., Christen, J.A., 2005. Radiocarbon peat chronologies and environmental change. *Journal of the Royal Statistical Society: Series C (Applied Statistics)* 54, 805-816.
- Blaauw, M., Heegaard, E., 2012. Estimation of age-depth relationships, Tracking environmental change using lake sediments. Springer, pp. 379-413.
- Blisniuk, P.M., Stern, L.A., 2005. Stable isotope paleoaltimetry: A critical review. *American Journal of Science* 305, 1033-1074.
- Blisniuk, P.M., Stern, L.A., Chamberlain, C.P., Idleman, B., Zeitler, P.K., 2005. Climatic and ecologic changes during Miocene surface uplift in the Southern Patagonian Andes. *Earth and Planetary Science Letters* 230, 125-142.
- Blumenthal, S.A., Cerling, T.E., Chritz, K.L., Bromage, T.G., Kozdon, R., Valley, J.W., 2014. Stable isotope time-series in mammalian teeth: In situ $\delta^{18}\text{O}$ from the innermost enamel layer. *Geochimica et Cosmochimica Acta* 124, 223-236.
- Böhme, M., 2003. The Miocene climatic optimum: evidence from ectothermic vertebrates of Central Europe. *Palaeogeography, Palaeoclimatology, Palaeoecology* 195, 389-401.

- Böhme, M., Winklhofer, M., Ilg, A., 2011. Miocene precipitation in Europe: Temporal trends and spatial gradients. *Palaeogeography, Palaeoclimatology, Palaeoecology* 304, 212-218.
- Bown, T.M., Fleagle, J.G., 1993. Systematics, biostratigraphy, and dental evolution of the Palaeothentidae, later Oligocene to early-middle Miocene (Deseadan-Santacrucian) caenolestoid marsupials of South America. *Memoir (The Paleontological Society)*, 1-76.
- Brea, M., Zucol, A., Iglesias, A., 2012. Fossil plant studies from late Early Miocene of the Santa Cruz Formation: paleoecology and paleoclimatology at the passive margin of Patagonia, Argentina, in: Vizcaino, S.F., Kay, R.F., Bargo, M.S. (Eds.), *Early Miocene Paleobiology in Patagonia: High-latitude Paleocommunities of the Santa Cruz Formation*. Cambridge University Press, Cambridge, pp. 104-128.
- Bronk Ramsey, C., 2008. Deposition Models For Chronological Records. *Quaternary Science Reviews* 27, 42-60.
- Brooks, S., Gelman, A., Jones, G., Meng, X.-L., 2011. *Handbook of markov chain monte carlo*. CRC press.
- Bruch, A.A., Utescher, T., Mosbrugger, V., 2011. Precipitation patterns in the Miocene of Central Europe and the development of continentality. *Palaeogeography, Palaeoclimatology, Palaeoecology* 304, 202-211.
- Bryant, D.J., Koch, P.L., Froelich, P.N., Showers, W.J., Genna, B.J., 1996. Oxygen isotope partitioning between phosphate and carbonate in mammalian apatite. *Geochimica et Cosmochimica Acta* 60, 5145-5148.
- Buckley, M., 2015. Ancient collagen reveals evolutionary history of the endemic South American 'ungulates'. *Proc. R. Soc. B* 282, 20142671.
- Cassini, G., Cerdeño, E., Villafañe, A., Muñoz, N., 2012. Paleobiology of Santacrucian native ungulates (Meridiungulata: Astrapotheria, Litopterna and Notoungulata), in: Vizcaino, S.F., Kay, R.F., Bargo, M.S. (Eds.), *Early Miocene Paleobiology in Patagonia: High-Latitude Paleocommunities of the Santa Cruz Formation*. Cambridge University Press, Cambridge, UK, pp. 243-286.

- Cassini, G.H., 2013. Skull geometric morphometrics and paleoecology of Santacrucian (late early Miocene; Patagonia) native ungulates (Astrapotheria, Litopterna, and Notoungulata). *Ameghiniana* 50, 193-216.
- Cassini, G.H., Vizcaíno, S.F., 2012. An Approach to the Biomechanics of the Masticatory Apparatus of Early Miocene (Santacrucian Age) South American Ungulates (Astrapotheria, Litopterna, and Notoungulata): Moment Arm Estimation Based on 3D Landmarks. *Journal of Mammalian Evolution* 19, 9-19.
- Cerling, T., Harris, J., 1999. Carbon isotope fractionation between diet and bioapatite in ungulate mammals and implications for ecological and paleoecological studies. *Oecologia* 120, 347-363.
- Cerling, T.E., Harris, J.M., MacFadden, B.J., Leakey, M.G., Quade, J., Eisenmann, V., Ehleringer, J.R., 1997. Global vegetation change through the Miocene/Pliocene boundary. *Nature* 389, 153-158.
- Cerling, T.E., Sharp, Z.D., 1996. Stable carbon and oxygen isotope analysis of fossil tooth enamel using laser ablation. *Palaeogeography, Palaeoclimatology, Palaeoecology* 126, 173-186.
- Chenery, C., Mueldner, G., Evans, J., Eckardt, H., Lewis, M., 2010. Strontium and stable isotope evidence for diet and mobility in Roman Gloucester, UK. *Journal of archaeological Science* 37, 150-163.
- Cherniak, D., 2000. Rare earth element diffusion in apatite. *Geochimica et Cosmochimica Acta* 64, 3871-3885.
- Chib, S., Greenberg, E., 1995. Understanding the metropolis-hastings algorithm. *The american statistician* 49, 327-335.
- Clementz, M.T., 2012. New insight from old bones: stable isotope analysis of fossil mammals. *Journal of Mammalogy* 93, 368-380.
- Clementz, M.T., Holroyd, P.A., Koch, P.L., 2008. Identifying aquatic habits of herbivorous mammals through stable isotope analysis. *Palaaios* 23, 574-585.

- Condon, D., Schoene, B., McLean, N., Bowring, S., Parrish, R., 2015. Metrology and traceability of U–Pb isotope dilution geochronology (EARTHTIME Tracer Calibration Part I). *Geochimica et Cosmochimica Acta* 164, 464-480.
- Costeur, L., Legendre, S., 2008. Mammalian communities document a latitudinal environmental gradient during the Miocene Climatic Optimum in Western Europe. *Palaios* 23, 280-288.
- Cramer, B., Miller, K., Barrett, P., Wright, J., 2011. Late Cretaceous–Neogene trends in deep ocean temperature and continental ice volume: reconciling records of benthic foraminiferal geochemistry ($\delta^{18}\text{O}$ and Mg/Ca) with sea level history. *Journal of Geophysical Research: Oceans* (1978–2012) 116.
- Croft, D.A., 2001. Cenozoic environmental change in South America as indicated by mammalian body size distributions (cenograms). *Diversity and Distributions* 7, 271-287.
- Croft, D.A., 2013. What constitutes a fossil mammal community in the early Miocene Santa Cruz Formation? *Journal of Vertebrate Paleontology* 33, 401-409.
- Cuitiño, J.I., Fernicola, J.C., Kohn, M.J., Trayler, R.B., Naipauer, M., Bargo, M.S., Kay, R.F., Vizcaíno, S.F., 2016. U–Pb geochronology of the Santa Cruz Formation (early Miocene) at the Río Bote and Río Santa Cruz (southernmost Patagonia, Argentina): Implications for the correlation of fossil vertebrate localities. *Journal of South American Earth Sciences* 70, 198-210.
- Cuitiño, J.I., Scasso, R.A., 2010. Sedimentología y paleoambientes del Patagoniano y su transición a la Formación Santa Cruz al sur del Lago Argentino, Patagonia Austral. *Revista de la Asociación Geológica Argentina* 66, 406-417.
- Cuitiño, J.I., Ventura Santos, R., Alonso Muruaga, P.J., Scasso, R.A., 2015. Sr-stratigraphy and sedimentary evolution of early Miocene marine foreland deposits in the northern Austral (Magallanes) Basin, Argentina. *Andean Geology* 42.
- Cuitiño, J.I., Vizcaíno, S.F., Bargo, M.S., Aramendía, I., in press. Sedimentology and fossil vertebrates of the Santa Cruz Formation (early Miocene) in Lago Posadas, southwestern Patagonia, Argentina. *Andean Geology*.

- Davydov, V.I., Crowley, J.L., Schmitz, M.D., Poletaev, V.I., 2010. High-precision U-Pb zircon age calibration of the global Carboniferous time scale and Milankovitch band cyclicity in the Donets basin, eastern Ukraine. *Geochemistry, Geophysics, Geosystems* 11.
- De Vleeschouwer, D., Parnell, A.C., 2014. Reducing time-scale uncertainty for the Devonian by integrating astrochronology and Bayesian statistics. *Geology* 42, 491-494.
- Diefendorf, A.F., Mueller, K.E., Wing, S.L., Koch, P.L., Freeman, K.H., 2010. Global patterns in leaf ^{13}C discrimination and implications for studies of past and future climate. *Proceedings of the National Academy of Sciences* 107, 5738-5743.
- Domingo, L., Cuevas-González, J., Grimes, S.T., Fernández, M.H., López-Martínez, N., 2009. Multiproxy reconstruction of the palaeoclimate and palaeoenvironment of the Middle Miocene Somosaguas site (Madrid, Spain) using herbivore dental enamel. *Palaeogeography, Palaeoclimatology, Palaeoecology* 272, 53-68.
- Driessens, F.C., Verbeeck, R., 1990. *Biomaterials*. CRC Press.
- Dutton, J.F., Barron, E.J., 1997. Miocene to present vegetation changes: A possible piece of the Cenozoic cooling puzzle. *Geology* 25, 39-41.
- Ehleringer, J.R., 1989. Carbon isotope ratios and physiological processes in aridland plants. *Stable isotopes in ecological research*. Springer, New York, 41-54.
- Ehleringer, J.R., Cooper, T.A., 1988. Correlations between carbon isotope ratio and microhabitat in desert plants. *Oecologia* 76, 562-566.
- Elliott, J.C., 2002. Calcium Phosphate Biomaterials. *Reviews in Mineralogy and Geochemistry* 48, 427-453.
- Evernden, J., Savage, D., Curtis, G., James, G., 1964. Potassium-argon dates and the Cenozoic mammalian chronology of North America. *American Journal of Science* 262, 145-198.
- Farquhar, G.D., Ehleringer, J.R., Hubick, K.T., 1989. Carbon isotope discrimination and photosynthesis. *Annual review of plant biology* 40, 503-537.

- Feranec, R., Hadly, E., Paytan, A., 2009. Stable isotopes reveal seasonal competition for resources between late Pleistocene bison (*Bison*) and horse (*Equus*) from Rancho La Brea, southern California. *Palaeogeography, Palaeoclimatology, Palaeoecology* 271, 153-160.
- Feranec, R., MacFadden, B., 2006. Isotopic discrimination of resource partitioning among ungulates in C₃-dominated communities from the Miocene of Florida and California. *Paleobiology* 32, 191-205.
- Feranec, R.S., 2005. Growth rate and duration of growth in the adult canine of *Smilodon gracilis* and inferences on diet through stable isotope analysis. *Bulletin of the Florida Museum of Natural History* 45, 369-377.
- Fernicola, J., Albino, A., 2012. Amphibians and squamate reptiles from the Santa Cruz Formation (late Early Miocene), Santa Cruz Province, Argentina: paleoenvironmental and paleobiological considerations. *Early Miocene Paleobiology in Patagonia: High-Latitude Paleocommunities of the Santa Cruz Formation*. Cambridge University Press, New York, 129-137.
- Fleagle, J.G., Bown, T., Swisher, C., Buckley, G., 1995. Age of the Pinturas and Santa Cruz formations, Congreso Argentino de Paleontología y Bioestratigrafía pp. 129-135.
- Fleagle, J.G., Perkins, M.E., Heizler, M.T., Nash, B., Bown, T.M., Tauber, A.A., Dozo, M.T., Tejedor, M.F., 2012. Absolute and relative ages of fossil localities in the Santa Cruz and Pinturas Formations, in: Vizcaíno, S.F., Kay, R.F., Bargo, M.S. (Eds.), *Early Miocene Paleobiology in Patagonia: High-Latitude Paleocommunities of the Santa Cruz Formation* pp. 41-58.
- Flower, B.P., Kennett, J.P., 1993. Relations between Monterey Formation deposition and middle Miocene global cooling: Naples Beach section, California. *Geology* 21, 877-880.
- Flower, B.P., Kennett, J.P., 1994. The middle Miocene climatic transition: East Antarctic ice sheet development, deep ocean circulation and global carbon cycling. *Palaeogeography, palaeoclimatology, palaeoecology* 108, 537-555.

- Föllmi, K.B., Badertscher, C., de Kaenel, E., Stille, P., John, C.M., Adatte, T., Steinmann, P., 2005. Phosphogenesis and organic-carbon preservation in the Miocene Monterey Formation at Naples Beach, California—The Monterey hypothesis revisited. *Geological Society of America Bulletin* 117, 589-619.
- Fosdick, J.C., Grove, M., Hourigan, J.K., Calderon, M., 2013. Retroarc deformation and exhumation near the end of the Andes, southern Patagonia. *Earth and Planetary Science Letters* 361, 504-517.
- Fox, D.L., Fisher, D.C., 2001. Stable isotope ecology of a late Miocene population of *Gomphotherium productus* (Mammalia, Proboscidea) from Port of Entry Pit, Oklahoma, USA. *Palaios* 16, 279-293.
- Fricke, H.C., Clyde, W.C., O'Neil, J.R., 1998. Intra-tooth variations in $\delta^{18}\text{O}$ (PO_4) of mammalian tooth enamel as a record of seasonal variations in continental climate variables. *Geochimica et Cosmochimica Acta* 62, 1839-1850.
- Fricke, H.C., O'Neil, J.R., 1996. Inter-and intra-tooth variation in the oxygen isotope composition of mammalian tooth enamel phosphate: implications for palaeoclimatological and palaeobiological research. *Palaeogeography, Palaeoclimatology, Palaeoecology* 126, 91-99.
- Gelman, A., Roberts, G.O., Gilks, W.R., 1996. Efficient Metropolis jumping rules. *Bayesian statistics* 5, 42.
- Greenop, R., Foster, G.L., Wilson, P.A., Lear, C.H., 2014. Middle Miocene climate instability associated with high-amplitude CO₂ variability. *Paleoceanography* 29, 845-853.
- Haslett, J., Parnell, A.C., 2008. A Simple Monotone Process With Application To Radiocarbon-Dated Depth Chronologies. *Applied Statistics* 57, 399-418.
- Henrot, A.-J., François, L., Favre, E., Butzin, M., Ouberdous, M., Munhoven, G., 2010. Effects of CO₂, continental distribution, topography and vegetation changes on the climate at the Middle Miocene: a model study. *Climate of the Past* 6, 675-694.
- Herold, N., Huber, M., Müller, R., 2011. Modeling the Miocene climatic optimum. Part I: Land and atmosphere. *Journal of Climate* 24, 6353-6372.

- Herold, N., Müller, R., Seton, M., 2010. Comparing early to middle Miocene terrestrial climate simulations with geological data. *Geosphere* 6, 952-961.
- Hiller, C.R., Robinson, C., Weatherell, J.A., 1975. Variations in the composition of developing rat incisor enamel. *Calcified tissue research* 18, 1-12.
- Hillson, S., 1986. *Teeth*. Cambridge University Press, Cambridge, UK.
- Hinojosa, L.F., Villagrán, C., 2005. Did South American Mixed Paleofloras evolve under thermal equability or in the absence of an effective Andean barrier during the Cenozoic? *Palaeogeography, Palaeoclimatology, Palaeoecology* 217, 1-23.
- Holbourn, A., Kuhnt, W., Kochhann, K.G., Andersen, N., Meier, K.S., 2015. Global perturbation of the carbon cycle at the onset of the Miocene Climatic Optimum. *Geology* 43, 123-126.
- Holbourn, A., Kuhnt, W., Schulz, M., Flores, J.-A., Andersen, N., 2007. Orbitally-paced climate evolution during the middle Miocene “Monterey” carbon-isotope excursion. *Earth and Planetary Science Letters* 261, 534-550.
- Holroyd, P.A., Barrón-Ortiz, C.R., Cammidge, T., Rankin, B.D., Hoppe, K.A., 2014. Serial Sampling of Mammalian Enamel Does Not Equal Seasonal Sampling. *Geological Society of America Abstracts with Programs* 46, 164.
- Hoppe, K., 2006. Correlation between the oxygen isotope ratio of North American bison teeth and local waters: Implication for paleoclimatic reconstructions. *Earth and Planetary Science Letters* 244, 408-417.
- Hoppe, K.A., Stover, S.M., Pascoe, J.R., Amundson, R., 2004. Tooth enamel biomineralization in extant horses: implications for isotopic microsampling. *Palaeogeography, Palaeoclimatology, Palaeoecology* 206, 355-365.
- IPCC, 2014. *Climate Change 2014: Synthesis Report. Contribution of Working Groups I, II and III to the Fifth Assessment Report of the Intergovernmental Panel on Climate Change* Geneva, Switzerland.

- Jaffey, A., Flynn, K., Glendenin, L., Bentley, W.t., Essling, A., 1971. Precision measurement of half-lives and specific activities of U235 and U238. *Physical Review C* 4, 1889.
- Janis, C.M., Damuth, J., Theodor, J.M., 2000. Miocene ungulates and terrestrial primary productivity: where have all the browsers gone? *Proceedings of the National Academy of Sciences* 97, 7899-7904.
- Jicha, B.R., Singer, B.S., Sobol, P., 2016. Re-Evaluation Of The Ages Of $^{40}\text{Ar}/^{39}\text{Ar}$ Sanidine Standards And Supereruptions In The Western Us Using A Noblesse Multi-Collector Mass Spectrometer. *Chemical Geology* 431, 54-66.
- Kay, R.F., Perry, J.M., Malinzak, M., Allen, K.L., Kirk, E.C., Plavcan, J.M., Fleagle, J., 2012a. The paleobiology of Santacrucian primates. *Early Miocene Paleobiology in Patagonia: High-Latitude Paleocommunities of the Santa Cruz Formation*, 306-330.
- Kay, R.F., Vizcaino, S.F., Bargo, M.S., 2012b. A review of the paleoenvironment and paleoecology of the Miocene Santa Cruz Formation, in: Vizcaino, S.F., Kay, R.F., Bargo, M.S. (Eds.), *Early Miocene Paleobiology in Patagonia: high-latitude paleocommunities of the Santa Cruz Formation*. Cambridge: Cambridge University Press, pp. 331-365.
- Kierdorf, H., Kierdorf, U., 1997. Disturbances of the secretory stage of amelogenesis in fluorosed deer teeth: a scanning electron-microscopic study. *Cell and tissue research* 289, 125-135.
- Kierdorf, H., Kierdorf, U., Frölich, K., Witzel, C., 2013. Lines of evidence—incremental markings in molar enamel of Soay sheep as revealed by a fluorochrome labeling and backscattered electron imaging study. *PloS one* 8, e74597.
- Kierdorf, H., Witzel, C., Upex, B., Dobney, K., Kierdorf, U., 2012. Enamel hypoplasia in molars of sheep and goats, and its relationship to the pattern of tooth crown growth. *Journal of anatomy* 220, 484-495.

- Kierdorf, H., Zeiler, J., Kierdorf, U., 2006. Problems and pitfalls in the diagnosis of linear enamel hypoplasia in cheek teeth of cattle. *Journal of archaeological science* 33, 1690-1695.
- Kim, S.-T., O'Neil, J.R., 1997. Equilibrium and nonequilibrium oxygen isotope effects in synthetic carbonates. *Geochimica et Cosmochimica Acta* 61, 3461-3475.
- Koch, P., Tuross, N., Fogel, M., 1997. The Effects Of Sample Treatment And Diagenesis On The Isotopic Integrity Of Carbonate In Biogenic Hydroxylapatite. *Journal of Archaeological Science* 24, 417-429.
- Koch, P.L., 1998. Isotopic reconstruction of past continental environments. *Annual Review of Earth and Planetary Sciences* 26, 573-613.
- Koch, P.L., 2007. Isotopic study of the biology of modern and fossil vertebrates, in: Michener, R., Lajtha, K. (Eds.), *Stable Isotopes in Ecology And Environmental Science*. Blackwell Publishing, pp. 99-154.
- Koenigswald, W.V., Martin, T., Pfretzschner, H.U., 1993. Phylogenetic Interpretations of Enamel Structures in Mammalian Teeth: Possibilities and Problems, in: Szalay, F.S., Novacek, M.J., McKenna, M.C. (Eds.), *Mammalian Phylogeny: Placentals*. Springer-Verlag, New York, pp. 303-314.
- Koenigswald, W.v., Sander, P., 1997. Glossary of terms used for enamel microstructures, *Tooth enamel microstructure*. A.A. Balkema/ Rotterdam/ Brookfield, pp. 267-280.
- Kohn, M., 2010. Carbon Isotope Composition of Terrestrial C₃ Plants as Indicators of (Paleo)Ecology and (Paleo)Climate. *Proceedings of the National Academy of Sciences* 107.46.
- Kohn, M., 2016. Carbon isotope discrimination in C₃ land plants is independent of natural variations in *p*CO₂. *Geophys. Perspect. Lett* 2, 35-43.
- Kohn, M.J., 1996. Predicting animal $\delta^{18}\text{O}$: Accounting for diet and physiological adaptation. *Geochimica et Cosmochimica Acta* 60, 4811-4829.

- Kohn, M.J., 2004. Comment: Tooth Enamel Mineralization in Ungulates: Implications for Recovering a Primary Isotopic Time-Series, by B. H. Passey and T. E. Cerling (2002). *Geochimica et Cosmochimica Acta* 68, 403-405.
- Kohn, M.J., Cerling, T.E., 2002. Stable Isotope Compositions Of Biological Apatite. *Reviews in Mineralogy and Geochemistry* 48, 455-488.
- Kohn, M.J., Dettman, D.L., 2007. Paleoaltimetry from stable isotope compositions of fossils. *Reviews in Mineralogy and Geochemistry* 66, 119-154.
- Kohn, M.J., Law, J.M., 2006. Stable isotope chemistry of fossil bone as a new paleoclimate indicator. *Geochimica et Cosmochimica Acta* 70, 931-946.
- Kohn, M.J., McKay, M.P., 2012. Paleoeology of late Pleistocene-Holocene faunas of eastern and central Wyoming, USA, with implications for LGM climate models. *Palaeogeography, Palaeoclimatology, Palaeoecology* 326-328, 42-53.
- Kohn, M.J., McKay, M.P., Knight, J.L., 2005. Dining in the Pleistocene-Who's on the menu? *Geology* 33, 649-652.
- Kohn, M.J., Schoeninger, M.J., Barker, W.W., 1999. Altered States: Effects Of Diagenesis On Fossil Tooth Chemistry. *Geochimica et Cosmochimica Acta* 63, 2737-2747.
- Kohn, M.J., Schoeninger, M.J., Valley, J.W., 1996. Herbivore tooth oxygen isotope compositions: effects of diet and physiology. *Geochimica et Cosmochimica Acta* 60, 3889-3896.
- Kohn, M.J., Strömberg, C.A., Madden, R.H., Dunn, R.E., Evans, S., Palacios, A., Carlini, A.A., 2015. Quasi-static Eocene–Oligocene climate in Patagonia promotes slow faunal evolution and mid-Cenozoic global cooling. *Palaeogeography, Palaeoclimatology, Palaeoecology* 435, 24-37.
- Kruschke, J., 2015. *Doing Bayesian Data Analysis: A Tutorial With R, JAGS, and Stan*. Academic Press.

- Kürschner, W.M., Kvaček, Z., Dilcher, D.L., 2008. The impact of Miocene atmospheric carbon dioxide fluctuations on climate and the evolution of terrestrial ecosystems. *Proceedings of the National Academy of Sciences* 105, 449-453.
- Laurie, W., Lang, E., Groves, C., 1983. *Rhinoceros unicornis*. Mammalian species, 1-6.
- Levin, N.E., Cerling, T.E., Passey, B.H., Harris, J.M., Ehleringer, J.R., 2006. A stable isotope aridity index for terrestrial environments. *Proceedings of the National Academy of Sciences* 103, 11201-11205.
- Luz, B., Kolodny, Y., 1985. Oxygen isotope variations in phosphate of biogenic apatites, IV. Mammal teeth and bones. *Earth and Planetary Science Letters* 75, 29-36.
- Ma, W., Tian, J., Li, Q., Wang, P., 2011. Simulation of long eccentricity (400-kyr) cycle in ocean carbon reservoir during Miocene Climate Optimum: Weathering and nutrient response to orbital change. *Geophysical Research Letters* 38.
- Malumián, N., Ardolino, A., Franchi, M., Remesal, M., Salani, F., 1999. La sedimentación y el volcanismo terciarios en la Patagonia extraandina, *Geología Argentina*. Instituto de Geología y Recursos Minerales, Anales, pp. 557-612.
- Marshall, L.G., 1976. Fossil localities for Santacrucian (early Miocene) mammals, Santa Cruz Province, southern Patagonia, Argentina. *Journal of Paleontology*, 1129-1142.
- Marshall, L.G., Drake, R.E., Curtis, G.H., Butler, R.F., Flanagan, K.M., Naeser, C.W., 1986. Geochronology of type Santacrucian (middle Tertiary) land mammal age, Patagonia, Argentina. *The Journal of Geology* 94, 449-457.
- Marshall, L.G., Pascual, R., Curtis, G.H., Drake, R.E., 1977. South American geochronology: radiometric time scale for middle to late Tertiary mammal-bearing horizons in Patagonia. *Science* 195, 1325-1328.
- Martin, C., Bentaleb, I., Kaandorp, R., Iacumin, P., Chatri, K., 2008. Intra-tooth study of modern rhinoceros enamel $\delta^{18}\text{O}$: Is the difference between phosphate and carbonate $\delta^{18}\text{O}$ a sound diagenetic test? *Palaeogeography, Palaeoclimatology, Palaeoecology* 266, 183-189.

- Matheos, S.D., Raigemborn, M.S., 2012. Sedimentology and paleoenvironment of the Santa Cruz Formation, in: Vizcaíno, S.F., Kay, R.F., Bargo, M.S. (Eds.), *Early Miocene Paleobiology in Patagonia: High-latitude Paleocommunities of the Santa Cruz Formation*. Cambridge University Press, Cambridge, pp. 59-82.
- Mattinson, J.M., 2005. Zircon U–Pb Chemical Abrasion (“Ca-Tims”) Method: Combined Annealing and Multi-Step Partial Dissolution Analysis For Improved Precision And Accuracy Of Zircon Ages. *Chemical Geology* 220, 47-66.
- Mayr, C., Lücke, A., Stichler, W., Trimborn, P., Ercolano, B., Oliva, G., Ohlendorf, C., Soto, J., Fey, M., Haberzettl, T., Janssen, S., Schäbitz, F., Schleser, G.H., Wille, M., Zolitschka, B., 2007. Precipitation origin and evaporation of lakes in semi-arid Patagonia (Argentina) inferred from stable isotopes ($\delta^{18}\text{O}$, $\delta^2\text{H}$). *Journal of Hydrology* 334, 53-63.
- McDougall, I., Harrison, T.M., 1999. *Geochronology and Thermochronology by the $^{40}\text{Ar}/^{39}\text{Ar}$ Method*. Oxford University Press on Demand.
- McLean, N.M., Condon, D.J., Schoene, B., Bowring, S.A., 2015. Evaluating uncertainties in the calibration of isotopic reference materials and multi-element isotopic tracers (EARTHTIME Tracer Calibration Part II). *Geochimica et Cosmochimica Acta* 164, 481-501.
- Michel, L.A., Schmitz, M.D., Tabor, N.J., Moontañez, I.P., Davydov, V.I., 2016. Reply to the comment on “Chronostratigraphy and paleoclimatology of the Lodève Basin, France: Evidence for a pan-tropical aridification event across the Carboniferous–Permian boundary” by Michel et al., (2015). *Palaeogeography, Palaeoclimatology, Palaeoecology* 430, 118–131. *Paleogeogr. Paleoclimatol. Paleoecol.* 441, 1000-1004.
- Mosbrugger, V., Utescher, T., Dilcher, D.L., 2005. Cenozoic continental climatic evolution of Central Europe. *Proceedings of the National Academy of Sciences of the United States of America* 102, 14964-14969.

- Moss-Salentijn, L., Moss, M., Yuan, M.S.-T., 1997. The Ontogeny of Mammalian Enamel, in: Koengswald, W.V., Sander, P.M. (Eds.), *Tooth Enamel Microstructure*. A.A. Balkema/ Rotterdam/ Brookfield, pp. 5-30.
- Pagani, M., Arthur, M.A., Freeman, K.H., 1999. Miocene evolution of atmospheric carbon dioxide. *Paleoceanography* 14, 273-292.
- Pagani, M., Zachos, J.C., Freeman, K.H., Tipple, B., Bohaty, S., 2005. Marked decline in atmospheric carbon dioxide concentrations during the Paleogene. *Science* 309, 600-603.
- Parnell, A.C., Buck, C.E., Doan, T.K., 2011. A Review Of Statistical Chronology Models For High-Resolution, Proxy-Based Holocene Palaeoenvironmental Reconstruction. *Quaternary Science Reviews* 30, 2948-2960.
- Pascual, R., Ortiz Jaureguizar, E., 1990. Evolving climates and mammal faunas in Cenozoic South America, *The Platyrrhine Fossil Record*. Elsevier, pp. 23-60.
- Passey, B.H., Cerling, T.E., 2002. Tooth enamel mineralization in ungulates: implications for recovering a primary isotopic time-series. *Geochimica et Cosmochimica Acta* 66, 3225-3234.
- Passey, B.H., Cerling, T.E., Perkins, M.E., Voorhies, M.R., Harris, J.M., Tucker, S.T., 2002. Environmental change in the Great Plains: an isotopic record from fossil horses. *The Journal of Geology* 110, 123-140.
- Passey, B.H., Cerling, T.E., Schuster, G.T., Robinson, T.F., Roeder, B.L., Krueger, S.K., 2005. Inverse methods for estimating primary input signals from time-averaged isotope profiles. *Geochimica et Cosmochimica Acta* 69, 4101-4116.
- Passey, B.H., Robinson, T.F., Ayliffe, L.K., Cerling, T.E., Sponheimer, M., Dearing, M.D., Roeder, B.L., Ehleringer, J.R., 2005. Carbon isotope fractionation between diet, breath CO₂, and bioapatite in different mammals. *Journal of Archaeological Science* 32, 1459-1470.
- Pekar, S.F., Christie-Blick, N., 2008. Resolving apparent conflicts between oceanographic and Antarctic climate records and evidence for a decrease in *p*CO₂

- during the Oligocene through early Miocene (34–16 Ma). *Palaeogeography, Palaeoclimatology, Palaeoecology* 260, 41-49.
- Pekar, S.F., DeConto, R.M., 2006. High-resolution ice-volume estimates for the early Miocene: Evidence for a dynamic ice sheet in Antarctica. *Palaeogeography, Palaeoclimatology, Palaeoecology* 231, 101-109.
- Pellegrini, M., Lee-Thorp, J.A., Donahue, R.E., 2011. Exploring the variation of the $\delta^{18}\text{O}_p$ and $\delta^{18}\text{O}_c$ relationship in enamel increments. *Palaeogeography, Palaeoclimatology, Palaeoecology* 310, 71-83.
- Perkins, M.E., Fleagle, J.G., Heizler, M.T., Nash, B., Bown, T., Tauber, A., Dozo, M., 2012. Tephrochronology of the Miocene Santa Cruz and Pinturas Formations, Argentina, in: Vizcaíno, S.F., Kay, R.F., Bargo, M.S. (Eds.), *Early Miocene Paleobiology in Patagonia: High-Latitude Paleocommunities of the Santa Cruz Formation*, pp. 23-40.
- Pfretzschner, H., 1992. Enamel microstructure and hypsodonty in large mammals, in: Smith, P., Tchernov, E. (Eds.), *Structure, function and evolution of teeth*. Freund Publishing House Ltd., London and Tel Aviv, pp. 147-162.
- Poage, M.A., Chamberlain, C.P., 2001. Empirical relationships between elevation and the stable isotope composition of precipitation and surface waters: considerations for studies of paleoelevation change. *American Journal of Science* 301, 1-15.
- Podlesak, D.W., Torregrossa, A.-M., Ehleringer, J.R., Dearing, M.D., Passey, B.H., Cerling, T.E., 2008. Turnover of oxygen and hydrogen isotopes in the body water, CO_2 , hair, and enamel of a small mammal. *Geochimica et Cosmochimica Acta* 72, 19-35.
- R Core Team, 2017. *R: A Language and Environment for Statistical Computing*. R Foundation for Statistical Computing, Vienna, Austria.
- Raigemborn, M.S., Matheos, S.D., Krapovickas, V., Vizcaíno, S.F., Bargo, M.S., Kay, R.F., Fernicola, J.C., Zapata, L., 2015. Paleoenvironmental reconstruction of the coastal Monte León and Santa Cruz formations (Early Miocene) at Rincón del

- Buque, Southern Patagonia: A revisited locality. *Journal of South American Earth Sciences* 60, 31-55.
- Retallack, G.J., 2009. Refining a pedogenic-carbonate CO₂ paleobarometer to quantify a middle Miocene greenhouse spike. *Palaeogeography, Palaeoclimatology, Palaeoecology* 281, 57-65.
- Reynard, B., Balter, V., 2014. Trace elements and their isotopes in bones and teeth: Diet, environments, diagenesis, and dating of archeological and paleontological samples. *Palaeogeography, Palaeoclimatology, Palaeoecology* 416, 4-16.
- Rivera, T.A., Storey, M., Schmitz, M.D., Crowley, J.L., 2013. Age Intercalibration Of ⁴⁰Ar/³⁹Ar Sanidine And Chemically Distinct U/Pb Zircon Populations From The Alder Creek Rhyolite Quaternary Geochronology Standard. *Chemical Geology* 345, 87-98.
- Robinson, C., Briggs, H., Atkinson, P., Weatherell, J., 1979. Matrix and mineral changes in developing enamel. *Journal of dental research* 58, 871-882.
- Robinson, C., Fuchs, P., Deutsch, D., Weatherell, J., 1978. Four chemically distinct stages in developing enamel from bovine incisor teeth. *Caries research* 12, 1-11.
- Robinson, C., Hiller, C.R., Weatherell, J.A., 1974. Uptake of ³²P-labelled phosphate into developing rat incisor enamel. *Calcified tissue research* 15, 143-152.
- Roche, D., Ségalen, L., Balan, E., Delattre, S., 2010. Preservation Assessment Of Miocene–Pliocene Tooth Enamel From Tugen Hills (Kenyan Rift Valley) Through FTIR, Chemical And Stable-Isotope Analyses. *Journal of Archaeological Science* 37, 1690-1699.
- Sahy, D., Condon, D.J., Terry Jr., D.O., Fischer, A.U., Kuiper, K.F., 2015. Synchronizing terrestrial and marine records of environmental change across the Eocene–Oligocene transition. *Earth and Planetary Science Letters* 427, 171-182.
- Schmitz, M.D., Davydov, V.I., 2012. Quantitative Radiometric And Biostratigraphic Calibration Of The Pennsylvanian–Early Permian (Cisuralian) Time Scale And Pan-Euramerican Chronostratigraphic Correlation. *Geological Society of America Bulletin* 124, 549-577.

- Schmitz, M.D., Schoene, B., 2007. Derivation Of Isotope Ratios, Errors, And Error Correlations For U-Pb Geochronology Using ^{205}Pb - ^{235}U -(^{233}U)-Spiked Isotope Dilution Thermal Ionization Mass Spectrometric Data. *Geochemistry, Geophysics, Geosystems* 8.
- Schmitz, W.J., 1995. On the interbasin-scale thermohaline circulation. *Reviews of Geophysics* 33, 151-173.
- Schubert, B.A., Jahren, A.H., 2012. The effect of atmospheric CO_2 concentration on carbon isotope fractionation in C_3 land plants. *Geochimica et Cosmochimica Acta* 96, 29-43.
- Shevenell, A.E., Kennett, J.P., Lea, D.W., 2004. Middle Miocene southern ocean cooling and Antarctic cryosphere expansion. *Science* 305, 1766-1770.
- Stipp, S.L., Hochella, M.F., Parks, G.A., Leckie, J.O., 1992. Cd^{2+} uptake by calcite, solid-state diffusion, and the formation of solid-solution: Interface processes observed with near-surface sensitive techniques (XPS, LEED, and AES). *Geochimica et Cosmochimica Acta* 56, 1941-1954.
- Suga, S., 1979. Comparative histology of progressive mineralization pattern of developing incisor enamel of rodents. *Journal of dental research* 58, 1025-1026.
- Suga, S., 1982. Progressive mineralization pattern of developing enamel during the maturation stage. *Journal of Dental Research* 61, 1532-1542.
- Sydney-Zax, M., Mayer, I., Deutsch, D., 1991. Carbonate content in developing human and bovine enamel. *Journal of dental research* 70, 913-916.
- Tafforeau, P., Bentaleb, I., Jaeger, J.-J., Martin, C., 2007. Nature of laminations and mineralization in rhinoceros enamel using histology and X-ray synchrotron microtomography: Potential implications for palaeoenvironmental isotopic studies. *Palaeogeography, Palaeoclimatology, Palaeoecology* 246, 206-227.
- Tauber, A.A., 1994. Estratigrafía y vertebrados fósiles de la Formación Santa Cruz (Mioceno inferior) en la costa atlántica entre las rías del Coyle y Río Gallegos, Provincia de Santa Cruz, República Argentina, República Argentina [Ph. D.

- dissertation]: Facultad de Ciencias Exactas, Físicas y Naturales, Córdoba, Universidad Nacional de Córdoba.
- Tauber, A.A., 1997a. Bioestratigrafía de la Formación Santa Cruz (Mioceno Inferior) en el extremo sudeste de la Patagonia. *Ameghiniana* 34, 413-426.
- Tauber, A.A., 1997b. Paleoecología de la Formación Santa Cruz (Mioceno inferior) en el extremo sudeste de la Patagonia. *Ameghiniana* 34, 517-529.
- Tejedor, M.F., Tauber, A.A., Rosenberger, A.L., Swisher, C.C., Palacios, M.E., 2006. New primate genus from the Miocene of Argentina. *Proceedings of the National Academy of Sciences* 103, 5437-5441.
- Telford, R.J., Heegaard, E., Birks, H.J.B., 2004. All age–depth models are wrong: but how badly? *Quaternary science reviews* 23, 1-5.
- Tipple, B.J., Meyers, S.R., Pagani, M., 2010. Carbon isotope ratio of Cenozoic CO₂: A comparative evaluation of available geochemical proxies. *Paleoceanography* 25, PA3202.
- Tong, J., You, Y., Müller, R., Seton, M., 2009. Climate model sensitivity to atmospheric CO₂ concentrations for the middle Miocene. *Global and Planetary Change* 67, 129-140.
- Townsend, K.B., Croft, D.A., 2008. Diets of notoungulates from the Santa Cruz Formation, Argentina: new evidence from enamel microwear. *Journal of Vertebrate Paleontology* 28, 217-230.
- Trayler, R.B., Dundas, R.G., Fox-Dobbs, K., Van de Water, P.K., 2015. Inland California during the Pleistocene-Megafaunal stable isotope records reveal new paleoecological and paleoenvironmental insights. *Paleogeogr. Paleoclimatol. Paleoecol.* 437, 132-140.
- Trayler, R.B., Kohn, M.J., 2017. Tooth enamel maturation reequilibrates oxygen isotope compositions and supports simple sampling methods. *Geochimica Et Cosmochimica Acta* 198, 32-47.

- Trayler, R.B., Schmitz, M.D., Cuitiño, J.I., Kohn, M.J., Bargo, M.S., Kay, R.F., Strömberg, C.A.E., Vizcaíno, S.F., in review. An improved approach to age-depth modeling in deep time: implications for the Santa Cruz Formation, Argentina. *Earth and Planetary Science Letters*.
- Trueman, C.N., Tuross, N., 2002. Trace elements in recent and fossil bone apatite. *Reviews in mineralogy and geochemistry* 48, 489-521.
- Van Der Merwe, N.J., Medina, E., 1991. The canopy effect, carbon isotope ratios and foodwebs in Amazonia. *Journal of Archaeological Science* 18, 249-259.
- Vincent, E., Berger, W.H., 1985. Carbon Dioxide and Polar Cooling In The Miocene: The Monterey Hypothesis. *The Carbon Cycle and Atmospheric CO₂: Natural Variations Archean to Present*, 455-468.
- Vizcaíno, S.F., Bargo, M.S., Kay, R.F., Fariña, R.A., Di Giacomo, M., Perry, J.M., Prevosti, F.J., Toledo, N., Cassini, G.H., Fernicola, J.C., 2010. A Baseline Paleocological Study for The Santa Cruz Formation (Late–Early Miocene) At the Atlantic Coast Of Patagonia, Argentina. *Palaeogeography, Palaeoclimatology, Palaeoecology* 292, 507-519.
- Vizcaíno, S.F., Bargo, M.S., Kay, R.F., Milne, N., 2006. The Armadillos (Mammalia, Xenarthra, Dasypodidae) Of the Santa Cruz Formation (Early–Middle Miocene): An Approach to Their Paleobiology. *Palaeogeography, Palaeoclimatology, Palaeoecology* 237, 255-269.
- Vizcaíno, S.F., Kay, R.F., Bargo, M.S., 2012a. Background for A Paleocological Study Of The Santa Cruz Formation (Late Early Miocene) On The Atlantic Coast Of Patagonia, in: Vizcaíno, S.F., Kay, R.F., Bargo, M.S. (Eds.), *Early Miocene Paleobiology in Patagonia: High-Latitude Paleocommunities of the Santa Cruz Formation*, pp. 1-22.
- Vizcaíno, S.F., Kay, R.F., Bargo, M.S., 2012b. *Early Miocene Paleobiology In Patagonia: High-Latitude Paleocommunities Of the Santa Cruz Formation*. Cambridge University Press.

- Wetherill, G.W., 1956. Discordant uranium-lead ages. *Eos, Transactions American Geophysical Union* 37, 320-326.
- Wetherill, G.W., 1963. Discordant uranium-lead ages: 2. Discordant ages resulting from diffusion of lead and uranium. *Journal of Geophysical Research* 68, 2957-2965.
- Wolfe, J.A., 1985. Distribution of Major Vegetational Types During The Tertiary. *The Carbon Cycle and Atmospheric CO₂: Natural Variations Archean to Present*, 357-375.
- Wolfe, J.A., 1994. Tertiary Climatic Changes at Middle Latitudes Of Western North America. *Palaeogeography, Palaeoclimatology, Palaeoecology* 108, 195-205.
- Wotzlaw, J.-F., Brack, P., Storck, J.-C., 2018. High-Resolution Stratigraphy and Zircon U–Pb Geochronology Of The Middle Triassic Buchenstein Formation (Dolomites, Northern Italy): Precession-Forcing Of Hemipelagic Carbonate Sedimentation And Calibration Of The Anisian–Ladinian Boundary Interval. *Journal of the Geological Society* 175, 71-85.
- You, Y., Huber, M., Müller, R., Poulsen, C., Ribbe, J., 2009. Simulation of The Middle Miocene Climate Optimum. *Geophysical Research Letters* 36.
- Zachos, J., Pagani, M., Sloan, L., Thomas, E., Billups, K., 2001. Trends, Rhythms, And Aberrations in Global Climate 65 Ma To Present. *Science* 292, 686-693.
- Zanazzi, A., Kohn, M.J., MacFadden, B.J., Terry, D.O., 2007. Large Temperature Drop Across the Eocene–Oligocene Transition In Central North America. *Nature* 445, 639-642.
- Zazzo, A., Balasse, M., Patterson, W.P., 2005. High-resolution $\delta^{13}\text{C}$ intratooth profiles in bovine enamel: Implications for mineralization pattern and isotopic attenuation. *Geochimica et Cosmochimica Acta* 69, 3631-3642.
- Zazzo, A., Bendrey, R., Vella, D., Moloney, A.P., Monahan, F.J., Schmidt, O., 2012. A refined sampling strategy for intra-tooth stable isotope analysis of mammalian enamel. *Geochimica et Cosmochimica Acta* 84, 1-13.

Zazzo, A., Lécuyer, C., Sheppard, S.M.F., Grandjean, P., Mariotti, A., 2004. Diagenesis and the reconstruction of paleoenvironments: a method to restore original $\delta^{18}\text{O}$ values of carbonate and phosphate from fossil tooth enamel. *Geochimica et Cosmochimica Acta* 68, 2245-2258.

APPENDIX A

Supplementary Material for Chapter 1

Table A1. Stable isotope data from all sampled teeth. IMHM = Idaho Museum of Natural History. BSU = Boise State University. Superscript and subscript indicate upper or lower tooth, respectively

Taxa	Collection	Tooth	Position (mm)	$\delta^{18}\text{O}_p$	$\delta^{18}\text{O}_c$
<i>Bison</i> sp.	IMHM 28150	M ³	3.6	8.7	12.0
<i>Bison</i> sp.	IMHM 28150	M ³	5.7	6.5	15.1
<i>Bison</i> sp.	IMHM 28150	M ³	7.6	9.6	15.6
<i>Bison</i> sp.	IMHM 28150	M ³	9.2	9.5	15.6
<i>Bison</i> sp.	IMHM 28150	M ³	11.2	9.1	15.2
<i>Bison</i> sp.	IMHM 28150	M ³	14.0	9.7	15.2
<i>Bison</i> sp.	IMHM 28150	M ³	16.4	10.1	15.7
<i>Bison</i> sp.	IMHM 28150	M ³	18.6	10.9	15.8
<i>Bison</i> sp.	IMHM 28150	M ³	20.5	12.0	17.4
<i>Bison</i> sp.	IMHM 28150	M ³	22.3	12.7	17.7
<i>Bison</i> sp.	IMHM 28150	M ³	25.3	13.4	19.1
<i>Bison</i> sp.	IMHM 28150	M ³	27.4	14.0	19.9
<i>Bison</i> sp.	IMHM 28150	M ³	28.9	14.3	20.6
<i>Bison</i> sp.	IMHM 28150	M ³	31.0	15.1	19.3
<i>Bison</i> sp.	IMHM 28150	M ³	33.0	15.6	21.1
<i>Bison</i> sp.	IMHM 28150	M ³	35.1	15.7	22.9
<i>Bison</i> sp.	IMHM 28150	M ³	36.9	15.8	22.6
<i>Bison</i> sp.	IMHM 28150	M ³	38.0	16.3	23.1
<i>Bison</i> sp.	IMHM 28150	M ³	40.6	15.8	22.6
<i>Equus ferus caballus</i>	BSU	M ₃	5.2	15.7	24.4
<i>Equus ferus caballus</i>	BSU	M ₃	11.6	14.6	24.7
<i>Equus ferus caballus</i>	BSU	M ₃	13.4	14.2	22.8
<i>Equus ferus caballus</i>	BSU	M ₃	15.0	14.5	23.9
<i>Equus ferus caballus</i>	BSU	M ₃	16.7	14.1	23.2
<i>Equus ferus caballus</i>	BSU	M ₃	18.4	14.1	22.6

<i>Equus ferus caballus</i>	BSU	M ₃	20.1	12.9	22.1
<i>Equus ferus caballus</i>	BSU	M ₃	21.9	12.4	22.1
<i>Equus ferus caballus</i>	BSU	M ₃	23.6	12.1	22.0
<i>Equus ferus caballus</i>	BSU	M ₃	25.0	12.7	21.9
<i>Equus ferus caballus</i>	BSU	M ₃	26.6	12.1	21.5
<i>Equus ferus caballus</i>	BSU	M ₃	28.2	10.6	21.0
<i>Equus ferus caballus</i>	BSU	M ₃	30.2	10.5	21.0
<i>Equus ferus caballus</i>	BSU	M ₃	32.0	10.4	19.6
<i>Equus ferus caballus</i>	BSU	M ₃	33.2	9.2	18.9
<i>Equus ferus caballus</i>	BSU	M ₃	35.3	8.5	18.6
<i>Equus ferus caballus</i>	BSU	M ₃	37.0	8.8	18.1
<i>Equus ferus caballus</i>	BSU	M ₃	38.3	8.1	18.9
<i>Equus ferus caballus</i>	BSU	M ₃	41.5	8.5	18.4
<i>Equus ferus caballus</i>	BSU	M ₃	44.0	7.5	17.8
<i>Equus ferus caballus</i>	BSU	M ₃	45.5	8.2	18.2
<i>Equus ferus caballus</i>	BSU	M ₃	47.3	8.3	17.4
<i>Equus ferus caballus</i>	BSU	M ₃	50.8	9.6	17.3
<i>Equus ferus caballus</i>	BSU	M ₃	52.8	8.5	18.3
<i>Equus ferus caballus</i>	BSU	M ₃	53.4	8.8	18.2
<i>Equus ferus caballus</i>	BSU	M ₃	57.1	10.1	16.9
<i>Equus ferus caballus</i>	BSU	M ₃	59.2	10.6	18.0
<i>Equus ferus caballus</i>	BSU	M ₃	61.2	11.2	17.5
<i>Equus ferus caballus</i>	BSU	M ₃	64.3	11.0	19.4
<i>Equus ferus caballus</i>	BSU	M ₃	66.6	11.1	19.8
<i>Capra hircus</i>	BSU	M ₃	4.4	11.1	20.6
<i>Capra hircus</i>	BSU	M ₃	5.5	12.2	20.8
<i>Capra hircus</i>	BSU	M ₃	8.1	12.9	20.7
<i>Capra hircus</i>	BSU	M ₃	10.1	13.0	21.1
<i>Capra hircus</i>	BSU	M ₃	12.3	12.7	21.4
<i>Capra hircus</i>	BSU	M ₃	14.5	13.7	21.9

<i>Capra hircus</i>	BSU	M ₃	16.6	13.8	22.3
<i>Capra hircus</i>	BSU	M ₃	18.3	13.2	22.3
<i>Capra hircus</i>	BSU	M ₃	20.5	14.2	22.8
<i>Capra hircus</i>	BSU	M ₃	22.5	13.9	22.6
<i>Capra hircus</i>	BSU	M ₃	24.5	14.4	23.2
<i>Capra hircus</i>	BSU	M ₃	27.0	14.0	23.1
<i>Capra hircus</i>	BSU	M ₃	28.0	13.8	23.0
<i>Capra hircus</i>	BSU	M ₃	30.0	13.2	22.7
<i>Capra hircus</i>	BSU	M ₃	32.4	12.1	21.9
<i>Capra hircus</i>	BSU	M ₃	34.8	11.1	21.4
<i>Capra hircus</i>	BSU	M ₃	37.0	10.4	20.7
<i>Capra hircus</i>	BSU	M ₃	38.8	10.2	20.0
<i>Capra hircus</i>	BSU	M ₃	40.8	9.5	20.7
<i>Capra hircus</i>	BSU	M ₃	42.1	10.1	19.6
<i>Cervus elaphus</i> (1)	BSU M-00-49	M ₃	3.2	7.4	16.4
<i>Cervus elaphus</i> (1)	BSU M-00-49	M ₃	5.0	7.1	14.9
<i>Cervus elaphus</i> (1)	BSU M-00-49	M ₃	7.3	6.1	14.5
<i>Cervus elaphus</i> (1)	BSU M-00-49	M ₃	10.5	5.5	13.9
<i>Cervus elaphus</i> (1)	BSU M-00-49	M ₃	11.9	5.6	13.5
<i>Cervus elaphus</i> (1)	BSU M-00-49	M ₃	14.9	5.6	13.8
<i>Cervus elaphus</i> (1)	BSU M-00-49	M ₃	17.5	6.1	13.9
<i>Cervus elaphus</i> (1)	BSU M-00-49	M ₃	19.7	4.9	13.7
<i>Cervus elaphus</i> (2)	BSU M-00-59	M ₃	2.6	8.7	16.8
<i>Cervus elaphus</i> (2)	BSU M-00-59	M ₃	3.9	6.6	15.6
<i>Cervus elaphus</i> (2)	BSU M-00-59	M ₃	5.8	6.7	15.2
<i>Cervus elaphus</i> (2)	BSU M-00-59	M ₃	9.0	6.4	14.1
<i>Cervus elaphus</i> (2)	BSU M-00-59	M ₃	11.0	7.1	15.0
<i>Cervus elaphus</i> (2)	BSU M-00-59	M ₃	12.7	6.4	14.9
<i>Cervus elaphus</i> (2)	BSU M-00-59	M ₃	14.7	6.8	15.2
<i>Cervus elaphus</i>	PLCE		2	19.9	28.3

<i>Cervus elaphus</i>	PLCE	3.9	19.6	28
<i>Cervus elaphus</i>	PLCE	6	18.6	27.4
<i>Cervus elaphus</i>	PLCE	8.5	18.1	26.6
<i>Cervus elaphus</i>	PLCE	11	17	26.3
<i>Cervus elaphus</i>	PLCE	13	16.8	25.6
<i>Cervus elaphus</i>	PLCE	15.1	16.6	25.9
<i>Cervus elaphus</i>	PLCE	17.1	16.3	25.8
<i>Cervus elaphus</i>	PLCE	19.4	16	25.3
<i>Equus hydruntinus</i>	PLEH	3.8	17.4	26.5
<i>Equus hydruntinus</i>	PLEH	8.8	17.6	26.8
<i>Equus hydruntinus</i>	PLEH	12	18.5	26.9
<i>Equus hydruntinus</i>	PLEH	14.9	18.5	27.2
<i>Equus hydruntinus</i>	PLEH	19	18.2	27.1
<i>Equus hydruntinus</i>	PLEH	23.5	17.4	27.1
<i>Equus hydruntinus</i>	PLEH	28	17.1	26.1
<i>Equus hydruntinus</i>	PLEH	31.3	16	26.4
<i>Equus hydruntinus</i>	PLEH	34.7	16.5	26.2
<i>Equus hydruntinus</i>	PLEH	37.5	16.8	26.3
<i>Equus hydruntinus</i>	PLEH	39.8	17	26.4
<i>Equus hydruntinus</i>	PLEH	42	17.3	26.3
<i>Equus hydruntinus</i>	PLEH	44.1	17.3	26.2
<i>Equus hydruntinus</i>	PLEH	47	17.2	26.4
<i>Equus hydruntinus</i>	PLEH	49.1	17.2	26.2
<i>Equus hydruntinus</i>	PLEH	52	17.9	26.5
<i>Equus hydruntinus</i>	PLEH	54	18.3	26.7
<i>Equus hydruntinus</i>	PLEH	56.3	18.4	27.1
<i>Equus hydruntinus</i>	PLEH	58.3	18.9	27.1
<i>Equus hydruntinus</i>	PLEH	60.4	17.8	27.3
<i>Equus hydruntinus</i>	PLEH	62.8	18.9	27.3

<i>Equus hydruntinus</i>	PLEH	65.7	18.4	27.2
<i>Cervus elaphus</i>	CACE	1.8	17	26.1
<i>Cervus elaphus</i>	CACE	3.6	16.7	26.2
<i>Cervus elaphus</i>	CACE	5.4	16.9	26.5
<i>Cervus elaphus</i>	CACE	7.3	17.3	26.8
<i>Cervus elaphus</i>	CACE	9.3	18.1	27.4
<i>Cervus elaphus</i>	CACE	11.2	18.6	27.8
<i>Cervus elaphus</i>	CACE	13.2	19.5	28.4
<i>Cervus elaphus</i>	CACE	14.9	19.3	28.4
<i>Cervus elaphus</i>	PZCE	2.9	18.8	27.9
<i>Cervus elaphus</i>	PZCE	4.7	18.8	27.2
<i>Cervus elaphus</i>	PZCE	6.8	18.3	26.5
<i>Cervus elaphus</i>	PZCE	8.5	17.9	27.1
<i>Cervus elaphus</i>	PZCE	10.4	17.3	26.2
<i>Cervus elaphus</i>	PZCE	12.2	16.9	25.7
<i>Cervus elaphus</i>	PZCE	14.6	16.4	25.3
<i>Cervus elaphus</i>	PZCE	16.7	16.1	24.7
<i>Cervus elaphus</i>	PZCE	18.5	15.6	24.7
<i>Cervus elaphus</i>	PZCE	21	15.3	24.9
<i>Equus hydruntinus</i>	PZEH	19	15.5	24.2
<i>Equus hydruntinus</i>	PZEH	22.2	15.9	24.4
<i>Equus hydruntinus</i>	PZEH	25.5	14.9	24.2
<i>Equus hydruntinus</i>	PZEH	29	14.9	24.2
<i>Equus hydruntinus</i>	PZEH	31.6	15.7	24.2
<i>Equus hydruntinus</i>	PZEH	33.9	15.5	24.3
<i>Equus hydruntinus</i>	PZEH	36.4	15.5	24.4
<i>Equus hydruntinus</i>	PZEH	39.5	15.4	24.7
<i>Equus hydruntinus</i>	PZEH	42.1	15.7	24.3
<i>Equus hydruntinus</i>	PZEH	45	16.5	24.6

<i>Equus hydruntinus</i>	PZEH	47.9	17.1	24.3
<i>Equus hydruntinus</i>	PZEH	50.9	17.3	25.1
<i>Equus hydruntinus</i>	PZEH	53.6	16.6	24.7
<i>Equus hydruntinus</i>	PZEH	56.7	16.2	25.2
<i>Equus hydruntinus</i>	PZEH	60.9	15.5	24.2
<i>Cervus elaphus</i>	STCE	3.2	18.2	26.9
<i>Cervus elaphus</i>	STCE	5.2	17.9	27.2
<i>Cervus elaphus</i>	STCE	7.8	18.1	27.6
<i>Cervus elaphus</i>	STCE	10.5	18.6	27.7
<i>Cervus elaphus</i>	STCE	12.5	18.8	28.4
<i>Cervus elaphus</i>	STCE	15.2	19.4	27.7
<i>Equus hydruntinus</i>	STEH	4.5	18.3	27.1
<i>Equus hydruntinus</i>	STEH	12	18.4	27.4
<i>Equus hydruntinus</i>	STEH	15.8	18.6	27.4
<i>Equus hydruntinus</i>	STEH	20.1	18.6	28
<i>Equus hydruntinus</i>	STEH	25.5	19	27.8
<i>Equus hydruntinus</i>	STEH	30	19.1	27.5
<i>Equus hydruntinus</i>	STEH	35.6	18.4	27.4
<i>Equus hydruntinus</i>	STEH	40.9	18.4	27.6
<i>Equus hydruntinus</i>	STEH	45.2	18.7	27.8
<i>Equus hydruntinus</i>	STEH	50	19.2	27.6
<i>Equus hydruntinus</i>	STEH	53.2	19.3	27.4
<i>Equus hydruntinus</i>	STEH	57	18.5	27.3
<i>Equus hydruntinus</i>	VAEH	2.2	19.3	28
<i>Equus hydruntinus</i>	VAEH	4	18.2	26.8
<i>Equus hydruntinus</i>	VAEH	6.6	17.1	26
<i>Equus hydruntinus</i>	VAEH	8.8	16.9	26.2
<i>Equus hydruntinus</i>	VAEH	11	16.8	26.1
<i>Equus hydruntinus</i>	VAEH	12.8	17.8	26.6

<i>Equus hydruntinus</i>	VAEH	15.3	18.5	27.1
<i>Equus hydruntinus</i>	VAEH	18.3	18.8	27.6
<i>Equus hydruntinus</i>	VAEH	21.2	18.8	27.5
<i>Equus hydruntinus</i>	VAEH	23.7	18.7	27.6
<i>Equus hydruntinus</i>	VAEH	25.9	18.7	27.8
<i>Equus hydruntinus</i>	VAEH	28.1	18.7	27.5
<i>Equus hydruntinus</i>	VAEH	29.9	18.8	27.6
<i>Equus hydruntinus</i>	VAEH	32.1	19	27.6
<i>Equus hydruntinus</i>	VAEH	34.7	19.1	27.9
<i>Equus hydruntinus</i>	VAEH	36.5	19.4	27.8
<i>Equus hydruntinus</i>	VAEH	39.4	19.5	28
<i>Equus hydruntinus</i>	VAEH	42	19.4	27.2
<i>Equus hydruntinus</i>	VAEH	44.2	19.1	27.5
<i>Equus hydruntinus</i>	VAEH	46.7	18.9	27.3
<i>Equus hydruntinus</i>	VAEH	49.6	18.6	27.3
<i>Equus hydruntinus</i>	VAEH	51.8	18.2	27
<i>Equus hydruntinus</i>	VAEH	54	17.7	27.2
<i>Equus hydruntinus</i>	VAEH	56.2	17.7	26.7
<i>Equus hydruntinus</i>	VAEH	58.8	17.7	26.7
<i>Equus hydruntinus</i>	VAEH	61.3	17.8	26.9
<i>Equus hydruntinus</i>	VAEH	63.5	17.9	27.1
<i>Equus hydruntinus</i>	VAEH	66.4	18.4	27.2
<i>Equus hydruntinus</i>	VAEH	69	18.3	26.9
<i>Equus hydruntinus</i>	VAEH	71.2	18.6	27.1
<i>Equus hydruntinus</i>	VAEH	73	18.8	26.9
<i>Equus hydruntinus</i>	VAEH	75.2	18.8	26.8
<i>Equus hydruntinus</i>	VAEH	77	18.7	26.8
<i>Equus hydruntinus</i>	VAEH	78.8	18.1	26.9
<i>Equus hydruntinus</i>	VAEH	80.7	17.7	27.1

<i>Equus hydruntinus</i>	VAEH	82.9	17.2	26.6
--------------------------	------	------	------	------

APPENDIX B

U-Pb Methods

Zircon was separated from each sample using density and magnetic methods. The resulting separates were heated in a muffle furnace at 900°C for 60 hours to anneal minor radiation damage and prepare crystals for chemical abrasion. After annealing, individual grains were selected, mounted in epoxy, hand polished using 0.3 µm alumina and imaged by cathodoluminescence (CL).

After imaging, we analyzed 30 – 40 crystals from each sample via laser ablation inductively coupled plasma mass spectrometry (LA-ICPMS) using a ThermoElectron X-Series II quadrupole ICPMS and a New Wave Research UP-213 Nd:YAG UV (213 nm) laser ablation system. We selected single zircon grains for CA-IDTIMS analysis on the basis of LA-ICPMS $^{206}\text{Pb}/^{238}\text{U}$, dates, U content, CL zoning pattern, and visual clarity. Individual crystals were chemically abraded in concentrated hydrofluoric acid at 180°C for 12 hours to remove mineral inclusions and mitigate open system behavior (Mattinson, 2005). Residual crystals were then spiked with the ET535 isotope dilution tracer (Condon et al., 2015; McLean et al., 2015) and processed for chemical abrasion isotope dilution thermal ionization mass spectrometry (CA-IDTIMS; Davydov et al., 2010; Schmitz and Davydov, 2012). Isotope ratios were measured using an IsotopX Phoenix X62 or Isoprobe-T mass spectrometer; U-Pb dates and uncertainties were calculated using the methods of Schmitz and Schoene (2007) and the U decay constants of Jaffey et al. (1971). Errors for calculated weighted means are reported in the form $\pm X(Y)[Z]$ where X is the analytical uncertainty, Y is the combined analytical and tracer (EARTHTIME 535; Condon et al., 2015; McLean et al., 2015) uncertainties, and Z is the combined analytical, tracer, and decay constant uncertainties.

We selected individual grains for CA-ID-TIMS analysis on the basis of LA-ICPMS $^{206}\text{Pb}/^{238}\text{U}$ date, simple CL zoning patterns and in some cases total U content. To minimize uncertainties, we excluded all resultant analyses with a radiogenic to common lead ratio of < 1 .

Locality and Sample Descriptions for Chapter 2

Killik Aike Norte (KAN)

Killik Aike Norte (KAN; $51^{\circ} 34' \text{ S}$, $69^{\circ} 25' \text{ W}$) is a series of exposures along the banks of the Río Gallegos estuary, located ~ 100 km south of Cerro Observatorio along the Atlantic coast. The Santa Cruz Formation is exposed in the walls of a deep canyon that enters the river channel from the north, with continuous exposures along the river itself (Marshall, 1976). Tejedor et al. (2006) illustrated a stratigraphic column and reported an $^{40}\text{Ar}/^{39}\text{Ar}$ age of 16.68 ± 0.05 Ma (recalibrated by Perkins et al., 2012) for a vitric tuff from KAN. However, analysis of a pumice clast within the tephra by gives an $^{40}\text{Ar}/^{39}\text{Ar}$ age of 17.06 ± 0.07 Ma (Perkins et al., 2012). We collected a new sample of the KAN tuff for analysis to address this discrepancy.

KAN-1 – (KAN): CL imaging of zircon from the KAN-1 tuff revealed predominantly equant, oscillatory zoned crystals. A minority of grains exhibited an elongate, prismatic morphology but were otherwise similar to the equant population. CL-dark inherited cores were common and were avoided. Fourteen grains were selected for CA-ID-TIMS analysis on the basis of CL zoning patterns and LA-ICPMS $^{206}\text{Pb}/^{238}\text{U}$ date. Of these, four analyses had a radiogenic to common lead ratio < 1 and were discarded. Of the remaining crystals, six analyses were concordant, of equivalent age, and returned a weighted mean $^{206}\text{Pb}/^{238}\text{U}$ date of $16.996 \pm 0.014(0.017)[0.025]$ Ma (MSWD =

2.51; $n = 6$) which is interpreted as the eruption age of the tuff. One ~ 0.1 Ma older analysis was excluded from the weighted mean calculation and is assumed to represent either an inherited or detrital grain. Four slightly older grains were also excluded and may represent an older period of zircon growth.

Cerro Observatorio (CO) and Cañadón de las Vacas (CV)

Cerro Observatorio (previously known as Monte Observación; $50^{\circ} 36' \text{ S}, 69^{\circ} 05' \text{ W}$) is a series of exposures along the Atlantic coast. Historically Cerro Observatorio has been synonymous with the Cañadón de las Vacas locality (CV; $50^{\circ} 34' \text{ S}, 69^{\circ} 09'$) which is located ~ 6 km NW of the coastal exposures of Cerro Observatorio. In this study we consider Cerro Observatorio to refer only to the coastal exposures and refer to the slightly inland exposures as Cañadón de las Vacas. Together, these localities are the richest and most studied of the Santa Cruz Formation, and have produced thousands of fossils (Bown and Fleagle, 1993; Fleagle et al., 2012; Vizcaíno et al., 2012a). We collected 4 tuffs for analysis from these localities; CV-13, KARG-15-01, Toba Blanca, and CV-10. Several tuffs from Cerro Observatorio and Cañadón de las Vacas were previously analyzed or recalibrated by Perkins et al. (2012). With the exception of the Toba Blanca, which we reanalyze, we choose undated tuffs for analysis.

KARG-15-01 – (CV): CL imaging of zircon from the KARG-15-01 tuff revealed a uniform population of prismatic, oscillatory zoned crystals. A minority of grains contained CL distinct inherited cores and were avoided in all subsequent analyses. Five grains were selected for CA-ID-TIMS analysis on the basis of LA-ICPMS $^{206}\text{Pb}/^{238}\text{U}$ date and CL zoning. These analyses were concordant, of equivalent isotope ratios, and

returned a weighted mean $^{206}\text{Pb}/^{238}\text{U}$ date of $16.850 \pm 0.009(0.013)[0.022]$ Ma (MSWD = 0.43; n = 5) which is interpreted as the eruption age of the tuff.

CV-10 – (CV): CL imaging of zircon from the CV-10 tuff revealed a uniform population of poorly zoned, elongate prismatic crystals. Inherited cores and large inclusions were rare and avoided. Eleven grains were selected for CA-ID-TIMS analysis. Five analyses had a radiogenic to common lead ratio of < 1 and were discarded. Two grains yielded $^{206}\text{Pb}/^{238}\text{U}$ date > 19 Ma and were discarded as inheritance. The remaining four grains are concordant and have equivalent isotope ratios with a weighted mean $^{206}\text{Pb}/^{238}\text{U}$ date of $16.825 \pm 0.030(0.031)[0.036]$ Ma (MSWD = 3.17; n = 4) which is interpreted as the eruption age.

Toba Blanca – (CV): CL imaging of zircon from the Toba Blanca revealed a mixed population of poorly zoned, equant and elongate prismatic crystals. Large inclusions were common and were avoided. Ten grains were selected for CA-ID-TIMS analysis. Five grains had a radiogenic to common lead ratio < 1 and were discarded. An additional grain yielded a $^{206}\text{Pb}/^{238}\text{U}$ date of > 23 Ma and was discarded as inheritance. Of the four remaining grains, three are concordant and have equivalent isotope ratios, with a weighted mean $^{206}\text{Pb}/^{238}\text{U}$ date of $16.868 \pm 0.025(0.026)[0.032]$ Ma (MSWD = 1.82; n = 3) which is interpreted as the eruption age. A single grain with a $^{206}\text{Pb}/^{238}\text{U}$ date ~ 0.15 Ma older than the weighted mean was also excluded as detrital or inherited.

CV-13 – (CO): CL imaging of zircon from the CV-13 tuff revealed a uniform population of elongate, prismatic, oscillatory zoned crystals. CL dark inherited cores were common and were avoided. Sixteen grains were selected for CA-ID-TIMS analysis. Two analyses had a radiogenic to common lead ratio < 1 and were discarded. Four

additional grains with $^{206}\text{Pb}/^{238}\text{U}$ dates > 19 Ma were also discarded as inheritance. Five of the nine remaining grains yielded concordant and equivalent isotope ratios with a weighted mean $^{206}\text{Pb}/^{238}\text{U}$ date of $17.62 \pm 0.015(0.017)[0.026]$ Ma (MSWD = 1.44; n = 5), which is interpreted as the eruption age of the tuff. Four slightly older grains were excluded from the weighted mean calculation and are assumed to represent either detrital or inherited grains.

Cabo Buen Tiempo (CBT)

At Cabo Buen Tiempo (CBT; $51^{\circ} 34' \text{ S}$, $68^{\circ} 57' \text{ W}$), Santa Cruz Formation strata (including fossiliferous levels and numerous tuffs) are exposed on a tidal platform at low tide and in an adjacent sea cliff. Perkins et al. (2012) correlates several CBT tuffs to other localities. The only direct date of a CBT tuff is imprecise (< 17.73 Ma; Perkins et al., 2012). We collected a sample of the lowest exposed tuff (~ 41 m above sea level) at Cabo Buen Tiempo (KARG-15-08). Based on the stratigraphic scheme of Perkins et al. (2012), this is likely the KAN-2 tuff.

KAN-2 (CBT): CL imaging of zircon from the KARG-15-08 tuff revealed a mixed population of elongate and equant, prismatic, oscillatory zoned crystals. Inherited cores were uncommon and avoided. Nineteen grains were selected for CA-ID-TIMS analysis. Six analyses had a radiogenic to common lead ratio < 1 and were rejected. An additional grain with a $^{206}\text{Pb}/^{238}\text{U}$ date of > 19 Ma was also rejected as probable inheritance. Of the remaining twelve grains the six youngest grains are concordant and of equivalent isotope ratio, with a weighted mean $^{206}\text{Pb}/^{238}\text{U}$ date of $16.949 \pm 0.022(0.023) [0.030]$ Ma (MSWD = 0.68; n = 6), which is interpreted as the eruption age. Four slightly older grains were excluded from the weighted mean calculation and are assumed to represent

either inheritance or an earlier period of zircon growth. Two other grains with high $^{206}\text{Pb}/^{238}\text{U}$ date uncertainties ($2\sigma > 0.15$ Ma) were also excluded.

Rincón del Buque 3

Located ~ 10 km S-SE of Cerro Observatorio and Cañadón de las Vacas, Rincón del Buque 3 (RB3; 50° 39' S, 69° 12' W) is a large half-moon shaped amphitheater (Marshall, 1976; Raigemborn et al., 2015; Vizcaíno et al., 2012a) exposing the Santa Cruz formation as a series of benches and cliffs. We collected a single tuff for analysis from this locality (KARG-15-09).

KARG-15-09 (RB3): CL imaging of zircon from the KARG-15-09 tuff revealed a mixture of equant and elongate, prismatic, oscillatory zoned crystals. Inherited cores and large inclusions were common and avoided. Seventeen grains were selected for CA-ID-TIMS analysis. Eleven analyses had a radiogenic to common lead ratio of < 1 and were discarded. One analysis yielded a Cretaceous date of ~ 106 Ma and was discarded. Of the remaining five grains, two grains are concordant, of equivalent isotope ratio with a weighted mean $^{206}\text{Pb}/^{238}\text{U}$ date of $17.006 \pm 0.034(0.035)$ [0.039] Ma (MSWD = 1.83; n = 2) which is interpreted as the eruption age. A single grain with a high (> 0.1 Ma) uncertainty was excluded from the weighted mean calculation. Two ~0.3 - 0.4 Ma older grains were also excluded from the weighted mean calculation and are assumed to be detrital or inherited.

Puesto Estancia La Costa (PLC)

Puesto Estancia La Costa (PLC; 51° 11' S, 69° 05' W) is the most productive fossil locality of the Santa Cruz formation (Fleagle et al., 2012; Vizcaíno et al., 2012a), with the Santa Cruz Formation exposures partial below sea level except at low tide,

leading to constant tidal excavation of new material. The locality has produced numerous complete skeletons and some of the southernmost examples of primate fossils (Vizcaíno et al., 2010; Vizcaíno et al., 2012a). We collected a single tuff (KARG-15-12) exposed near the top of the section at Puesto Estancia La Costa.

KARG-15-12 (PLC): CL imaging of zircon from the KARG-15-12 tuff revealed a mixed population of equant to elongate, prismatic, oscillatory zoned crystals. Inherited cores and large inclusions are uncommon and were avoided. Eight grains were selected for CA-ID-TIMS analysis. One grain had a radiogenic to common lead ratio of < 1 and was discarded. Of the remaining eight grains, seven are concordant and have equivalent isotope ratios, with a weighed $^{206}\text{Pb}/^{238}\text{U}$ date of $16.783 \pm 0.047(0.048)$ [0.032] Ma (MSWD = 0.72; n = 6). An eighth grain with a $^{206}\text{Pb}/^{238}\text{U}$ date > 18 Ma was excluded from the weighted mean calculation as inherited or detrital.

Zircon LA-ICPMS Data

Table B1. Zircon LA-ICPMS concentrations. Ablation using a 213 nm wavelength laser, spot size of 25 microns, repetition rate of 10 Hz, and fluence of ~5 J/cm². Trace element concentrations in ppm, calculated using the mean count rate method, internal standardization to ²⁹Si, and calibration to NIST 610 and 612 glass standards

Analysis	P	Ti	Y	Nb	La	Ce	Pr	Nd	Sm	Eu	Gd	Tb	Dy	Ho	Er	Tm	Yb	Lu	Hf	Ta	Th	U
KARG-15-01																						
51	263	5.71	766	1.53		15.42	0.03	0.74	1.81	0.88	14.4	5.12	68.26	25.43	123	32.55	374	50.24	8036	0.83	161	172
52	536	5.12	2187	7.25		25.84	0.04	0.83	3.97	1.23	27.6	12.55	173.54	74.61	352	97.61	1127	151.65	8964	2.16	276	425
53	777	7.29	3305	5.06	0.01	37.44	0.22	6.04	13.86	5.34	68.9	24.34	304.68	114.66	507	127.89	1384	176.30	7574	1.55	706	540
54	212	6.55	816	0.44		8.41	0.08	1.71	3.88	1.71	21.3	6.56	76.73	29.68	127	33.26	362	45.68	7454	0.32	67	62
55	494	8.24	2838	2.43	0.03	19.65	0.81	14.59	24.98	8.68	86.9	26.56	279.77	94.10	407	106.49	1214	162.49	7017	0.83	531	343
56	266	3.74	904	1.22		9.26	0.05	0.84	3.42	0.77	17.8	6.65	79.14	31.05	140	39.17	439	58.75	8518	0.82	96	130
57	247	2.75	994	3.76		19.26	0.02	0.88	2.09	0.37	14.6	5.61	83.68	34.79	157	46.20	535	68.10	9631	2.31	266	471
58	289	9.39	1824	1.46	0.07	17.49	0.31	4.84	9.38	4.57	51.9	16.92	192.73	69.80	280	68.50	732	91.44	7428	0.62	166	122
59	768	6.17	2928	11.13		23.49	0.05	1.41	4.39	0.63	34.4	16.61	226.58	98.59	465	127.12	1472	199.14	9631	3.81	352	677
60	300	4.05	1170	1.21		10.71	0.07	2.60	4.32	1.49	26.2	8.05	106.71	40.35	189	48.58	558	74.70	8935	0.63	124	156
61	259	2.83	1406	2.17	0.08	17.64	0.05	1.39	2.97	0.60	24.0	8.83	120.94	47.65	217	55.84	560	92.80	12213	1.13	361	298
62	850	4.19	3477	9.45		24.19	0.07	1.53	4.13	0.90	42.9	18.72	267.92	112.90	550	138.95	1448	236.17	12043	3.91	496	668
63	486	3.08	1730	1.70		12.17	0.01	1.12	4.36	1.04	28.0	10.42	145.05	58.74	275	70.03	727	120.22	11738	0.88	228	258
64	536	5.93	2708	3.10		26.22	0.08	3.57	7.13	2.54	47.1	17.82	220.96	91.63	422	103.76	1054	177.51	9659	1.30	728	406
65	342	7.14	2324	1.71	0.02	19.74	0.19	5.54	9.03	3.20	59.4	18.51	218.55	80.05	357	85.82	852	130.50	9616	0.64	237	165
66	440	3.73	1698	5.17		20.98	0.06	1.30	3.09	0.51	25.3	9.10	136.97	56.48	267	69.71	746	114.54	11441	2.48	503	534
67	784	3.22	2791	6.67		19.10	0.02	1.06	5.27	0.70	36.2	16.46	227.94	94.42	437	108.04	1126	170.61	12107	3.15	715	825
68	742	2.04	2110	4.20	0.03	18.33	0.04	1.01	3.14	0.45	26.3	11.27	159.76	69.20	341	90.93	991	156.94	11166	2.10	418	617
69	544	3.92	2151	2.17	0.04	21.28	0.18	3.18	8.12	2.79	37.4	14.46	183.23	70.58	331	84.51	887	133.80	9911	1.06	364	290
70	604	5.96	2428	5.46		27.94	0.06	1.36	4.52	1.73	38.9	15.04	204.63	82.97	391	100.62	1076	164.24	9311	2.00	327	368
71	3866	6.36	2492	6.57	63.61	142.38	16.63	86.41	23.99	1.14	55.0	18.29	217.89	84.75	384	98.27	1014	148.28	11229	2.78	733	832
73	584	4.84	2237	2.88	0.12	17.32	0.12	3.03	7.16	1.71	40.6	14.76	194.19	74.46	353	89.91	976	138.73	9902	1.32	286	334
74	401	4.51	1255	1.79		10.09	0.06	1.06	3.37	1.14	20.3	7.98	103.88	42.23	202	54.03	590	87.32	9470	1.01	140	191
75	391	9.30	2335	3.20		26.20	0.18	2.37	8.01	2.84	45.3	16.06	210.88	80.47	363	93.98	988	140.37	8033	1.31	318	263
76	484	6.00	1688	1.53	1.38	19.58	0.48	4.75	8.18	3.24	42.1	13.68	165.09	59.76	267	66.07	748	98.29	7422	0.61	271	244
77	455	6.89	527	1.22	2.13	11.69	0.59	2.58	1.19	0.52	8.4	3.01	43.32	17.06	80	23.92	299	42.77	9085	0.81	61	94
79	1062	3.05	2956	8.64		14.70	0.04	0.79	5.85	0.75	35.1	15.80	231.67	98.38	475	131.58	1540	191.43	9281	2.97	290	628
80	846	4.22	2194	2.43	0.07	16.97	0.10	1.98	5.65	1.64	35.9	13.65	187.62	72.65	338	93.55	1064	137.72	8249	1.18	255	367
81	818	4.02	2335	3.79	0.12	16.28	0.04	0.81	4.12	0.98	34.8	13.30	194.54	78.38	364	100.54	1128	147.38	9489	1.52	243	435

82	911	3.64	2397	4.65	0.07	10.78	0.05	0.86	3.70	0.52	27.4	12.82	190.63	81.48	392	107.80	1214	159.94	9567	1.93	227	489
83	880	4.76	3039	3.71	0.04	21.83	0.11	2.95	8.61	2.60	47.4	19.49	249.12	102.47	472	123.30	1321	195.62	9162	1.51	485	468
84	618	8.96	4953	3.94	0.10	57.73	0.99	18.63	36.10	11.59	148.3	44.41	510.32	175.52	715	166.10	1588	229.85	8298	1.09	941	383
85	232	8.39	826	1.59		18.85	0.67	10.25	14.14	5.87	39.6	9.09	86.24	27.29	114	27.58	282	44.64	10968	0.57	187	188
86	818	3.05	3179	9.51		15.01	0.01	0.81	3.81	0.40	34.1	15.80	234.83	100.39	504	130.54	1366	229.02	13712	3.72	306	557
87	687	3.61	2215	2.00		12.21	0.04	1.00	3.74	1.07	31.6	11.97	169.21	71.62	347	85.68	891	152.04	11359	1.10	223	280
88	502	7.27	2122	2.29	0.08	23.38	0.07	2.38	4.74	2.21	35.0	13.46	173.60	71.66	332	80.77	838	142.22	8887	0.78	323	218
89	529	4.40	1685	1.81		11.95	0.08	1.53	4.27	0.90	27.5	9.47	137.53	55.66	261	69.52	717	113.42	10727	0.90	208	245
90	1014	3.95	3213	7.33	0.55	24.94	0.09	3.45	6.99	1.07	44.6	18.72	253.59	106.42	520	130.58	1389	217.31	11107	2.72	591	687

KANI

132	283	1.90	1126	3.77		15.37		0.62	2.80	0.35	16.8	7.79	93.55	38.83	187	52.83	603	79.99	9099	2.49	402	607
133	199	7.91	618	0.52		4.72	0.05	0.72	1.79	0.76	8.5	3.09	46.81	20.64	99	29.75	383	51.37	7475	0.29	19	35
134	145	3.85	451	0.48		6.83	0.05	1.16	2.48	0.90	9.7	3.18	42.64	16.10	79	22.19	269	42.11	9198	0.30	85	118
135	363	12.39	3024	2.50	0.05	22.12	0.30	7.70	14.84	4.90	75.8	25.88	302.02	111.36	468	119.18	1283	156.77	7729	1.17	396	328
136	205	4.25	702	1.25		7.41	0.02	0.67	1.94	1.17	12.7	4.53	58.26	22.66	105	30.06	359	50.41	9374	0.66	101	249
137	353	1.59	961	1.99		10.10		0.56	2.22	0.19	11.6	5.54	79.31	33.14	163	45.09	546	73.50	8830	1.24	167	339
138	222	4.97	606	1.33		6.91	0.03	0.60	0.95	0.59	7.6	3.47	44.76	19.87	100	28.88	367	57.86	8331	0.60	80	128
139	265	4.84	841	2.06	0.03	12.23	0.09	1.58	2.62	1.39	16.1	5.70	76.20	27.34	138	36.99	466	65.80	9070	0.95	159	227
140	308	2.30	1511	5.61		28.51	0.02	0.72	3.28	0.58	22.9	9.53	130.82	52.31	241	67.56	767	98.73	9774	3.25	688	855
141	307	1.97	1349	6.07		21.96		0.84	2.94	0.30	17.8	7.67	110.48	45.19	225	61.07	733	98.14	9488	3.07	482	674
142	220	7.74	717	0.91		5.41	0.01	0.49	1.65	0.56	11.4	3.69	56.23	23.49	121	36.39	455	68.66	7759	0.55	33	66
143	227	12.38	578	1.39		9.48	0.06	0.40	1.75	0.48	12.6	4.60	53.49	19.46	91	23.82	256	34.22	9146	1.07	99	106
144	258	12.29	756	1.01		6.83	0.01	1.01	2.84	0.78	15.4	5.75	72.59	27.38	129	33.85	387	54.10	8148	0.58	37	59
145	205	1.83	1247	1.67		14.01	0.07	0.87	4.15	0.38	23.0	7.73	103.12	43.39	207	54.31	597	83.32	10169	1.11	242	327
146	305	10.79	1672	2.40	0.08	14.99	0.07	0.92	3.63	1.88	22.7	9.35	137.22	54.24	263	77.60	935	127.55	8108	0.69	141	203
147	358	3.39	1432	2.11	0.67	15.43	0.45	4.42	7.51	2.44	30.0	10.15	126.45	48.11	223	63.31	766	102.49	7248	0.95	345	440
148	293	12.56	1680	1.80		9.03	0.09	2.74	5.51	1.34	34.5	13.23	162.89	61.84	274	69.05	736	87.92	7450	0.76	137	196
149	256	10.41	814	1.16		6.18	0.01	1.05	2.20	0.43	14.8	6.06	72.61	29.39	129	35.57	402	47.93	8054	0.90	63	119
150	173	8.39	1077	0.50		5.62	0.05	1.27	3.81	1.37	21.2	7.46	96.16	37.00	172	47.96	578	76.37	7833	0.28	35	52
151	257	1.76	1509	1.82		16.76	0.03	1.86	5.07	0.62	27.7	10.96	135.84	53.04	245	65.31	768	94.81	8697	1.43	337	469
152	319	7.58	1803	1.53		11.17	0.31	5.41	12.53	4.54	53.6	17.06	190.18	64.49	284	72.74	836	102.18	6669	0.63	129	122
153	205	5.11	552	1.60	0.00	7.42		0.68	1.47	0.61	5.8	2.97	43.52	18.37	91	27.69	376	52.59	7563	0.55	66	124
154	531	6.51	2149	6.35	0.56	32.81	0.19	3.01	7.66	2.44	43.2	16.05	199.95	77.61	353	95.81	1127	139.68	6841	2.38	1299	1106
155	245	18.78	1004	1.71		9.39	0.05	1.31	2.88	1.27	17.3	7.02	91.65	34.04	156	43.23	509	64.47	7359	0.75	81	105
156	177	4.44	420	1.48		8.91		0.41	1.08	0.81	7.5	2.54	33.96	13.85	66	19.94	261	38.10	7567	0.87	128	235
157	259	2.27	966	3.72		16.56		0.54	1.99	0.36	13.8	5.48	78.36	32.09	159	45.45	521	66.80	8590	1.72	360	526

158	237	2.58	780	1.03		8.75	0.03	0.93	2.16	0.59	13.2	5.22	65.74	26.56	121	34.22	432	56.65	7978	0.54	129	181
159	276	8.08	752	0.82		5.12	0.16	1.49	3.34	1.32	18.1	5.36	73.18	24.88	116	32.53	389	51.00	7307	0.42	42	61
160	260	3.74	1026	4.29		17.05	0.05	0.84	2.06	1.29	17.7	6.25	88.86	35.65	159	47.40	618	74.31	9185	1.76	195	367
161	256	7.92	984	1.13	0.05	7.12	0.08	2.47	5.71	1.90	25.6	8.08	102.55	34.51	150	42.72	501	61.42	7776	0.49	74	79
162	238	6.39	683	1.80		6.42	0.07	0.44	3.30	0.88	12.6	4.54	59.31	23.15	109	29.78	363	47.80	8138	0.98	48	92
163	243	8.50	788	1.11		6.68	0.02	1.75	4.27	1.51	15.5	5.96	73.24	27.21	121	33.68	392	52.38	7732	0.49	47	62
164	198	10.04	771	0.90		6.83	0.05	1.60	3.48	1.29	17.1	5.51	74.06	26.95	117	30.85	332	42.43	7547	0.47	25	38
165	350	3.27	1280	2.06	0.03	13.77	0.08	2.22	5.08	1.19	25.0	8.48	115.32	43.93	203	55.08	647	88.26	8452	0.99	348	333
166	668	3.33	2650	9.13	0.44	45.06	0.16	2.03	6.46	0.69	42.3	16.16	231.17	93.36	431	117.42	1285	177.20	9724	3.67	907	1002
167	333	12.07	1871	2.43		13.60	0.04	2.13	5.97	2.81	40.0	14.35	176.77	65.18	291	73.94	814	111.40	7718	0.77	170	137
168	258	3.03	1066	3.41		14.24	0.01	0.49	1.73	0.49	14.7	6.12	84.86	35.87	180	49.83	578	84.74	10027	1.67	254	357
169	226	10.34	724	1.55		5.72	0.04	0.32	2.10	0.67	9.4	4.46	58.31	24.14	117	32.88	366	57.96	9266	0.59	42	59
170	244	4.28	870	1.90		14.20	0.10	1.56	2.42	1.03	14.7	5.25	69.77	28.60	139	39.26	456	76.62	11293	1.09	255	338

CV-13

171	800	12.45	7863	17.02	0.11	145.51	0.85	17.89	42.00	14.58	228.8	76.91	873.47	295.21	1166	265.59	2627	320.99	8856	3.40	3667	1417
172	126	4.11	212	0.21		3.12		0.18	0.54	0.32	2.9	1.05	16.47	6.78	34	11.05	130	21.47	9942	0.21	26	43
173	297	4.28	828	0.76	0.07	5.89	0.06	1.02	3.69	0.81	13.1	5.57	76.32	28.07	135	37.82	407	55.67	9316	0.40	47	72
174	213	1.78	659	2.75		6.47		0.22	1.04	0.41	9.2	3.88	56.79	22.90	113	31.74	385	49.97	10721	2.00	73	221
175	260	8.25	782	1.13		7.99	0.09	0.48	2.10	0.88	12.1	4.44	60.54	26.44	130	37.55	461	68.53	7898	0.48	49	60
176	337	4.61	1443	9.03		10.33	0.03	0.78	3.58	0.67	21.3	9.14	126.77	52.33	245	65.76	740	98.34	10419	4.01	249	677
177	356	6.40	1272	4.00	0.24	12.16	0.08	0.94	2.85	1.21	20.0	7.63	110.32	44.32	212	58.94	691	89.76	9806	1.80	199	386
178	216	7.58	634	0.87		6.44	0.07	1.70	3.12	1.13	14.3	4.88	62.30	22.50	98	26.82	303	42.20	8582	0.48	83	107
179	377	12.37	1765	1.89		17.48	0.15	2.17	4.80	2.57	28.9	11.49	156.99	61.17	284	81.51	961	130.71	7366	0.78	171	182
180	276	3.18	1241	2.17		11.00	0.07	1.91	5.15	1.35	28.2	9.26	116.56	44.51	196	53.85	619	78.81	9639	1.62	206	362
181	194	5.57	912	0.59		4.80	0.04	1.41	3.08	1.09	18.0	6.12	79.65	30.15	141	39.81	483	64.58	8056	0.31	60	87
182	129	5.14	452	0.40		4.80	0.01	1.49	2.44	1.12	11.0	3.62	39.69	14.98	70	20.89	268	36.80	8074	0.06	30	35
183	177	10.76	1240	0.50		5.99	0.13	2.54	5.57	1.29	30.6	10.80	128.27	48.14	189	46.64	504	60.28	7820	0.42	118	137
184	267	10.15	841	1.60		11.05	0.05	1.07	3.64	0.62	16.8	5.77	82.09	29.81	135	35.09	409	47.91	8291	0.82	109	156
185	161	5.42	343	0.64		9.58	0.02	0.54	1.32	0.37	6.2	2.35	27.64	11.01	57	16.50	218	29.36	9184	0.69	90	164
186	166	6.71	496	0.49	0.03	5.47	0.10	1.53	1.68	0.87	9.9	3.07	38.85	15.75	79	24.01	322	45.02	7328	0.36	35	45
187	551	5.95	3073	6.90		39.14	0.16	3.98	9.70	3.64	59.9	23.15	291.11	111.34	483	124.97	1357	171.91	9489	1.88	806	669
188	399	3.48	1304	2.54	0.05	8.62	0.10	1.59	5.38	1.03	28.7	8.94	119.47	46.88	207	56.63	640	78.21	10075	1.45	136	333
189	208	3.98	548	1.03	0.00	5.80	0.10	0.62	1.29	0.92	9.5	3.65	44.67	18.00	96	26.57	347	47.69	9142	0.60	120	232
190	342	4.99	2169	4.71		13.95	0.12	2.58	7.43	1.18	49.1	17.95	225.53	85.83	357	84.23	895	103.94	7984	2.10	487	575
191	1013	11.98	7154	17.58		71.71	0.49	12.11	29.98	9.84	171.2	59.32	731.32	260.10	1080	267.06	2859	342.38	7182	3.54	2120	1573
192	205	3.20	794	3.68		10.97	0.03	0.53	1.60	0.54	10.2	5.06	64.07	25.39	132	37.82	470	63.58	9637	2.05	133	300

193	301	4.95	1285	4.70		9.43	0.04	0.99	3.38	0.65	18.0	6.71	100.09	42.44	220	63.57	762	104.97	8244	1.57	107	221
194	272	2.68	1068	6.42		15.74	0.03	0.70	1.86	0.80	16.3	6.74	92.48	37.19	179	50.30	576	74.58	10030	3.44	303	590
195	247	6.93	657	2.72	0.10	5.06	0.05	0.90	2.28	0.71	10.2	3.87	52.47	21.58	106	34.12	451	66.13	9728	1.69	109	515
196	295	7.34	955	2.96	0.67	14.04	0.32	3.20	5.46	1.55	22.3	7.18	85.72	32.23	153	43.74	516	69.12	9296	1.48	245	402
197	357	4.35	1827	7.44		19.80	0.02	1.93	6.07	1.64	33.3	12.48	161.11	64.09	301	78.64	907	122.66	10617	3.40	379	525
198	252	3.92	925	3.81		14.84	0.07	0.75	1.85	0.73	12.4	4.94	76.31	30.64	149	42.91	523	80.35	11003	2.41	234	393
199	355	3.82	1474	5.73		13.63	0.03	0.92	2.03	0.85	19.5	8.56	122.81	51.06	246	68.43	777	116.78	11751	3.27	238	480
200	319	3.47	1248	5.84		16.32	0.05	0.91	3.20	0.91	19.6	8.19	102.76	41.57	207	55.88	623	91.60	11207	2.83	344	521

KARG-15-08

201	248	5.33	736	2.05		6.07	0.00	0.48	1.79	0.65	12.8	4.67	65.47	25.08	124	33.76	386	54.79	9403	1.05	43	108
202	261	18.41	1125	1.03	0.15	9.37	0.19	4.39	5.80	2.73	27.1	9.71	113.40	40.89	174	45.83	508	71.35	7905	0.70	75	75
203	329	1.83	1406	5.37		29.42	0.01	1.07	3.03	0.40	22.5	9.14	124.79	47.86	227	64.59	743	98.19	10200	3.05	475	672
204	202	9.94	1154	0.66		8.72	0.16	4.05	8.72	3.01	38.0	11.44	134.26	43.58	175	40.05	440	52.61	7617	0.40	42	43
205	597	10.31	1558	2.91	1.71	18.78	0.48	3.95	4.35	1.10	26.4	9.40	135.02	55.10	257	69.12	798	105.98	9238	1.14	128	174
206	257	3.81	1118	4.10	0.03	14.82	0.03	1.25	2.17	0.30	14.2	5.75	87.76	37.86	190	53.34	633	91.34	10079	2.57	245	427
207	283	3.24	1285	4.47		17.29	0.01	0.94	2.70	0.35	18.7	6.82	98.89	42.81	215	60.97	725	109.48	9471	2.65	267	442
208	189	5.94	748	2.59		13.92	0.04	1.59	3.21	1.96	19.1	6.64	72.40	24.69	117	29.76	347	49.19	9604	1.19	173	161
209	247	3.37	979	1.64		10.19	0.04	0.68	3.09	1.42	21.5	6.23	80.70	32.77	154	40.92	461	83.41	12545	0.97	149	264
210	232	14.21	1566	1.11	0.21	6.36	0.13	2.34	4.47	1.65	30.3	11.95	146.80	56.59	248	59.15	591	92.62	10702	0.48	46	47
212	269	2.71	1290	4.08		21.70	0.03	1.25	3.12	0.43	18.3	7.68	104.61	43.16	212	55.89	597	96.51	12054	2.52	466	531
213	192	9.51	527	0.64		4.72	0.04	0.67	2.53	0.64	12.0	4.57	50.10	18.52	83	20.57	206	32.29	9466	0.31	14	21
214	282	7.85	1307	1.43		11.63	0.08	1.09	3.72	1.16	24.5	8.88	116.84	45.57	216	57.52	629	84.19	9327	0.81	151	149
215	275	5.49	918	0.92		7.95	0.01	0.82	2.70	1.10	18.6	7.14	89.09	33.56	140	36.57	390	54.33	9177	0.29	50	65
216	353	5.11	1058	3.39		15.08	0.07	0.78	2.54	0.97	15.2	6.11	86.28	34.53	178	50.23	613	90.06	12014	1.60	219	473
217	205	3.11	462	0.68	0.01	6.58	0.03	0.82	2.48	1.27	12.5	3.64	45.12	16.76	70	19.62	231	34.78	9206	0.37	32	61
218	242	8.52	1048	2.15		8.85	0.05	1.32	4.15	1.37	17.5	6.59	90.16	36.72	177	49.58	562	81.48	8326	0.91	65	100
219	271	10.80	1224	2.63	0.03	9.86	0.11	1.22	3.04	1.05	20.9	7.65	104.26	42.72	199	56.02	648	92.49	8072	1.10	83	114
220	179	7.00	348	0.53		4.30		0.22	1.08	0.34	6.0	2.30	29.19	12.04	56	16.39	205	31.81	8547	0.29	41	65
222	285	8.60	1710	1.63		11.75	0.30	4.97	10.11	4.39	47.0	15.67	179.88	62.18	263	68.40	755	98.59	7746	0.62	129	113
225	291	8.82	1182	1.25		7.34	0.06	2.29	4.15	1.46	21.2	8.05	106.34	40.03	195	51.42	570	91.27	9365	0.47	78	83
226	276	8.38	1726	0.89		5.99	0.13	3.05	6.94	2.47	41.0	14.70	180.31	66.44	280	66.13	644	94.13	9635	0.68	52	52
228	354	7.37	2245	1.96	0.26	18.70	0.34	6.68	11.64	3.11	50.4	18.71	210.16	76.40	352	86.95	921	145.30	11691	0.83	345	232
229	309	9.85	1315	0.69		6.04	0.04	1.44	5.63	1.16	28.1	10.54	130.38	48.15	206	47.06	459	67.69	11788	0.66	91	94
230	431	6.40	2839	2.15		25.16	0.34	7.12	15.45	3.89	70.8	23.46	265.42	99.82	448	110.70	1156	197.87	12104	0.94	738	406
231	246	3.30	1037	2.17	0.17	3.45	0.18	3.00	4.43	0.92	29.0	8.45	96.08	33.57	148	40.91	433	75.69	12479	1.25	166	394
232	230	5.72	947	1.95		8.28	0.01	0.91	2.41	1.20	15.4	6.08	77.49	31.04	152	38.65	422	76.77	12122	0.86	79	104

233	152	7.29	574	1.01		5.92		0.87	2.24	0.60	10.4	3.73	45.35	18.43	89	23.44	262	47.37	11234	0.46	31	46
234	327	7.11	3097	2.27		24.42	0.29	7.06	14.73	3.58	67.8	24.40	270.24	103.46	467	114.81	1209	211.69	12027	0.89	642	353
235	208	11.91	1075	1.37		8.60	0.04	1.28	4.14	1.11	19.6	6.34	87.12	36.37	169	41.33	419	73.95	9646	0.66	41	49
236	256	9.15	2017	1.09		6.71	0.08	2.66	6.55	1.95	42.1	15.42	193.41	73.12	327	75.88	718	118.09	10403	0.47	58	54
237	262	3.05	1190	3.23		16.75	0.04	0.41	2.48	0.17	14.4	6.57	94.38	40.85	199	53.21	564	99.76	12306	1.95	318	389
238	586	4.66	2250	4.39	1.19	13.38	0.46	4.50	4.63	1.01	34.5	13.83	185.57	75.11	374	99.78	1022	173.94	12858	2.94	361	548
239	195	3.86	1026	2.17	0.07	4.63	0.07	1.66	5.40	1.01	27.5	9.46	103.80	33.87	138	32.24	323	51.83	13376	1.49	216	536
240	1586	15.20	1446	1.20	15.67	41.24	5.97	40.31	12.47	1.48	35.6	11.10	136.12	51.42	234	55.04	541	82.99	10446	0.66	114	133
241	725	8.97	1010	2.16	3.01	15.40	0.92	5.65	4.59	1.15	18.0	6.38	78.43	34.46	164	43.95	491	80.41	10369	0.93	64	86
242	315	12.79	1350	1.41	0.05	12.84	0.05	2.00	5.03	0.58	28.8	10.30	120.24	48.68	212	50.66	506	74.53	11494	0.98	291	249

KARG-15-09

243	308	4.55	1530	1.60	0.59	3.82	0.45	3.78	5.77	0.21	38.4	14.12	166.74	60.59	252	60.20	640	71.58	7896	0.97	135	235
244	229	4.72	1022	0.64		6.57	0.11	2.02	4.61	1.13	21.0	8.20	99.07	36.82	170	44.79	522	67.42	7811	0.36	76	100
245	410	4.31	1259	4.33	1.75	19.86	0.55	5.66	4.04	0.93	25.4	9.67	121.67	47.48	211	55.21	589	69.53	8306	1.73	132	212
246	328	10.88	2263	15.97	0.17	68.21	0.14	3.08	9.93	4.67	55.3	18.26	219.63	79.89	361	96.65	1100	137.78	8309	4.36	1201	1046
247	190	5.21	477	1.26		6.29	0.05	0.48	1.47	0.69	6.7	2.78	37.32	15.65	83	24.80	320	49.10	7745	0.62	75	136
248	229	5.97	865	1.60		7.69	0.02	0.67	2.40	0.38	11.9	4.97	71.21	28.02	141	41.77	511	67.96	8870	1.07	95	183
249	257	7.48	823	0.47		7.09	0.03	1.01	1.61	0.69	14.4	5.28	73.41	30.21	137	37.92	432	56.97	7857	0.26	40	56
250	422	7.13	2401	9.90	0.77	21.74	0.23	2.85	5.18	2.03	36.8	13.43	182.12	77.99	378	104.33	1090	199.81	11030	3.13	230	274
251	264	6.78	2374	2.01		14.76	0.11	3.26	7.47	2.05	55.8	18.41	228.43	86.41	386	90.86	872	146.46	12127	0.72	298	189
252	475	8.19	2737	2.78		12.92	0.10	3.31	9.53	3.03	53.8	18.82	239.35	93.85	430	105.66	1058	184.26	9920	1.22	375	375
253	235	14.10	919	1.01	0.03	11.20	0.03	0.82	2.33	0.75	17.1	6.08	83.41	33.58	148	35.51	342	57.06	11690	0.49	122	98
254	232	7.36	1460	0.62		8.12	0.16	3.67	5.87	1.24	36.4	10.95	134.90	51.87	224	55.15	535	91.14	11474	0.50	120	90
255	187	5.23	1293	0.80		9.09	0.09	2.78	4.79	1.15	29.4	8.78	111.31	42.80	205	51.04	489	92.33	12402	0.34	168	125
256	252	7.63	1148	2.42		13.58	0.03	1.28	2.78	1.00	21.1	8.47	105.43	40.71	187	46.64	460	72.35	11473	0.98	124	125
257	249	7.28	1279	1.80		5.52	0.08	2.16	3.91	1.85	24.2	8.85	104.96	42.49	196	50.32	537	96.16	9208	0.79	167	217
258	287	5.94	969	2.14	0.37	4.66	0.13	1.51	3.55	0.41	16.5	6.48	80.31	31.44	151	39.31	422	69.91	11509	1.37	124	234
259	210	8.05	1568	0.41		7.83	0.09	2.69	6.29	1.60	37.5	12.84	148.61	54.86	248	59.20	584	91.30	11308	0.32	101	81
260	2261	4.56	1594	2.02	16.04	40.30	3.73	15.38	6.22	2.17	27.4	9.97	129.22	54.22	256	70.08	759	138.02	11116	1.00	373	330
261	303	9.18	1704	0.82		9.20	0.10	2.35	6.47	1.77	37.9	12.88	159.42	60.06	268	63.64	636	98.18	10528	0.63	111	90
262	338	8.61	1254	1.13		4.23	0.14	2.44	6.04	0.48	33.6	10.76	129.54	47.25	207	46.55	481	67.53	12851	0.74	106	177
263	359	11.23	1455	1.67		4.46	0.14	2.62	5.70	1.68	27.7	10.05	137.56	52.52	233	58.77	622	94.58	10394	0.94	87	114
264	305	6.58	1912	3.13		21.55	0.09	1.86	4.12	2.24	24.9	10.65	148.69	61.77	314	87.83	1011	178.53	10195	1.31	494	519
265	216	2.95	844	1.63		14.14	0.05	1.08	1.80	0.92	13.3	4.84	62.31	26.77	140	38.69	468	85.06	11834	0.75	201	290
266	183	4.16	1001	1.94	0.02	13.74	0.05	1.32	3.06	1.41	17.7	5.94	82.50	33.24	164	46.82	560	93.14	11623	1.06	242	330
267	311	9.51	1444	2.79		9.09	0.08	1.26	2.39	1.60	19.1	8.68	117.19	47.20	228	64.19	729	123.82	9101	1.11	167	197

268	442	8.98	1455	3.07	2.29	26.19	0.68	3.84	6.55	1.49	30.6	10.70	129.90	50.47	238	61.31	680	95.18	11028	1.29	901	458
269	357	7.27	2327	1.57	1.00	20.76	0.53	5.84	12.75	2.87	61.4	18.81	231.83	82.95	353	90.40	934	123.24	10979	0.90	352	229
270	220	7.37	1556	3.27	0.03	10.22	0.12	2.86	9.66	1.49	43.9	14.37	174.46	57.25	242	56.82	548	70.64	10152	1.10	143	246
271	233	8.48	834	0.56		6.41	0.05	0.91	2.71	0.74	17.1	6.43	79.21	30.82	134	34.44	371	51.46	9298	0.38	48	59
272	167	3.42	628	1.77	0.02	11.23	0.04	0.95	1.64	0.86	10.3	3.57	50.18	20.17	102	30.38	400	67.30	9742	0.86	211	356
273	203	8.62	1431	1.00		8.95	0.08	2.74	5.70	1.78	31.0	10.89	138.45	52.06	233	57.49	606	80.05	9108	0.66	99	102
274	139	6.67	944	1.07		8.53	0.13	4.08	7.54	0.76	33.3	9.26	103.94	35.07	144	33.77	346	43.99	8271	0.46	84	139
275	425	3.77	1761	4.59		9.47	0.00	1.24	3.76	0.69	28.4	11.43	155.67	63.31	292	77.92	888	121.21	10356	2.15	297	514
276	260	9.28	1516	2.20		16.88	0.04	1.92	3.87	2.09	24.8	9.57	129.35	50.98	243	66.49	805	123.16	8287	1.01	273	293

CV-10

277	275	4.17	1777	1.50	0.01	3.70	0.46	7.21	11.38	3.00	53.5	17.11	203.86	68.07	274	64.72	654	73.32	7126	0.79	20	41
278	458	4.00	1850	2.48	0.60	12.23	0.50	5.28	9.05	1.86	50.1	15.59	196.86	68.26	299	74.87	799	102.96	9408	1.34	268	349
279	290	6.18	2206	3.29		13.91	0.46	9.07	15.27	1.32	76.6	20.75	249.23	88.67	365	90.13	1000	105.75	8391	0.87	274	261
280	471	7.27	2336	2.03		18.13	0.21	5.78	12.01	4.99	62.7	20.14	249.39	86.54	377	92.62	1004	122.53	7938	0.67	244	238
282	396	3.76	1476	5.21		10.91	0.05	1.04	3.57	0.71	21.4	9.02	123.39	52.19	245	66.85	783	105.62	9278	2.28	191	412
283	188	6.79	631	1.01		8.65	0.02	0.40	1.38	0.78	11.3	3.63	50.04	20.29	103	29.40	385	56.33	8979	0.72	82	106
286	415	4.57	1822	4.06		23.99	0.10	1.23	5.58	2.17	34.4	12.01	158.58	61.13	291	78.28	928	129.01	9851	1.97	442	654
287	329	3.74	1239	3.89		9.44	0.03	0.18	3.93	0.71	17.9	8.39	108.42	44.34	209	58.26	643	83.59	10067	2.21	205	409
288	772	3.50	2517	6.20		19.02	0.08	1.16	4.98	0.67	37.4	15.39	210.46	85.58	424	113.06	1277	170.84	9600	2.97	323	539
289	246	5.28	962	1.87	0.01	11.31	0.04	1.06	2.64	1.18	15.9	5.53	80.87	32.89	156	46.07	592	89.20	9136	0.98	204	279
290	358	7.25	2052	1.06	0.42	10.16	0.27	3.41	6.55	2.07	43.0	14.61	197.18	73.03	325	77.00	853	107.64	8446	0.69	174	171
291	218	5.46	1277	5.36		26.11	0.07	1.08	2.45	1.33	20.0	6.82	99.28	42.45	211	59.69	726	112.76	9015	1.94	560	580
292	528	3.99	1641	1.67		11.08	0.08	1.76	4.87	2.06	36.2	11.77	144.33	56.53	245	64.75	711	95.93	9098	0.95	209	352
293	277	5.96	1297	2.80	0.03	20.08	0.14	1.49	3.60	1.06	21.8	8.11	106.89	44.96	214	58.51	684	101.35	10515	1.45	480	367
294	493	6.39	2624	3.14	0.03	28.65	0.17	4.26	10.47	3.20	59.4	20.58	253.66	96.94	421	106.36	1125	148.06	8645	0.96	481	343
295	275	5.48	1483	1.43	0.05	9.22	0.12	3.64	6.49	1.67	32.9	11.64	145.60	54.12	237	60.46	642	84.50	9083	0.97	192	226
296	1993	8.33	2283	1.43	27.72	63.22	8.32	40.25	16.99	2.65	61.5	18.16	233.17	83.90	354	88.00	910	122.36	9680	0.79	283	228
297	391	4.13	1520	3.67		10.10	0.04	1.56	4.14	0.54	24.2	9.85	133.39	55.23	250	65.57	711	98.59	10554	1.97	224	365
298	328	1.82	1853	11.34	0.07	3.49	0.08	0.62	2.63	0.05	23.3	10.97	166.70	67.09	319	80.17	847	107.86	12517	8.70	410	1220
299	255	4.19	1126	2.90		15.26	0.04	1.03	2.92	0.96	18.8	6.26	89.90	36.66	185	50.21	594	93.47	9909	1.03	241	338
300	2672	3.35	2731	10.67	19.48	77.01	11.39	79.95	29.97	0.66	81.5	24.05	291.79	103.85	448	103.96	1007	126.36	11968	4.33	445	722

Toba Blanca

301	840	3.27	3211	8.73		17.19	0.06	0.85	6.28	0.54	42.5	19.36	271.01	114.13	528	139.92	1495	218.52	12565	4.05	432	724
302	352	6.23	1743	3.53	0.02	19.18	0.04	1.12	3.13	1.01	28.6	10.40	143.56	59.22	293	76.07	839	131.41	10200	1.59	255	255
303	230	12.20	870	0.80		6.60	0.04	0.59	2.13	0.39	16.6	6.23	79.80	30.72	132	32.81	322	48.53	10740	0.69	85	93

304	271	3.23	1320	2.43	0.02	13.86	0.05	1.30	2.50	0.40	23.5	7.87	115.72	46.70	219	58.69	610	98.94	11823	1.63	295	349
305	1331	6.01	1745	2.40	8.97	26.67	2.16	11.87	5.90	1.44	34.5	10.81	147.20	60.43	283	72.40	771	121.96	10169	0.96	291	341
306	308	5.44	2334	8.98		37.34	0.04	3.03	8.38	4.51	52.8	16.57	216.61	80.12	351	90.39	973	163.06	12177	2.84	778	693
308	294	13.83	1450	0.88		8.59	0.08	3.24	5.99	1.21	34.2	10.68	141.70	52.44	214	50.99	499	72.98	11122	0.63	111	102
309	232	15.61	911	0.90		5.57	0.07	1.29	4.43	0.60	21.2	7.16	86.57	33.65	141	33.22	324	44.65	11195	0.57	85	79
310	351	4.36	1230	2.90		6.66	0.05	0.41	2.18	0.32	17.6	7.41	104.76	43.50	211	52.90	572	91.32	11681	1.56	159	303
311	346	5.01	1861	4.89		14.04	0.01	1.57	4.25	1.37	32.1	12.99	163.93	62.72	302	74.67	787	122.95	11273	1.96	338	427
312	629	5.38	3202	7.00		24.51	0.07	4.43	10.57	2.43	65.8	23.40	301.66	115.78	499	119.48	1211	182.75	10947	2.32	835	779
313	833	2.87	3431	8.23		16.72	0.05	1.43	6.08	0.71	45.0	18.82	281.34	117.22	578	142.30	1473	238.47	13024	4.18	392	628
314	2813	5.52	1730	4.90	49.16	99.26	12.77	69.86	19.36	1.90	42.4	12.46	159.57	62.76	281	70.68	725	110.54	12510	2.51	449	454
316	326	6.09	2183	1.84	0.11	8.82	0.29	4.77	8.68	2.15	47.1	16.35	201.60	78.95	343	84.17	825	132.91	10658	1.13	244	263
317	913	4.61	4059	11.07	0.08	24.84	0.08	2.39	6.72	0.99	50.4	22.81	324.90	138.55	685	172.72	1761	293.13	12878	4.32	631	790
318	935	3.28	4135	10.92		15.55	0.04	1.52	5.93	0.92	45.3	20.53	325.67	140.90	690	177.06	1848	313.44	13776	3.61	357	635
319	175	9.59	1301	1.17	0.05	4.78	0.38	4.67	8.66	3.22	35.6	11.07	127.10	45.47	202	49.67	507	87.61	8113	1.03	131	113
320	549	9.50	4014	3.36	0.33	34.12	0.45	9.39	17.21	7.44	94.3	30.59	359.58	138.63	646	153.62	1508	263.18	8460	0.97	718	361
321	523	7.26	1006	1.55	1.92	17.30	0.45	4.26	2.86	0.84	16.2	5.94	78.66	33.45	164	44.88	489	86.26	12066	0.83	190	160
322	898	7.18	4371	6.89	0.08	22.01	0.41	8.80	17.40	7.06	94.6	31.23	389.48	152.64	672	165.20	1644	271.13	13140	2.44	563	518
323	219	3.68	1158	1.94		9.09		0.37	2.23	0.41	18.6	7.00	98.49	41.34	202	51.25	524	88.02	13792	1.08	154	213
324	394	4.96	2237	2.25		23.53	0.24	5.24	8.95	2.68	52.8	15.37	213.04	81.51	365	90.72	905	145.79	12274	0.89	551	290
325	713	5.77	3512	9.20	0.25	24.31	0.14	1.59	6.08	0.88	50.4	21.27	299.69	128.95	609	154.94	1572	264.47	14362	4.62	622	782
326	1005	4.68	4220	7.16	0.27	19.99	0.17	2.51	8.09	1.12	58.5	25.14	357.98	151.11	712	179.04	1792	302.35	13844	3.11	658	796
327	566	11.06	3135	2.43	1.60	35.91	0.91	9.03	13.88	3.62	74.0	26.18	317.61	116.76	504	117.80	1115	171.92	11149	1.35	452	221
328	607	3.74	1544	4.09	3.85	23.27	0.69	7.41	3.87	0.70	28.1	10.22	134.55	54.38	266	68.97	738	122.57	12533	2.38	755	604
330	262	10.06	1356	2.22		12.37	0.05	1.14	2.54	0.97	20.2	7.16	104.37	44.43	229	63.47	728	130.71	10652	0.98	102	110
331	605	3.30	2285	3.78	0.02	17.71	0.04	1.71	4.48	1.29	37.4	14.13	197.25	79.58	389	99.76	1021	170.17	12485	1.61	338	388
332	438	12.75	2111	2.84	0.12	22.25	0.13	1.85	6.13	2.10	36.4	13.71	188.83	74.63	354	85.39	883	137.57	9964	1.08	241	169
333	408	3.64	1321	2.56	0.06	7.20	0.07	1.20	2.93	0.70	23.0	8.33	117.50	47.27	224	56.81	612	100.21	12205	1.25	198	332

KARG-15-12

335	185	6.05	401	0.70		6.12		0.41	1.16	0.40	7.6	2.24	33.87	14.03	69	20.54	263	40.51	9740	0.43	57	84
336	271	7.18	1203	1.04		8.70	0.03	0.58	2.29	1.03	18.7	8.33	111.72	43.02	200	51.92	570	81.21	9509	0.34	34	69
337	300	4.32	842	1.01	0.01	9.16	0.03	0.68	2.25	0.87	19.1	6.61	87.72	31.39	144	37.00	394	54.60	10304	0.42	84	126
338	1356	5.45	1696	1.48	5.17	23.28	1.45	9.00	7.38	1.65	40.0	13.51	175.78	62.98	271	67.29	715	95.87	9918	0.41	84	150
339	242	4.07	835	1.27		6.76	0.03	1.63	3.57	1.48	21.2	6.66	84.16	31.75	137	35.86	388	53.06	9513	0.66	57	121
340	585	5.15	3591	4.20	0.03	14.97	0.49	8.03	17.87	4.61	86.0	29.89	356.04	128.33	573	147.02	1663	228.18	9043	1.58	509	606
341	289	15.56	992	0.79		8.30	0.08	1.15	3.75	0.72	21.4	8.64	101.11	38.86	169	41.26	453	59.37	9299	0.50	72	79
343	707	8.52	1976	4.35	2.03	30.89	0.76	5.36	7.10	2.75	39.7	13.78	187.85	73.77	346	91.21	1074	128.42	7638	1.53	221	247

345	147	9.86	646	0.28		2.17	0.05	1.87	4.88	1.51	19.1	6.29	72.30	25.34	105	28.13	316	35.88	6716	0.23	51	71
346	118	3.35	216	0.50		3.86		0.28	0.44	0.27	3.8	1.38	18.91	7.75	37	11.18	148	20.36	9635	0.28	30	68
347	1148	12.04	6577	10.59	0.48	96.20	3.56	61.72	88.95	28.20	290.1	79.66	814.45	257.57	965	241.28	2624	291.15	7351	2.22	1673	794
349	244	5.59	774	0.68	0.04	6.76	0.03	0.76	2.34	0.82	14.1	5.87	75.52	27.95	129	33.91	400	49.45	8123	0.19	18	46
350	210	4.46	591	3.91	0.06	13.85	0.03	0.80	2.54	0.95	12.9	4.63	52.45	20.67	93	27.65	359	49.66	8408	2.25	210	399
351	508	9.68	2075	2.67	0.00	22.69	0.14	2.81	7.95	3.27	45.2	17.25	218.08	79.33	353	90.45	1059	121.77	7387	1.00	163	190
352	317	5.45	808	1.50	0.94	9.66	0.31	2.04	2.38	0.48	12.3	4.64	70.77	28.40	137	41.14	508	62.27	9150	1.00	84	172
353	548	7.84	2549	2.19		28.81	0.38	7.49	15.37	6.11	68.1	21.70	255.48	93.83	411	109.47	1256	159.84	7329	0.51	338	394
355	309	11.02	1124	3.57	0.07	45.18	0.17	2.67	6.91	1.18	33.4	10.01	123.20	43.18	180	46.56	524	56.33	8915	2.18	603	485
356	721	6.28	3339	7.60		24.32	0.16	4.97	14.91	5.32	75.1	26.12	336.94	122.90	548	144.09	1629	194.55	8753	1.94	706	752
358	556	20.82	1481	0.77	2.06	15.99	0.79	10.84	13.49	3.91	52.3	15.76	171.81	59.75	242	57.98	611	65.01	8066	0.29	138	101
359	300	18.09	1892	1.03	0.05	19.62	0.42	7.56	15.97	4.98	74.4	21.62	219.74	77.79	295	72.91	748	80.55	7744	0.51	209	141
360	222	6.70	891	0.55		7.39	0.12	2.02	3.78	1.10	20.1	7.14	87.17	32.22	145	39.83	457	56.70	8721	0.38	86	94
361	286	18.53	1958	1.18	0.03	17.63	0.28	6.99	14.53	4.00	67.7	19.16	217.54	75.49	311	74.59	765	89.18	8028	0.33	217	144
362	275	17.97	1980	0.78	0.01	17.78	0.31	8.33	16.19	4.79	71.4	20.92	242.38	77.95	304	72.11	741	87.54	7968	0.32	192	129
363	296	19.05	1955	0.96	0.26	16.97	0.43	7.26	13.77	4.36	67.2	19.83	224.29	73.66	292	71.22	740	85.15	7604	0.47	183	124
365	336	18.13	2719	1.52	0.07	23.30	0.45	9.56	18.44	6.55	101.5	29.22	309.81	105.61	428	99.06	1005	121.91	8574	0.53	299	176
366	487	6.68	2261	3.61		32.90	0.20	3.01	9.13	1.77	55.0	18.19	226.85	84.00	363	89.39	924	120.28	10170	1.35	404	376
367	270	18.47	2383	1.02	0.02	19.30	0.42	7.90	16.18	5.25	79.3	23.07	267.42	90.99	377	85.93	826	113.42	9716	0.62	239	139
368	300	21.52	2412	0.88	0.06	17.12	0.38	9.90	18.13	5.84	84.1	23.86	265.08	87.99	354	83.84	754	104.77	9479	0.36	208	111
369	311	19.94	1411	0.97		12.69	0.12	2.77	4.30	1.66	32.7	10.20	129.65	49.30	225	55.31	553	87.13	10158	0.56	121	102
371	247	18.83	2314	0.67	0.01	12.99	0.34	7.30	13.40	4.25	67.6	20.12	250.35	87.37	363	80.01	742	115.79	10548	0.39	190	103
372	384	6.13	981	1.15	2.11	11.93	0.61	3.28	3.29	0.92	18.0	6.21	84.19	33.43	167	44.22	506	89.67	11965	0.79	100	88
374	212	213.36	842	1.27	3.44	14.73	0.90	5.65	4.29	1.45	21.9	6.97	81.50	30.91	131	30.17	301	46.49	8111	0.44	67	49
375	253	13.77	1460	0.42		12.38	0.19	5.32	8.95	2.53	43.1	13.59	149.35	55.54	224	51.79	502	68.15	9595	0.28	123	84

Table B2. Zircon LA-ICPMS U-Pb geochronology. Isotope ratios and ages are reported without initial common Pb correction; gas blank-corrected mass 204 signals were generally irresolvable from zero. Isotope ratio and apparent age errors do NOT include systematic calibration errors of 0.19% for the 207Pb/206Pb ratio, and 0.63% for the 206Pb/238U ratio (1s). Trace element concentrations in ppm, calculated using the mean count rate method, internal standardization to 29Si, and calibration to NIST 610 and 612 glass standards. Ablation using a 213 nm wavelength laser, spot size of 25 microns, repetition rate of 10 Hz, and fluence of ~5 J/cm2. % disc. = relative discordance calculated as 100*(1-(206Pb/238U date/207Pb/206Pb date))

Analysis	Composition				Corrected isotope ratios									Apparent ages (Ma)							
	U	Th	Pb	Th/U	$\frac{206\text{Pb}}{204\text{Pb}}$	$\frac{207\text{Pb}}{235\text{U}}$	$\pm 2s$	$\frac{206\text{Pb}}{238\text{U}}$	$\pm 2s$	error	$\frac{238\text{U}}{206\text{Pb}}$	$\pm 2s$	$\frac{207\text{Pb}}{206\text{Pb}}$	$\pm 2s$	$\frac{207\text{Pb}}{206\text{Pb}}$	$\pm 2s$	$\frac{207\text{Pb}}{235\text{U}}$	$\pm 2s$	$\frac{206\text{Pb}}{238\text{U}}$	$\pm 2s$	%
	ppm	ppm	ppm				(%)	(%)	corr.	(%)	(%)	(%)	(%)	(%)	(abs)	(abs)	(abs)	(abs)	(abs)	(abs)	disc.
KARG-15-01																					
51	172	161	1	0.94	55.4	0.017	26.0	0.0025	8.5	0.33	395.80	8.5	0.0492	24.6	155	575	17.2	4.4	16.3	1.4	90
52	425	276	1	0.65	407.8	0.017	20.6	0.0028	7.8	0.38	356.80	7.8	0.0446	19.1	-80	467	17.3	3.5	18.0	1.4	123
53	540	706	2	1.31	53.0	0.018	15.7	0.0029	7.2	0.46	346.64	7.2	0.0447	14.0	-74	342	17.9	2.8	18.6	1.3	125
54	62	67	0	1.08	53.5	0.058	95.1	0.0028	9.7	0.10	354.16	9.7	0.1477	94.6	2319	1623	56.8	52.5	18.2	1.8	99
55	343	531	1	1.55	129.5	0.009	49.9	0.0026	6.8	0.14	383.44	6.8	0.0255	49.4	-1692	1719	9.3	4.6	16.8	1.1	101
56	130	96	0	0.74	58.6	0.025	32.5	0.0027	10.3	0.32	376.29	10.3	0.0691	30.8	902	636	25.4	8.2	17.1	1.8	98
57	471	266	1	0.57	38.7	0.014	20.3	0.0024	8.2	0.40	412.73	8.2	0.0412	18.6	-277	472	13.9	2.8	15.6	1.3	106
58	122	166	1	1.36	10.8	0.039	33.8	0.0029	5.8	0.17	346.59	5.8	0.0982	33.4	1590	623	38.9	12.9	18.6	1.1	99
59	677	352	2	0.52	219.2	0.019	10.5	0.0027	4.7	0.45	372.46	4.7	0.0526	9.3	314	213	19.6	2.0	17.3	0.8	94
60	156	124	1	0.79	32.8	0.061	262.0	0.0026	6.4	0.02	380.40	6.4	0.1675	261.9	2533	4394	59.9	152.3	16.9	1.1	99
61	298	361	1	1.21	126.1	0.012	27.1	0.0027	4.8	0.18	369.95	4.8	0.0328	26.6	-892	771	12.3	3.3	17.4	0.8	102
62	668	496	2	0.74	63.8	0.019	12.0	0.0027	5.9	0.49	364.69	5.9	0.0507	10.4	229	241	19.3	2.3	17.7	1.0	92
63	258	228	1	0.89	24.1	0.011	67.6	0.0025	7.0	0.10	394.85	7.0	0.0318	67.2	-981	1984	11.2	7.5	16.3	1.1	102
64	406	728	2	1.79	21.2	0.013	28.6	0.0026	6.4	0.22	387.05	6.4	0.0377	27.9	-505	743	13.6	3.9	16.6	1.1	103
65	165	237	1	1.44	11.9	0.015	35.0	0.0029	5.3	0.15	345.06	5.3	0.0371	34.6	-547	930	15.0	5.2	18.7	1.0	103
66	534	503	2	0.94	237.9	0.020	14.4	0.0028	6.8	0.47	353.81	6.8	0.0501	12.7	201	294	19.6	2.8	18.2	1.2	91
67	825	715	3	0.87	103.7	0.019	11.7	0.0027	3.9	0.33	368.90	3.9	0.0498	11.0	188	257	18.7	2.2	17.5	0.7	91
68	617	418	2	0.68	92.8	0.019	9.6	0.0026	4.0	0.41	389.96	4.0	0.0525	8.8	308	200	18.7	1.8	16.5	0.7	95
69	290	364	1	1.25	28.6	0.016	26.5	0.0026	6.1	0.23	391.34	6.1	0.0452	25.7	-44	626	16.0	4.2	16.5	1.0	137
70	368	327	1	0.89	58.3	0.016	23.3	0.0029	5.0	0.21	346.16	5.0	0.0395	22.7	-385	591	15.8	3.7	18.6	0.9	105
71	832	733	3	0.88	67.8	0.028	12.6	0.0028	3.6	0.28	357.36	3.6	0.0718	12.1	981	246	27.8	3.4	18.0	0.6	98
73	334	286	1	0.86	89.8	0.019	18.5	0.0026	4.5	0.24	387.00	4.5	0.0546	18.0	396	403	19.6	3.6	16.6	0.8	96
74	191	140	1	0.73	11.4	0.018	36.7	0.0028	6.6	0.18	352.24	6.6	0.0467	36.1	32	865	18.4	6.7	18.3	1.2	42
75	263	318	1	1.21	224.5	0.012	30.0	0.0025	5.1	0.17	392.66	5.1	0.0348	29.6	-727	826	12.3	3.7	16.4	0.8	102
76	244	271	1	1.11	432.0	0.021	65.7	0.0025	7.7	0.12	404.73	7.7	0.0619	65.3	670	1396	21.2	13.8	15.9	1.2	98
77	94	61	2	0.65	88.2	0.102	18.4	0.0154	5.7	0.31	64.96	5.7	0.0482	17.5	107	414	98.8	17.4	98.5	5.6	8
79	628	290	2	0.46	102.7	0.012	23.5	0.0027	5.6	0.24	365.07	5.6	0.0331	22.8	-868	657	12.6	2.9	17.6	1.0	102
80	367	255	1	0.70	39.2	0.017	24.9	0.0027	5.3	0.21	368.98	5.3	0.0454	24.4	-37	591	17.1	4.2	17.4	0.9	148

81	435	243	2	0.56	23.7	0.015	18.5	0.0029	5.3	0.29	346.74	5.3	0.0366	17.7	-584	480	14.7	2.7	18.6	1.0	103
82	489	227	2	0.46	38.2	0.022	11.8	0.0027	5.0	0.42	372.74	5.0	0.0600	10.7	603	231	22.3	2.6	17.3	0.9	97
83	468	485	2	1.04	47.0	0.020	15.6	0.0025	5.7	0.37	394.02	5.7	0.0563	14.5	464	321	19.8	3.1	16.3	0.9	96
84	383	941	2	2.46	29.8	0.014	26.6	0.0025	5.3	0.20	395.00	5.3	0.0388	26.1	-427	683	13.7	3.6	16.3	0.9	104
85	188	187	1	1.00	114.2	0.019	27.1	0.0027	7.0	0.26	368.50	7.0	0.0500	26.2	196	609	18.8	5.1	17.5	1.2	91
86	557	306	2	0.55	44.5	0.010	39.5	0.0027	4.5	0.11	364.51	4.5	0.0262	39.2	-1590	1331	10.0	3.9	17.7	0.8	101
87	280	223	1	0.79	125.9	0.015	25.6	0.0025	7.2	0.28	392.61	7.2	0.0423	24.6	-208	618	15.0	3.8	16.4	1.2	108
88	218	323	1	1.48	426.8	0.015	64.2	0.0026	8.6	0.13	388.14	8.6	0.0410	63.6	-287	1622	14.7	9.4	16.6	1.4	106
89	245	208	1	0.85	9.8	0.023	68.5	0.0026	12.1	0.18	380.46	12.1	0.0624	67.4	689	1438	22.7	15.4	16.9	2.0	98
90	687	591	2	0.86	35.0	0.017	14.5	0.0026	4.6	0.32	391.21	4.6	0.0495	13.8	171	322	17.6	2.5	16.5	0.8	90

KANI

132	607	402	2	0.66	249.5	0.019	11.0	0.0027	4.5	0.40	377.18	4.5	0.0510	10.1	241	233	18.8	2.1	17.1	0.8	93
133	35	19	1	0.55	92.6	0.095	23.1	0.0161	7.5	0.32	62.27	7.5	0.0428	21.8	-177	544	92.0	20.3	102.7	7.6	158
134	118	85	2	0.72	38.6	0.102	12.4	0.0149	4.2	0.34	67.01	4.2	0.0497	11.6	181	271	98.9	11.6	95.5	4.0	47
135	328	396	6	1.21	212.7	0.087	7.8	0.0125	3.8	0.48	80.28	3.8	0.0508	6.9	231	159	84.9	6.4	79.8	3.0	65
136	249	101	1	0.40	40.4	0.021	19.5	0.0040	4.8	0.24	251.24	4.8	0.0378	18.9	-496	502	20.9	4.0	25.6	1.2	105
137	339	167	1	0.49	177.4	0.018	17.9	0.0027	6.1	0.34	375.64	6.1	0.0501	16.8	198	391	18.5	3.3	17.1	1.0	91
138	128	80	3	0.63	83.5	0.127	12.6	0.0196	4.4	0.35	51.04	4.4	0.0471	11.7	56	280	121.7	14.4	125.1	5.5	-123
139	227	159	2	0.70	254.5	0.031	17.8	0.0065	5.3	0.30	154.57	5.3	0.0352	17.0	-690	470	31.4	5.5	41.6	2.2	106
140	855	688	3	0.80	646.8	0.018	13.2	0.0026	5.1	0.39	382.84	5.1	0.0495	12.1	170	283	17.9	2.3	16.8	0.9	90
141	674	482	2	0.72	118.5	0.014	16.4	0.0026	5.5	0.33	380.75	5.5	0.0389	15.4	-420	404	14.2	2.3	16.9	0.9	104
142	66	33	1	0.49	25.2	0.109	17.7	0.0168	5.0	0.28	59.70	5.0	0.0470	16.9	49	404	104.6	17.6	107.1	5.4	-120
143	106	99	2	0.93	27.3	0.076	23.2	0.0124	4.5	0.19	80.74	4.5	0.0447	22.8	-71	557	74.7	16.7	79.4	3.5	212
144	59	37	1	0.63	163.3	0.117	17.5	0.0149	6.1	0.35	67.10	6.1	0.0570	16.4	492	362	112.5	18.7	95.4	5.8	81
145	327	242	1	0.74	29.5	0.020	14.8	0.0026	8.6	0.58	377.93	8.6	0.0556	12.0	436	268	20.4	3.0	17.0	1.5	96
146	203	141	4	0.70	214.2	0.120	9.0	0.0158	4.9	0.54	63.31	4.9	0.0551	7.6	415	169	115.0	9.8	101.0	4.9	76
147	440	345	2	0.78	612.2	0.016	26.0	0.0026	4.1	0.16	380.00	4.1	0.0430	25.6	-168	638	15.7	4.0	16.9	0.7	110
148	196	137	1	0.70	34.8	0.012	61.5	0.0027	6.9	0.11	368.21	6.9	0.0318	61.1	-984	1806	12.0	7.4	17.5	1.2	102
149	119	63	1	0.52	22.0	0.179	612.6	0.0033	9.9	0.02	303.84	9.9	0.3947	612.5	3889	9221	167.3	944.9	21.2	2.1	99
150	52	35	1	0.68	32.6	0.084	27.4	0.0165	5.9	0.21	60.46	5.9	0.0368	26.8	-569	724	81.9	21.6	105.8	6.1	119
151	469	337	2	0.72	101.7	0.010	17.9	0.0025	4.5	0.25	397.10	4.5	0.0296	17.3	-1201	536	10.4	1.8	16.2	0.7	101
152	122	129	0	1.06	100.7	0.027	155.3	0.0028	8.1	0.05	351.80	8.1	0.0680	155.1	870	3214	26.7	41.0	18.3	1.5	98
153	124	66	2	0.53	79.2	0.106	11.9	0.0155	3.3	0.27	64.59	3.3	0.0496	11.4	179	267	102.3	11.6	99.0	3.2	45
154	1106	1299	4	1.18	168.4	0.017	13.3	0.0024	4.2	0.31	408.85	4.2	0.0518	12.7	276	290	17.6	2.3	15.7	0.7	94
155	105	81	0	0.77	34.5	0.011	62.6	0.0027	7.5	0.12	375.38	7.5	0.0292	62.1	-1246	1946	10.8	6.7	17.2	1.3	101
156	235	128	4	0.54	273.9	0.088	6.7	0.0135	3.0	0.44	74.18	3.0	0.0473	6.0	63	144	85.5	5.5	86.3	2.6	-38
157	526	360	2	0.68	88.7	0.018	17.4	0.0028	2.9	0.17	354.60	2.9	0.0459	17.2	-7	414	18.0	3.1	18.2	0.5	375
158	181	129	1	0.71	17.7	0.024	30.0	0.0028	6.2	0.21	359.62	6.2	0.0624	29.4	686	627	24.0	7.1	17.9	1.1	97
159	61	42	0	0.69	9.6	0.027	116.6	0.0029	10.7	0.09	345.57	10.7	0.0669	116.1	835	2418	26.8	30.8	18.6	2.0	98
160	367	195	7	0.53	75.2	0.098	12.4	0.0146	6.7	0.54	68.38	6.7	0.0487	10.5	135	246	95.2	11.3	93.6	6.2	31
161	79	74	0	0.94	18.4	-0.036	131.8	0.0024	11.9	0.09	416.71	11.9	-0.1084	131.2	0	#DIV/0!	-37.1	-49.8	15.5	1.8	0
162	92	48	0	0.52	13.5	0.191	636.9	0.0027	11.7	0.02	367.96	11.7	0.5096	636.8	4269	9372	177.4	1036.9	17.5	2.0	100
163	62	47	0	0.76	84.0	0.018	133.1	0.0032	12.4	0.09	312.47	12.4	0.0404	132.5	-328	3407	17.9	23.6	20.6	2.5	106
164	38	25	0	0.65	1.1	0.130	270.6	0.0026	14.6	0.05	391.96	14.6	0.3686	270.2	3786	4095	123.8	315.4	16.4	2.4	100
165	333	348	2	1.05	81.9	0.016	35.1	0.0035	8.3	0.24	284.75	8.3	0.0325	34.1	-918	992	15.9	5.5	22.6	1.9	102

166	1002	907	3	0.91	61.3	0.019	14.8	0.0026	3.9	0.26	387.06	3.9	0.0534	14.2	345	322	19.1	2.8	16.6	0.6	95
167	137	170	0	1.24	15.7	0.021	51.8	0.0026	12.7	0.25	378.81	12.7	0.0571	50.2	495	1107	20.9	10.7	17.0	2.2	97
168	357	254	1	0.71	234.0	0.013	35.7	0.0027	6.0	0.17	374.49	6.0	0.0359	35.2	-641	964	13.3	4.7	17.2	1.0	103
169	59	42	0	0.71	9.4	0.301	541.7	0.0033	14.4	0.03	301.03	14.4	0.6577	541.5	4641	7816	267.4	1273.4	21.4	3.1	100
170	338	255	5	0.75	56.3	0.078	10.5	0.0127	5.4	0.51	78.56	5.4	0.0444	9.0	-86	220	76.3	7.7	81.5	4.4	195

CV-13

171	1417	3667	7	2.59	402.1	0.019	7.9	0.0026	2.7	0.33	378.09	2.7	0.0521	7.5	288	170	19.1	1.5	17.0	0.5	94
172	43	26	1	0.61	20.2	0.092	44.8	0.0148	7.1	0.16	67.68	7.1	0.0451	44.2	-48	1076	89.3	38.3	94.5	6.7	297
173	72	47	0	0.65	37.1	0.057	249.1	0.0028	11.5	0.05	361.64	11.5	0.1503	248.8	2350	4253	56.6	137.1	17.8	2.0	99
174	221	73	1	0.33	128.8	0.022	94.1	0.0030	6.8	0.07	337.29	6.8	0.0530	93.8	331	2128	21.8	20.3	19.1	1.3	94
175	60	49	1	0.82	40.3	0.102	20.0	0.0142	7.3	0.36	70.41	7.3	0.0520	18.7	287	427	98.5	18.8	90.9	6.6	68
176	677	249	9	0.37	262.5	0.100	29.1	0.0115	27.6	0.95	87.24	27.6	0.0633	9.2	717	195	96.8	26.9	73.5	20.2	90
177	386	199	1	0.52	108.7	0.017	22.7	0.0029	6.2	0.27	346.04	6.2	0.0436	21.8	-132	539	17.5	3.9	18.6	1.2	114
178	107	83	0	0.77	20.6	0.020	32.2	0.0029	8.0	0.25	339.70	8.0	0.0489	31.1	144	731	20.0	6.4	18.9	1.5	87
179	182	171	1	0.94	19.1	0.014	43.1	0.0033	7.3	0.17	299.34	7.3	0.0308	42.5	-1075	1281	14.3	6.1	21.5	1.6	102
180	362	206	1	0.57	162.7	0.018	20.3	0.0030	6.5	0.32	330.08	6.5	0.0432	19.3	-157	479	18.2	3.7	19.5	1.3	112
181	87	60	0	0.69	6.7	0.047	141.2	0.0032	11.0	0.08	317.07	11.0	0.1078	140.8	1762	2573	46.5	64.2	20.3	2.2	99
182	35	30	1	0.86	9.9	0.081	36.2	0.0150	7.4	0.20	66.70	7.4	0.0392	35.4	-401	923	79.2	27.5	95.9	7.0	124
183	137	118	1	0.86	71.0	0.016	70.1	0.0030	6.3	0.09	333.92	6.3	0.0399	69.8	-358	1805	16.6	11.5	19.3	1.2	105
184	156	109	1	0.70	81.4	0.063	360.8	0.0030	8.2	0.02	330.81	8.2	0.1515	360.8	2362	6158	62.2	217.6	19.5	1.6	99
185	164	90	9	0.55	410.7	0.329	8.0	0.0465	5.5	0.69	21.49	5.5	0.0513	5.8	252	134	288.7	20.1	293.2	15.8	-16
186	45	35	1	0.77	27.0	0.104	19.3	0.0146	6.6	0.34	68.31	6.6	0.0513	18.2	256	418	100.1	18.4	93.7	6.1	63
187	669	806	3	1.20	35.2	0.015	16.5	0.0026	3.9	0.23	384.92	3.9	0.0420	16.1	-224	404	15.2	2.5	16.7	0.7	107
188	333	136	19	0.41	2495.5	0.491	38.7	0.0447	38.3	0.99	22.36	38.3	0.0796	4.9	1186	97	405.4	129.2	282.1	105.8	76
189	232	120	1	0.52	20.7	0.009	114.8	0.0026	8.9	0.08	391.29	8.9	0.0256	114.4	-1673	3963	9.1	10.4	16.5	1.5	101
190	575	487	2	0.85	134.4	0.020	9.9	0.0030	5.7	0.57	332.55	5.7	0.0488	8.1	137	191	20.3	2.0	19.4	1.1	86
191	1573	2120	7	1.35	116.7	0.017	7.9	0.0029	5.3	0.67	349.21	5.3	0.0434	5.8	-143	144	17.3	1.3	18.4	1.0	113
192	300	133	1	0.44	26.6	0.014	30.5	0.0028	4.4	0.14	361.04	4.4	0.0379	30.2	-494	803	14.6	4.4	17.8	0.8	104
193	221	107	1	0.48	135.6	0.034	135.8	0.0029	5.4	0.04	345.51	5.4	0.0855	135.7	1326	2627	34.1	45.5	18.6	1.0	99
194	590	303	2	0.51	312.9	0.018	18.3	0.0027	4.7	0.26	365.20	4.7	0.0484	17.7	119	416	18.4	3.3	17.6	0.8	85
195	515	109	8	0.21	836.3	0.114	18.2	0.0151	17.3	0.95	66.04	17.3	0.0546	5.9	395	133	109.6	18.9	96.9	16.6	75
196	402	245	4	0.61	70.3	0.067	19.1	0.0090	17.2	0.90	110.88	17.2	0.0541	8.2	373	186	66.1	12.2	57.9	9.9	84
197	525	379	2	0.72	210.1	0.018	14.6	0.0027	7.2	0.49	370.14	7.2	0.0478	12.7	90	300	17.9	2.6	17.4	1.2	81
198	393	234	1	0.60	43.5	0.016	25.8	0.0028	5.8	0.23	362.11	5.8	0.0431	25.1	-160	624	16.5	4.2	17.8	1.0	111
199	480	238	2	0.50	32.7	0.017	22.9	0.0029	7.1	0.31	347.43	7.1	0.0426	21.8	-189	544	17.0	3.9	18.5	1.3	110
200	521	344	2	0.66	87.0	0.015	23.5	0.0027	5.1	0.21	368.55	5.1	0.0408	23.0	-299	588	15.4	3.6	17.5	0.9	106

KARG-15-08

201	108	43	0	0.40	6.7	0.087	266.1	0.0028	8.1	0.03	354.99	8.1	0.2237	266.0	3007	4273	84.6	216.0	18.1	1.5	99
202	75	75	0	1.00	12.7	0.122	308.0	0.0030	10.7	0.03	331.09	10.7	0.2937	307.9	3437	4780	117.2	340.8	19.4	2.1	99
203	672	475	2	0.71	663.3	0.015	21.7	0.0027	5.5	0.25	366.69	5.5	0.0407	21.0	-308	538	15.4	3.3	17.6	1.0	106
204	43	42	0	0.96	8.0	0.114	126.1	0.0034	14.1	0.11	296.47	14.1	0.2460	125.3	3159	1987	110.0	131.4	21.7	3.0	99
205	174	128	1	0.73	31.2	0.042	282.7	0.0029	7.6	0.03	347.50	7.6	0.1059	282.6	1729	5187	41.8	115.7	18.5	1.4	99
206	427	245	2	0.57	49.7	0.050	8.6	0.0030	5.6	0.65	332.51	5.6	0.1197	6.5	1951	116	49.2	4.1	19.4	1.1	99
207	442	267	2	0.60	35.6	0.013	17.6	0.0026	5.4	0.31	378.17	5.4	0.0358	16.7	-643	459	13.2	2.3	17.0	0.9	103

208	161	173	1	1.07	28.0	0.015	18.2	0.0029	8.0	0.44	349.17	8.0	0.0386	16.3	-445	430	15.4	2.8	18.4	1.5	104
209	264	149	5	0.56	1542.1	0.089	10.9	0.0157	5.3	0.48	63.82	5.3	0.0413	9.6	-269	243	86.8	9.1	100.2	5.3	137
210	47	46	0	0.99	4.9	0.065	54.9	0.0034	13.2	0.24	295.81	13.2	0.1403	53.3	2231	922	64.3	34.2	21.8	2.9	99
212	531	466	2	0.88	24.7	0.017	15.4	0.0027	5.0	0.33	369.36	5.0	0.0459	14.5	-10	351	17.2	2.6	17.4	0.9	283
213	21	14	0	0.68	35.4	0.177	182.8	0.0032	16.3	0.09	309.88	16.3	0.3979	182.1	3901	2739	165.5	279.2	20.8	3.4	99
214	149	151	1	1.02	166.2	0.017	45.2	0.0028	6.8	0.15	363.60	6.8	0.0446	44.6	-78	1092	17.0	7.6	17.7	1.2	123
215	65	50	0	0.76	129.8	0.021	77.6	0.0027	11.8	0.15	377.14	11.8	0.0574	76.7	508	1687	21.1	16.2	17.1	2.0	97
216	473	219	21	0.46	15767.7	0.300	26.1	0.0382	25.1	0.96	26.15	25.1	0.0570	6.9	491	152	266.8	61.2	241.9	59.7	51
217	61	32	0	0.53	34.8	0.086	217.3	0.0029	12.4	0.06	343.57	12.4	0.2147	217.0	2941	3506	83.9	175.1	18.7	2.3	99
218	100	65	0	0.65	31.6	0.011	88.0	0.0028	11.6	0.13	354.75	11.6	0.0281	87.2	-1367	2810	11.0	9.6	18.1	2.1	101
219	114	83	0	0.73	17.6	0.018	31.7	0.0025	7.2	0.23	399.36	7.2	0.0530	30.9	327	702	18.4	5.8	16.1	1.2	95
220	65	41	1	0.63	32.0	0.127	12.8	0.0170	5.9	0.46	58.67	5.9	0.0540	11.4	370	256	121.3	14.6	108.9	6.3	71
222	113	129	0	1.14	17.8	0.024	77.7	0.0026	8.9	0.11	384.70	8.9	0.0680	77.2	869	1601	24.5	18.8	16.7	1.5	98
225	83	78	1	0.93	6.8	0.053	45.8	0.0040	25.9	0.57	250.13	25.9	0.0955	37.8	1538	711	52.1	23.3	25.7	6.6	98
226	52	52	0	1.01	9.5	0.155	281.7	0.0026	16.2	0.06	378.06	16.2	0.4239	281.3	3996	4206	146.0	383.0	17.0	2.8	100
228	232	345	1	1.49	35.4	0.021	58.4	0.0025	8.1	0.14	403.74	8.1	0.0612	57.8	647	1242	21.0	12.1	15.9	1.3	98
229	94	91	0	0.96	6.1	0.027	30.0	0.0027	13.1	0.44	367.60	13.1	0.0717	27.0	978	551	27.0	8.0	17.5	2.3	98
230	406	738	2	1.82	71.8	0.014	36.8	0.0025	5.4	0.15	403.93	5.4	0.0417	36.4	-244	920	14.4	5.2	15.9	0.9	107
231	394	166	6	0.42	549.1	0.085	27.7	0.0122	24.6	0.89	81.67	24.6	0.0506	12.6	224	291	83.3	22.1	78.5	19.2	65
232	104	79	0	0.76	11.3	0.022	27.2	0.0027	7.1	0.26	370.04	7.1	0.0603	26.3	616	568	22.6	6.1	17.4	1.2	97
233	46	31	0	0.68	3.6	0.060	77.8	0.0029	12.4	0.16	341.61	12.4	0.1479	76.8	2322	1317	58.9	44.5	18.8	2.3	99
234	353	642	1	1.82	68.6	0.018	20.9	0.0024	11.0	0.53	412.75	11.0	0.0534	17.7	344	402	17.9	3.7	15.6	1.7	95
235	49	41	0	0.83	2.7	0.027	77.5	0.0029	18.8	0.24	346.17	18.8	0.0673	75.1	847	1563	26.9	20.5	18.6	3.5	98
236	54	58	0	1.07	18.0	0.240	340.0	0.0027	12.7	0.04	368.68	12.7	0.6416	339.7	4605	4912	218.4	668.0	17.5	2.2	100
237	389	318	1	0.82	66.6	0.011	52.8	0.0026	4.3	0.08	378.40	4.3	0.0313	52.6	-1030	1571	11.5	6.0	17.0	0.7	102
238	548	361	20	0.66	300.8	0.213	18.1	0.0275	17.6	0.97	36.36	17.6	0.0563	4.4	464	97	196.5	32.3	174.9	30.3	62
239	536	216	2	0.40	40.4	0.015	18.9	0.0026	5.2	0.28	389.09	5.2	0.0425	18.1	-198	454	15.2	2.8	16.5	0.9	108
240	133	114	1	0.86	6.0	0.016	39.1	0.0027	9.5	0.24	370.62	9.5	0.0434	38.0	-144	941	16.3	6.3	17.4	1.6	112
241	86	64	0	0.74	5.4	0.018	86.4	0.0028	10.5	0.12	358.31	10.5	0.0481	85.8	103	2028	18.6	15.9	18.0	1.9	82
242	249	291	1	1.17	27.3	0.019	25.2	0.0028	7.9	0.31	356.32	7.9	0.0487	23.9	131	562	18.9	4.7	18.1	1.4	86

KARG-15-09

243	235	135	7	0.57	179.4	0.149	9.8	0.0230	4.0	0.41	43.51	4.0	0.0469	9.0	44	214	140.7	12.9	146.5	5.8	-229
244	100	76	0	0.76	24.9	0.009	116.9	0.0026	10.7	0.09	379.93	10.7	0.0249	116.4	-1767	4123	9.2	10.6	16.9	1.8	101
245	212	132	5	0.62	6840.0	0.146	14.3	0.0196	5.2	0.36	51.04	5.2	0.0540	13.3	370	300	138.2	18.5	125.1	6.5	66
246	1046	1201	35	1.15	168.6	0.321	5.8	0.0186	4.1	0.69	53.91	4.1	0.1256	4.2	2037	74	282.9	14.4	118.5	4.8	94
247	136	75	3	0.55	198.6	0.097	12.6	0.0151	4.7	0.37	66.16	4.7	0.0466	11.7	26	280	94.0	11.3	96.7	4.5	-267
248	183	95	1	0.52	10.9	0.021	25.7	0.0028	7.3	0.28	362.53	7.3	0.0547	24.7	398	553	20.9	5.3	17.8	1.3	96
249	56	40	1	0.72	68.1	0.058	27.8	0.0090	5.7	0.21	111.06	5.7	0.0471	27.2	54	649	57.7	15.6	57.8	3.3	-7
250	274	230	1	0.84	18.5	0.018	23.0	0.0026	9.1	0.40	385.88	9.1	0.0492	21.1	155	494	17.7	4.0	16.7	1.5	89
251	189	298	4	1.57	335.4	0.097	15.2	0.0143	3.7	0.24	69.80	3.7	0.0489	14.7	144	346	93.7	13.6	91.7	3.3	36
252	375	375	1	1.00	38.7	0.017	20.3	0.0026	6.6	0.32	381.80	6.6	0.0474	19.2	71	457	17.2	3.5	16.9	1.1	76
253	98	122	2	1.24	60.0	0.140	23.5	0.0165	5.8	0.25	60.46	5.8	0.0615	22.8	658	488	133.3	29.4	105.8	6.1	84
254	90	120	0	1.32	33.0	0.054	220.4	0.0030	12.4	0.06	334.64	12.4	0.1312	220.0	2114	3858	53.4	114.7	19.2	2.4	99
255	125	168	0	1.34	41.2	0.011	72.8	0.0026	10.0	0.14	381.33	10.0	0.0296	72.1	-1206	2239	10.8	7.8	16.9	1.7	101
256	125	124	3	0.99	205.4	0.113	15.4	0.0157	5.4	0.35	63.63	5.4	0.0520	14.5	285	331	108.4	15.9	100.5	5.3	65

257	217	167	1	0.77	88.8	0.017	74.5	0.0027	6.3	0.08	374.87	6.3	0.0468	74.2	41	1776	17.3	12.8	17.2	1.1	58
258	234	124	1	0.53	61.1	0.027	27.4	0.0030	7.0	0.25	331.63	7.0	0.0658	26.5	799	555	27.4	7.4	19.4	1.4	98
259	81	101	0	1.24	11.4	0.065	127.9	0.0026	9.2	0.07	381.58	9.2	0.1795	127.5	2648	2116	63.8	79.1	16.9	1.6	99
260	330	373	8	1.13	845.6	0.111	8.8	0.0163	5.0	0.56	61.37	5.0	0.0492	7.2	159	169	106.5	8.9	104.2	5.1	35
261	90	111	0	1.24	18.7	0.033	55.7	0.0027	8.9	0.16	366.90	8.9	0.0888	55.0	1399	1054	33.3	18.3	17.5	1.6	99
262	177	106	36	0.60	1819.1	1.657	5.9	0.1612	4.5	0.75	6.20	4.5	0.0746	3.9	1057	78	992.4	37.6	963.3	40.1	9
263	114	87	0	0.76	36.6	0.014	100.7	0.0026	17.2	0.17	389.68	17.2	0.0403	99.2	-335	2553	14.4	14.4	16.5	2.8	105
264	519	494	11	0.95	13636.4	0.098	8.9	0.0153	5.1	0.57	65.29	5.1	0.0464	7.3	16	176	94.8	8.1	98.0	5.0	-514
265	290	201	8	0.69	349.9	0.143	8.7	0.0219	4.8	0.55	45.72	4.8	0.0473	7.3	65	173	135.5	11.1	139.5	6.7	-113
266	330	242	8	0.73	273.2	0.123	11.8	0.0182	1.9	0.16	54.85	1.9	0.0490	11.7	147	274	117.9	13.2	116.5	2.2	21
267	197	167	1	0.85	46.6	0.010	49.9	0.0025	8.4	0.17	393.86	8.4	0.0282	49.2	-1358	1583	10.0	4.9	16.3	1.4	101
268	458	901	2	1.97	37.6	0.015	32.8	0.0024	11.0	0.33	417.76	11.0	0.0455	30.9	-29	749	15.1	4.9	15.4	1.7	153
269	229	352	1	1.54	10.2	0.017	35.3	0.0024	12.7	0.36	418.50	12.7	0.0506	32.9	221	762	16.8	5.9	15.4	2.0	93
270	246	143	16	0.58	1732.0	0.391	7.4	0.0526	5.5	0.73	18.99	5.5	0.0539	5.0	368	113	335.5	21.2	330.7	17.6	10
271	59	48	0	0.82	7.7	0.028	53.6	0.0027	11.7	0.22	366.82	11.7	0.0734	52.3	1025	1058	27.6	14.6	17.5	2.1	98
272	356	211	7	0.59	257.4	0.113	8.0	0.0162	4.5	0.56	61.92	4.5	0.0508	6.6	230	153	108.7	8.3	103.3	4.6	55
273	102	99	0	0.97	22.3	0.025	61.2	0.0027	7.5	0.12	365.02	7.5	0.0662	60.7	812	1270	25.1	15.1	17.6	1.3	98
274	139	84	59	0.60	1911.6	5.144	3.2	0.3286	3.0	0.92	3.04	3.0	0.1135	1.2	1857	21	1843.4	27.0	1831.7	47.2	1
275	514	297	2	0.58	50.1	0.013	22.9	0.0023	4.4	0.19	438.68	4.4	0.0423	22.5	-206	564	13.4	3.1	14.7	0.6	107
276	293	273	6	0.93	220.4	0.102	9.7	0.0151	5.3	0.54	66.04	5.3	0.0486	8.1	129	191	98.2	9.1	96.9	5.1	25

CV-10

277	41	20	7	0.48	108.5	1.316	8.8	0.1379	7.0	0.80	7.25	7.0	0.0692	5.2	905	108	852.8	50.6	832.8	54.9	8
278	349	268	1	0.77	495.5	0.018	35.8	0.0024	4.7	0.13	420.70	4.7	0.0563	35.5	463	786	18.6	6.6	15.3	0.7	97
279	261	274	8	1.05	140.8	0.148	13.5	0.0190	5.6	0.41	52.56	5.6	0.0563	12.3	465	273	139.9	17.7	121.5	6.7	74
280	238	244	1	1.03	14.3	0.015	24.6	0.0027	4.7	0.19	370.47	4.7	0.0415	24.1	-254	610	15.6	3.8	17.4	0.8	107
282	412	191	2	0.46	512.5	0.026	16.3	0.0032	4.9	0.30	308.40	4.9	0.0571	15.5	496	341	25.6	4.1	20.9	1.0	96
283	106	82	2	0.78	56.8	0.088	17.6	0.0152	5.0	0.28	65.72	5.0	0.0418	16.8	-236	425	85.4	14.4	97.3	4.8	141
286	654	442	13	0.68	503.0	0.125	5.2	0.0155	3.2	0.61	64.59	3.2	0.0587	4.1	557	89	119.9	5.9	99.0	3.2	82
287	409	205	1	0.50	28.8	0.019	24.6	0.0025	7.3	0.30	403.92	7.3	0.0544	23.5	386	528	18.7	4.6	15.9	1.2	96
288	539	323	2	0.60	15.5	0.020	16.5	0.0026	5.9	0.36	379.06	5.9	0.0541	15.4	374	346	19.8	3.2	17.0	1.0	95
289	279	204	6	0.73	321.8	0.118	7.7	0.0164	5.0	0.64	60.98	5.0	0.0523	5.9	300	134	113.6	8.3	104.8	5.2	65
290	171	174	1	1.01	47.1	0.018	41.8	0.0028	6.1	0.15	360.37	6.1	0.0473	41.3	64	984	18.2	7.5	17.9	1.1	72
291	580	560	14	0.96	268.7	0.116	5.6	0.0171	2.8	0.49	58.65	2.8	0.0491	4.9	154	114	111.0	5.9	109.0	3.0	29
292	352	209	7	0.59	201.3	0.100	8.5	0.0148	4.3	0.51	67.47	4.3	0.0487	7.3	134	171	96.4	7.8	94.8	4.1	29
293	367	480	9	1.31	268.6	0.117	7.4	0.0157	3.4	0.46	63.54	3.4	0.0539	6.6	369	148	112.4	7.9	100.7	3.4	73
294	343	481	1	1.40	421.8	0.014	25.2	0.0027	7.7	0.30	367.10	7.7	0.0382	24.0	-474	635	14.5	3.6	17.5	1.3	104
295	226	192	1	0.85	76.3	0.027	15.1	0.0027	6.1	0.41	364.94	6.1	0.0719	13.8	983	280	27.2	4.0	17.6	1.1	98
296	228	283	1	1.25	8.0	0.024	36.8	0.0027	6.0	0.16	372.10	6.0	0.0650	36.4	773	765	24.1	8.8	17.3	1.0	98
297	365	224	1	0.61	56.7	0.016	21.3	0.0024	5.4	0.25	409.58	5.4	0.0471	20.6	53	491	16.0	3.4	15.7	0.8	70
298	1220	410	37	0.34	534.2	0.216	5.4	0.0245	3.4	0.63	40.80	3.4	0.0638	4.2	735	88	198.2	9.7	156.1	5.3	79
299	338	241	5	0.71	127.5	0.085	8.9	0.0122	3.6	0.40	81.93	3.6	0.0505	8.1	216	189	82.8	7.1	78.2	2.8	64
300	722	445	20	0.62	387.3	0.158	7.2	0.0220	4.2	0.58	45.52	4.2	0.0523	5.8	298	132	149.3	10.0	140.1	5.8	53

Toba Blanca

301	724	432	2	0.60	396.1	0.017	11.0	0.0026	4.6	0.41	382.60	4.6	0.0483	10.0	115	237	17.5	1.9	16.8	0.8	85
-----	-----	-----	---	------	-------	-------	------	--------	-----	------	--------	-----	--------	------	-----	-----	------	-----	------	-----	----

302	255	255	1	1.00	42.2	0.015	26.1	0.0027	5.6	0.21	373.37	5.6	0.0414	25.5	-265	647	15.4	4.0	17.2	1.0	107
303	93	85	0	0.91	5.2	0.016	63.1	0.0027	11.1	0.18	372.67	11.1	0.0434	62.1	-143	1539	16.2	10.1	17.3	1.9	112
304	349	295	1	0.85	21.6	0.016	28.4	0.0027	7.0	0.25	366.71	7.0	0.0414	27.5	-263	698	15.7	4.4	17.6	1.2	107
305	341	291	1	0.85	75.5	0.019	30.2	0.0029	10.8	0.36	341.95	10.8	0.0463	28.2	15	677	18.8	5.6	18.8	2.0	-25
306	693	778	15	1.12	3780.7	0.104	8.0	0.0158	4.7	0.58	63.39	4.7	0.0479	6.5	95	154	100.7	7.7	100.9	4.7	-6
308	102	111	0	1.09	57.3	0.014	81.5	0.0026	7.2	0.09	390.18	7.2	0.0407	81.2	-306	2077	14.5	11.7	16.5	1.2	105
309	79	85	0	1.08	20.4	0.312	1814.8	0.0028	11.4	0.01	354.85	11.4	0.8020	1814.8	4925	25843	275.4	4378.0	18.1	2.1	100
310	303	159	2	0.52	138.0	0.030	20.1	0.0043	14.5	0.72	234.73	14.5	0.0506	14.0	222	324	29.7	5.9	27.4	4.0	88
311	427	338	1	0.79	37.6	0.016	18.0	0.0025	5.5	0.30	403.63	5.5	0.0463	17.2	15	413	15.9	2.9	16.0	0.9	-5
312	779	835	3	1.07	34.4	0.020	11.9	0.0027	7.8	0.65	370.92	7.8	0.0533	9.0	340	203	19.9	2.3	17.4	1.3	95
313	628	392	2	0.62	208.5	0.017	15.8	0.0027	3.7	0.23	375.27	3.7	0.0474	15.3	69	365	17.5	2.7	17.2	0.6	75
314	454	449	2	0.99	54.1	0.022	11.7	0.0027	4.3	0.36	364.77	4.3	0.0583	10.9	539	239	22.1	2.6	17.6	0.8	97
316	263	244	1	0.93	17.5	0.030	42.1	0.0026	6.3	0.15	380.54	6.3	0.0824	41.6	1255	814	29.9	12.4	16.9	1.1	99
317	790	631	3	0.80	159.9	0.018	12.6	0.0026	4.8	0.38	385.53	4.8	0.0512	11.6	248	267	18.4	2.3	16.7	0.8	93
318	635	357	2	0.56	184.9	0.015	16.3	0.0025	5.7	0.35	394.51	5.7	0.0437	15.3	-129	377	15.4	2.5	16.3	0.9	113
319	113	131	0	1.16	7.3	0.026	39.3	0.0028	8.4	0.21	352.95	8.4	0.0661	38.4	809	803	25.9	10.0	18.2	1.5	98
320	361	718	1	1.99	26.7	0.014	23.5	0.0026	7.4	0.31	388.34	7.4	0.0383	22.3	-468	590	13.7	3.2	16.6	1.2	104
321	160	190	3	1.18	62.8	0.117	15.7	0.0144	4.2	0.27	69.40	4.2	0.0589	15.2	564	330	112.4	16.8	92.2	3.9	84
322	518	563	2	1.09	535.6	0.030	25.5	0.0029	5.1	0.20	342.78	5.1	0.0757	25.0	1087	500	30.5	7.6	18.8	1.0	98
323	213	154	1	0.72	783.8	0.015	34.7	0.0027	5.6	0.16	365.54	5.6	0.0410	34.2	-285	873	15.6	5.4	17.6	1.0	106
324	290	551	4	1.90	37.3	0.244	21.0	0.0049	13.2	0.63	205.18	13.2	0.3632	16.4	3763	248	221.8	41.9	31.3	4.1	99
325	782	622	3	0.79	120.6	0.017	13.3	0.0026	4.3	0.32	385.90	4.3	0.0479	12.5	95	297	17.2	2.3	16.7	0.7	82
326	796	658	3	0.83	73.2	0.015	11.3	0.0026	4.3	0.37	379.04	4.3	0.0408	10.5	-299	268	15.0	1.7	17.0	0.7	106
327	221	452	1	2.04	97.5	0.028	60.0	0.0030	9.2	0.15	331.10	9.2	0.0677	59.2	860	1229	28.2	16.7	19.4	1.8	98
328	604	755	2	1.25	98.3	0.018	19.5	0.0027	3.3	0.17	367.68	3.3	0.0475	19.2	73	456	17.9	3.5	17.5	0.6	76
330	110	102	2	0.93	92.0	0.123	14.3	0.0158	6.1	0.42	63.43	6.1	0.0568	12.9	484	286	118.2	16.0	100.8	6.1	79
331	388	338	1	0.87	17.3	0.011	39.1	0.0026	5.8	0.15	382.78	5.8	0.0316	38.7	-1004	1147	11.5	4.5	16.8	1.0	102
332	169	241	1	1.42	91.7	0.027	98.4	0.0027	10.1	0.10	374.71	10.1	0.0744	97.9	1053	1971	27.4	26.6	17.2	1.7	98
333	332	198	1	0.60	18.8	0.040	17.3	0.0029	5.3	0.31	349.62	5.3	0.1018	16.4	1657	304	40.0	6.8	18.4	1.0	99

KARG-15-12

335	84	57	2	0.68	152.1	0.099	14.8	0.0154	5.4	0.36	64.75	5.4	0.0466	13.8	28	330	96.0	13.5	98.8	5.3	-251
336	69	34	0	0.48	11.0	0.251	770.6	0.0026	10.5	0.01	377.67	10.5	0.6867	770.6	4703	11087	227.1	1568.4	17.0	1.8	100
337	126	84	0	0.67	9.2	0.020	28.8	0.0025	10.0	0.35	393.20	10.0	0.0574	27.1	508	595	20.2	5.8	16.4	1.6	97
338	150	84	1	0.56	1713.9	0.021	47.2	0.0026	6.1	0.13	377.64	6.1	0.0576	46.8	514	1029	21.1	9.9	17.0	1.0	97
339	121	57	1	0.47	9.4	0.020	35.7	0.0036	10.9	0.30	274.66	10.9	0.0390	34.0	-416	889	19.7	7.0	23.4	2.5	106
340	606	509	2	0.84	141.7	0.015	15.1	0.0027	4.0	0.26	374.25	4.0	0.0401	14.6	-347	377	14.9	2.2	17.2	0.7	105
341	79	72	0	0.91	31.4	0.024	40.8	0.0031	8.2	0.20	322.80	8.2	0.0563	40.0	466	885	24.1	9.7	19.9	1.6	96
343	247	221	1	0.89	76.4	0.021	24.3	0.0028	6.8	0.28	361.48	6.8	0.0539	23.3	368	526	20.7	5.0	17.8	1.2	95
345	71	51	0	0.71	7.3	0.049	111.9	0.0023	14.3	0.13	432.21	14.3	0.1529	110.9	2379	1891	48.4	52.8	14.9	2.1	99
346	68	30	1	0.45	15.1	0.182	673.2	0.0064	7.7	0.01	157.03	7.7	0.2067	673.1	2880	10933	169.4	1050.2	40.9	3.1	99
347	794	1673	9	2.11	129.5	0.037	9.5	0.0062	2.6	0.27	162.04	2.6	0.0439	9.1	-114	225	37.3	3.5	39.7	1.0	135
349	46	18	0	0.40	4.4	0.055	93.3	0.0031	11.4	0.12	324.85	11.4	0.1289	92.6	2082	1629	54.1	49.1	19.8	2.3	99
350	399	210	3	0.53	1924.6	0.038	9.8	0.0062	4.6	0.47	162.25	4.6	0.0446	8.6	-77	211	37.8	3.6	39.6	1.8	151
351	190	163	1	0.86	32.3	0.014	28.0	0.0029	6.2	0.22	342.11	6.2	0.0356	27.4	-659	753	14.5	4.0	18.8	1.2	103
352	172	84	1	0.49	7.5	0.012	22.8	0.0029	8.0	0.35	350.32	8.0	0.0299	21.4	-1165	659	11.9	2.7	18.4	1.5	102

353	394	338	5	0.86	65.7	0.209	15.2	0.0043	9.1	0.59	235.22	9.1	0.3567	12.2	3736	186	192.8	26.8	27.3	2.5	99
355	485	603	31	1.24	1496.3	0.291	4.5	0.0414	3.1	0.68	24.18	3.1	0.0510	3.3	239	76	259.0	10.4	261.2	8.0	-9
356	752	706	3	0.94	171.0	0.017	20.0	0.0026	8.5	0.43	387.61	8.5	0.0490	18.0	146	423	17.5	3.5	16.6	1.4	89
358	101	138	0	1.36	7.2	0.056	292.4	0.0024	13.3	0.05	422.26	13.3	0.1726	292.1	2584	4877	55.7	158.5	15.2	2.0	99
359	141	209	1	1.48	7.9	0.040	138.4	0.0023	9.8	0.07	440.60	9.8	0.1288	138.0	2081	2430	40.1	54.4	14.6	1.4	99
360	94	86	0	0.92	35.3	0.096	292.3	0.0028	6.1	0.02	356.19	6.1	0.2472	292.3	3167	4633	92.8	259.3	18.1	1.1	99
361	144	217	1	1.51	55.9	0.022	45.1	0.0026	9.9	0.22	390.37	9.9	0.0620	44.0	675	940	22.0	9.8	16.5	1.6	98
362	129	192	1	1.49	9.7	0.019	130.0	0.0025	10.1	0.08	394.53	10.1	0.0534	129.6	345	2932	18.8	24.2	16.3	1.7	95
363	124	183	1	1.48	16.5	0.022	75.6	0.0027	8.0	0.11	374.12	8.0	0.0598	75.2	597	1629	22.1	16.6	17.2	1.4	97
365	176	299	1	1.70	80.7	0.021	71.7	0.0027	7.8	0.11	368.33	7.8	0.0560	71.3	452	1583	21.1	15.0	17.5	1.4	96
366	376	404	1	1.08	178.0	0.017	19.5	0.0026	5.6	0.29	390.34	5.6	0.0493	18.7	162	437	17.5	3.4	16.5	0.9	90
367	139	239	1	1.71	7.6	0.017	72.1	0.0027	7.6	0.11	365.13	7.6	0.0446	71.7	-77	1754	17.0	12.1	17.6	1.3	123
368	111	208	0	1.88	19.3	0.018	60.5	0.0028	11.0	0.18	362.53	11.0	0.0473	59.5	64	1418	18.1	10.9	17.8	1.9	72
369	102	121	0	1.19	11.7	0.068	209.3	0.0025	9.1	0.04	395.68	9.1	0.1961	209.1	2794	3422	67.1	135.9	16.3	1.5	99
371	103	190	0	1.84	4.9	0.033	70.1	0.0027	18.2	0.26	370.85	18.2	0.0900	67.7	1425	1292	33.4	23.0	17.4	3.2	99
372	88	100	2	1.14	290.7	0.101	12.5	0.0158	4.2	0.34	63.37	4.2	0.0464	11.7	19	282	97.7	11.6	100.9	4.2	-440
374	49	67	2	1.35	544.1	1.082	26.0	0.0134	21.6	0.83	74.60	21.6	0.5853	14.4	4472	210	744.5	137.0	85.8	18.4	98
375	84	123	0	1.46	8.0	0.018	73.2	0.0026	9.5	0.13	379.52	9.5	0.0504	72.6	215	1682	18.4	13.4	17.0	1.6	92

Supplementary R Code

```
library(modifiedBChron)
dates <- read.csv("~/tableB2.csv")
means <- read.csv("~/tableB1.csv")
##-----
## generate the age model using the full PDF
model <- ageModel(ages = dates$age,
  ageSds = dates$ageSds,
  positions = dates$position,
  positionThicknesses = dates$thickness,
  ids = dates$ids,
  distTypes = dates$distType,
  predictPositions = seq(min(dates$position),
    max(dates$position),
    length = 500),
  MC = 100000,
  burn = 5000,
  truncateUp = 16)
##-----
## generate the age model using the weighted means PDF
meanModel <- ageModel(ages = means$age,
  ageSds = means$ageSds,
  positions = means$position,
  positionThicknesses = means$thickness,
  ids = means$ids,
  predictPositions = seq(min(dates$position),
    max(dates$position),
    length = 500),
  distTypes = means$distType,
  MC = 100000,
  burn = 5000,
  truncateUp = 16)
##-----
## plot the model results
modelPlot(meanModel)
modelPlot(model)
```

Table B3. Input file for the summed probability distribution model. Tracer and decay constant uncertainties were propagated onto individual zircon grain ages to allow direct comparison to $^{40}\text{Ar}/^{39}\text{Ar}$ ages included in the model. See Supplementary Methods for more details. 1Data for individual $^{40}\text{Ar}/^{39}\text{Ar}$ laser fusion analyses from Perkins et al. (2012) provided by Matthew Heizler at the New Mexico Geochronological Research Laboratory (personal communication).

ids	age	ageSds	position	thickness	distType
CV-13	17.634	0.016	48.25	3.125	G
CV-13	17.629	0.025	48.25	3.125	G
CV-13	17.603	0.029	48.25	3.125	G
CV-13	17.599	0.019	48.25	3.125	G
CV-13	17.592	0.020	48.25	3.125	G
^1CO	17.119	0.113	84.5	2.5	G
^1CO	17.119	0.113	84.5	2.5	G
^1CO	17.180	0.133	84.5	2.5	G
^1CO	17.240	0.103	84.5	2.5	G
^1CO	17.351	0.104	84.5	2.5	G
^1CO	17.401	0.123	84.5	2.5	G
^1CO	17.431	0.113	84.5	2.5	G
^1CO	17.492	0.123	84.5	2.5	G
^1CO	17.613	0.133	84.5	2.5	G
KARG-15-09	17.028	0.032	151.5	1.8	G
KARG-15-09	16.997	0.023	151.5	1.8	G
KARG-15-01	16.854	0.012	161	0	G
KARG-15-01	16.850	0.014	161	0	G
KARG-15-01	16.849	0.016	161	0	G
KARG-15-01	16.846	0.021	161	0	G

KARG-15-01	16.836	0.015	161	0	G
Toba Blanca	16.883	0.018	175	0	G
Toba Blanca	16.859	0.038	175	0	G
Toba Blanca	16.823	0.030	175	0	G
CV-10	16.877	0.029	179	0	G
CV-10	16.833	0.025	179	0	G
CV-10	16.760	0.034	179	0	G
CV-10	16.751	0.057	179	0	G
¹ CO3	16.397	0.088	193.5	1.5	G
¹ CO3	16.468	0.098	193.5	1.5	G
¹ CO3	16.601	0.086	193.5	1.5	G
¹ CO3	16.644	0.081	193.5	1.5	G
¹ CO3	16.656	0.083	193.5	1.5	G
¹ CO3	16.667	0.113	193.5	1.5	G
¹ CO3	16.678	0.079	193.5	1.5	G
¹ CO3	16.685	0.082	193.5	1.5	G

Table B4. Input file for the weighted mean model. ¹Weighed mean ages recalculated from individual laser fusion analyses of Perkins et al. (2012) provided by Matthew Heizler at the New Mexico Geochronological Research Laboratory (personal communication).

ids	age	ageSds	position	thickness	distType
CV-13	17.615	0.013	48.25	3.125	G
¹ CO	17.31	0.056	84.5	2.5	G
KARG-15-09	17.006	0.02	151.5	1.8	G
KARG-15-01	16.85	0.011	161	0	G
Toba Blanca	16.868	0.016	175	0	G
CV-10	16.825	0.018	179	0	G
¹ CO3	16.605	0.031	193.5	1.5	G

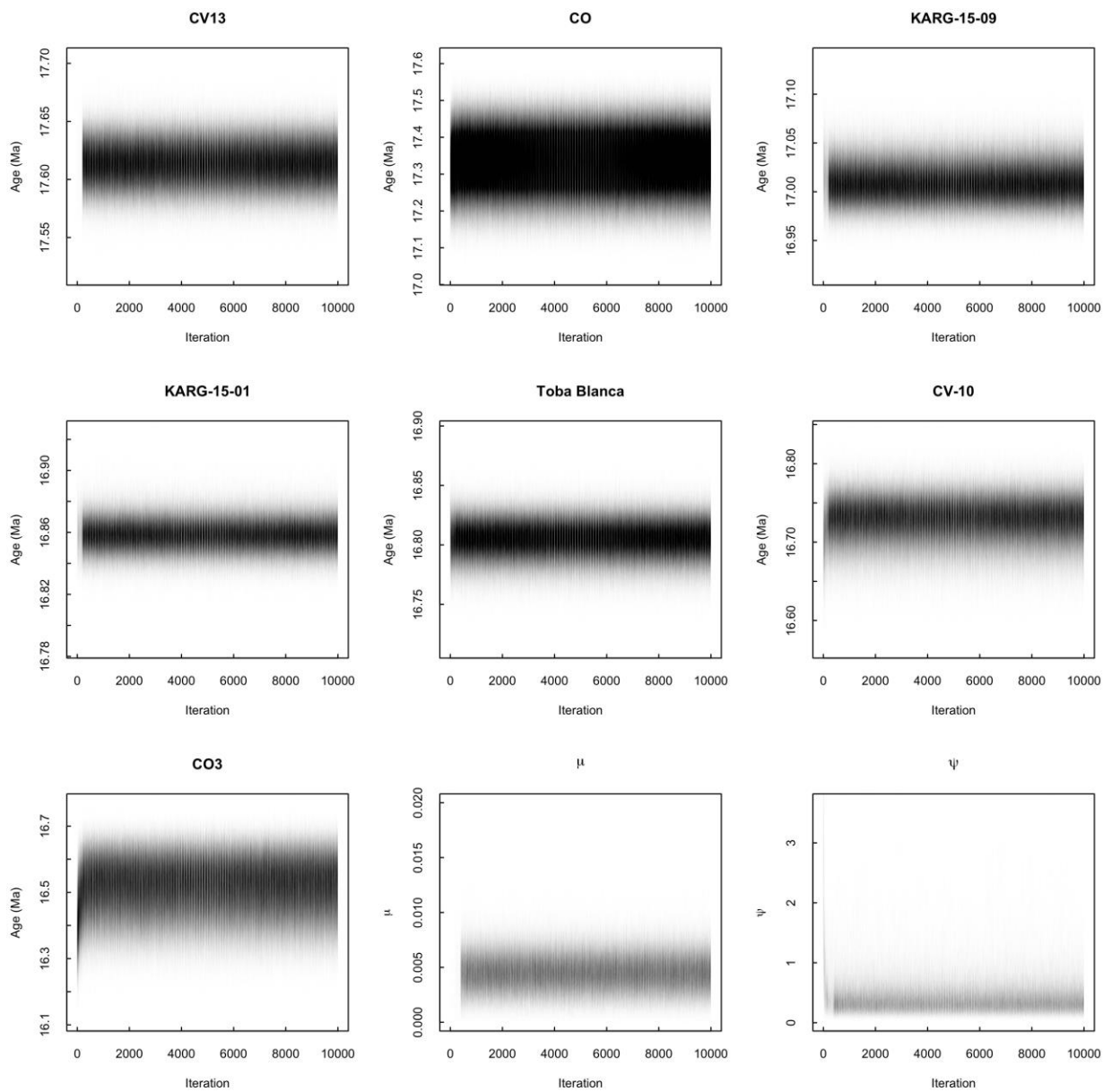


Figure B1. Superimposed trace plots of each model parameter from 500 independent simulations

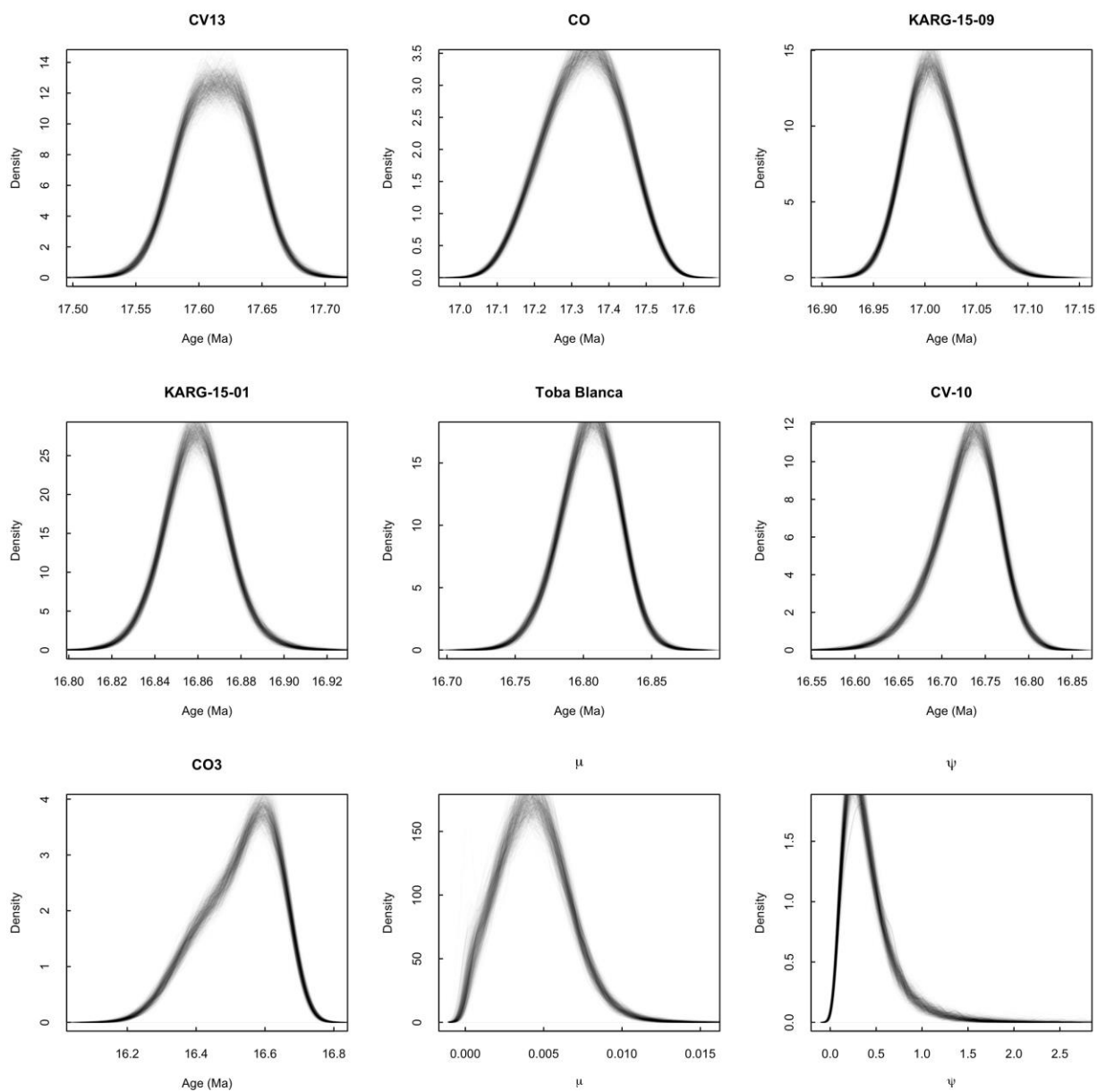


Figure B2. Superimposed density plots of each model parameter from 500 independent simulations.

APPENDIX C

Table C1. Bulk stable isotope data for Chapter 3

Family	Genus	sample ID	Tissue	$\delta^{13}\text{C}$	$\delta^{18}\text{O}$	Stratigraphic Position (m)	Locality
Astrapotheriidae	<i>Astrapotherium</i>	RB3- MK-15-003	enamel	-11.2	20.3	84.5	RB2
	<i>Astrapotherium</i>	RB3-MK-15-011	enamel	-10.7	20.1	84.5	RB2
	<i>Astrapotherium</i>	CV-RT-15-042	enamel	-8.8	21.3	91	CV
	<i>Astrapotherium</i>	CV-RT-15-043	enamel	-10.8	22.1	97	CV
	<i>Astrapotherium</i>	CV-RT-15-047	enamel	-10.8	20.5	97	CV
	<i>Astrapotherium</i>	CV-RT-15-046	enamel	-13.0	19.6	98.5	CV
	<i>Astrapotherium</i>	CV-RT-15-069	enamel	-11.7	21.1	125	CV
	<i>Astrapotherium</i>	CV-RT-15-072	enamel	-10.8	20.9	136.25	CV
	<i>Astrapotherium</i>	RB3-RT-15-010	enamel	-10.0	20.5	149	RB2
	<i>Astrapotherium</i>	CV-RT-15-002	enamel	-10.7	21.2	170	CV
	<i>Astrapotherium</i>	CV-RT-15-019	enamel	-11.2	21.8	183.5	CV
	Homalodotheriidae	<i>Homalodotherium</i>	CV-RT-15-040	enamel	-11.9	24.2	110.5
<i>Homalodotherium</i>		RB3-RT-15-007	enamel	-10.4	23.9	177.5	RB2
<i>Homalodotherium</i>		CV-RT-15-030	enamel	-8.8	25.8	181	CV
<i>Homalodotherium</i>		CV-RT-15-017	enamel	-10.5	24.8	200	CV
<i>Homalodotherium</i>		CV-RT-15-034	enamel	-11.5	23.5	200	CV
Intratheriidae	<i>Protypotherium</i>	CV-RT-15-011	enamel	-9.7	26.3	170	CV
	<i>Protypotherium</i>	CV-RT-15-011.2	enamel	-9.3	26.1	170	CV
Toxodontidae	<i>Adinotherium</i>	CV-RT-15-021	enamel	-11.9	22.5	75.5	CV
	<i>Adinotherium</i>	CV-RT-15-037	enamel	-13.3	23.8	79.9	CV
	<i>Adinotherium</i>	RB2-MK-15-005	enamel	-14.8	23.3	81	RB2
	<i>Adinotherium</i>	RB2-MK-15-011	enamel	-13.3	25.9	84.5	RB2
	<i>Adinotherium</i>	CV-RT-15-044	enamel	-12.2	22.4	92.3	CV
	<i>Adinotherium</i>	CV-MK-15-002	enamel	-12.3	25.4	92.5	CV
	<i>Adinotherium</i>	CV-MK-15-004	enamel	-12.8	24.0	93.5	CV
	<i>Adinotherium</i>	CV-RT-15-043	enamel	-11.0	22.4	97	CV
	<i>Adinotherium</i>	CV-RT-15-046	enamel	-12.1	23.0	98.5	CV

<i>Adinotherium</i>	CV-RT-15-086	enamel	-11.8	23.1	106.5	CV
<i>Adinotherium</i>	CV-RT-15-048	enamel	-11.0	21.4	108	CV
<i>Adinotherium</i>	CV-RT-15-069	enamel	-13.9	22.9	125	CV
<i>Adinotherium</i>	CV-RT-15-087	enamel	-12.3	20.6	131.5	CV
<i>Adinotherium</i>	RB3-RT-15-011	enamel	-12.4	25.3	147	RB2
<i>Adinotherium</i>	RB3-RT-15-002	enamel	-13.2	23.2	151	RB2
<i>Adinotherium</i>	RB3-RT-15-005	enamel	-9.8	23.0	177	RB2
<i>Adinotherium</i>	CV-RT-15-031	enamel	-12.6	22.2	179	CV
<i>Adinotherium</i>	CV-RT-15-014	enamel	-10.5	25.2	190	CV
<i>Nesodon</i>	CV-RT-15-020	enamel	-12.0	22.2	75.5	CV
<i>Nesodon</i>	CV-RT-15-007	enamel	-12.1	24.7	76	CV
<i>Nesodon</i>	CV-RT-15-037	enamel	-11.5	20.6	79.9	CV
<i>Nesodon</i>	CV-RT-15-027	enamel	-11.5	22.6	82.2	CV
<i>Nesodon</i>	CV-RT-15-027	enamel	-11.8	22.3	82.2	CV
<i>Nesodon</i>	RB2-MK-15-009	enamel	-12.8	24.0	84	RB2
<i>Nesodon</i>	RB2-MK-15-003	enamel	-12.5	22.3	84.5	RB2
<i>Nesodon</i>	RB2-MK-15-010	enamel	-11.9	22.5	84.5	RB2
<i>Nesodon</i>	RB2-MK-15-014	enamel	-12.2	21.7	84.5	RB2
<i>Nesodon</i>	RB2-MK-15-016	enamel	-12.5	22.2	84.5	RB2
<i>Nesodon</i>	RB3-MK-15-010	enamel	-11.1	25.6	84.5	RB2
<i>Nesodon</i>	CV-MK-15-002	enamel	-10.4	22.9	92.5	CV
<i>Nesodon</i>	CV-MK-15-003	enamel	-10.8	20.3	93.5	CV
<i>Nesodon</i>	CV-RT-15-008	enamel	-11.1	23.8	96.5	CV
<i>Nesodon</i>	CV-RT-15-043	enamel	-11.0	23.7	97	CV
<i>Nesodon</i>	CV-RT-15-085	enamel	-11.4	23.6	105.5	CV
<i>Nesodon</i>	CV-RT-15-040	enamel	-11.1	22.4	107.5	CV
<i>Nesodon</i>	CV-RT-15-049	enamel	-12.5	23.3	107.5	CV
<i>Nesodon</i>	CV-RT-15-038	enamel	-12.5	21.4	110.5	CV
<i>Nesodon</i>	CV-RT-15-068	enamel	-10.7	20.7	121.25	CV
<i>Nesodon</i>	CV-RT-15-053	enamel	-9.8	22.0	121.5	CV

<i>Nesodon</i>	CV-RT-15-080	enamel	-10.3	22.1	128.5	CV	
<i>Nesodon</i>	CV-RT-15-074	enamel	-9.4	23.8	134.75	CV	
<i>Nesodon</i>	RB3-RT-15-003	enamel	-10.7	23.5	160	RB2	
<i>Nesodon</i>	RB3-RT-15-003	enamel	-10.5	23.7	160	RB2	
<i>Nesodon</i>	CV-RT-15-010	enamel	-10.7	24.4	170	CV	
<i>Nesodon</i>	CV-RT-15-031	enamel	-12.8	23.6	179	CV	
<i>Nesodon</i>	CV-RT-15-019	enamel	-11.5	22.6	183.5	CV	
<i>Nesodon</i>	CV-RT-15-013	enamel	-11.3	23.8	190	CV	
<i>Nesodon</i>	CV-RT-15-016	enamel	-11.8	23.1	200	CV	
<i>Nesodon</i>	CV-RT-15-016	enamel	-11.3	23.6	200	CV	
<i>Nesodon</i>	CV-RT-15-009	enamel	-10.6	25.2	219	CV	
-	RB2-MK-15-008	enamel	-11.4	23.3	84	RB2	
-	RB2-MK-15-001	enamel	-12.6	24.5	84.5	RB2	
-	RB2-MK-15-006	enamel	-12.6	21.4	84.5	RB2	
-	RB2-MK-15-013	enamel	-12.3	23.4	84.5	RB2	
-	RB2-MK-15-015	enamel	-12.8	22.9	84.5	RB2	
-	CV-MK-15-002	enamel	-10.4	25.4	92.5	CV	
-	CV-RT-15-011	enamel	-10.7	24.1	170	CV	
-	CV-RT-15-013	enamel	-10.2	23.4	190	CV	
<hr/>							
Macraucheniiidae/ Proterotheriidae	-	RB2-MK-15-007	enamel	-12.8	26.7	83.3	RB2
-	-	RB3-MK-15-013	enamel	-11.0	23.5	84.5	RB2
-	-	CV-RT-15-082	enamel	-12.8	24.6	102	CV
-	-	CV-RT-15-051	enamel	-11.1	24.4	127.5	CV
-	-	CV-RT-15-052	enamel	-12.6	22.5	128	CV
-	-	RB3-RT-15-006	enamel	-9.7	24.6	145	RB2
-	-	RB3-RT-15-008	enamel	-10.4	24.7	145	RB2
-	-	RB3-RT-15-009	enamel	-9.7	23.6	145	RB2
-	-	RB3-RT-15-002	enamel	-10.4	27.5	151	RB2
-	-	CV-RT-15-013	enamel	-10.2	28.6	190	CV
-	-	RB3-MK-15-013	enamel	-12.4	22.3	195	RB2

-	-	CV-RT-15-063	bone	-11.4	21.3	77.5	CV
-	-	CV-RT-15-059	bone	-9.0	21.8	78.9	CV
-	-	CV-RT-15-058	bone	-13.5	20.9	79	CV
-	-	CV-RT-15-060	bone	-8.6	21.7	79.5	CV
-	-	RB2-MK-15-004	bone	-11.1	22.4	83.3	RB2
-	-	CV-RT-15-061	bone	-13.9	21.0	84.5	CV
-	-	RB2-MK-15-011	bone	-11.9	21.5	84.5	RB2
-	-	RB2-MK-15-013	bone	-14.7	21.9	84.5	RB2
-	-	RB2-MK-15-014	bone	-15.2	22.1	84.5	RB2
-	-	CV-RT-15-062	bone	-15.6	20.5	84.75	CV
-	-	CV-RT-15-066	bone	-8.8	22.4	89.5	CV
-	-	CV-RT-15-057	bone	-12.0	20.6	91.25	CV
-	-	CV-RT-15-067	bone	-10.3	22.7	92	CV
-	-	CV-MK-15-002	bone	-11.3	22.3	92.5	CV
-	-	CV-RT-15-054	bone	-9.8	21.9	93	CV
-	-	CV-RT-15-056	bone	-9.0	21.7	101.25	CV
-	-	CV-RT-15-064	bone	-8.3	21.8	101.25	CV
-	-	CV-RT-15-083	bone	-9.7	22.8	102	CV
-	-	CV-RT-15-065	bone	-8.8	23.1	102.5	CV
-	-	CV-RT-15-081	bone	-10.8	22.2	104.5	CV
-	-	CV-RT-15-084	bone	-13.2	19.6	105.5	CV
-	-	CV-RT-15-085	bone	-10.6	21.6	105.5	CV
-	-	CV-RT-15-068	bone	-11.0	20.6	121.25	CV
-	-	CV-RT-15-069	bone	-9.6	22.2	125	CV
-	-	CV-RT-15-080	bone	-10.2	22.1	128.5	CV
-	-	CV-RT-15-087	bone	-8.6	23.7	131.5	CV
-	-	CV-RT-15-073	bone	-10.1	22.4	134.75	CV
-	-	CV-RT-15-072	bone	-8.5	21.8	136.25	CV
-	-	CV-RT-15-071	bone	-8.9	21.5	142	CV

-	-	CV-RT-15-079	bone	-9.5	21.8	143.5	CV
-	-	CV-RT-15-070	bone	-10.3	22.1	145.5	CV
-	-	RB3-RT-15-011	bone	-10.8	21.3	147	RB2
-	-	RB3-RT-15-010	bone	-9.8	20.1	149	RB2
-	-	CV-RT-15-075	bone	-10.7	21.1	159	CV
-	-	CV-RT-15-076	bone	-10.0	20.8	159	CV
-	-	CV-RT-15-077	bone	-9.3	23.6	159	CV
-	-	CV-RT-15-002	bone	-12.8	22.9	170	CV
-	-	RB3-MK-15-007	bone	-8.6	23.1	172.5	RB2
-	-	RB3-RT-15-007	bone	-9.5	21.1	177.5	RB2
-	-	RB3-MK-15-001	bone	-9.3	22.5	179	RB2
-	-	RB3-MK-15-005	bone	-14.1	21.6	179.5	RB2
-	-	RB3-MK-15-014	bone	-9.7	21.6	181.5	RB2
-	-	RB3-MK-15-009	bone	-9.4	22.3	184.5	RB2
-	-	RB3-MK-15-004	bone	-10.0	20.6	189.5	RB2
-	-	RB3-MK-15-002	bone	-9.7	22.5	191	RB2
-	-	RB3-MK-15-003	bone	-9.6	22.7	192	RB2
-	-	RB3-MK-15-013	bone	-11.0	20.5	195	RB2
-	-	RB3-MK-15-012	bone	-8.9	22.3	210.5	RB2

Table C2. Serial sampled stable isotope data for Chapter 3.

Position (mm)	taxa	sample	subsample	tissue	$\delta^{13}\text{C}$	$\delta^{18}\text{O}$	Stratigraphic position (m)	locality
3.73	<i>Astrapotherium</i>	CV-RT-15-002	A	enamel	-10.54	22.03	92.5	CV
6.16	<i>Astrapotherium</i>	CV-RT-15-002	B	enamel	-10.58	21.82	92.5	CV
7.83	<i>Astrapotherium</i>	CV-RT-15-002	C	enamel	-10.55	21.96	92.5	CV
9.68	<i>Astrapotherium</i>	CV-RT-15-002	D	enamel	-10.49	22.23	92.5	CV
12.2	<i>Astrapotherium</i>	CV-RT-15-002	E	enamel	-10.85	21.90	92.5	CV
14.56	<i>Astrapotherium</i>	CV-RT-15-002	F	enamel	-10.54	21.40	92.5	CV
16.56	<i>Astrapotherium</i>	CV-RT-15-002	G	enamel	-10.44	21.24	92.5	CV
18.9	<i>Astrapotherium</i>	CV-RT-15-002	H	enamel	-10.68	21.74	92.5	CV
21.08	<i>Astrapotherium</i>	CV-RT-15-002	I	enamel	-10.73	20.50	92.5	CV
22.88	<i>Astrapotherium</i>	CV-RT-15-002	J	enamel	-10.77	20.85	92.5	CV
25.26	<i>Astrapotherium</i>	CV-RT-15-002	K	enamel	-10.88	19.05	92.5	CV
27.49	<i>Astrapotherium</i>	CV-RT-15-002	L	enamel	-10.87	20.30	92.5	CV
29.08	<i>Astrapotherium</i>	CV-RT-15-002	M	enamel	-10.78	20.84	92.5	CV
32.89	<i>Astrapotherium</i>	CV-RT-15-002	O	enamel	-10.84	20.77	92.5	CV
34.9	<i>Astrapotherium</i>	CV-RT-15-002	P	enamel	-10.63	22.17	92.5	CV
37.12	<i>Astrapotherium</i>	CV-RT-15-002	Q	enamel	-10.52	21.62	92.5	CV
38.86	<i>Astrapotherium</i>	CV-RT-15-002	R	enamel	-10.51	20.47	92.5	CV
41.14	<i>Astrapotherium</i>	CV-RT-15-002	S	enamel	-10.49	21.69	92.5	CV
43.39	<i>Astrapotherium</i>	CV-RT-15-002	T	enamel	-10.53	22.03	92.5	CV
45.41	<i>Astrapotherium</i>	CV-RT-15-002	U	enamel	-10.55	20.75	92.5	CV
47.6	<i>Astrapotherium</i>	CV-RT-15-002	V	enamel	-10.65	20.74	92.5	CV
49.72	<i>Astrapotherium</i>	CV-RT-15-002	W	enamel	-10.92	20.93	92.5	CV
51.97	<i>Astrapotherium</i>	CV-RT-15-002	X	enamel	-10.91	20.70	92.5	CV
53.75	<i>Astrapotherium</i>	CV-RT-15-002	Y	enamel	-11.05	19.76	92.5	CV
2.32	<i>Nesodon</i>	CV-RT-15-016	A	enamel	-11.79	24.32	200	CV
46.87	<i>Nesodon</i>	CV-RT-15-016	AA	enamel	-12.29	24.07	200	CV
48.52	<i>Nesodon</i>	CV-RT-15-016	AB	enamel	-12.39	23.95	200	CV

50.78	<i>Nesodon</i>	CV-RT-15-016	AC	enamel	-12.29	23.32	200	CV
54.41	<i>Nesodon</i>	CV-RT-15-016	AD	enamel	-12.21	22.54	200	CV
56.88	<i>Nesodon</i>	CV-RT-15-016	AE	enamel	-11.74	21.85	200	CV
59.08	<i>Nesodon</i>	CV-RT-15-016	AF	enamel	-11.74	21.01	200	CV
60.98	<i>Nesodon</i>	CV-RT-15-016	AG	enamel	-11.39	21.15	200	CV
63.02	<i>Nesodon</i>	CV-RT-15-016	AH	enamel	-11.22	21.55	200	CV
65.15	<i>Nesodon</i>	CV-RT-15-016	AI	enamel	-10.85	22.01	200	CV
66.55	<i>Nesodon</i>	CV-RT-15-016	AJ	enamel	-10.40	22.11	200	CV
3.79	<i>Nesodon</i>	CV-RT-15-016	B	enamel	-11.93	24.31	200	CV
5.79	<i>Nesodon</i>	CV-RT-15-016	C	enamel	-11.83	24.00	200	CV
7.52	<i>Nesodon</i>	CV-RT-15-016	D	enamel	-11.81	24.21	200	CV
9.09	<i>Nesodon</i>	CV-RT-15-016	E	enamel	-11.83	24.02	200	CV
11.21	<i>Nesodon</i>	CV-RT-15-016	F	enamel	-11.79	24.02	200	CV
13.22	<i>Nesodon</i>	CV-RT-15-016	G	enamel	-11.65	23.99	200	CV
14.62	<i>Nesodon</i>	CV-RT-15-016	H	enamel	-11.75	23.81	200	CV
16.55	<i>Nesodon</i>	CV-RT-15-016	I	enamel	-11.98	22.90	200	CV
17.94	<i>Nesodon</i>	CV-RT-15-016	J	enamel	-11.89	23.62	200	CV
19.7	<i>Nesodon</i>	CV-RT-15-016	K	enamel	-11.81	23.28	200	CV
21.58	<i>Nesodon</i>	CV-RT-15-016	L	enamel	-11.60	23.19	200	CV
23.14	<i>Nesodon</i>	CV-RT-15-016	M	enamel	-11.63	23.63	200	CV
25.22	<i>Nesodon</i>	CV-RT-15-016	N	enamel	-11.65	22.69	200	CV
26.54	<i>Nesodon</i>	CV-RT-15-016	O	enamel	-11.64	23.62	200	CV
28.22	<i>Nesodon</i>	CV-RT-15-016	P	enamel	-11.62	23.63	200	CV
29.8	<i>Nesodon</i>	CV-RT-15-016	Q	enamel	-11.53	23.36	200	CV
31.45	<i>Nesodon</i>	CV-RT-15-016	R	enamel	-11.35	23.54	200	CV
33.29	<i>Nesodon</i>	CV-RT-15-016	S	enamel	-11.66	22.88	200	CV
35.3	<i>Nesodon</i>	CV-RT-15-016	T	enamel	-12.13	22.99	200	CV
36.82	<i>Nesodon</i>	CV-RT-15-016	U	enamel	-12.28	22.48	200	CV
40.54	<i>Nesodon</i>	CV-RT-15-016	W	enamel	-12.19	22.85	200	CV
42.35	<i>Nesodon</i>	CV-RT-15-016	X	enamel	-12.02	22.17	200	CV

44	<i>Nesodon</i>	CV-RT-15-016	Y	enamel	-12.30	22.84	200	CV
45.47	<i>Nesodon</i>	CV-RT-15-016	Z	enamel	-12.17	23.67	200	CV
2.11	<i>Nesodon</i>	CV-RT-15-027	A	enamel	-10.99	23.04	82.2	CV
45.21	<i>Nesodon</i>	CV-RT-15-027	AA	enamel	-12.60	22.32	82.2	CV
3.94	<i>Nesodon</i>	CV-RT-15-027	B	enamel	-11.10	20.42	82.2	CV
5.67	<i>Nesodon</i>	CV-RT-15-027	C	enamel	-11.09	22.85	82.2	CV
6.93	<i>Nesodon</i>	CV-RT-15-027	D	enamel	-10.91	22.67	82.2	CV
8.58	<i>Nesodon</i>	CV-RT-15-027	E	enamel	-11.04	22.52	82.2	CV
10.06	<i>Nesodon</i>	CV-RT-15-027	F	enamel	-11.02	22.75	82.2	CV
11.32	<i>Nesodon</i>	CV-RT-15-027	G	enamel	-11.05	22.45	82.2	CV
12.84	<i>Nesodon</i>	CV-RT-15-027	H	enamel	-11.07	21.50	82.2	CV
14.03	<i>Nesodon</i>	CV-RT-15-027	I	enamel	-11.07	22.68	82.2	CV
15.46	<i>Nesodon</i>	CV-RT-15-027	J	enamel	-11.08	22.61	82.2	CV
16.85	<i>Nesodon</i>	CV-RT-15-027	K	enamel	-11.06	23.10	82.2	CV
18.55	<i>Nesodon</i>	CV-RT-15-027	L	enamel	-11.16	23.27	82.2	CV
19.99	<i>Nesodon</i>	CV-RT-15-027	M	enamel	-10.99	22.97	82.2	CV
21.86	<i>Nesodon</i>	CV-RT-15-027	N	enamel	-11.08	22.53	82.2	CV
1	<i>Nesodon</i>	CV-RT-15-027	NA	enamel	-11.78	22.27	82.2	CV
23.16	<i>Nesodon</i>	CV-RT-15-027	O	enamel	-11.19	22.21	82.2	CV
24.92	<i>Nesodon</i>	CV-RT-15-027	P	enamel	-11.31	23.08	82.2	CV
26.88	<i>Nesodon</i>	CV-RT-15-027	Q	enamel	-11.53	23.43	82.2	CV
28.77	<i>Nesodon</i>	CV-RT-15-027	R	enamel	-11.56	23.39	82.2	CV
30.12	<i>Nesodon</i>	CV-RT-15-027	S	enamel	-11.50	23.41	82.2	CV
31.88	<i>Nesodon</i>	CV-RT-15-027	T	enamel	-11.68	22.88	82.2	CV
33.26	<i>Nesodon</i>	CV-RT-15-027	U	enamel	-11.66	22.21	82.2	CV
35.8	<i>Nesodon</i>	CV-RT-15-027	V	enamel	-12.00	22.54	82.2	CV
37.26	<i>Nesodon</i>	CV-RT-15-027	W	enamel	-12.46	22.11	82.2	CV
39.06	<i>Nesodon</i>	CV-RT-15-027	X	enamel	-12.27	22.45	82.2	CV
41.05	<i>Nesodon</i>	CV-RT-15-027	Y	enamel	-12.43	22.45	82.2	CV
43.07	<i>Nesodon</i>	CV-RT-15-027	Z	enamel	-12.44	22.30	82.2	CV

1.61	<i>Nesodon</i>	RB3-RT-15-003	A	enamel	-10.12	25.93	160	RB3
48.98	<i>Nesodon</i>	RB3-RT-15-003	AA	enamel	-10.99	24.35	160	RB3
50.37	<i>Nesodon</i>	RB3-RT-15-003	AB	enamel	-11.07	23.97	160	RB3
51.8	<i>Nesodon</i>	RB3-RT-15-003	AC	enamel	-10.82	23.24	160	RB3
53.4	<i>Nesodon</i>	RB3-RT-15-003	AD	enamel	-10.83	23.03	160	RB3
54.5	<i>Nesodon</i>	RB3-RT-15-003	AE	enamel	-11.02	23.24	160	RB3
55.87	<i>Nesodon</i>	RB3-RT-15-003	AF	enamel	-10.65	24.10	160	RB3
59.35	<i>Nesodon</i>	RB3-RT-15-003	AH	enamel	-10.85	22.93	160	RB3
61.11	<i>Nesodon</i>	RB3-RT-15-003	AI	enamel	-10.79	23.39	160	RB3
3.18	<i>Nesodon</i>	RB3-RT-15-003	B	enamel	-10.51	25.11	160	RB3
5.42	<i>Nesodon</i>	RB3-RT-15-003	C	enamel	-10.44	24.96	160	RB3
7.1	<i>Nesodon</i>	RB3-RT-15-003	D	enamel	-10.68	23.68	160	RB3
9.11	<i>Nesodon</i>	RB3-RT-15-003	E	enamel	-10.42	22.18	160	RB3
11.05	<i>Nesodon</i>	RB3-RT-15-003	F	enamel	-10.62	22.54	160	RB3
13.04	<i>Nesodon</i>	RB3-RT-15-003	G	enamel	-10.77	23.21	160	RB3
14.64	<i>Nesodon</i>	RB3-RT-15-003	H	enamel	-10.77	22.58	160	RB3
16.38	<i>Nesodon</i>	RB3-RT-15-003	I	enamel	-10.81	23.99	160	RB3
18.35	<i>Nesodon</i>	RB3-RT-15-003	J	enamel	-10.68	23.02	160	RB3
19.84	<i>Nesodon</i>	RB3-RT-15-003	K	enamel	-10.83	21.34	160	RB3
21.2	<i>Nesodon</i>	RB3-RT-15-003	L	enamel	-10.53	21.93	160	RB3
24.27	<i>Nesodon</i>	RB3-RT-15-003	M	enamel	-10.52	21.45	160	RB3
26.43	<i>Nesodon</i>	RB3-RT-15-003	N	enamel	-10.51	21.76	160	RB3
27.71	<i>Nesodon</i>	RB3-RT-15-003	O	enamel	-10.48	22.60	160	RB3
29.97	<i>Nesodon</i>	RB3-RT-15-003	P	enamel	-10.38	24.53	160	RB3
32.03	<i>Nesodon</i>	RB3-RT-15-003	Q	enamel	-10.44	24.77	160	RB3
34	<i>Nesodon</i>	RB3-RT-15-003	R	enamel	-10.47	24.23	160	RB3
36.11	<i>Nesodon</i>	RB3-RT-15-003	S	enamel	-10.44	24.10	160	RB3
37.94	<i>Nesodon</i>	RB3-RT-15-003	T	enamel	-10.72	24.06	160	RB3
39.01	<i>Nesodon</i>	RB3-RT-15-003	U	enamel	-10.60	24.52	160	RB3
40.53	<i>Nesodon</i>	RB3-RT-15-003	V	enamel	-10.70	23.73	160	RB3

41.96	<i>Nesodon</i>	RB3-RT-15-003	W	enamel	-10.88	24.03	160	RB3
43.81	<i>Nesodon</i>	RB3-RT-15-003	X	enamel	-10.84	23.83	160	RB3
45.82	<i>Nesodon</i>	RB3-RT-15-003	Y	enamel	-11.06	22.50	160	RB3
47.48	<i>Nesodon</i>	RB3-RT-15-003	Z	enamel	-10.96	23.27	160	RB3
3.82	<i>Homalodotherium</i>	RB3-RT-15-007	A	enamel	-10.35	25.12	177.5	RB3
4.48	<i>Homalodotherium</i>	RB3-RT-15-007	B	enamel	-10.16	24.92	177.5	RB3
6.39	<i>Homalodotherium</i>	RB3-RT-15-007	C	enamel	-10.38	24.48	177.5	RB3
8.31	<i>Homalodotherium</i>	RB3-RT-15-007	D	enamel	-10.33	23.81	177.5	RB3
9.77	<i>Homalodotherium</i>	RB3-RT-15-007	E	enamel	-10.24	23.99	177.5	RB3
10.84	<i>Homalodotherium</i>	RB3-RT-15-007	F	enamel	-10.29	23.99	177.5	RB3
12.95	<i>Homalodotherium</i>	RB3-RT-15-007	G	enamel	-10.46	23.10	177.5	RB3
14.38	<i>Homalodotherium</i>	RB3-RT-15-007	H	enamel	-10.66	22.80	177.5	RB3
16.04	<i>Homalodotherium</i>	RB3-RT-15-007	I	enamel	-10.70	22.69	177.5	RB3
17.35	<i>Homalodotherium</i>	RB3-RT-15-007	J	enamel	-10.39	23.87	177.5	RB3
19.01	<i>Homalodotherium</i>	RB3-RT-15-007	K	enamel	-10.64	23.90	177.5	RB3
